

THE FUNDAMENTALS AND APPLICATIONS OF PHASE  
FIELD METHOD IN QUANTITATIVE  
MICROSTRUCTURAL MODELING

DISSERTATION

Presented in Partial Fulfillment of the Requirements for  
the Degree Doctor of Philosophy in the  
Graduate School of The Ohio State University

By

Chen Shen, M.S.

\* \* \* \* \*

The Ohio State University

2004

Dissertation Committee:

Yunzhi Wang, Adviser

Glenn S. Daehn

Suliman A. Dregia

Michael J. Mills

Approved by

---

Adviser

Department of Materials  
Science and Engineering

© Copyright by

Chen Shen

2004

## ABSTRACT

The key to predicting and therefore controlling properties of materials is the knowledge of microstructure. As computer modeling and simulation is becoming an important part of materials science and engineering, there is an ever-increasing demand for quantitative models that are able to handle microstructures of realistic complexity at length and time scales of practical interest. The phase field approach has become the method of choice for modeling complicated microstructural evolutions during various phase transformations, grain growth and plastic deformation. Using gradient thermodynamics of non-uniform systems and Langevin dynamics, the method characterizes arbitrary microstructures and their spatial-temporal evolution with field variables, and is capable of simulating microstructures and their evolution under various realistic conditions.

However, the adoption of the phase field method in practical applications has been slow because the current phase field microstructure modeling is qualitative in nature. In this thesis, recent efforts in developing the phase field method for quantitative microstructure modeling are presented. This includes extension of the phase field method to situations where nucleation, growth and coarsening occur concurrently, incorporation of anisotropic elastic energy into the nucleation activation energy, and comparison of phase field kinetics for diffusion-controlled phase transformations with Johnson-Mehl-Avrami-Kolmogorov (JMAK) theory. The most recent extensions of

the phase field method to modeling dislocation networks, dislocation core structures and partial dislocations, and dislocation interactions with  $\gamma/\gamma'$  microstructures in superalloys are also presented. The length scale limitations and practical approaches to increase simulation length scales for quantitative modeling are discussed for a quite general category of phase field applications.

These extensions enable various new understandings of microstructure. For example, coherent precipitates are found to behave similar to dislocations and grain boundaries, causing solute segregation, correlated nucleation and autocatalytic effect. The overall kinetics in diffusion-controlled precipitation agrees with the JMAK prediction only at early stages, and due to soft-impingement and the Gibbs-Thomson effect the later kinetics could deviate considerably. The new formulations of the crystalline energy and gradient energy in phase field model of dislocations allow to study complex dislocation structures, including networks and dissociated nodes, in a self-consistent way. The introduction of  $\gamma$ -surfaces for constituent phases enables treating dislocation motion in multi-phase microstructure in one model. Finally, the discussion on the length scale clarifies the applicability of the conventional approaches for increasing simulation length scales, and their respective consequence to the quantitative results.

## ACKNOWLEDGMENTS

I came to the department of MSE with a different background and little knowledge on materials science (metallurgy, plasticity, and so on). Prof. Yunzhi Wang carried me through that hard initial time and let me start my first day of research in materials science. Most importantly, as the adviser, he has constantly supported me over these years, with great tolerance to allow me to do things I felt interested in. My sincere thanks should go to him first. Prof. Glenn Daehn, Prof. Suliman Dregia, and Prof. Michael Mills, who served as the dissertation committee members, brought my sight out of computer simulations. They let me think computer simulations in a broad background of both experiments and theories. I received many creative suggestions from Prof. Ju Li. His insight in crystalline defects inspired a number of exciting simulation problems for dislocation. I will always keep a good memory of the days with my group members, from whom, especially Kaisheng Wu and Qing Chen, I learned a lot of things. During my early time of dislocation modeling, Yongmei Jin and Yu Wang kindly offered me their firsthand understanding on the phase field dislocation model. I should not forget Prof. Qiangji Zhang and Prof. Ming Lu at Fudan University. They are the mentors that brought me to scientific research, and who trusted me and encouraged me to make best effort along that path.

This is probably the first time that I put into words to thank my parents. They gave me the life, and they told me I can do well since the day I left home. My dear

wife, Yuexiong, seems always happy to make me some trouble, never missed a chance to stand by me in front of real troubles. My son came to this world during my thesis writing. Without the great help from my parents in law, I would not be able to put down meaningful words, and our tiny boy would not smile that beautifully.

## VITA

1996 .....	B.S., Fudan University, Shanghai, China.
2001 .....	M.S., Ohio State University, Columbus, Ohio
1998-present .....	Graduate Research Associate, Ohio State University, Columbus, Ohio.

## PUBLICATIONS

### Journal papers

C. Shen and Y. Wang, “Incorporation of  $\gamma$ -surface to phase field model of dislocations: simulating dislocation dissociation in fcc crystals”. *Acta Materialia*, 52:683-691, 2004.

J.P. Simmons, Y.H. Wen, C. Shen, C. Woodward and Y. Wang, “Microstructural development involving nucleation and growth phenomena simulated with the phase field method”. *Materials Science and Engineering A*, 365:136–143, 2004.

C. Shen, Q. Chen, Y. Wang, Y.H. Wen, and J.P. Simmons, “Increasing length scale of quantitative phase field modeling of growth-dominant or coarsening-dominant process”. *Scripta Materialia*, 50(7):1023–1028, 2004.

C. Shen, Q. Chen, Y. Wang, Y.H. Wen, and J.P. Simmons, “Increasing length scale of quantitative phase field modeling of concurrent growth and coarsening processes”. *Scripta Materialia*, 50(7):1029–1034, 2004.

C. Shen and Y. Wang, “Phase field model of dislocation networks”. *Acta Materialia*, 51:2595–2610, 2003.

C. Shen and Y. Wang, “Modeling dislocation network and dislocationprecipitate interaction at mesoscopic scale using phase field method”. *International Journal for Multiscale Computational Engineering*, 1(1):103–117, 2003.

Y.H. Wen, J.P. Simmons, C. Shen, C. Woodward and Y. Wang, “Phase-field modeling of bimodal particle size distributions during continuous cooling”. *Acta Materialia*, 51:1123–1132, 2003.

J.P. Simmons, C. Shen and Y. Wang, “Phase field modeling of simultaneous nucleation and growth by explicit incorporating nucleation events”. *Scripta Materialia*, 43:935–942, 2000.

### Conference proceedings

C. Shen, M.J. Mills and Y. Wang, “Modeling dislocation dissociation and cutting of g’ precipitates in Ni-based superalloys by the phase field method”. *Materials Research Society Symposium Proceedings*, 753:BB5.21.1, 2003.

C. Shen, A. Kazaryan, P.M. Anderson and Y. Wang, “Phase field modeling of dislocation network coarsening, dislocation-impurity and dislocation-precipitate interactions”. *Proceedings of the second International Conference on Computational Nanoscience and Nanotechnology*, M. Laudon and B. Romanowicz, Eds., 259–262, Computational Publications, Cambridge, MA, 2002.

C. Shen; J.P. Simmons, K. Wu and and Y. Wang, “Development of computational tools for microstructural engineering of Ni-based superalloys by means of the phase field method”. *Materials Design Approaches and Experiences*, J-C. Zhao, M. Fahrmann and T.M. Pollock, Eds., 57–74, TMS, Warrendale, PA, 2001.

J.P. Simmons, C. Shen, and Y. Wang, “Phase field approach to transformations involving concurrent nucleation and growth”. *Materials Research Society Symposium Proceedings*, 580:417, 2000.

A. Kazaryan, C. Shen, Y. Wang and B.R. Patton, “Generalized phase-field modeling of microstructural evolution in solids: incorporation of rigid-body motion of grains and mobility/energy anisotropy of grain boundaries”. *Phase Transformations and Evolution in Materials*, P.E.A. Turchi and A. Gonis, Eds., TMS, Warrendale, PA, 2000.

## **FIELDS OF STUDY**

Major Field: Materials Science and Engineering

Studies in Microstructure and dislocation modeling: Prof. Yunzhi Wang

## TABLE OF CONTENTS

	Page
Abstract . . . . .	ii
Acknowledgments . . . . .	iv
Vita . . . . .	vi
List of Tables . . . . .	xii
List of Figures . . . . .	xiii
Chapters:	
1. Introduction . . . . .	1
1.1 Motivations . . . . .	1
1.2 Organization of the thesis . . . . .	4
2. Phase field method . . . . .	7
2.1 Energy and equations of motion . . . . .	7
2.2 The coarse-grain approximation . . . . .	11
2.3 Statistical mechanical basis of the phase field dynamic equations . .	14
2.3.1 Conserved variable: Cahn-Hilliard equation . . . . .	18
2.3.2 Non-conserved variable: Allen-Cahn equation . . . . .	22
2.4 Phase field model and sharp interface models . . . . .	23
2.4.1 Non-conserved field . . . . .	24
2.4.2 Conserved field . . . . .	26
2.4.3 Asymptotic analyses . . . . .	28
2.5 Phase field microelasticity theory . . . . .	31
2.5.1 Homogeneous elastic modulus ( $C_{ijkl} = C_{ijkl}^0$ ) . . . . .	34

2.5.2	Inhomogeneous elastic modulus ( $C_{ijkl} = C_{ijkl}(\mathbf{x})$ ) . . . . .	37
2.6	Some discussion on phase field applications to coherent phase transformations . . . . .	40
3.	Computational model for microstructural evolution via concurrent nucleation, growth, and coarsening . . . . .	45
3.1	Introduction . . . . .	45
3.2	The explicit nucleation algorithm . . . . .	49
3.3	Computation of nucleation rate . . . . .	53
3.4	Simulation of nucleation, growth, and coarsening under isothermal condition . . . . .	57
3.5	Modeling coherent nucleation . . . . .	64
3.5.1	Coherency strain energy in nucleation driving force . . . . .	66
3.5.2	Simulation of strain induced nucleation . . . . .	71
3.6	Comparison to JMAK theory with soft impingement . . . . .	83
3.6.1	Growth of single precipitate . . . . .	89
3.6.2	Periodic versus random array of precipitates . . . . .	94
3.6.3	Nucleation, growth, and coarsening . . . . .	99
3.7	Summary . . . . .	107
4.	Phase field model for dislocations . . . . .	110
4.1	Field description of dislocations . . . . .	112
4.2	Formulation of energies and equation of motion . . . . .	115
4.2.1	Original formulations . . . . .	116
4.2.2	Limitations . . . . .	118
4.2.3	Extension and generalization . . . . .	121
4.2.4	Dimensionless form of energies and equation of motion . . .	128
4.3	Simulation of dislocation networks . . . . .	129
4.3.1	Two coplanar dislocation loops . . . . .	131
4.3.2	Two dislocation loops from intersecting slip planes . . . .	131
4.3.3	Dislocation networks on a single slip plane . . . . .	133
4.3.4	Dislocation network with free surface . . . . .	138
4.4	Introducing $\gamma$ -surface to crystalline energy . . . . .	141
4.5	Simulation of dislocation dissociation . . . . .	145
4.5.1	Dissociation of a straight perfect dislocation into two Shockley partials . . . . .	145
4.5.2	Dissociation of dislocation nodes . . . . .	152
4.5.3	Dissociation of a bent dislocation on two intersecting planes	153
4.6	Summary . . . . .	155

5.	Dislocation-microstructure interaction in Ni-based superalloys . . . . .	158
5.1	Dislocation glide in $\gamma$ channels . . . . .	159
5.2	Threading dislocation in multilayer $\gamma/\gamma'$ thin film . . . . .	165
5.3	Dislocation dissociation and cutting of $\gamma'$ precipitates . . . . .	166
5.3.1	Dissociation of superdislocation in $\gamma'$ phase . . . . .	171
5.3.2	Straight screw dislocation cutting a flat $\gamma/\gamma'$ interface . . .	172
5.3.3	Dislocation interactions with $\gamma'$ particles . . . . .	174
6.	Length scale and quantitative phase field modeling . . . . .	176
6.1	The length scales of a phase field model . . . . .	176
6.2	Increase simulation length scale for individual processes . . . . .	179
6.2.1	Anti-phase domain (APD) coarsening and grain growth . .	180
6.2.2	Precipitate growth . . . . .	183
6.2.3	Coarsening . . . . .	185
6.2.4	Development of coherent microstructures . . . . .	185
6.3	Increase simulation length scale for concurrent processes . . . .	187
6.4	Summary and discussion . . . . .	196
7.	Conclusions . . . . .	199
7.1	Conclusions . . . . .	199
7.2	Directions for future research . . . . .	201

## Appendices:

A.	Strain energy of a two-dimensional coherent precipitate . . . . .	204
B.	Concentrations at a curved interface . . . . .	206
	Bibliography . . . . .	209

## LIST OF TABLES

<b>Table</b>	<b>Page</b>
3.1 Elastic energies near a cubic precipitate calculated by Eqs.(3.34) and (3.35) and the volume driving force for nucleation calculated from $16\pi\sigma^3/3\Delta f^2 = 50k_B T$ . . . . .	71
3.2 Dimensionless variables. . . . .	74
3.3 Values of Avrami exponent (from ref. [1]). $d$ is the spatial dimensionality.	85
3.4 The parameters employed in the nucleation rate (Eq.(3.21)). . . . .	100
4.1 Scaling factors that reduce each physical parameter into a dimensionless quantity. . . . .	129
4.2 The coordinates of the selected fitting points (Fig. 4.15) on the $\gamma$ -surface and the corresponding energy. . . . .	146
4.3 The fitted expansion coefficients in Eq.(4.26) (in unit of mJ/m <sup>2</sup> ). . .	146
4.4 Elastic constants of Al [2] and Pd <sup>1</sup> [3], Pd <sup>2</sup> [4], in unit of ( $\times 10^{10}$ Pa). .	147
5.1 The fitted expansion coefficients in Eq.(5.3) (in unit of mJ/m <sup>2</sup> ). . . .	171
6.1 Summary of the treatments for individual processes to produce right kinetics at a wider interface. . . . .	197

## LIST OF FIGURES

<b>Figure</b>	<b>Page</b>
2.1 Schematic drawing of the coarse-grained free energy $f(c)$ and the thermodynamic free energy $\tilde{f}(c)$ . The thermodynamic extrapolation into the two-phase region is represented by the dashed curves. After Langer [5].	14
2.2 (a) Free energy for the non-conserved system, and (b) the interface profile in the local frame. . . . .	25
2.3 a) Free energy for the conserved system, and (b) the interface profile in the local frame. . . . .	27
2.4 Schematic drawing of the incoherent (solid line) and coherent (dotted line) free energies in an elastically isotropic solid solution. The equilibrium compositions in both cases are determined by the common tangent construction. $c_0$ is the average composition (after [6]). . . . .	43
3.1 Dark-field transmission electron micrograph of $\gamma'$ Ni <sub>3</sub> Al precipitates in Ni-17at.%Al, from Ref. [7]. . . . .	46
3.2 The fluctuations simulated in a mesoscale phase field model are much more extended in the space than the actual ones. Since nucleation events occur much less frequently due to the use of the time scale for growth, to maintain a same magnitude of the nucleation rate the amplitude of the fluctuations is artificially increased. . . . .	49
3.3 Mesoscale phase field cells and the uniformly divided sub-cells of size similar to a critical nucleus. . . . .	50
3.4 Double-well free energy given by Eq.(3.16). The nucleation driving force $\Delta f$ at composition $c_0$ is obtained by the parallel tangent construction. Shown also is the approximated driving force $\Delta f'$ used in the simulation. . . . .	57

3.5	Simulated microstructures of concurrent nucleation, growth, and coarsening at reduced time (a) $t^* = 20$ , (b) $t^* = 100$ , (c) $t^* = 200$ , (d) $t^* = 1000$ , (e) $t^* = 4000$ , (f) $t^* = 20000$ . . . . .	59
3.6	(a) Average nucleation rate and area fraction of the transformed phase. (b) The transformation fraction plotted in a larger time range. . . . .	61
3.7	(a) Mean radius of precipitates and (b) the number of precipitates. . . . .	62
3.8	Size distribution of precipitates at stages of nucleation, growth, and coarsening. . . . .	63
3.9	A mesoscale microstructure has a narrower spectrum than a critical nucleus in the reciprocal space. . . . .	68
3.10	The chemical free energies (regular solution model, Eq.(3.36)) at $1000K$ and $1085K$ . . . . .	75
3.11	The chemical driving force for nucleation at $1000K$ . . . . .	76
3.12	Simulated coherent nucleation near a pre-existing particle formed and equilibrated at a higher temperature in an elastically anisotropic medium. (a)-(c) $\epsilon^T = 0.5\%$ , (d)-(f) $\epsilon^T = 1.6\%$ . . . . .	78
3.13	Nucleation driving forces along the elastically soft direction at (a) $\epsilon^T = 0.5\%$ and (b) $\epsilon^T = 1.6\%$ . The profiles are taken from the precipitate:matrix interface (left end of the x-axis). The distance $x^*$ is normalized by the edge length of the particle. . . . .	79
3.14	Simulated microstructures during a concurrent nucleation and growth process in a uniform matrix with $\epsilon^T = 1.6\%$ ((a)-(c)) and $\epsilon^T = 3.2\%$ ((d)-(f)). $t^*$ is reduced time. . . . .	81
3.15	The relative error $\delta =  \Delta E_{int}^{el} - \Delta E_{int}^{el,approx}  / \Delta E_{int}^{el}$ vs. ratio of the radii of the particle ( $R_0$ ) and the nucleus ( $r_0$ ), where $\Delta E_{int}^{el}$ is calculated numerically from Eq.(3.26) and $\Delta E_{int}^{el,approx}$ is from the approximate solution Eq.(3.42). The particular configuration for the calculation is shown by the inset. . . . .	82

3.16 Comparison of (a) area fraction and (b) concentration profiles from the phase field equation, diffusion equation with constant $M$ , with Gibbs-Thomson correction, and with constant $D$ . . . . .	91
3.17 Plot of the Avrami exponent for single precipitate growth. . . . .	93
3.18 Effect of finite initial precipitate size on the Avrami exponent. . . . .	94
3.19 Final microstructures of the randomly (a-c) and the periodically (e-f) arranged precipitates. Different numbers of precipitates are used: (a,d) $N=16$ , (b,e) 64, and (c,f) 256. The initial precipitates are equal in size.	96
3.20 Transformed area fractions of the periodic and the random precipitates with different number: (a) $N=16$ , (b) 64, and (c) 256. . . . .	97
3.21 Plot of the Avrami exponent for growth of periodic and random precipitates. . . . .	98
3.22 Final microstructures: (a-j) correspond to the tests 1 to 10 in Table 3.4.101	
3.23 Plot of the Avrami exponent for concurrent nucleation, growth and coarsening (upper panel) and the nucleation rate (lower panel). . . . .	102
3.24 Plot of the Avrami exponent vs. the extended transformed fraction from a simple analytic model with exponentially decaying nucleation rate and growth rate. . . . .	105
4.1 Lattice correspondence between an edge dislocation and a sheared thin plate. . . . .	112
4.2 Field description of (a) a dislocation loop in terms of (b) a thin platelet by phase field $\eta$ , corresponding to (c) the atomic lattice picture. Typical profiles of $\eta$ across a dislocation line (the green bar in (b)) are plotted at (d) microscopic and (e) mesoscopic scales, depending on the choice of model parameters. . . . .	114
4.3 (a) Burgers vector relationship among perfect dislocations on (111) slip planes in an fcc crystal; (b) As two dislocations with $\mathbf{b}_1$ and $\mathbf{b}_2$ encounter (in the dashed box) they form a new dislocation with $-\mathbf{b}_3$ , which follows the Burgers vector relationship in (a). . . . .	120

4.4	The Burgers vectors of the three types of perfect dislocations on the (111) slip plane of an fcc crystal. . . . .	123
4.5	A contour plot of the crystalline energy density (given by the integrand in Eq.(4.17)) projected on the (111) plane. The minima are located at the centers of the circular contours and they correspond to the lattice sites of an fcc crystal. This construction reflects the equivalence of representing a slip by either ( $\eta_1 = \eta_2 = 1, \eta_3 = 0$ ) or ( $\eta_1 = \eta_2 = 0, \eta_3 = -1$ ). . . . .	125
4.6	Distribution of $\eta$ values on the cross-section plane of an edge dislocation, where the gray area ( $\eta = 1$ ) represents the slipped region and the white area ( $\eta = 0$ ) represents the unslipped region. Cell $C$ contains the dislocation core. The right figure corresponds to a larger scale meshing ( $l_0 > d$ , where $d$ is the interplanar spacing of the slip plane). The shadowed region is the ‘resolvable’ $\eta$ distribution while the actual distribution is indicated by the solid gray region. . . . .	130
4.7	Reaction between two dislocation loops on a (111) plane of an fcc crystal: (a) the initial configuration of the loops and their Burgers vectors and sense vectors; (b) the loops expand by the applied shear stress $\tau$ , react and form a new dislocation segment of Burgers vector $\mathbf{b}_2$ ; (c) result obtained from the original model, no interaction taking place between the two expanding loops. The relation among the Burgers vectors is defined in Fig.4.4. . . . .	132
4.8	Reaction between two dislocation loops from different slip planes: (a) initial configuration with one loop placed on the (111) plane with $\mathbf{b}_1 = [0\bar{1}1]/2$ and the other on the ( $\bar{1}\bar{1}\bar{1}$ ) plane with $\mathbf{b}_2 = [\bar{1}\bar{1}0]/2$ ; (b) under the applied stress the two loops expand and react, forming an immobile dislocation segment with $\mathbf{b}_3 = [101]/2$ which belongs to neither of the initial slip plane; (c) result obtained using the original phase field model, no reaction taking place. . . . .	133
4.9	Evolution of a dislocation network on a (111) plane. The network consists of two arrays of near screw dislocations of $\mathbf{b}_1$ and $\mathbf{b}_2$ that defined in Fig. 4.4. (a) Initial configuration with the sense vectors specified, (b)-(f) the evolution of the network (b) $t^* = 5$ , (c) $t^* = 15$ , (d) $t^* = 18$ , (e) $t^* = 40$ , (f) $t^* = 75$ . Note in (d) decomposition of the network starts to occur (see the circle). . . . .	134

4.10 The schematic drawing (a) illustrates the two types of the node (A and B) presented in the network in Fig. 4.9. The nodes C and D are equivalent to A and B respectively, except that their sense directions are reversed. (b) and (c) show the nodal reaction at the nodes A and B.	135
4.11 Time evolution of a dislocation network on (111) plane consisting of three types of dislocations loops of $\mathbf{b}_1$ , $\mathbf{b}_2$ and $\mathbf{b}_3$ . (a) $t^* = 2.5$ , (b) $t^* = 54$ , (c) $t^* = 12.5$ , (d) $t^* = 25$ , (e) $t^* = 50$ , (f) $t^* = 75$ , the sense vectors in the same color have the same Burgers vectors. . . . .	137
4.12 Profiles of $\eta_1$ , $\eta_2$ , and $\eta_3$ along the dashed line in Fig. 4.9(e) indicate the existence of sharp interfaces (marked by $\mathbf{I}$ ). These interfaces are actually the boundary between two equivalent representations of slip and also the initial location of the dislocation lines. The actual present locations are marked by $\mathbf{I}'$ . . . . .	139
4.13 A particular distribution of $\eta$ produces three parallel dislocations of $b$ in the matrix, while due to the periodic boundary condition, an opposite dislocation of $3b$ at the right hand side boundary. . . . .	140
4.14 Evolution of a random dislocation network with non-zero net Burgers vector. The boundaries are set as free surfaces where elastic stress is zero. The initial configuration is given in (a), and (b)-(d) correspond to reduced time $t^* = 10, 50, 300$ . The colors from blue, green, to red represent the increasingly higher energy density. . . . .	142
4.15 The coordinate system $(y, z)$ chosen on the (111) slip plane for the $\gamma$ -surface and its relation to the coordinate system $(x_0, y_0, z_0)$ of the fcc lattice. $\mathbf{b}_1$ , $\mathbf{b}_2$ , and $\mathbf{b}_3$ are the three Burgers vectors on the (111) plane and $a$ is the lattice parameter. The fitting points $A$ , $G$ , and $T$ are marked in the graph. Point $G_1$ is located in the middle of $A$ and $G$ . Points $T_{1-3}$ are uniformly located between $A$ and $T$ . . . . .	144
4.16 The equilibrium core profiles of infinitely long straight dislocations in Al obtained by the phase field simulation. The dotted lines are for an edge dislocation and the solid lines for a screw dislocation. $\mathbf{b}_0$ is the Burgers vector of the perfect dislocation. . . . .	148

4.17 The equilibrium core profiles of infinitely long dislocations in Pd obtained by the phase field simulation. The dotted lines are for an edge dislocation and the solid lines for a screw dislocation. $\mathbf{b}_0$ is the Burgers vector of the perfect dislocation. . . . .	149
4.18 Effect of the gradient-energy coefficient $\xi^*$ on the dislocation core profile. The vertical dashed lines indicate the position of the two partial peaks for $\xi^* = 0.1$ . Reducing $\xi^*$ does change the core profile but has little influence on the peak spacing. . . . .	151
4.19 Three perfect dislocations initially joined at a node as shown in the inset dissociate into an extended node with partial dislocations enclosing a stacking fault. Thompson notation is used in identifying the partial dislocations. The shade of gray in the plot corresponds to the crystalline energy density ( $f$ in Eq.(4.26)). . . . .	153
4.20 Three perfect dislocations initially joined at a node as shown in the inset dissociate into a contracted node (a). Thompson notations are used for the perfect and partial dislocations. A close look at the node (b) reveals a high-energy stacking fault region at the node (e.g., a-c-b-b-a-c stacking sequence), as schematically shown in (c). The size of the node is determined by the balance between the stacking fault energy and the line tension of the partials. . . . .	154
4.21 A periodic array of perfect dislocations originally lie on the $(111)$ and $(\bar{1}\bar{1}1)$ slip planes (a). They have the same Burgers vector $a[\bar{1}10]/2$ and alternating sense vectors. The dislocations dissociate into Shockley partials (b) and result in stair-rod segments as shown by the enlarged image in (c). . . . .	155
5.1 (a) Schematic diagram showing the geometry used in the simulation. The red dotted line is the dislocation loop that is confined in a $\gamma$ layer. (b) Simulation result of the $S$ dependence of the critical resolved stress $\tau$ (in reduced unit) that drives the dislocation loop through the $\gamma$ layer, where $S$ is the width of the layer (in reduced unit). . . . .	160
5.2 The migration of dislocation is approximated by a translation from the solid line to the dashed line over a distance of $dx$ . The swept area, denoted by the shadow lines, is $Sdx$ . . . . .	160

5.3 A $1/2\langle 110 \rangle$ type screw dislocation enters $\gamma$ channels in a cuboidal $\gamma/\gamma'$ microstructure. (a) schematic drawing of the $\gamma/\gamma'$ microstructure. Periodic boundary condition is used in all three directions. The glide plane in the $\gamma$ channel is shown by the shaded area. (b)-(f) Channel filling processes by the matrix dislocations at different lattice misfit (only the glide plane is shown). The dislocation lines are given by the boundaries between regions of different colors. The two segments in the horizontal and the $60^\circ$ channels appear symmetrical in (b, c) where $\gamma/\gamma'$ misfit strain is small ( $\epsilon^T = 0.56\%$ ). It becomes non-symmetrical in (d, e) where $\epsilon^T = 5.6\%$ and in (f) where $\epsilon^T = -5.6\%$ . . . . .	162
5.4 Contour plot of the resolved misfit stress (in reduced unit) on the dislocation, (a) with positive misfit (lattice parameter of $\gamma'$ is greater than that of $\gamma$ ), (b) with negative misfit, and (c) with positive misfit and isotropic elastic moduli. . . . .	164
5.5 Phase field modeling of threading dislocations propagating in multi-layer $\gamma/\gamma'$ thin film. (a) Co-deformation across layers at small lattice mismatch (0.2%) and (b) confined layer slip at larger lattice mismatch (1%). $t^*$ is the reduced time. The crystalline energies of the $\gamma$ and $\gamma'$ phases are assumed the same in these simulations, which is different from the simulations shown in Fig. 5.3. . . . .	167
5.6 Contour plot of the $\gamma$ -surface of (111) slip plane of $\text{Ni}_3\text{Al}$ (in $\text{mJ/m}^2$ ). The two types of dislocation dissociation given in Eqs.(5.1) and (5.2) are represented by the dashed and the solid lines, respectively. . . . .	168
5.7 A combined $\gamma$ -surface of $\gamma$ and $\gamma'$ phases each given by Eq.(5.3). Also shown are Burgers vectors of perfect (solid lines) and partial dislocations (dashed lines) in each phase. . . . .	172
5.8 Energy profile of the dissociated dislocation in $\gamma'$ phase after relaxation. $a$ is the lattice parameter of $\gamma$ phase. The flat region in the middle corresponds to the APB energy. The other two local minima correspond to the CSF energy. . . . .	173

5.9 Snap shots of profiles of two extended dislocations at consecutive moments from (a) to (c). The left side is in $\gamma'$ phase and the right side in $\gamma$ phase. The $\gamma/\gamma'$ interface is marked by the dashed line. Dislocations move toward the left side under an applied stress. At moment (b) one dislocation enters the $\gamma'$ phase, leaving an APB behind. At moment (c) a similar configuration to Fig. 5.8 is formed when the second extended dislocation enters the $\gamma'$ phase. . . . .	174
5.10 A screw dislocation with Burgers vector $1/2\langle 110 \rangle$ moves from the top to the bottom of the (111) slip plane under an applied stress, encountering two $\gamma'$ particles of different sizes. The dislocation bypasses the large particle while cuts through the small one. An APB is left in the small particle as the dislocation cuts through. The contrast in the figure reflects the relative value of the crystalline energy density. . . . .	175
6.1 A double-well free energy with two minima at $\phi_1$ and $\phi_2$ . $\Delta f_0$ is defined as the maximum height from the common tangent to the free energy curve. . . . .	177
6.2 (a) Simulated shrinkage rate of an island antiphase domain. The inset shows the initial configuration ( $\eta = 1$ in the island and -1 in the matrix). The solid line is the analytic solution, $R_0^2 - R^2(t) = 2M\kappa t$ , by integrating Eq.(2.50) at $H = 0$ . Domain boundary profiles across the interface ( $\eta = 0$ ) at different sizes are shown in (b) in three cases with $\kappa$ fixed and $\Delta f_0$ varied by two orders of magnitude. . . . .	182
6.3 Simulated growth kinetics of a 1D precipitate (a) with the initial configuration shown in the inset ( $c=1$ in the precipitate (in gray) and -0.77 in the matrix (in white)). The solid curve is the solution from the corresponding sharp-interface model. Concentration profiles across the interface at a particular moment are given in (b) for three cases with $\Delta f_0$ fixed and $\kappa$ varied by two orders of magnitude. The positions of interfaces are determined by the intersections of the concentration profiles with $c=0$ . . . . .	184

6.4 Simulated (a) coarsening kinetics for the configuration shown in the inset and (b) concentration profiles across the interface in three cases with $\kappa\Delta f_0$ fixed while $\kappa/\Delta f_0$ varied by two orders of magnitude. $R1$ and $R2$ are the positions of interface identified by $c=0$ . (c) The deviation of chemical potential $\delta\mu$ at different particle radii agrees with the predictions by the Gibbs-Thomson equation (solid line). Note that deviations occur as the particle radius becomes commensurate with the interface thickness. . . . .	186
6.5 (a) Contour plot of the free energy surface given by Eq.(6.5) on $\eta$ - $c$ plane. (b) Composition and lro parameter profiles across an interface. The profiles in (b) are mapped onto the contour plot in (a) (open circles) to show the relaxation path of both $c$ and $\eta$ on the $f$ - $c$ - $\eta$ surface during precipitate growth. . . . .	190
6.6 Modification of the $f$ - $c$ - $\eta$ surface (a) by a specially constructed function (b) to lower locally the energy hump between the two equilibrium phases to widen the interface thickness. The $f$ - $c$ - $\eta$ surface after the modification is shown in (c) and its contour plots on the $c$ - $\eta$ plane is shown in (d) (dash lines). For comparison, the contours of the free energy surface shown in (a) are also plotted in (d) by the solid lines. It is readily seen that the free energy surface along the $\eta = 0$ line that determines the growth kinetics is unchanged. . . . .	193
6.7 Comparison of composition profiles across an interface produced by the original and modified local free energy $f(c, \eta_1, \eta_2, \eta_3)$ . The interfacial energies associated with the two profiles are the same. . . . .	194
6.8 Composition profiles across the interface at different times obtained from the original (solid lines) and modified (dash lines) local free energy function. The well matched interface positions at all times indicate that the growth kinetics is the same in both cases even though the interface thickness is different. . . . .	195
6.9 Microstructural evolutions predicted by the conventional approach (a-d) and the new approach (e-h), starting from the same initial configuration consisting of 50 randomly distributed nuclei. It is readily seen that the conventional approach predicts a much slower growth rate. The system size is 92nm×92nm. . . . .	197
A.1 Vectors in $I_1$ . . . . .	205

B.1 Gibbs-Thomson effect on the molar free energy. . . . .	207
--	-----

# CHAPTER 1

## INTRODUCTION

### 1.1 Motivations

Materials of interest to metallurgical and materials science are mostly crystalline. A crystal is often simplified as a periodic array of atoms that extend in the infinite space. Real materials, however, always contain defects against this perfection. Surface, for example, exists because of the finite volume of the material body. Thermal vacancies are generated at finite temperature because of the entropy. More importantly, many defects are in fact introduced in the material on purpose during the manufacturing process. For example, cold work, a means to increase the dislocation density, is now a matured technique to increase the strength of metals. Hard particle inclusions and precipitates are often produced to improve the creep-resistance of materials at high-temperature. All these defects, which are generally referred to as microstructures, can have great influence on the macroscopic properties of materials. The insight knowledge of these defects thus becomes one of the most important goals of materials science.

The modern understanding of material properties is built upon the understanding of material structure via two constituents: the building blocks and the assembly

laws [8]. The building blocks, such as atoms, unit cells, grains, form a material body in a structural hierarchy. Each level has distinctive length scale and the associated defects. Metallurgists and materials scientists are mostly concerned with microstructures at mesoscopic level. Today, various experimental techniques have enabled people not only to reveal the crystal structure with an X-ray or electron beam, but also to directly observe microstructures at the atomic level. These advances clearly promote a deeper insight to the connections between the property and the underlying structure. Meanwhile, a comprehensive understanding of the dependence of the microstructure on the processing parameters solely by the experimental approach still poses a significant cost.

The goal of a microstructure modeling is thus twofold: it is hoped to reveal the connection between a microstructure and the processing parameters through a virtual experiment, i.e., to solve the governing physical laws; secondly, it is hoped to predict material properties for a given microstructure and furthermore the general dependence of the property on the microstructure. Although various fundamental aspects of microstructures have been studied in depth for decades, many problems associated with realistic microstructures are still extremely difficult to solve at this moment. The difficulties exist in several aspects. Firstly, real microstructures are inherently complex. They often involve inseparable multiple physical or chemical driving forces and simultaneous existence of multiple evolution paths. Creep process exemplifies this kind of nature that it is driven by both dislocation multiplication, due to the plastic deformation, and recovery process through diffusion, and that the characteristic parameters such as dislocation density are determined by both processes. Secondly, microstructure features pertinent to engineering problems usually exist at

a mesoscopic length scale. At this level a material body contains about  $10^9$  to  $10^{12}$  atoms. A direct use of the fundamental physical laws such by utilizing either first-principles calculation or molecular dynamics (MD) is still not affordable<sup>1</sup>. Thirdly, real microstructures are often the features far from an equilibrium state. Thermodynamics alone may not be sufficient for those problems. Instead, more complex non-equilibrium theories could be generally required.

Therefore, it appears that a suitable computation model for study of real microstructure related problems may require: being convenient in describing complex microstructures; being capable of including multiple mechanisms; using mesoscopic variables instead of microscopic variables; having solid physical foundation and containing dynamics.

Phase field method seems to meet these requirements. It is a field dynamic model with field variables (position and time dependent) describing arbitrary microstructures. For example, concentration field can be used to describe precipitates; long-range order parameters can be used for ordered particles; orientation field can be used for grain growth; slip field can be used for dislocations, to name a few. The dynamics is solved in terms of total free energy reduction by dynamic equations, both having fundamental interpretation in statistical mechanics. Depending on the physical nature of the problem, the field variables may be associated with either microscopic or mesoscopic length scale. The description of microstructures by phase field method reflects the nature of microstructures being the defects (non-uniformity) against perfection (uniformity): the same set of field variables being uniform in the

<sup>1</sup>Some recent MD simulation with simple Lennard-Jones potential has reached  $10^9$  atoms on the world's fastest supercomputer [9]. Nevertheless the typical time step is below  $10^{-9}$  seconds.

bulk phase (or domain) and varying rapidly at the defects (interfaces, grain boundaries, dislocation cores, etc). Accordingly, the general form of the total free energy consists of contributions from both the uniformity and the non-uniformity. Such kind of description makes the phase field method very flexible to deal with various types of microstructures, and to bridge them in a coherent way.

## 1.2 Organization of the thesis

For the purpose of illustrating this point, I choose to start with a general discussion of the phase field method regardless of any microstructure system. Focus on the generic features will prevent unnecessary complications arising from specific problems and thus help to provide the insight into the phase field method itself. A certain amount of effort is spent on the understanding of the fundamental aspect of phase field method from statistical mechanics, which may appear to deviate a little from the overall focus on microstructure, however, should receive sufficient attention in order to identify the capabilities of the phase field method<sup>2</sup>. These discussions are presented in Chapter 2.

The phase field method is then applied to two types of problem: microstructure development via nucleation, growth, and coarsening, and dislocations. The first problem was initiated by a particular interest in the multi-modal size distribution of  $\gamma'$  precipitates in Ni-Al  $\gamma/\gamma'$  alloy, which is related to its high temperature creep-resistance property. Such microstructure is complex since it involves simultaneous occurrence of nucleation, growth, and coarsening during heat treatment. Chapter 3

<sup>2</sup>For example, Langer *et al.* [10] illustrated through a statistical theory the necessary correction to the linearized Cahn-Hilliard spinodal decomposition theory.

presents a hybrid model [11] that is designed to efficiently simulate nucleation process with concurrent growth and coarsening. It is followed by a formulation of the anisotropic coherency strain energy that contributes to the nucleation barrier [12]. The corresponding effects on the microstructure will be discussed. The model has been applied to various problems, such as validation of the JMAK theory for diffusion controlled growth in the presence of soft-impingement, and the microstructure development during heat treatment in Ni-Al alloy [13].

Chapter 4 illustrates an emerging important application that extends the phase field method from phase transformation to plasticity problems. In this part, the phase field model of dislocation is firstly reviewed. It is followed by an illustration of the major drawbacks in the original formulation, which is mainly due to the absence of an appropriate invariant form in the energy functional with respect to crystal symmetry. An extended model [14] is introduced to correct these deficiencies. It is then applied to simulate complex dislocation networks, where free surfaces are introduced. The general framework of the extended model is further implemented by introducing the generalized stacking fault energy (a.k.a.  $\gamma$ -surface). Partial dislocations and dissociation of dislocation nodes are simulated for aluminum and palladium with the corresponding  $\gamma$ -surface data [15]. The model is currently being extended for an accurate evaluation of the activation energy for cross-slip and for simulation of 3D dislocation networks involving cross-slip and climb.

Chapter 5 studies the interaction between dislocation and microstructure. The purpose is to explore the possibilities of bridging microstructure and mechanical properties. It starts with the simulation of a confined dislocation in a  $\gamma$  channel of a  $\gamma/\gamma'$  microstructure [16, 17]. The critical stress to drive the dislocation into the  $\gamma$  channel

and its dependence on the layer thickness are calculated. In an alternate  $\gamma/\gamma'$  multi-layer microstructure the deformation mode of a threading dislocation subject to the applied stress and Peierls stress is simulated and compared with other simulation method. Finally, cutting  $\gamma'$  ordered particle by  $1/2\langle 110 \rangle$  type  $\gamma$ -matrix dislocations is simulated [18], where the formation and annihilation of anti-phase boundaries during the cutting is self-consistently described with the use of  $\gamma$ -surface. The corresponding  $\gamma/\gamma'$  microstructures may be produced by the model described in Chapter 3.

Phase field simulation of microstructures is often designed at a mesoscopic length scale. However, rigorous analysis shows that the actual simulation scale is limited by the physical thickness of the interface (or domain boundary) which in many material systems is around nanometers. In some cases there exist certain rules to increase the length scale. However, these rules have been inappropriately applied to various problems. In Chapter 6, we try to clarify these rules and, in addition, present a possible solution to the situation when these rules do not apply [19, 20].

The final conclusion and discussions on some future directions that extend the current work are presented in Chapter 7

## CHAPTER 2

### PHASE FIELD METHOD

This chapter provides a review of the basic ingredients of phase field method in terms of energy and dynamics. The concept of coarse-graining and the corresponding fundamental interpretation of the phase field dynamic equations are discussed. At the continuum level, some general characteristic of phase field models are compared with sharp interface models in terms of interface velocity and other interfacial properties. As an inseparable part of phase field applications in solids, theoretic formulations and recent development of coherency strain energy are summarized.

#### 2.1 Energy and equations of motion

In the phase field method it is postulated that the thermodynamic state of a material piece can be fully described by the Ginzburg-Landau type free energy:

$$\mathcal{F} = \int d\mathbf{x} [f(\phi(\mathbf{x}, t)) + \frac{\kappa_\phi}{2} (\nabla \phi(\mathbf{x}, t))^2] \quad (2.1)$$

Here the integral is taken over the entire volume of the material and  $\mathbf{x}$  is the spatial coordinate of dimension  $d$ . The field variable,  $\phi$ , is a continuous function that characterizes the property of the material at each position  $\mathbf{x}$  and time  $t$ . The local free energy density,  $f$ , is a coarse-grained free energy. It is the free energy per unit

volume as if the material were uniform with the property represented by  $\phi(\mathbf{x}, t)$ . The second term in the integrand is a necessary correction for the short-range correlation wherever the material is not uniform.  $\kappa_\phi$  is called gradient coefficient. The spatial variation of  $\phi$  is assumed to be small so that higher-order gradient terms can be neglected. In metallurgy, this energy form was proposed by Cahn and Hilliard [21] by a functional expansion of inhomogeneous free energy with respect to the non-uniformity of concentration distribution. The gradient term in Eq.(2.1) turns out to be the first non-trivial expansion term subject to the necessary constraints from crystal symmetry.

In this very generic form, Eq.(2.1) is applicable to any non-uniform material system. The exact choice of the field variable will depend on each particular problem and is to reflect the characteristic property of the system. In some cases, the field variable may be a measurable physical quantity, such as concentration of a chemical component in an alloy; while in many others such a quantity could be practically difficult to define. For instance, in liquid-to-solid transformations an infinite number of order parameters are required for a rigorous characterization of the structure of the liquid phase [22]. The use of single order parameter in the usual solidification study is much in a sense of a mathematical quantity to distinguish the solid and liquid phases, though the physical origin may be investigated in an transition from the microscopic picture to the continuum limit (for example, see [23]). The character of the field variable can be a scalar, a vector, or a tensor, depending on the nature of the system [24]: besides the scalar parameter as we have mentioned, in problems such as magnetization the field variable can be magnetic moment, which is a vector with three spatial components; it may also be a second-rank tensor for orientational

order as in liquid crystals. The forms in higher rank are seldom used. More detailed discussion can be found in Ref. [24].

If the thermodynamic state of a system is determined by multiple properties, e.g., both concentration and structure, the free energy functional in Eq.(2.1) generally contains multiple field variables:

$$\mathcal{F} = \int d\mathbf{x} [f(\phi_1, \phi_2, \dots, \phi_p, \dots) + \sum_{p,q} \frac{\kappa_{\phi,ij}(p, q)}{2} \nabla_i \phi_p \nabla_j \phi_q] \quad (2.2)$$

where the gradient coefficient  $\kappa_{\phi,ij}(p, q)$  couples the  $i$ - and  $j$ -th spatial components of the gradient of the field variables  $\phi_p$  and  $\phi_q$ , respectively. An example of such a coupling form will be illustrated in more detail in the dislocation model presented in Chapter 4.

The dynamic evolution of the field variables, and thus of the material system, is characterized by two types of phenomenological governing equations, distinguished by the nature of the field variable. For locally conserved variables, such as concentration, it is the generalized diffusion equation

$$\frac{\partial \phi_p(\mathbf{x}, t)}{\partial t} = -\nabla \cdot \left[ -\sum_q M_{pq} \nabla \frac{\delta \mathcal{F}}{\delta \phi_q(\mathbf{x}, t)} \right] \quad (2.3)$$

Here we write the equation in a multi-component form for generality. The term in the bracket is the diffusion flux of the  $p$ -th component. The variational derivative term,  $\delta \mathcal{F}/\delta \phi_q$ , is in fact the chemical potential of the  $q$ -th component.  $M_{pq}$  is a mobility term. For non-conserved variables, the dynamic equation is written as

$$\frac{\partial \phi_p(\mathbf{x}, t)}{\partial t} = -\sum_q M_{pq} \frac{\delta \mathcal{F}}{\delta \phi_q(\mathbf{x}, t)} \quad (2.4)$$

which implies a linear response of the rate of evolution to the driving force  $(\delta \mathcal{F}/\delta \phi_q)$ . The negative sign indicates that the evolution is driven to the energy minimum.

Taking time derivative of the total energy of the non-conserved system gives

$$\begin{aligned}
\frac{d\mathcal{F}}{dt} &= \int d\mathbf{x} \sum_p \frac{\delta\mathcal{F}}{\delta\phi_p} \frac{d\phi_p}{dt} \\
&= \int d\mathbf{x} \sum_p \frac{\delta\mathcal{F}}{\delta\phi_p} \left( - \sum_q M_{pq} \frac{\delta\mathcal{F}}{\delta\phi_q} \right) \\
&= - \sum_{p,q} \int d\mathbf{x} M_{pq} \frac{\delta\mathcal{F}}{\delta\phi_p} \frac{\delta\mathcal{F}}{\delta\phi_q}
\end{aligned} \tag{2.5}$$

where we have applied Eq.(2.4). Similarly, for the conserved system we apply Eq.(2.3) by integration by parts

$$\frac{d\mathcal{F}}{dt} = - \sum_{p,q} \int d\mathbf{x} M_{pq} \left( \nabla \frac{\delta\mathcal{F}}{\delta\phi_p} \right) \cdot \left( \nabla \frac{\delta\mathcal{F}}{\delta\phi_q} \right) \tag{2.6}$$

The total energy  $\mathcal{F}$  is shown, in both conserved and non-conserved systems, to monotonically decrease with time if  $M_{pq}$  is positive definite. Eqs.(2.3) and (2.4) thus correspond to pure relaxation models. In the study of the dynamics of critical phenomena, these two equations are classified by Hohenberg *et al.* as relaxation models of type A and B, respectively, and the coupled formed is of type C [25]. Eqs.(2.3) and (2.4) are also called time dependent Ginzburg-Landau equations [26]. In metallurgy, they are known as the Cahn-Hilliard equation [27] and the Allen-Cahn equation [28], initially developed for spinodal decomposition and antiphase domain coarsening, respectively.

To describe an activated process, fluctuation terms must be added to the driving force side of both Eqs.(2.3) and (2.4)

$$\frac{\partial\phi_p(\mathbf{x},t)}{\partial t} = -\nabla \cdot \left[ - \sum_q M_{pq} \nabla \frac{\delta\mathcal{F}}{\delta\phi_q(\mathbf{x},t)} \right] + \zeta_{\phi_p}(\mathbf{x},t) \tag{2.7}$$

$$\frac{\partial\phi_p(\mathbf{x},t)}{\partial t} = - \sum_q M_{pq} \frac{\delta\mathcal{F}}{\delta\phi_q(\mathbf{x},t)} + \zeta_{\phi_p}(\mathbf{x},t) \tag{2.8}$$

$\zeta_{\phi_p}$  is known as the Langevin noise term. For thermal fluctuations it follows the Gaussian distribution, and its mean and correlation satisfy

$$\langle \zeta_{\phi_p}(\mathbf{x}, t) \rangle = 0 \quad (2.9)$$

$$\langle \zeta_{\phi_p}(\mathbf{x}, t) \zeta_{\phi_q}(\mathbf{x}', t') \rangle = -2k_B T \nabla \cdot \Gamma_{pq} \nabla [\delta(\mathbf{x} - \mathbf{x}') \delta(t - t')] \quad (2.10)$$

$$\langle \zeta_{\phi_p}(\mathbf{x}, t) \zeta_{\phi_q}(\mathbf{x}', t') \rangle = 2k_B T \Gamma_{pq} \delta(\mathbf{x} - \mathbf{x}') \delta(t - t') \quad (2.11)$$

according to fluctuation-dissipation theorem. Eqs.(2.10) and (2.11) are for the conserved field and non-conserved field, respectively.  $\Gamma_{pq}$  is the symmetric part of  $M_{pq}$  [26]. The physical implication of these equations will be further discussed in the next section.

## 2.2 The coarse-grain approximation

The local free energy  $f$  in Eq.(2.1) is a coarse-grained free energy. The concept of coarse-graining originates from theoretic studies in critical phenomena in phase transitions. Near the critical point it is generally exhibited that the correlation length of a physical system approaches infinite. The correlation length, in a loose sense, gives a measure of the spatial extent of a fluctuating physical quantity [29]. The diverging behavior in length scale leads to an important postulate that the behaviors of system near the critical point become irrelevant to the atomic scale, and instead will depend on the much greater correlation length. It is thus expected that the degrees of freedom at shorter length scales can be ignored and that the fundamental behaviors of the phase transition can be studied at the coarser length scale. It must be noted that problems concerning microstructural evolutions usually involve first-order phase transitions, which do not exhibit divergence of correlation length as in the critical

problems [24]. Therefore degrees of freedom at short length scales cannot be generally neglected. Nevertheless, the common observations that many microstructural evolutions do not exhibit explicit dependence on the microscopic degrees of freedom indicate a similar scaling approach could be utilized with certain constraints.

A coarse-graining process is often to convert a system in microscopic depiction by statistical mechanics to an equivalent system in terms of a set of mesoscopic degrees of freedom. The Hamiltonian of a microscopic system can be written as

$$\mathcal{H} = \mathcal{H}_N\{\sigma_i\} \quad (2.12)$$

where  $\sigma_i$  are the microscopic variables in an  $N$ -atom material, with  $i$  the index of each atom. The equilibrium state can be derived from the partition function [30]

$$Q = \sum_{\{\sigma_i\}} \exp(-\mathcal{H}_N\{\sigma_i\}/k_B T) \quad (2.13)$$

If the system is not far from the critical point, the correlation length, though not necessarily infinite, is much greater than the lattice parameter  $a$ . Thus a system rescaled by a greater lattice parameter,  $a'$ , is assumed to have a close resemblance to the original one, with the partition function

$$Q = \sum_{\{\sigma'_i\}} \exp(-\mathcal{H}_{N'}\{\sigma'_i\}/k_B T) \quad (2.14)$$

Obviously, in order to maintain the same partition function the Hamiltonian of the coarse-grained system has to be related to the original Hamiltonian by

$$\exp(-\mathcal{H}_{N'}\{\sigma'_i\}/k_B T) = \sum_{\{\sigma_i\}-\{\sigma'_i\}} \exp(-\mathcal{H}_N\{\sigma_i\}/k_B T) \quad (2.15)$$

which is in fact a sum of the partition function over the microscopic degrees of freedom from the length scale  $a$  to  $a'$  subject to the constraint that any microscopic

configuration  $\{\sigma\}$  in the cell of  $a'$  corresponds to the identical coarse-grained configuration  $\{\sigma'\}$ . The coarse-grained variable  $\sigma'$  may simply be a spatial average of  $\sigma$  over a volume of  $a'^3$ , such as density being the average of the instantaneous numbers of atoms in a given volume. In more general cases (for example, for the long-range order parameter) it may require a transform from the original variable. Obviously  $\sigma'$  varies smoothly at the scale of  $a'$  and any fluctuation below this length scale is lost after coarse-graining. Associated with the coarse-graining there are two important issues [5]. First, the coarse-graining length scale  $a'$  should be much greater than the lattice parameter  $a$  so that the continuum description is valid, meanwhile it should be smaller than the relevant correlation length, so that the time for reaching local equilibrium within a coarse-grained cell  $a'$  will be sufficiently faster than that for the global non-equilibrium process under consideration. Choosing a too large  $a'$  will result in a useless description with every interesting features, such as phase separation, being lost in a huge cell. Second, the coarse-grained free energy obtained from Eq.(2.15) is not the thermodynamic free energy due to its dynamic nature (Fig. 2.1). In particular the former implies an intrinsic dependence on the coarse-graining length scale. By its very nature the thermodynamic free energy gives description for only the equilibrium states of a system and no information is provided for a metastable state, e.g., of a two phase mixture. The latter is, however, provided in the coarse-grained free energy. An alternate approach for treating the metastable state has been to extrapolate the thermodynamic free energy into the non-equilibrium regimes based on a particular thermodynamic model and parameters (Fig. 2.1). The latter approach

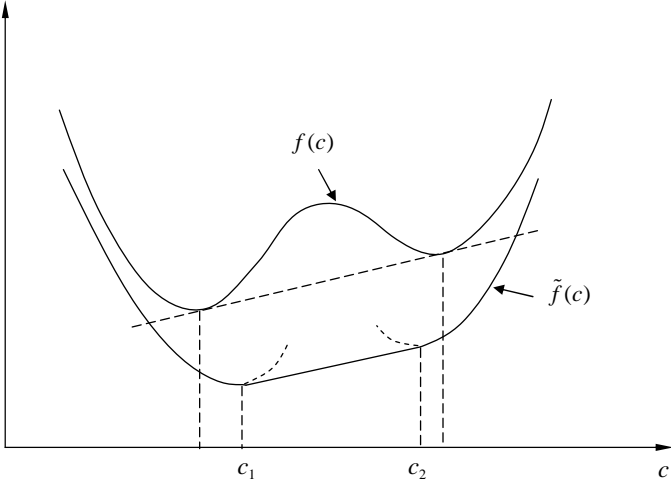


Figure 2.1: Schematic drawing of the coarse-grained free energy  $f(c)$  and the thermodynamic free energy  $\tilde{f}(c)$ . The thermodynamic extrapolation into the two-phase region is represented by the dashed curves. After Langer [5].

is often employed in thermodynamics based phase transition problems, including microstructure evolutions. Nevertheless the difference between the free energies from coarse-graining and the extrapolation of thermodynamics is often neglected.

### 2.3 Statistical mechanical basis of the phase field dynamic equations

Although Eqs.(2.3) and (2.4) are often accepted as phenomenological equations with linear response of the kinetic rate to the driving force, they in fact can be derived from the fundamental physical laws at microscopic level. To view this connection, we start with a brief review of the Hamiltonian dynamics for the classical system and the Langevin dynamics that explicitly separates the thermal fluctuations, and then illustrate the derivation of Eqs.(2.3) and (2.4) from the master equation of statistical mechanics.

We consider a classical system with  $2N$  degrees of freedom, among which there are  $N$  coordinates  $\mathbf{q} = \{q_1, q_2, \dots, q_i, \dots, q_N\}$  and  $N$  conjugate momenta  $\mathbf{p} = \{p_1, p_2, \dots, p_i, \dots, p_N\}$ .  $\mathbf{q}$  and  $\mathbf{p}$  may be the usual spatial coordinates and momenta of individual atoms, but more often they are defined as generalized variables that satisfy the Hamilton's equations:

$$\begin{aligned}\frac{\partial \mathbf{q}}{\partial t} &= \frac{\partial \mathcal{H}}{\partial \mathbf{p}} \\ \frac{\partial \mathbf{p}}{\partial t} &= -\frac{\partial \mathcal{H}}{\partial \mathbf{q}},\end{aligned}\tag{2.16}$$

where  $\mathcal{H} = \mathcal{H}(\mathbf{q}, \mathbf{p}, t)$  is the Hamiltonian. Equations (2.16) fully describe the system and are the basis of the Hamiltonian dynamics. For real systems consisting of some  $N = 10^{23}$  atoms, however, it is practically impossible to solve these coupled  $2N$  partial differential dynamic equations or, even if it is possible, to extract fundamental results from so many variables. The use of statistical mechanics is to reduce the degree of complexity by replacing the large degrees of freedom by a probability function that represents an averaged consequence. It defines a  $2N$ -dimensional phase space with the coordinates of  $\mathbf{q}$  and  $\mathbf{p}$ . A point in the phase space represents a particular state (microstate) of the system and the time development of the system is a trajectory that connects a sequence of points in the phase space. The probability of finding a state  $(\mathbf{q}, \mathbf{p})$  is equal to  $\rho(\mathbf{q}, \mathbf{p}, t)d\mathbf{q}d\mathbf{p}$ , where  $\rho(\mathbf{q}, \mathbf{p})$  is the density of the states in a small volume at position  $(\mathbf{q}, \mathbf{p})$  at time  $t$  and is normalized by  $\int d\mathbf{q}d\mathbf{p}\rho(\mathbf{q}, \mathbf{p}, t) = 1$ . An important utility of the phase space distribution function  $\rho$  is that it derives the macroscopic (or observable) property as the ensemble average

$$A^{obs}(t) = \langle A(\mathbf{q}, \mathbf{p}) \rangle = \int d\mathbf{q}d\mathbf{p} A(\mathbf{q}, \mathbf{p})\rho(\mathbf{q}, \mathbf{p}, t)\tag{2.17}$$

where  $A(\mathbf{q}, \mathbf{p})$  is the property with explicit dependence on the microstate  $(\mathbf{q}, \mathbf{p})$ . The corresponding dynamic equation for  $\rho$  is the Liouville equation:

$$\frac{\partial \rho}{\partial t} = - \left( \frac{\partial \mathcal{H}}{\partial \mathbf{p}} \cdot \frac{\partial}{\partial \mathbf{q}} - \frac{\partial \mathcal{H}}{\partial \mathbf{q}} \cdot \frac{\partial}{\partial \mathbf{p}} \right) \rho \equiv -\mathcal{L}\rho \quad (2.18)$$

Here  $\mathcal{L} \equiv \partial \mathcal{H} / \partial \mathbf{p} \cdot \partial / \partial \mathbf{q} - \partial \mathcal{H} / \partial \mathbf{q} \cdot \partial / \partial \mathbf{p}$  is the Liouville operator. Eq.(2.18) can be obtained directly by substituting Eqs.(2.16) into the continuity equation

$$\frac{\partial \rho}{\partial t} + \frac{\partial}{\partial \mathbf{x}} \cdot \left( \frac{\partial \mathbf{x}}{\partial t} \rho \right) = 0 \quad (2.19)$$

that implies the phase points are conserved. Here  $\mathbf{x} = (\mathbf{q}, \mathbf{p})$ .

Many thermodynamic problems are concerned with the behavior of a system in contact with a thermal reservoir. While the problem can be fully solved by either Hamiltonian equations or Liouville equation by treating the system and the reservoir as a whole, the detail of the thermal reservoir is often of little interest. Therefore, it is usually preferred to separate these two so as to reduce the complexity of the problem. The consequent dynamic equation is the so-called Langevin equation:

$$\frac{\partial \mathbf{x}}{\partial t} = \mathbf{v}(\mathbf{x}) + \mathbf{f} \quad (2.20)$$

Here  $\mathbf{x}$  represents the state variables similar to the previously defined  $\mathbf{q}$  and  $\mathbf{p}$ . The first term at the right hand side,  $\mathbf{v}(\mathbf{x})$ , is the internal force term and the second term,  $\mathbf{f}$ , is the random force (fluctuation) from the thermal reservoir. In the example of Brownian particle system,  $\mathbf{x}$  represents the momenta of particles,  $\mathbf{v}$  is the viscous force as a function of the velocity (or momentum), and  $\mathbf{f}$  is the instantaneous force on the particles from the environment. A similar distribution function,  $\rho = \rho(\mathbf{x})$ , can be defined for the Langevin system. If the fluctuation is Gaussian with delta-function correlation and  $\mathbf{v}$  only depends on the current state  $\mathbf{x}$  rather than on the

history (called Markovian), then combining Eq.(2.20) and the continuity equation (Eq.(2.19)) and taking the average over the fluctuation yield an equation for the noise-averaged distribution function [31]

$$\frac{\partial}{\partial t}\rho(\mathbf{x},t) = -\frac{\partial}{\partial \mathbf{x}} \cdot [\mathbf{v}(\mathbf{x})\rho(\mathbf{x},t)] + \frac{\partial}{\partial \mathbf{x}} \cdot [\mathbf{B} \cdot \frac{\partial}{\partial \mathbf{x}}\rho(\mathbf{x},t)] \quad (2.21)$$

where  $\mathbf{B}$  is a function of  $\mathbf{x}$ . Eq.(2.21) is known as Fokker-Planck equation and is the analogue of the Liouville equation in Hamiltonian dynamics. The similar derivation of Fokker-Planck equation for a general case is considerably more complex. An alternative derivation of the Fokker-Planck equation may start from a master equation [30]

$$\frac{\partial \rho(\mathbf{x},t)}{\partial t} = \int d\mathbf{x}' [-\rho(\mathbf{x},t)P(\mathbf{x},\mathbf{x}') + \rho(\mathbf{x}',t)P(\mathbf{x}',\mathbf{x})] \quad (2.22)$$

where  $P(\mathbf{x},\mathbf{x}')d\mathbf{x}$  denotes the rate of transition of the system from state  $\mathbf{x}$  to  $\mathbf{x}'$ . Thus, the two terms in the integrand represent the flow of  $\rho$  that leaves and enters the state  $\mathbf{x}$ , respectively. Their sum is the net flow that enters  $\mathbf{x}$ . If fluctuations are sufficiently low that the transition only occurs between the neighboring states, then  $P(\mathbf{x},\mathbf{x}')$  is a sharply peaked function centered at  $\mathbf{x}$  and decays rapidly with  $\mathbf{x}' - \mathbf{x}$ . Thus we may expand  $P(\mathbf{x},\mathbf{x}')$  and  $\rho(\mathbf{x},t)$  in the vicinity of  $\mathbf{x}$  into a Taylor series and Eq.(2.22) becomes

$$\begin{aligned} \frac{\partial \rho(\mathbf{x},t)}{\partial t} = & \int d\mathbf{x}' \left\{ -\rho(\mathbf{x},t)P(\mathbf{x};\mathbf{x}'-\mathbf{x}) + \right. \\ & \left[ \rho(\mathbf{x},t) + \frac{\partial \rho(\mathbf{x},t)}{\partial \mathbf{x}} \cdot (\mathbf{x}' - \mathbf{x}) + \frac{1}{2} \frac{\partial^2 \rho(\mathbf{x},t)}{\partial \mathbf{x}^2} \cdot (\mathbf{x}' - \mathbf{x})^2 + \dots \right] \\ & \left[ P(\mathbf{x};\mathbf{x}'-\mathbf{x}) + \frac{\partial P(\mathbf{x},\mathbf{x}'-\mathbf{x})}{\partial \mathbf{x}} \cdot (\mathbf{x}' - \mathbf{x}) \right. \\ & \left. + \frac{1}{2} \frac{\partial^2 P(\mathbf{x},\mathbf{x}'-\mathbf{x})}{\partial \mathbf{x}^2} \cdot (\mathbf{x}' - \mathbf{x})^2 + \dots \right] \} \end{aligned} \quad (2.23)$$

Here we rewrite  $P(\mathbf{x}; \mathbf{x}' - \mathbf{x})$  in an equivalent form that denotes the transition from  $\mathbf{x}$  with a step of  $\mathbf{x}' - \mathbf{x}$ . Keeping up to the second order expansion term, we have

$$\frac{\partial \rho(\mathbf{x}, t)}{\partial t} = -\frac{\partial}{\partial \mathbf{x}} \cdot [\mu_1(\mathbf{x})\rho(\mathbf{x}, t)] + \frac{1}{2}\frac{\partial}{\partial \mathbf{x}} \cdot \frac{\partial}{\partial \mathbf{x}}[\mu_2(\mathbf{x})\rho(\mathbf{x}, t)] \quad (2.24)$$

where,

$$\begin{aligned} \mu_1(\mathbf{x}) &= \int d\xi P(\mathbf{x}; \xi) \xi = \langle \delta \mathbf{x} \rangle / \delta t = \mathbf{v}(\mathbf{x}), \\ \mu_2(\mathbf{x}) &= \int d\xi P(\mathbf{x}; \xi) \xi^2 = \langle \delta \mathbf{x}^2 \rangle / \delta t \\ \xi &\equiv \mathbf{x}' - \mathbf{x} \end{aligned}$$

We notice that  $\mu_1$  is a velocity term that represents the overall rate at which the system leaves the state  $\mathbf{x}$ , and that  $\mu_2$  represents the fluctuation of  $\mathbf{x}$ . If  $\mu_2$  is independent of  $\mathbf{x}$ , Eq.(2.24) is in the same form of Eq.(2.21).

Fokker-Planck equation is a useful starting point of relating a number of phenomenological continuum equations to the master equations in statistical mechanics. Aside from the formal constructions as given above, a specific derivation often needs to explicitly specify the form of  $P(\mathbf{x}, \mathbf{x}')$ , for example, as a function of the free energy of the system. In the remaining part of this section, we follow the procedure by Langer [32, 33] to illustrate the derivation of the phase field dynamic equations.

### 2.3.1 Conserved variable: Cahn-Hilliard equation

We assume a  $d$ -dimensional binary system of total  $N$  atoms in contact with a thermal reservoir. The system is subdivided into  $N/\nu$  cells with each containing  $\nu$  atoms. The composition,  $c_\alpha$ , is defined as the average atomic fraction of the species A in the  $\alpha$ -th cell. Clearly, according to the coarse-graining approximation, the size of the cell should be about the characteristic length, which in a two-phase configuration

is about the width of the inter-phase interface. We assume the transition mechanism is the pair-exchange of atoms between the neighboring cells. Accordingly  $P$  can be written in the form

$$P(\mathbf{c}, \mathbf{c}') = \frac{1}{2} \sum_{\alpha, \alpha'} \prod_{\beta \neq \alpha, \alpha'} \delta(c'_\beta - c_\beta) D_{\alpha\alpha'} \int d\varepsilon R(\mathbf{c}, \mathbf{c}') \delta(c'_\alpha - \varepsilon - c_\alpha) \delta(c'_{\alpha'} + \varepsilon - c_{\alpha'})^3 \quad (2.25)$$

Here the indices  $\alpha, \alpha', \beta$  denote the cells and the symbols  $\mathbf{c}, \mathbf{c}'$  denote the initial and final states of the transition, respectively. The term  $\delta(c'_\beta - c_\beta)$  constrains the pair-exchange between the cell  $\alpha$  and  $\alpha'$ .  $D_{\alpha\alpha'}$  is a matrix with values unity if  $\alpha$  and  $\alpha'$  are neighboring cells and otherwise zero.  $\delta(c'_\alpha - \varepsilon - c_\alpha) \delta(c'_{\alpha'} + \varepsilon - c_{\alpha'})$  means a change of  $-\varepsilon$  in cell  $\alpha$  accompanies a change of  $+\varepsilon$  in cell  $\alpha'$ , for the local conservation of composition. The pair exchange rate  $R$  is written as

$$R(\mathbf{c}, \mathbf{c}') = \exp \left( \frac{\mathcal{F}\{\mathbf{c}\} - \mathcal{F}\{\mathbf{c}'\}}{2k_B T} \right) \bar{T}(\mathbf{c}, \mathbf{c}') \quad (2.26)$$

where

$$\begin{aligned} \bar{T}(\mathbf{c}, \mathbf{c}') &= \frac{1}{Z_R} \int ds \int ds' \exp \left[ -\frac{E_R(s) + E_R(s')}{2k_B T} \right] [W(\mathbf{c})W(\mathbf{c}')]^{1/2} T_{ss'}(\mathbf{c}, \mathbf{c}') \\ &\quad \delta(E_R(s) - E_R(s') + E(\mathbf{c}) - E(\mathbf{c}')) \end{aligned} \quad (2.27)$$

where  $E_R(s)$  and  $E_R(s')$  are the internal energy of the thermal reservoir at states  $s$  and  $s'$ , respectively. The thermal reservoir is assumed to be always at equilibrium.  $E(\mathbf{c})$  and  $E(\mathbf{c}')$  are the internal energy of the system at states  $\mathbf{c}$  and  $\mathbf{c}'$ . The total internal energy of the system and the reservoir is conserved, as indicated by the  $\delta$  term.  $W(\mathbf{c})$  is the number of microscopic configurations at a fixed configuration of  $\mathbf{c}$ , alternatively, it accounts for the configurational entropy from the atomic scale up

<sup>3</sup>Langer uses notation of  $P(\mathbf{c}', \mathbf{c})$  for the left-hand side term.

to the cell size, subject to the configuration at the coarse-grained length scale.  $T_{ss'}$  is proportional to the detailed transition rate between states  $s$ ,  $\mathbf{c}$  and  $s'$ ,  $\mathbf{c}'$ . It is seen that  $\bar{T}$  is in a symmetric form with respect to the transition between  $\mathbf{c}$  and  $\mathbf{c}'$ .

Substituting Eqs.(2.25) and (2.26) into the master equation (Eq.(2.22)) yields

$$\frac{\partial \rho(\mathbf{c}, t)}{\partial t} = \frac{1}{2} \sum_{\alpha, \alpha'} D_{\alpha \alpha'} \int d\varepsilon \bar{T}(\varepsilon) \left\{ \exp \left[ \frac{\mathcal{F}(c_{\alpha'} - \varepsilon, c_{\alpha} + \varepsilon) - \mathcal{F}(c_{\alpha'}, c_{\alpha})}{2k_B T} \right] \right. \\ \left. \rho(c_{\alpha'} - \varepsilon, c_{\alpha} + \varepsilon) - \exp \left[ \frac{\mathcal{F}(c_{\alpha'}, c_{\alpha}) - \mathcal{F}(c_{\alpha'} - \varepsilon, c_{\alpha} + \varepsilon)}{2k_B T} \right] \rho(c_{\alpha'}, c_{\alpha}) \right\} \quad (2.28)$$

Here  $\bar{T}(\mathbf{c}, \mathbf{c}')$  has been rewritten as  $\bar{T}(\varepsilon)$  because of the constrained transition between  $\mathbf{c}$  and  $\mathbf{c}'$  by Eq.(2.25). Because  $\mathbf{c}$  is a coarse-grained variable, its variation during the phase transition is expected to be small if  $\nu$  is large.  $\bar{T}(\varepsilon)$  is therefore expected to be peaked at  $\varepsilon = 0$ . The relatively smooth functions  $\mathcal{F}$  and  $\rho$  thus can be expanded in Taylor series and kept only to the second-order term

$$\mathcal{F}(c_{\alpha'} - \varepsilon, c_{\alpha} + \varepsilon) \approx \mathcal{F}(c_{\alpha'}, c_{\alpha}) + \varepsilon \left( \frac{\partial}{\partial c_{\alpha'}} - \frac{\partial}{\partial c_{\alpha}} \right) \mathcal{F}|_{c'_{\alpha}, c_{\alpha}} + \frac{\varepsilon^2}{2} \left( \frac{\partial}{\partial c_{\alpha'}} - \frac{\partial}{\partial c_{\alpha}} \right)^2 \mathcal{F}|_{c'_{\alpha}, c_{\alpha}} \\ \rho(c_{\alpha'} - \varepsilon, c_{\alpha} + \varepsilon) \approx \rho(c_{\alpha'}, c_{\alpha}) + \varepsilon \left( \frac{\partial}{\partial c_{\alpha'}} - \frac{\partial}{\partial c_{\alpha}} \right) \rho|_{c'_{\alpha}, c_{\alpha}} + \frac{\varepsilon^2}{2} \left( \frac{\partial}{\partial c_{\alpha'}} - \frac{\partial}{\partial c_{\alpha}} \right)^2 \rho|_{c'_{\alpha}, c_{\alpha}} \quad (2.29)$$

With substitution of Eq.(2.29) and noticing the first-order terms vanishes due to the symmetric function  $\bar{T}(\varepsilon)$ , Eq.(2.28) becomes

$$\frac{\partial \rho}{\partial t} = \frac{\Gamma}{4\nu^{1+2/d}} \sum_{\alpha, \alpha'} D_{\alpha \alpha'} \left( \frac{\partial}{\partial c_{\alpha'}} - \frac{\partial}{\partial c_{\alpha}} \right) \left[ \left( \frac{\partial \mathcal{F}/k_B T}{\partial c_{\alpha'}} - \frac{\partial \mathcal{F}/k_B T}{\partial c_{\alpha}} \right) \rho + \left( \frac{\partial \rho}{\partial c_{\alpha'}} - \frac{\partial \rho}{\partial c_{\alpha}} \right) \right] \quad (2.30)$$

Here  $\Gamma$  is defined by

$$\int d\varepsilon \varepsilon^2 \bar{T}(\varepsilon) \equiv \nu^{-(1+2/d)} \Gamma \quad (2.31)$$

and represents a phenomenological fluctuation frequency. Eq.(2.30) has the form of Fokker-Planck equation if  $D_{\alpha \alpha'}$  is explicitly replaced by the summation  $\sum_{\alpha'}^{(\text{n.n.})}$  over the

$2d$  nearest neighbors of the cell  $\alpha$ :

$$\frac{\partial \rho}{\partial t} = \sum_{\alpha} \frac{\partial}{\partial c_{\alpha}} \left[ \sum_{\beta} \frac{\Gamma}{2\nu^{1+2/d}} \left( 2d\delta_{\alpha\beta} - \sum_{\alpha'}^{(\text{n.n.})} \delta_{\alpha'\beta} \right) \left( \frac{\partial \mathcal{F}/k_B T}{\partial c_{\beta}} \rho + \frac{\partial \rho}{\partial c_{\beta}} \right) \right] \quad (2.32)$$

If the both sides of Eq.(2.32) are multiplied by  $c_{\omega}$  and integrated over the entire configuration  $\mathbf{c}$ , the left-hand side becomes

$$\int dc_{\omega} \frac{\partial \rho(c, t)}{\partial t} = \frac{\partial}{\partial t} \int dc_{\omega} \rho(c, t) = \frac{\partial \bar{c}_{\omega}}{\partial t} \quad (2.33)$$

and the right-hand side term becomes

$$\begin{aligned} & \int dc_{\omega} \sum_{\alpha} \frac{\partial}{\partial c_{\alpha}} \left[ \sum_{\beta} \frac{\Gamma}{2\nu^{1+2/d}} \left( 2d\delta_{\alpha\beta} - \sum_{\alpha'}^{(\text{n.n.})} \delta_{\alpha'\beta} \right) \left( \frac{\partial \mathcal{F}/k_B T}{\partial c_{\beta}} \rho + \frac{\partial \rho}{\partial c_{\beta}} \right) \right] \\ &= - \int dc_{\omega} \sum_{\beta} \frac{\Gamma}{2\nu^{1+2/d}} \left( 2d\delta_{\omega\beta} - \sum_{\alpha'}^{(\text{n.n.})} \delta_{\alpha'\beta} \right) \left( \frac{\partial \mathcal{F}/k_B T}{\partial c_{\beta}} \rho + \frac{\partial \rho}{\partial c_{\beta}} \right) \\ &= - \sum_{\beta} \frac{\Gamma}{2\nu^{1+2/d}} \left( 2d\delta_{\omega\beta} - \sum_{\alpha'}^{(\text{n.n.})} \delta_{\alpha'\beta} \right) \int dc_{\omega} \frac{\partial \mathcal{F}/k_B T}{\partial c_{\beta}} \rho \\ &= - \sum_{\beta} \frac{\Gamma}{2\nu^{1+2/d}} \left( 2d\delta_{\omega\beta} - \sum_{\alpha'}^{(\text{n.n.})} \delta_{\alpha'\beta} \right) \left\langle \frac{\partial \mathcal{F}/k_B T}{\partial c_{\beta}} \right\rangle \end{aligned} \quad (2.34)$$

By using the continuum representations in Eqs.(2.33) and (2.34)

$$\sum_{\alpha} \dots = (\nu a^d)^{-1} \int d\mathbf{x} \dots \quad (2.35)$$

$$\left( 2d\delta_{\omega\beta} - \sum_{\alpha'}^{(\text{n.n.})} \delta_{\alpha'\beta} \right) = -(a^d \nu)(a^2 \nu^{2/d}) \nabla^2(\mathbf{x} - \mathbf{x}') \quad (2.36)$$

$$\frac{\partial}{\partial c_{\alpha}} = (\nu a^d) \frac{\delta}{\delta \mathbf{c}} \quad (2.37)$$

Eq.(2.32) becomes

$$\frac{\partial \bar{c}(\mathbf{r})}{\partial t} = \frac{\Gamma a^{2+d}}{2k_B T} \nabla^2 \left\langle \frac{\delta \mathcal{F}}{\delta \mathbf{c}} \right\rangle \quad (2.38)$$

Here  $\bar{c}(\mathbf{r})$  and  $\langle \delta \mathcal{F} / \delta \mathbf{c} \rangle$  are values averaged over the fluctuation due to the thermal reservoir. The term  $\partial \rho / \partial c$  that corresponds to the fluctuations vanishes in Eq.(2.38)

by averaging. Finally, if the distribution function  $\rho(\mathbf{c})$  is sharply peaked at  $\mathbf{c} = \bar{\mathbf{c}}$  so that the average of any quantity over  $\rho$  can be well approximated by its value at  $\bar{\mathbf{c}}$ , then Eq.(2.38) reduces to

$$\frac{\partial \bar{\mathbf{c}}(\mathbf{x}, t)}{\partial t} = \frac{\Gamma a^{2+d}}{2k_B T} \nabla^2 \frac{\delta F[\bar{\mathbf{c}}(\mathbf{x}, t)]}{\delta \bar{\mathbf{c}}(\mathbf{x}, t)} \quad (2.39)$$

which is the Cahn-Hilliard equation.

### 2.3.2 Non-conserved variable: Allen-Cahn equation

Similarly we assume a  $d$ -dimensional system of total  $N$  microscopic degrees of freedom (for example,  $N$  spins in a magnetic system) in contact with a thermal reservoir <sup>4</sup>. The system is again divided into  $N/\nu$  cells with each containing  $\nu$  spins. The order parameter,  $\eta_\alpha$ , is defined as the average spin in the  $\alpha$ -th cell. The specific choice of  $P$  can be

$$P(\boldsymbol{\eta}, \boldsymbol{\eta}') = \sum_{\alpha} \prod_{\beta \neq \alpha} \delta(\eta'_\beta - \eta_\beta) R(\boldsymbol{\eta}, \boldsymbol{\eta}') \quad (2.40)$$

without the constraint of local conservation, where the transition rate  $R$  is defined in the same way as in Eq.(2.26). Eq.(2.22) then becomes

$$\begin{aligned} \frac{\partial \rho(\boldsymbol{\eta}, t)}{\partial t} &= \sum_{\alpha} \int d\varepsilon \bar{T}(\varepsilon) \left\{ \exp \left[ \frac{\mathcal{F}(\eta_\alpha + \varepsilon) - \mathcal{F}(\eta_\alpha)}{2k_B T} \right] \rho(\eta_\alpha + \varepsilon) \right. \\ &\quad \left. - \exp \left[ \frac{\mathcal{F}(\eta_\alpha) - \mathcal{F}(\eta_\alpha + \varepsilon)}{2k_B T} \right] \rho(\eta_\alpha) \right\} \end{aligned} \quad (2.41)$$

Again we can expand  $\mathcal{F}(\eta_\alpha + \varepsilon)$  and  $\rho(\eta_\alpha + \varepsilon)$  in Taylor series and keep up to the second order terms. Eq.(2.41) reduces to

$$\frac{\partial \rho}{\partial t} = \sum_{\alpha} \Gamma \frac{\partial}{\partial \eta_\alpha} \left( \frac{\partial \mathcal{F}/k_B T}{\partial \eta_\alpha} + \frac{\partial \rho}{\partial \eta_\alpha} \right) \quad (2.42)$$

<sup>4</sup>We do not follow exactly the procedure as in [32], which otherwise would require consideration of Hamiltonian dynamics between the general coordinates and their conjugate momenta. In that case  $\Gamma$  would be a matrix that contains an anti-symmetric component arising from the internal dynamics. It seems by following the derivation of [33] with certain modifications we can also derive the Allen-Cahn equation.

with a slightly different definition of  $\Gamma$

$$\int d\varepsilon \varepsilon^2 \bar{T}(\varepsilon) \equiv \nu^{-1} \Gamma \quad (2.43)$$

because the transition does not require the mechanism of pair-wise exchange. Applying the integration  $\int d\boldsymbol{\eta} \eta_\omega$  to both sides of Eq.(2.43) yields

$$\frac{\partial \bar{\eta}_\omega}{\partial t} = -\frac{\Gamma}{\nu} \int d\eta \frac{\partial \mathcal{F}/k_B T}{\partial \eta_\omega} \rho = -\frac{\Gamma}{\nu} \left\langle \frac{\partial \mathcal{F}/k_B T}{\partial \eta_\omega} \right\rangle \quad (2.44)$$

With the continuum representation (Eqs.(2.35) and (2.37)) and the assumption of localized  $\rho(\boldsymbol{\eta})$ , we obtain the Allen-Cahn equation

$$\frac{\partial \bar{\boldsymbol{\eta}}(\mathbf{x}, t)}{\partial t} = -\frac{\Gamma a^d}{k_B T} \frac{\delta \mathcal{F}[\bar{\boldsymbol{\eta}}(\mathbf{x}, t)]}{\delta \bar{\boldsymbol{\eta}}(\mathbf{x}, t)} \quad (2.45)$$

## 2.4 Phase field model and sharp interface models

Evolution of microstructural domains can often be modeled in terms of the motion of their interfaces in responding to driving forces from bulk energy difference, interface tension, or external fields. In such an approach, the interfaces are treated as sharp dividing surfaces and their internal structures are ignored. The instantaneous velocity of the interface movement is provided by  $\mathbf{v} = \mathbf{F}/M$ , the local driving force  $\mathbf{F}$  divided by the phenomenological mobility  $M$ . Meanwhile, topological changes such as generation or annihilation of interfaces are handled by sophisticated algorithms. The physical conditions at interface may also be treated explicitly. For example, in treating precipitate growth, concentrations at interface may be determined by both non-equilibrium (kinetic) and equilibrium conditions. Additional corrections for curved interface can also be applied. These treatments are the basic ingredients of sharp interface models. In a fundamentally different way, phase field models do not

explicitly describe interfaces, nor the velocity of the interface motion. Instead, interface is an inseparable non-uniformity portion of a phase field system and the velocity is reflected in an overall evolution of the field variables. The connection between phase field models and sharp interface models is often pursued by extracting from a phase field model the “sharp interface” properties (such as velocity and interface composition) and justifying their consistency. In fact some of these properties can be readily derived from the phase field dynamic equations (Eqs.(2.3) and (2.4)). For the purpose of illustration we consider a phase field model with only one field variable. The derivations that follow can be found in various literatures (e.g. [34], [35]).

### 2.4.1 Non-conserved field

We may consider a system characterized by a non-conserved field variable  $\eta$  which has two local minima,  $\pm\eta_s$ , in the free energy  $f(\eta)$  (Fig. 2.2(a)). The configuration under consideration is a sphere of radius  $R(t)$  in a matrix.  $\eta$  has the value of  $-\eta_s$  in the matrix and  $+\eta_s$  in the sphere, i.e.,

$$\eta(r) = \begin{cases} -\eta_s & (r > R) \\ +\eta_s & (r \leq R) \end{cases}$$

A uniform external field  $H$  in favor of the state  $+\eta_s$  is applied to the system. By assuming a radial symmetry the equation of motion can be written as

$$\frac{\partial\eta(r,t)}{\partial t} = -M \left( \frac{\partial f}{\partial\eta} - \kappa_\eta \frac{\partial^2\eta}{\partial r^2} - \kappa_\eta \frac{d-1}{r} \frac{\partial\eta}{\partial r} - H \right) \quad (2.46)$$

where  $d$  is the dimensionality. Transforming to a local frame that is fixed on the interface (Fig. 2.2(b)):  $\eta(r,t) \Rightarrow \eta(r',t)$ , where  $r' \equiv r - R(t)$ , we have

$$(\partial/\partial t)_r = (\partial/\partial t)_{r'} - (\partial/\partial r')_t dR/dt \quad (2.47)$$

$$\partial/\partial r = \partial/\partial r' \quad (2.48)$$

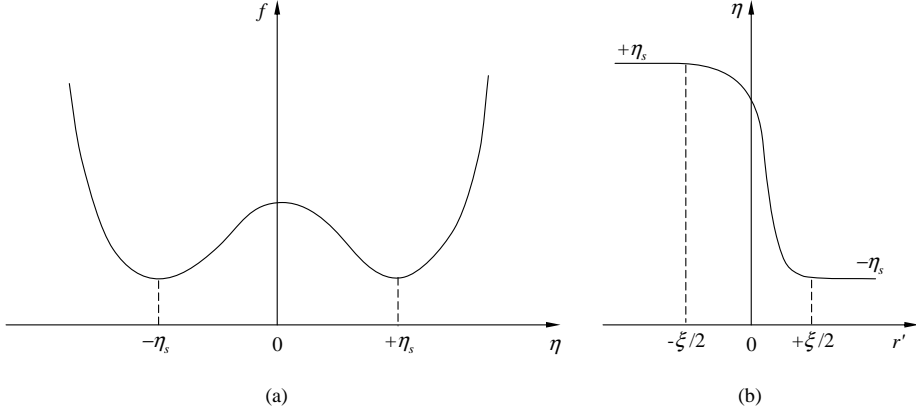


Figure 2.2: (a) Free energy for the non-conserved system, and (b) the interface profile in the local frame.

Since in the local frame the interface is stationary, the field variable variation  $(\partial\eta/\partial t)_{r'}$  vanishes approximately and  $(\partial\eta/\partial r')_t \Rightarrow d\eta/dr'$ . Combining Eqs.(2.46)-(2.48) gives

$$\kappa_\eta \frac{d^2\eta}{dr'^2} = \frac{\partial f}{\partial \eta} - H - \left( \frac{1}{M} \frac{dR}{dt} + \kappa_\eta \frac{d-1}{r'+R} \right) \frac{d\eta}{dr'} \quad (2.49)$$

With integration  $\int_{-\xi/2}^{+\xi/2} (d\eta/dr') dr'$ , the left hand side term becomes

$$\int_{-\xi/2}^{+\xi/2} \kappa_\eta \frac{d^2\eta}{dr'^2} \frac{d\eta}{dr'} dr' = \frac{\kappa_\eta}{2} \left( \frac{d\eta}{dr'} \right)^2 \Big|_{-\xi/2}^{+\xi/2} = 0$$

and the right hand side term becomes

$$\begin{aligned} & (f - \eta H) \Big|_{-\eta_s}^{+\eta_s} - \left( \frac{1}{M} \frac{dR}{dt} + \kappa_\eta \frac{d-1}{R} \right) \int_{-\xi/2}^{+\xi/2} \left( \frac{d\eta}{dr'} \right)^2 dr' \\ &= -2\eta_s H - \left( \frac{1}{M} \frac{dR}{dt} + \kappa_\eta \frac{d-1}{R} \right) \frac{\sigma}{\kappa_\eta} \end{aligned}$$

where  $\xi$  is the width of the interface.  $\sigma = \kappa_\eta \int_{-\xi/2}^{+\xi/2} (d\eta/dr')^2 dr'$  is assumed to be the equilibrium interfacial energy. Here we have used the fact that  $d\eta/dr'$  is sharply peaked near the interface ( $r' = 0$ ) and zero elsewhere. The interface velocity is thus

$$v \equiv dR/dt = \frac{2M\kappa_\eta\eta_s}{\sigma} H - \frac{M\kappa_\eta(d-1)}{R} \quad (2.50)$$

In the absence of external field  $H$ , Eq.(2.50) is identical to the analytic result by Allen and Cahn [28] for anti-phase boundary motion. In more general cases where the particles do not have spherical shape, the above results also applies if  $(d - 1)/R$  is replaced by local curvature [34].

### 2.4.2 Conserved field

Consider an A-B alloy.  $c$  is the concentration of component B.  $c_\alpha$  and  $c_\beta$  are equilibrium concentrations of phase  $\alpha$  and  $\beta$  (Fig. 2.3(a)). A spherical particle of  $\beta$  phase is embedded in an  $\alpha$  phase matrix. The  $\beta$  phase has the equilibrium concentration. Define the chemical potential difference with gradient term correction

$$\mu \equiv \mu_B - \mu_A = \frac{\delta \mathcal{F}}{\delta c} = \frac{\partial f}{\partial c} - \kappa_c \frac{\partial c^2}{\partial r^2} - \kappa_c \frac{d-1}{r} \frac{\partial c}{\partial r} \quad (2.51)$$

Here the radial symmetry is assumed.  $\mu_A$  and  $\mu_B$  are chemical potentials of the component A and B, respectively. In a local frame (Fig. 2.3(b)), apply integration across the interface and recall  $dc/dr'$  is sharply peaked near the interface ( $r' = 0$ )

$$\begin{aligned} \int_{-\xi/2}^{+\xi/2} \mu \frac{dc}{dr'} dr' &= \int_{-\xi/2}^{+\xi/2} \frac{\partial f}{\partial c} \frac{dc}{dr'} dr' - \kappa_c \int_{-\xi/2}^{+\xi/2} \frac{d^2 c}{dr'^2} \frac{dc}{dr'} dr' - \kappa_c \int_{-\xi/2}^{+\xi/2} \frac{d-1}{r'+R} \left( \frac{dc}{dr'} \right)^2 dr' \\ &= \Delta f - \frac{\kappa_c}{2} \left( \frac{dc}{dr'} \right)^2 \Big|_{-\xi/2}^{+\xi/2} + \kappa_c \frac{d-1}{R} \int_{-\xi/2}^{+\xi/2} \left( \frac{dc}{dr'} \right)^2 dr' \end{aligned}$$

Notice the second term at the right hand side vanishes. Thus,

$$\int_{-\xi/2}^{+\xi/2} \mu \frac{dc}{dr'} dr' = \Delta f + \frac{d-1}{R} \sigma = \mu_\infty^{eq} \Delta c + \frac{d-1}{R} \sigma \quad (2.52)$$

where  $\mu_\infty^{eq}$  is the equilibrium chemical potential determined by the free energy and  $\Delta c \equiv c_\beta - c_\alpha$  (Fig. 2.3(a)). At equilibrium, the chemical potential difference  $\mu (=$

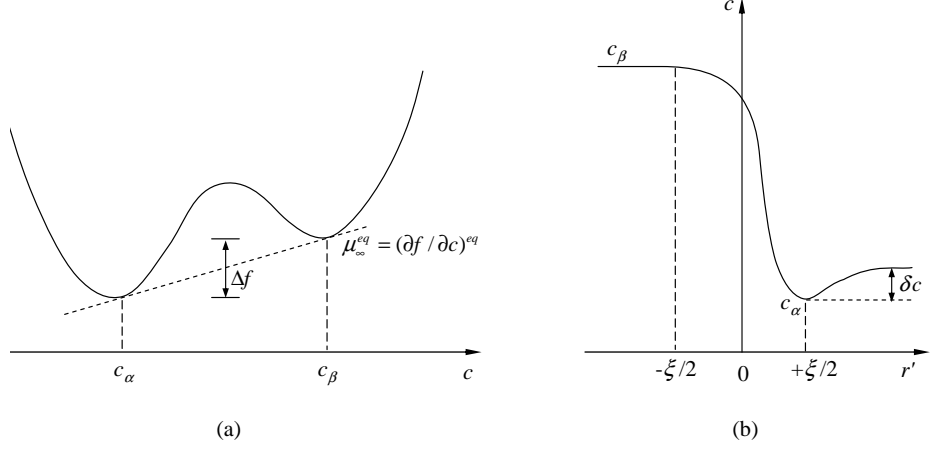


Figure 2.3: a) Free energy for the conserved system, and (b) the interface profile in the local frame.

$\mu(R)$ ) is uniform everywhere<sup>5</sup>. Eq.(2.52) becomes

$$\mu(R) - \mu_\infty^{eq} = \frac{\sigma}{\Delta c} \frac{d-1}{R} \quad (2.53)$$

which is in a form of Gibbs-Thomson equation.

To derive the interface velocity for a non-equilibrium process, consider the equation of motion

$$\frac{\partial c}{\partial t} = M \nabla^2 \frac{\delta \mathcal{F}}{\delta c} = M \nabla^2 \mu \quad (2.54)$$

in the local frame and near the interface

$$-\frac{dR}{dt} \frac{dc}{dr'} = M \left( \frac{d^2 \mu}{dr'^2} + \frac{d-1}{R} \frac{d\mu}{dr'} \right)$$

Integration  $\int dr'$  across the interface gives

$$\frac{dR}{dt} \Delta c = M \left( \frac{d\mu}{dr'} \Big|_{-\xi/2}^{+\xi/2} + \frac{d-1}{R} \mu \Big|_{-\xi/2}^{+\xi/2} \right)$$

<sup>5</sup>Recall the equilibrium state is determined by the minimization  $\frac{\delta}{\delta c} [\mathcal{F} - \mu \int c(\mathbf{x}) d\mathbf{x}] = 0$ , in which  $\mu$  serves as the Lagrangian multiplier for the constraint of mass conservation.

The term  $d\mu/dr'$  equals the mass flux  $J$  divided by mobility  $M$ . Since the  $\beta$  phase particle is at equilibrium,  $(d\mu/dr')_{-\xi/2} = 0$ . In addition,  $\mu|_{-\xi/2}^{+\xi/2} = -\sigma(d-1)/R\Delta c$  due to the curvature of the interface. The velocity therefore is

$$v \equiv \frac{dR}{dt} = \frac{M}{\Delta c} \left[ \frac{d\mu}{dr'} \Big|_{+\xi/2} - \left( \frac{d-1}{R} \right)^2 \frac{\sigma}{\Delta c} \right] \quad (2.55)$$

The first term at the right hand side is the contribution from the supersaturation in the matrix since  $(d\mu/dr')_{+\xi/2}$  represents the flux from the matrix to the particle. The second term is due to the Gibbs-Thomson effect. Eq.(2.55) may be written in a more familiar form [34]

$$\frac{dR}{dt} = \frac{D}{R} \left[ \Delta - \frac{(d-1)d_0}{R} \right] \quad (2.56)$$

where  $D = M(d\mu/dc)$  is diffusivity,  $\Delta \equiv \delta c/\Delta c$  and  $\delta c$  is the supersaturation,  $d_0 \equiv \sigma(d-1)/(d\mu/dc)/(\Delta c)^2$  is a capillary length.  $(d\mu/dr')_{+\xi/2} \approx (\partial\mu/\partial c)(\delta c/R)$ . It is seen that the first term is dominant if the supersaturation is large, thus the growth law is  $R \propto t^{1/2}$ ; Approaching late stages of growth, the supersaturation monotonically decays so that the second term starts to dominate. The growth law will then turn to  $R \propto t^{1/3}$ , which follows the coarsening law.

### 2.4.3 Asymptotic analyses

The preceding sections illustrated the derivation for interface velocity (Eqs.(2.50) and (2.55)) in simple models with single phase field, as well as the Gibbs-Thomson equation for a curved interface (Eq.(2.53)). In various realistic problems the similar analyses are demanded for more sophisticated models, which often involves multiple coupled (conserved and/or non-conserved) phase fields. This is especially true when certain quantitative features of a phase field model are critically required. In a quite general case, the task is to derive a correspondence to the conventional moving

boundary problem:

$$\partial c / \partial t = D \nabla^2 c \quad (2.57)$$

$$v \Delta c = -D(\mathbf{n} \cdot \nabla c|_{0+} - \mathbf{n} \cdot \nabla c|_{0-}) \quad (2.58)$$

$$\delta c_0 / \Delta c = -d_0 \kappa - \beta v \quad (2.59)$$

Eq.(2.57) is simply a diffusion equation and Eq.(2.58) is the condition of mass conservation at interface.  $v$  is the normal local velocity of the interface. Here the concentration  $c$  may be substituted by other conserved field, such as temperature. Subscripts  $0^+$  and  $0^-$  represent the two sides of the interface (denoted by 0).  $\mathbf{n}$  is the unit normal that points from  $0^-$  to  $0^+$ .  $\Delta c \equiv c_{0-} - c_{0+}$  is the concentration jump. Eq.(2.59) represents the departure of concentration from the equilibrium value at interface, as a function of interface curvature and velocity.

The basic strategy to find the connection between Eqs.(2.57)-(2.59) and the phase field model is to divide the space into a region that contains only the interface (called inner region) and the remaining region (called outer region) [36]. In the inner region, the phase fields vary rapidly at a length scale of the interface width, while in the outer region they vary more smoothly at a length scale approximately of the diffusion distance. By expanding the phase fields in each region with respect to appropriate small parameter, such as matrix supersaturation or interface curvature, asymptotic solutions can be found in each region [37]. The undetermined parameters are then obtained by bridging the inner and outer solutions at their junctions (matching both the functions and their first derivatives). At the limit of zero interface width, the phase field equations were found [36, 38] to reduce to the standard moving boundary equations (Eqs.(2.57)-(2.59)). Later, asymptotic analyses were performed by Karma

and Rappel [39, 40], with a physically more realistic assumption of a finite interface width (called thin-interface limit). The thin-interface model reproduces the results from the earlier models and, in addition, relieves the stringent constraints required by the zero interface width. The works by Karma and Rappel [39, 40] and later by various workers [41, 42] are focused on dendritic growth in solidification. More recently, Elder *et al.* [37] analyzed the problem in a more general way with the use of projection operator method. Their approach does not assume specific forms for the free energy and defines the interface location with the Gibbs surface. The latter eliminated several ambiguities in the previous models. Elder *et al.*'s results can be applied to phase field models with coupled fields as well as single conserved or non-conserved field. These advantages make it very flexible to analyze a broad range of problems.

The asymptotic analyses indicate a velocity dependence of the conserved field at interface (Eq.(2.59)), even in models that contain only single concentration field, i.e. Cahn-Hilliard system [37]. This outcome may first appear unphysical since the Cahn-Hilliard equation is essentially a diffusion equation and the interface concentration at the diffusion-controlled limit should be fixed to the equilibrium values. Indeed, this makes a physical sense in that the Cahn-Hilliard equation does not enforce an infinitely fast interface relaxation. Consider a small perturbation  $\delta c(\mathbf{x})$  to an interface previously in equilibrium with matrix. It raises the energy of the interface to  $(\delta\mathcal{F}/\delta c)_i\delta c$  and the energy of the matrix to  $(\delta\mathcal{F}/\delta c)_m\delta c$  by a small mass flux, where  $i$  stands for interface and  $m$  for matrix.  $(\delta\mathcal{F}/\delta c)_i = (\delta\mathcal{F}/\delta c)_m$  because of the previous equilibrium. The restoring force (proportional to this energy increase) is therefore same for both interface and matrix to relax to the original states. However, the extra

mass due to  $\delta c$  has to be transported away from each region because of mass conservation. The relaxation rate is inversely proportional to the distance of transport in each region, which are the interface width  $\xi$  and the diffusion distance  $\Lambda$  in the matrix. In fact, following Elder *et al.*'s analysis [37] the concentration departure in Eq.(2.59) (only the kinetic part) is found  $\delta c_0/\Delta c = -\beta v \propto \xi/\Lambda$ . Thus this kinetic dependence of the interface concentration is attributed to the finite relaxation rate in the interface of finite width. This effect is always expected despite the diffusion nature of the system, unless at a zero interface width or a zero velocity, where  $\xi/\Lambda$  vanishes. For models with coupled fields,  $\beta$  is a sum of a positive contribution from the non-conserved field and a negative contribution from the conserved field [37]. In any cases the non-conserved field does not exhibit such kinetic dependence at interface. It always exponentially decays with time to its equilibrium value [37].

## 2.5 Phase field microelasticity theory

Microstructural domains in a non-uniform crystalline solid often differ in crystal structure, lattice parameter, or crystallographic orientation. In forming a coherent interface where the atomic lattice planes are continuous from one domain to another, the lattices in both domains are necessarily distorted to accommodate their mismatch at interface. Such accommodation reduces the interfacial energy, which is associated with the number density of broken bonds at interface, while causes the elastic energy (the coherency strain energy) stored in all domains. The coherency stress fields from each domain extend and overlap in the space, and their mutual interactions may considerably influence the shape and location of the neighboring domains, as well as various evolution kinetics. In a phase field model where a microstructural evolution is

described in terms of total energy minimization, identify the coherency strain energy for a given microstructure clearly has its important role.

The theoretical treatment of coherency elasticity problems originates from the classic work by Eshelby [43, 44], in which the elastic strain field was derived for an ellipsoidal coherent inclusion in an isotropic elastic medium with equal elastic moduli (the homogeneous moduli approximation). Other inclusion shapes were later considered for both isotropic (for example, [45, 46, 47]) and anisotropic elastic medium [48]. Furthermore Lee *et al.* [49] extended the treatment for ellipsoidal inclusion to the inhomogeneous elastic moduli. A general theory of elastic energy of a coherent inclusion mixture was developed by Khachaturyan *et al.* [50, 51, 52]. It describes an arbitrary distribution of the inclusions by a set of spatially dependent shape functions, with values 0 or 1 for the sites outside or inside the inclusion, respectively. An alternative diffuse interface description was made later [53, 54, 55] by replacing the shape function directly by phase field variables. The theory was extended to inhomogeneous elastic moduli by utilizing perturbation theory (for example, [56, 57, 58], see more complete reference in [59]). A general treatment based on the equivalence principle was later proposed [59]. Below we summarize the basic procedure and results from the literature [52, 60, 59].

The general procedure is solve the mechanical equilibrium equation for a given spatial distribution of transformation strain (stress-free strain) subject to particular boundary conditions. The basic statement of a mechanical equilibrium is the vanishing of the elastic stress gradient

$$\partial\sigma_{ij}(\mathbf{x})/\partial x_j = 0 \quad (2.60)$$

where  $\mathbf{x}$  is the spatial coordinate. Here we use the Einstein notation, i.e., summation over the dummy (repeated) index  $j$ . The elastic stress  $\sigma_{ij}$  is related via the constitutive equation to the elastic strain  $e_{ij}$

$$\sigma_{ij} = C_{ijkl}e_{kl} \quad (2.61)$$

where  $C_{ijkl}$  is the elastic moduli. The elastic strain is the difference between the total strain  $\epsilon_{ij}$  and the transformation strain  $\epsilon_{ij}^T$

$$e_{ij}(\mathbf{x}) = \epsilon_{ij}(\mathbf{x}) - \epsilon_{ij}^T(\mathbf{x}) \quad (2.62)$$

The total strain can be expressed by the displacement  $\mathbf{u}$

$$\epsilon_{ij}(\mathbf{x}) = \frac{1}{2} \left[ \frac{\partial u_i(\mathbf{x})}{\partial x_j} + \frac{\partial u_j(\mathbf{x})}{\partial x_i} \right] \quad (2.63)$$

With substitution of Eqs.(2.61)-(2.63), Eq.(2.60) is rewritten as

$$\frac{\partial}{\partial x_j} C_{ijkl} \frac{1}{2} \left[ \frac{\partial u_k(\mathbf{x})}{\partial x_l} + \frac{\partial u_l(\mathbf{x})}{\partial x_k} \right] = \frac{\partial}{\partial x_j} C_{ijkl} \epsilon_{kl}^T(\mathbf{x}) \quad (2.64)$$

which is a second-order partial differential equation. The form of the equation can be reduced to an ordinary differential equation by using the identity

$$\nabla_{\mathbf{x}} \rightarrow i\mathbf{g} \quad (2.65)$$

in the Fourier space <sup>6</sup>, where  $i \equiv \sqrt{-1}$  when not used as an index. However, the identity does not directly apply to Eq.(2.64) because  $\mathbf{u}$  and its gradient  $\nabla\mathbf{u}$  do not generally vanish at external surface, which is the homogeneous boundary condition required by the transform Eq.(2.65) <sup>7</sup>. Such conditions can be valid, however, if the

<sup>6</sup>By writing in this way we define the Fourier transform as  $\tilde{f}(\mathbf{g}) = \int d\mathbf{x} f(\mathbf{x}) e^{-i\mathbf{g}\cdot\mathbf{x}}$ , and the inverse transform is  $f(\mathbf{x}) = (2\pi)^d \int d\mathbf{g} \tilde{f}(\mathbf{g}) e^{i\mathbf{g}\cdot\mathbf{x}}$ , where  $d$  is dimensionality.

<sup>7</sup>In fact this is also a condition for the existence of the Fourier transform itself.

total strain is separated into a homogeneous and a heterogeneous part as

$$\epsilon_{ij}(\mathbf{x}) = \bar{\epsilon}_{ij} + \delta\epsilon_{ij}(\mathbf{x}) \quad (2.66)$$

and the displacement  $\mathbf{u}(\mathbf{x}) = \bar{\mathbf{u}} + \delta\mathbf{u}(\mathbf{x})$ , where  $\bar{\mathbf{u}}$  and  $\delta\mathbf{u}$  correspond to  $\bar{\epsilon}_{ij}$  and  $\delta\epsilon_{ij}$  respectively. The homogeneous strain is defined in a way that

$$\int d\mathbf{x} \delta\epsilon_{ij}(\mathbf{x}) \equiv 0 \quad (2.67)$$

By removing the homogeneous part of the displacement, Eq.(2.64) is reduced to

$$\frac{\partial}{\partial x_j} C_{ijkl} \frac{1}{2} \left[ \frac{\partial \delta u_k(\mathbf{x})}{\partial x_l} + \frac{\partial \delta u_l(\mathbf{x})}{\partial x_k} \right] = \frac{\partial}{\partial x_j} C_{ijkl} \epsilon_{kl}^T(\mathbf{x}) \quad (2.68)$$

If the volume of the medium is much greater than that of the inclusions, the heterogeneous displacement  $\delta\mathbf{u}$  and its gradient vanish at the external surface. Thus we can apply Eq.(2.65) to Eq.(2.68). It should be noted that since the theory is for the coherency strain energy, the boundary conditions for all internal boundaries are implied as the coherent interface.

### 2.5.1 Homogeneous elastic modulus ( $C_{ijkl} = C_{ijkl}^0$ )

In the Fourier space Eq.(2.68) is written as

$$-C_{ijkl}^0 g_j g_l \delta \tilde{u}_k(\mathbf{g}) = i C_{ijkl}^0 g_j \tilde{\epsilon}_{kl}^T(\mathbf{g}) \quad (2.69)$$

where quantities with the tilde symbol  $\sim$  are the corresponding Fourier transforms.

The solution is readily obtained as

$$\delta \tilde{u}_k(\mathbf{g}) = -ig^{-2} \Omega_{ik}^0(\mathbf{n}) g_j \tilde{\sigma}_{ij}^T(\mathbf{g}) \quad (2.70)$$

where  $\tilde{\sigma}_{ij}^T(\mathbf{g}) \equiv C_{ijkl}^0 \tilde{\epsilon}_{kl}^T(\mathbf{g})$ ,  $[\Omega^{0-1}(\mathbf{n})]_{ik} \equiv C_{ijkl}^0 n_j n_l$ ,  $\mathbf{n} \equiv \mathbf{g}/|\mathbf{g}|$ . Followed immediately is the total strain (by Eq.(2.66))

$$\begin{aligned}\epsilon_{ij}(\mathbf{x}) &= \bar{\epsilon}_{ij} + \frac{1}{2} [\partial \delta u_i(\mathbf{x}) / \partial x_j + \partial \delta u_j(\mathbf{x}) / \partial x_i] \\ &= \bar{\epsilon}_{ij} + \frac{1}{2} \left\{ [n_j \Omega_{ki}^0(\mathbf{n}) + n_i \Omega_{kj}^0(\mathbf{n})] n_l \tilde{\sigma}_{kl}^T(\mathbf{g}) \right\}_{\mathbf{x}}\end{aligned}\quad (2.71)$$

where  $\{\dots\}_{\mathbf{x}}$  is an abbreviated notation for the inverse Fourier transform. Therefore we obtained the elastic strain from Eq.(2.62)

$$e_{ij}(\mathbf{x}) = \bar{\epsilon}_{ij} + \frac{1}{2} \left\{ [n_j \Omega_{ki}^0(\mathbf{n}) + n_i \Omega_{kj}^0(\mathbf{n})] n_l \tilde{\sigma}_{kl}^T(\mathbf{g}) \right\}_{\mathbf{x}} - \epsilon_{ij}^T(\mathbf{x}) \quad (2.72)$$

and the total elastic energy

$$\begin{aligned}E^{el} &= \frac{1}{2} \int d\mathbf{x} C_{ijkl}^0 e_{ij}(\mathbf{x}) e_{kl}(\mathbf{x}) \\ &= \frac{1}{2} \int d\mathbf{x} C_{ijkl}^0 \epsilon_{ij}^T(\mathbf{x}) \epsilon_{kl}^T(\mathbf{x}) + \frac{V}{2} C_{ijkl}^0 \bar{\epsilon}_{ij} \bar{\epsilon}_{kl} - \bar{\epsilon}_{ij} \int d\mathbf{x} C_{ijkl}^0 \epsilon_{kl}^T(\mathbf{x}) \\ &\quad - \frac{1}{2} \int \frac{d\mathbf{g}}{(2\pi)^3} n_i \tilde{\sigma}_{ij}^T(\mathbf{g}) \Omega_{jk}^0(\mathbf{n}) \tilde{\sigma}_{kl}^{T*}(\mathbf{g}) n_j\end{aligned}\quad (2.73)$$

Here  $V$  is the volume of the system.  $\int$  is the principle value of the integral, which excludes a reciprocal small volume of  $(2\pi)^3/V$  at  $\mathbf{g} = 0$ . The asterisk denotes complex conjugate. It is seen that the final results of the elastic strain (Eq.(2.72)) and the elastic energy (Eq.(2.73)) are functions of the transformation strain,  $\epsilon_{ij}^T(\mathbf{x})$ . In the phase field model, it is usually linearly coupled to the field variable. In general, the transformation strain is a sum over each individual contribution  $\epsilon_{ij}^{T0}(p)$ , with the weight of  $\phi_p(\mathbf{x})$ :

$$\epsilon_{ij}^T(\mathbf{x}) = \sum_p \epsilon_{ij}^{T0}(p) \phi_p(\mathbf{x}) \quad (2.74)$$

$\epsilon_{ij}^{T0}(p)$  is the transformation strain of the  $p$ -th field at unity  $\phi_p$ . For example, in a dilatational solid solution with lattice parameter,  $a$ , varying linearly with the solute

concentration (Vegard's law),

$$\epsilon_{ij}^{T0}(solute) = \frac{1}{a(\bar{c})} \frac{da}{dc} \Big|_{\bar{c}} \delta_{ij} \quad (2.75)$$

where  $\bar{c}$  is the average concentration of the system and  $\delta_{ij}$  is the Kronecker delta.

Another example is

$$\epsilon_{ij}^{T0}(p) = \frac{n_i^{(p)} b_j^{(p)} + n_j^{(p)} b_i^{(p)}}{2d^{(p)}} \quad (2.76)$$

for a dislocation with slip plane normal  $\mathbf{n}^{(p)}$ , Burgers vector  $\mathbf{b}^{(p)}$ , and interplanar distance  $d^{(p)}$  of the  $p$ -th slip system (i.e., slip plane and slip direction). It should be emphasized that Eq.(2.74) can include contributions from different types of elastic defects, such as a mixture of dislocations and impurity atoms, as long as their stress-free strains can be linearly coupled. This enables a unified formulation of the elastic energy that counts both the self-energies of the individual kind and their interaction energies.

So far we have not mentioned the value of  $\bar{\epsilon}_{ij}$  in Eqs.(2.72) and (2.73), which in fact is determined by the boundary condition. Two kinds of boundary conditions are commonly used in the phase field model [61]. The first kind is the strain-controlled condition, where the external surface (or equivalently, the macroscopic shape) is specified and

$$\bar{\epsilon}_{ij} = \epsilon_{ij}(surface) = \bar{\epsilon}_{ij}^{appl} \quad (2.77)$$

since  $\delta\epsilon_{ij}(\mathbf{x})$  vanishes at the surface. The governing potential in this case is the Helmholtz free energy

$$\mathcal{F} = \mathcal{F}^\phi + E^{el} \quad (2.78)$$

where  $\mathcal{F}^\phi$  is the Ginzburg-Landau free energy give in Eq.(2.1) or (2.2).

The second kind is the stress-controlled boundary condition, where the surface force  $\mathbf{T}$  is specified. The corresponding governing potential is the Gibbs free energy

$$\mathcal{G} = \mathcal{F}^\phi + E^{el} - \int dA T_i \bar{u}_i \equiv \mathcal{F}^\phi + E^{el} - V \sigma_{ij}^{appl} \bar{\epsilon}_{ij} \quad (2.79)$$

The integral is taken over the surface of the elastic body and  $T_i \equiv \sigma_{ij}^{appl} n_j$ , where  $\mathbf{n}$  is the surface normal. The macroscopic shape is determined via the minimization of the total elastic energy, i.e.,  $\partial E^{el}/\partial \bar{\epsilon}_{ij} = 0$ , which yields

$$\bar{\epsilon}_{ij} = S_{ijkl} \sigma_{kl}^{appl} + \frac{1}{V} \int d\mathbf{x} \epsilon_{ij}^T(\mathbf{x}) \quad (2.80)$$

where  $S_{ijkl} \equiv C_{ijkl}^{-1}$ . The total elastic energy for the stress-controlled boundary condition is thus, by substituting Eq.(2.80) into Eq.(2.73)

$$\begin{aligned} E^{el} &= \frac{1}{2} \int d\mathbf{x} C_{ijkl}^0 \epsilon_{ij}^T(\mathbf{x}) \epsilon_{kl}^T(\mathbf{x}) - \frac{1}{2V} C_{ijkl}^0 \int d\mathbf{x} \epsilon_{ij}^T(\mathbf{x}) \int d\mathbf{x}' \epsilon_{kl}^T(\mathbf{x}') \\ &\quad - \frac{1}{2} \int \frac{d\mathbf{g}}{(2\pi)^3} n_i \sigma_{ij}^T(\mathbf{g}) \Omega_{jk}^0(\mathbf{n}) \sigma_{kl}^{T*}(\mathbf{g}) n_l - \sigma_{ij}^{appl} \int d\mathbf{x} \epsilon_{ij}^T(\mathbf{x}) - \frac{V}{2} S_{ijkl}(\mathbf{x}) \sigma_{ij}^{appl} \sigma_{kl}^{appl} \end{aligned} \quad (2.81)$$

### 2.5.2 Inhomogeneous elastic modulus ( $C_{ijkl} = C_{ijkl}(\mathbf{x})$ )

With the elastic modulus now being a function of position  $\mathbf{x}$ , Eq.(2.68) or Eq.(2.64) can no longer be solved directly with the use of Fourier transform as in the preceding case. To solve for the equilibrium condition, we may write the elastic modulus as

$$C_{ijkl}(\mathbf{x}) = C_{ijkl}^0 + \Delta C_{ijkl}(\mathbf{x}) \quad (2.82)$$

The choice of the constant  $C_{ijkl}^0$  is rather arbitrary, as long as it is non-zero. A common choice is to have the value of the major elastic body. With  $\partial u_i(\mathbf{x})/\partial x_j = \partial(\bar{u}_i + \delta u_i(\mathbf{x}))/\partial x_j = \partial \delta u_i(\mathbf{x})/\partial x_j$  in mind, Eq.(2.68) becomes

$$C_{ijkl}^0 \frac{\partial}{\partial x_j} \frac{1}{2} \left[ \frac{\partial \delta u_k(\mathbf{x})}{x_l} + \frac{\partial \delta u_l(\mathbf{x})}{\partial x_k} \right] = \frac{\partial}{\partial x_j} \left\{ C_{ijkl}^0 \epsilon_{kl}^T(\mathbf{x}) - \Delta C_{ijkl}(\mathbf{x}) [\epsilon_{kl}(\mathbf{x}) - \epsilon_{kl}^T(\mathbf{x})] \right\} \quad (2.83)$$

Similar to the preceding case the solution is obtained in the Fourier space as

$$\delta\tilde{u}_k(\mathbf{g}) = -ig^{-2}\Omega_{ik}^0(\mathbf{n})g_j \left\{ C_{ijkl}^0 \epsilon_{kl}^T(\mathbf{x}) - \Delta C_{ijkl}(\mathbf{x}) [\epsilon_{kl}(\mathbf{x}) - \epsilon_{kl}^T(\mathbf{x})] \right\}_{\mathbf{g}} \quad (2.84)$$

Here  $\{\dots\}_{\mathbf{g}}$  denotes a Fourier transform. The total strain is given by Eq.(2.66)

$$\epsilon_{ij}(\mathbf{x}) = \bar{\epsilon}_{ij} + \frac{1}{2} \left\{ \left[ n_j \Omega_{ki}^0(\mathbf{n}) + n_i \Omega_{kj}^0(\mathbf{n}) \right] n_j \left\{ C_{klmn}^0 \epsilon_{mn}^T(\mathbf{x}) - \Delta C_{klmn}(\mathbf{x}) [\epsilon_{mn}(\mathbf{x}) - \epsilon_{mn}^T(\mathbf{x})] \right\}_{\mathbf{g}} \right\}_{\mathbf{x}} \quad (2.85)$$

It is seen that because of the position dependence of the elastic modulus the total strain now is contained in both sides of Eq.(2.85), compared to its counterpart (Eq.(2.71)) in the homogeneous modulus case. Solving the explicit solution of  $\epsilon_{ij}(\mathbf{x})$  will finally give the solution to the mechanical equilibrium.

As proposed by Wang *et al.* [59], the computation of Eq.(2.85) may be significantly simplified by recognizing an equivalent elastic system with a homogeneous modulus. Define a virtual strain  $\epsilon_{ij}^0(\mathbf{x})$  by

$$C_{ijkl}^0 \epsilon_{kl}^0(\mathbf{x}) \equiv C_{ijkl}^0 \epsilon_{kl}^T(\mathbf{x}) - \Delta C_{ijkl}(\mathbf{x}) [\epsilon_{kl}(\mathbf{x}) - \epsilon_{kl}^T(\mathbf{x})] \quad (2.86)$$

makes Eq.(2.85)

$$\epsilon_{ij}(\mathbf{x}) = \bar{\epsilon}_{ij} + \frac{1}{2} \left\{ \left[ n_j \Omega_{ki}^0(\mathbf{n}) + n_i \Omega_{kj}^0(\mathbf{n}) \right] n_l C_{klmn}^0 \tilde{\epsilon}_{mn}^0(\mathbf{g}) \right\}_{\mathbf{x}} \quad (2.87)$$

This is an identical form as Eq.(2.71) in the preceding case with homogeneous elastic modulus if the original transformation strain  $\epsilon_{ij}^T(\mathbf{x})$  is replaced by the virtual strain  $\epsilon_{ij}^0(\mathbf{x})$ . To further illustrate this equivalence, we may subtract  $C_{ijkl}^0 \epsilon_{kl}(\mathbf{x})$  at both sides of Eq.(2.86):

$$C_{ijkl}^0 [\epsilon_{kl}(\mathbf{x}) - \epsilon_{kl}^0(\mathbf{x})] = [C_{ijkl}^0 + \Delta C_{ijkl}(\mathbf{x})] [\epsilon_{kl}(\mathbf{x}) - \epsilon_{kl}^T(\mathbf{x})] \quad (2.88)$$

This means that the elastic stress in an *elastically inhomogeneous* system with modulus  $C_{ijkl}(\mathbf{x}) \equiv C_{ijkl}^0 + \Delta C_{ijkl}(\mathbf{x})$  and transformation strain  $\epsilon_{ij}^0(\mathbf{x})$  is identical to the elastic stress in an *elastically homogeneous* system with modulus  $C_{ijkl}^0$  and transformation strain  $\epsilon_{ij}^T(\mathbf{x})$ . Therefore if we can identify such an equivalent virtual strain  $\epsilon_{ij}^0(\mathbf{x})$  the elastic problem for the elastically inhomogeneous system can be solved in an equivalent elastically homogeneous system with the solutions developed previously. It may worth of noticing that the elastic strains in the two equivalent systems (i.e.,  $\epsilon_{ij}(\mathbf{x}) - \epsilon_{ij}^0(\mathbf{x})$  and  $\epsilon_{ij}(\mathbf{x}) - \epsilon_{ij}^T(\mathbf{x})$ ) do not equal, however, it is the elastic stress that determines the equivalence of the mechanical equilibrium condition. Eliminating  $\epsilon_{ij}(\mathbf{x})$  in Eqs.(2.86) and (2.87) yields the equilibrium condition identical to Eq.(2.85) but in terms of  $\epsilon_{ij}^0(\mathbf{x})$

$$\begin{aligned} & -\Delta S_{ijkl}(\mathbf{x})C_{klmn}^0[\epsilon_{mn}^0(\mathbf{x}) - \epsilon_{mn}^T(\mathbf{x})] + \epsilon_{ij}^T(\mathbf{x}) \\ & = \bar{\epsilon}_{ij} + \frac{1}{2}\left\{[n_j\Omega_{ki}(\mathbf{n}) + n_i\Omega_{kj}(\mathbf{n})]n_lC_{klmn}^0\tilde{\epsilon}_{mn}^0(\mathbf{g})\right\}_{\mathbf{x}} \end{aligned} \quad (2.89)$$

where  $\Delta S_{ijkl}(\mathbf{x}) \equiv [\Delta C^{-1}(\mathbf{x})]_{ijkl}$ . Now to find this  $\epsilon_{ij}^0(\mathbf{x})$ , we may write the total elastic energy

$$\begin{aligned} E^{el} &= \frac{1}{2} \int d\mathbf{x} [C_{ijkl}^0 + \Delta C_{ijkl}(\mathbf{x})][\epsilon_{ij}(\mathbf{x}) - \epsilon_{ij}^T(\mathbf{x})][\epsilon_{kl}(\mathbf{x}) - \epsilon_{kl}^T(\mathbf{x})] \\ &= \frac{1}{2} \int d\mathbf{x} C_{ijkl}^0 [\epsilon_{ij}(\mathbf{x}) - \epsilon_{ij}^0(\mathbf{x})][\epsilon_{kl}(\mathbf{x}) - \epsilon_{kl}^0(\mathbf{x})] \\ &\quad + \frac{1}{2} \int d\mathbf{x} C_{ijkl}^0 [\epsilon_{ij}^0(\mathbf{x}) - \epsilon_{ij}^T(\mathbf{x})][\epsilon_{kl}(\mathbf{x}) - \epsilon_{kl}^0(\mathbf{x})] \end{aligned} \quad (2.90)$$

where we have used Eq.(2.88). Notice the first term simply corresponds to Eq.(2.73) in the homogeneous modulus case with  $\epsilon_{ij}^T$  replaced by  $\epsilon_{ij}^0$ . The second term

$$\begin{aligned} &= \frac{1}{2} \int d\mathbf{x} C_{ijkl}^0 [\epsilon_{ij}^0(\mathbf{x}) - \epsilon_{ij}^T(\mathbf{x})] \left\{ [\epsilon_{kl}(\mathbf{x}) - \epsilon_{kl}^T(\mathbf{x})] - [\epsilon_{kl}^0(\mathbf{x}) - \epsilon_{kl}^T(\mathbf{x})] \right\} \\ &= \frac{1}{2} \int d\mathbf{x} C_{ijkl}^0 [\epsilon_{ij}^0(\mathbf{x}) - \epsilon_{ij}^T(\mathbf{x})] \left\{ -\Delta S_{klpq}(\mathbf{x}) C_{pqmn}^0 [\epsilon_{mn}^0(\mathbf{x}) - \epsilon_{mn}^T(\mathbf{x})] - [\epsilon_{kl}^0(\mathbf{x}) - \epsilon_{kl}^T(\mathbf{x})] \right\} \\ &= \frac{1}{2} \int d\mathbf{x} [-C_{ijmn}^0 \Delta S_{mnpq}(\mathbf{x}) C_{pqkl}^0 - C_{ijkl}^0] [\epsilon_{ij}^0(\mathbf{x}) - \epsilon_{ij}^T(\mathbf{x})] [\epsilon_{kl}^0(\mathbf{x}) - \epsilon_{kl}^T(\mathbf{x})] \end{aligned}$$

The second step has used Eq.(2.86). With all terms together we can write the elastic energy in terms of the virtual strain field  $\epsilon_{ij}^0(\mathbf{x})$

$$\begin{aligned} E^{el} &= \frac{1}{2} \int d\mathbf{x} [-C_{ijmn}^0 \Delta S_{mnpq}(\mathbf{x}) C_{pqkl}^0 - C_{ijkl}^0] [\epsilon_{ij}^0(\mathbf{x}) - \epsilon_{ij}^T(\mathbf{x})] [\epsilon_{kl}^0(\mathbf{x}) - \epsilon_{kl}^T(\mathbf{x})] \\ &\quad + \frac{1}{2} \int d\mathbf{x} C_{ijkl}^0 \epsilon_{ij}^0(\mathbf{x}) \epsilon_{kl}^0(\mathbf{x}) + \frac{V}{2} C_{ijkl}^0 \bar{\epsilon}_{ij} \bar{\epsilon}_{kl} - \bar{\epsilon}_{ij} \int d\mathbf{x} C_{ijkl}^0 \epsilon_{kl}^0(\mathbf{x}) \\ &\quad - \frac{1}{2} \int \frac{d\mathbf{g}}{(2\pi)^3} n_i \tilde{\sigma}_{ij}^0(\mathbf{g}) \Omega_{jk}^0(\mathbf{n}) \tilde{\sigma}_{kl}^{0*}(\mathbf{g}) n_j \end{aligned} \quad (2.91)$$

The functional variation  $\delta E^{el}/\delta \epsilon_{ij}^0(\mathbf{x}) = 0$  in fact yields the equilibrium condition Eq.(2.89). Therefore the virtual strain  $\epsilon_{ij}^0(\mathbf{x})$  can be obtained at the minimum of the energy functional in Eq.(2.91). The actual computation may rely on numerical iteration methods such as the steepest decent method [62]. Alternatively the minimization may adopt the conventional phase field approach (e.g. Eq.(2.4)) with  $\epsilon_{ij}^0(\mathbf{x})$  being treated as a non-conserved field [59]. As the virtual strain  $\epsilon_{ij}^0(\mathbf{x})$  is obtained (simultaneously is the elastic energy), the elastic strain can be computed with Eqs.(2.87) and (2.62).

## 2.6 Some discussion on phase field applications to coherent phase transformations

In a series of classical papers [63, 64, 65, 6], Cahn laid the theoretical foundation for coherent transformations in crystalline solids. He distinguished the atomic misfit

energy (part of the mixing energy of a solid solution) from the coherency elastic strain energy, and incorporated the latter into the total free energy to study coherent processes. He analyzed the effect of coherency strain energy on phase equilibrium, nucleation, and spinodal decomposition. Since the free energy is formulated within the framework of gradient thermodynamics [21], these studies are actually the earliest applications of the phase field method to coherent transformations.

### **Atomic misfit energy and coherency strain energy**

A macroscopically stress-free solid solution with uniform composition can be in a strained state if the constituent atoms differ in size. The elastic energy from this microscopic origin is often referred to as the atomic misfit energy in solid solution theories [66]. It is the difference between the free energy of a real, homogeneous solution and the free energy of a hypothetical solution of the same system in which all the atoms have the same size. This atomic misfit energy is a part of the physically measurable chemical free energy and is included in thermodynamic databases in literature. The elastic energy associated with coherent compositional or structural non-uniformities (such as fluctuations and precipitates) is referred to as the coherency strain energy. The reference state for the measure of the coherency strain energy is a system of identical fluctuations or precipitatematrix mixture, but with the fluctuations or precipitates/matrix separated into stress-free portions [6]. Since the coherency strain energy is in general a function of size, shape, spatial orientation and mutual arrangement of precipitates [52], it cannot be incorporated into the chemical free energy except for very special cases [63]. Thus the coherency strain energy is usually not included in the free energy from thermodynamic databases.

## Coherent and incoherent phase diagrams

Different from the atomic misfit energy, the coherency strain energy is zero for homogeneous solid solutions and positive for any non-uniform coherent systems. It always promotes a homogeneous solid solution and suppresses phase separation. For a given system, the phase diagram determined by minimizing solely the bulk chemical free energy, or measured from a stage when precipitates already loose their coherency with the matrix, is referred to as incoherent phase diagram. Correspondingly the phase diagram determined by minimizing the sum of the bulk chemical free energy and the coherency strain energy, or measured from coherent stages of the system is referred to as coherent phase diagram. A coherent phase diagram, which is relevant to the study of coherent precipitation, could differ significantly from an incoherent one. This has been demonstrated clearly by Cahn [63]) using an elastically isotropic system with a linear dependence of lattice parameter on composition. In this particular case the equilibrium compositions and volume fractions of coherent precipitates can be determined by the common-tangent rule with respect to the total bulk free energy (Fig.2.4). Cahn showed that a coherent miscibility gap lies within an incoherent miscibility gap, with the differences in critical point and width of the miscibility gap determined by the amount of lattice misfit. In an elastically anisotropic system, the coherency strain energy becomes a function of precipitate size, shape and spatial location. In this case precipitates of different configurations will have different coherency strain energies, leading to a series of miscibility gaps lying within the incoherent one.

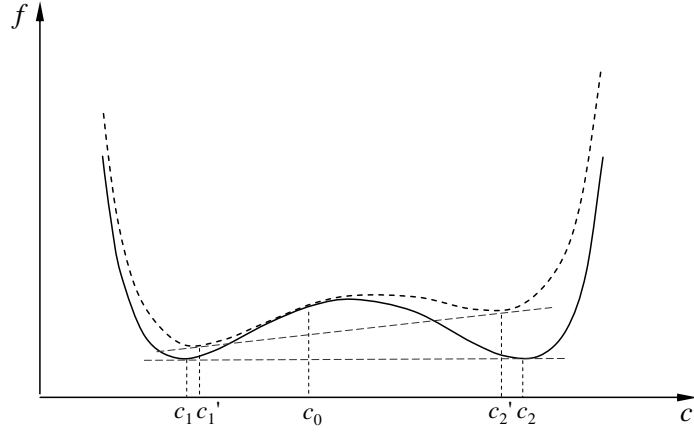


Figure 2.4: Schematic drawing of the incoherent (solid line) and coherent (dotted line) free energies in an elastically isotropic solid solution. The equilibrium compositions in both cases are determined by the common tangent construction.  $c_0$  is the average composition (after [6]).

The total free energy is the sum of the chemical free energy and the coherency strain energy.

$$\mathcal{F} = \mathcal{F}^{ch} + E^{el} \quad (2.92)$$

Since a coherent chemical free energy contains part of the coherency strain energy, it is necessary to subtract this part of the coherency strain energy from  $E^{el}$  so that it will not appear twice in the total energy (Eq.(2.92)). Following the same treatment as that presented in the microscopic elasticity theory of solid solutions [52], we may rewrite the coherency strain energy (for example, Eq.(2.73)) as

$$E^{el} = E_{self}^{el} + E_{int}^{el} \quad (2.93)$$

where,

$$E_{self}^{el} = \frac{1}{2} \sum_{p=1}^N \sum_{q=1}^N \int C_{ijkl}^0 \epsilon_{ij}^{T0}(p) \epsilon_{kl}^{T0}(q) \phi_p(\mathbf{x}) \phi_q(\mathbf{x}) d\mathbf{x} + \frac{V}{2} C_{ijkl}^0 \bar{\epsilon}_{ij} \bar{\epsilon}_{kl} - \bar{\epsilon}_{ij} \sum_{p=1}^N \int C_{ijkl}^0 \epsilon_{kl}^{T0}(p) \phi_p(\mathbf{x}) d\mathbf{x} - \frac{1}{2} \sum_{p=1}^N \sum_{q=1}^N Q \delta_{pq} \int \tilde{\phi}_p(\mathbf{g}) \tilde{\phi}_q^*(\mathbf{g}) \frac{d\mathbf{g}}{(2\pi)^3} \quad (2.94)$$

$$E_{int}^{el} = -\frac{1}{2} \sum_{p=1}^N \sum_{q=1}^N \int [n_i \sigma_{ij}^{00}(p) \Omega_{jk}(\mathbf{n}) \sigma_{kl}^{00}(q) n_l - Q \delta_{pq}] \tilde{\phi}_p(\mathbf{g}) \tilde{\phi}_q^*(\mathbf{g}) \frac{d\mathbf{g}}{(2\pi)^3} \quad (2.95)$$

and  $Q = \langle n_i \sigma_{ij}^{00}(p) \Omega_{jk}(\mathbf{n}) \sigma_{kl}^{00}(q) n_l \rangle_{\mathbf{g}}$  is the average of  $n_i \sigma_{ij}^{00}(p) \Omega_{jk}(\mathbf{n}) \sigma_{kl}^{00}(q) n_l$  over the entire reciprocal space and  $\delta_{pq}$  is the Kronecker delta.  $E_{self}^{el}$  is configuration-independent and equals the elastic energy of placing a coherent precipitate of unit volume into an infinite uniform matrix multiplying the total volume of the precipitates.  $E_{int}^{el}$  is configuration-dependent and contains the pair-wise interactions between precipitates and between volume elements within a finite precipitate. Since the self energy  $E_{self}^{el}$  depends only on the total volume of the precipitates and is independent of their morphology and spatial arrangement, it could be incorporated into and renormalizes the chemical free energy. Clearly, the self energy should be subtracted from the coherency strain energy if the chemical free energy is already a coherent one.

## CHAPTER 3

# COMPUTATIONAL MODEL FOR MICROSTRUCTURAL EVOLUTION VIA CONCURRENT NUCLEATION, GROWTH, AND COARSENING

### 3.1 Introduction

Metals and alloys in today's engineering applications are seldom uniform inside. The materials comprise mixture of domains either in different phases (e.g., precipitates) or in a same phase but with different crystallography (e.g., grains, orientational variants, anti-phase domains). Figure 3.1 shows a typical  $\gamma/\gamma'$  (fcc and  $L1_2$ ) microstructure of nickel-aluminum alloys. Various experimental evidences have revealed that the strength of the alloy is closely related to the volume fraction, the size and spatial distributions of these ordered  $\gamma'$  precipitates (see, for example, review in Ref [67]). In general, it has become a well established portion of our understandings of materials that controlling these non-uniformities, or the microstructure, can create a broad spectrum of new material properties.

Microstructures in metals are usually produced by phase transformations under controlled conditions. A typically used process is to cool a homogenized alloy solution to a metastable state at a lower temperature. Depending on the degree of cooling,

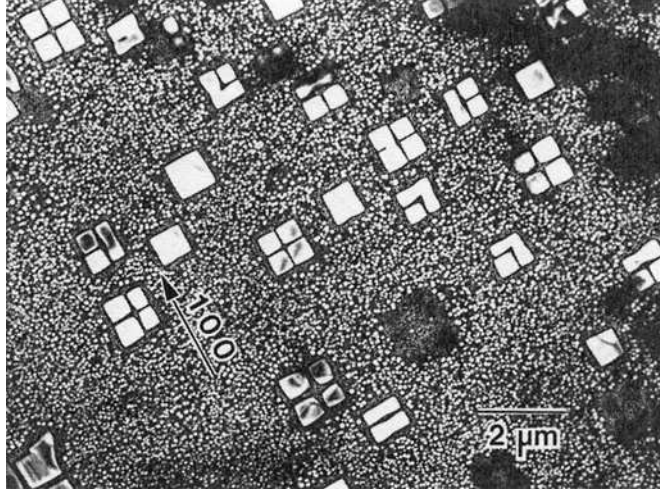


Figure 3.1: Dark-field transmission electron micrograph of  $\gamma'$   $\text{Ni}_3\text{Al}$  precipitates in Ni-17at.%Al, from Ref. [7].

decomposition of the alloy solution may be initiated by the formation of (1) hetero-phase nuclei from strong but localized thermal fluctuations, or (2) low amplitude but spatially extended homo-phase fluctuations which lead to spinodal decomposition. The subsequent reaction proceeds to further decomposition of the alloy into distinctive phases, and the growth of the new phase domains until an equilibrium volume fraction is reached. The reaction may further extend to a coarsening stage, where large precipitates grow at the expense of the shrinkage of small ones, during which the excess energy associated with interfaces or boundaries decreases.

The characteristic of the final microstructure, including particle size, shape, mutual position and distance, could have a general dependence on the entire kinetic path via the stages of nucleation, growth, and coarsening. A major concern is that these stages may not act in a sequential fashion. This may be particularly likely in solid-state phase transformations since nucleation in solids is usually much less

sensitive to the undercooling (or supersaturation) than in liquids [5], which may considerably extend the nucleation to the stage of growth. Meanwhile, the non-uniform solute concentration owing to relatively slow mass transport in solids often result in the simultaneous occurrence of growth in the solute-rich regions and coarsening in the solute-poor regions. Moreover, non-isothermal heat treatment commonly utilized in contemporary material processing could continuously supply driving forces for all these processes, which makes them compete and overlap in both time and space.

These concerns lead to a call for a methodology with the capabilities to treat nucleation, growth, and coarsening as *concomitant* processes. Early attempts in this direction are represented by the cluster-dynamic approach by Binder and Stauffer [68, 69] and the decomposition theory by Langer and Schwartz [70] and its modifications [71, 72, 72]. Review of these approaches can be found in Ref [73]. Particle size distribution during the stages from nucleation to coarsening can be directly computed from these models and compared to experiment. On the other hand, the morphological aspect of the microstructure, such as the particles' shape and spatial distribution are not provided by these models. These information could become equally important in real situations. For example, when a metal's deformation is controlled by the looping of dislocations around precipitates, it is the precipitates' interspacing rather than their diameter that determines the critical stress for dislocation motion. Furthermore, precipitate growth at relatively high supersaturation typically depletes the matrix non-uniformly, which influences the local driving force for subsequent growth and coarsening. These effects in general cannot be accounted for without the knowledge of the actual microstructure. The phase field method, as a microstructure-based

approach, has been acting as a promising candidate for dealing with these complexities. The use of the diffusion potential, i.e.,  $\delta\mathcal{F}/\delta\phi$  in Eq.(2.3), as driving force allows a unified description for growth and coarsening. Some detailed analyses on growth and coarsening are provided in Chapter 6. To include nucleation, phase field method introduces the Langevin noise terms, e.g.,  $\zeta_{\phi_p}$  in Eqs.(2.7) and (2.8), that mimic the effects of thermal fluctuation.

Nevertheless there exists a theoretical inconsistency in the present use of Langevin terms in describing nucleation at a mesoscopic level. Unlike in second-order phase transitions, fluctuations at any length scale contribute to nucleation (see Section 2.2). However microstructures described by a *mesoscale* phase field model have averaged all the fluctuations below the mesoscopic length scale by the coarse-graining process. The Langevin noises applied at the meso-scales are thus theoretically irrelevant to the nucleation and the reproducibility of the nucleation rate is doubtful no matter whether the amplitude of these fluctuations is derived from the fluctuation-dissipation relation in Eqs.(2.9)-(2.11). It is also noted that the time scale for nucleation (roughly at the same order of atomic jump) is order of magnitude smaller than the one for growth. If every nucleation event were to be assessed, the simulation time step would have to be constrained to the smaller one, at which growth and coarsening would be practically frozen. Owing to this practical concern, the actual simulation time step is conventionally chosen for the growth while the amplitude of the fluctuations is artificially increased to compensate the dramatic decrease of the sampling frequency for nucleation (Fig. 3.2). This amplitude, however, often becomes sufficiently large to interfere with the existing profile (e.g. composition) of the microstructure. Therefore

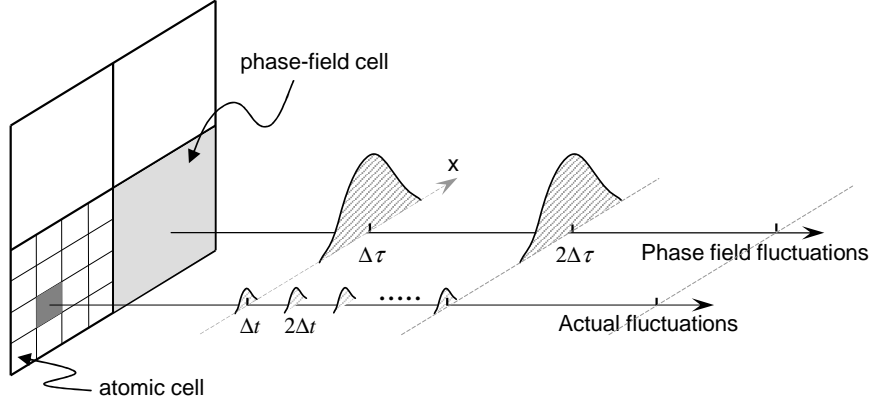


Figure 3.2: The fluctuations simulated in a mesoscale phase field model are much more extended in the space than the actual ones. Since nucleation events occur much less frequently due to the use of the time scale for growth, to maintain a same magnitude of the nucleation rate the amplitude of the fluctuations is artificially increased.

the use of the Langevin noise has been inevitably restricted to nucleation at the very beginning of phase separation, i.e., the site-saturation limit.

### 3.2 The explicit nucleation algorithm

The explicit nucleation algorithm [11] was developed to overcome this limitation so that nucleation events are allowed to occur at any time when the driving force permits. Since an actual nucleation event is neither spatially nor temporally “visible” at a mesoscale level<sup>8</sup>, the task resorts to an indirect way in which nuclei are explicitly (or manually) introduced. Specifically, instead of actually simulating a decaying fluctuation, it generates stochastic nucleation events according to an instantaneous assessment of local nucleation rate. This raises two questions: at what rate such events should occur, and how the nuclei should be introduced.

<sup>8</sup>The time scale is associated with the length scale, e.g.,  $t \propto \sqrt{L}$  in a diffusional process. In a mesoscale model the time scale is typically related to the domain growth.

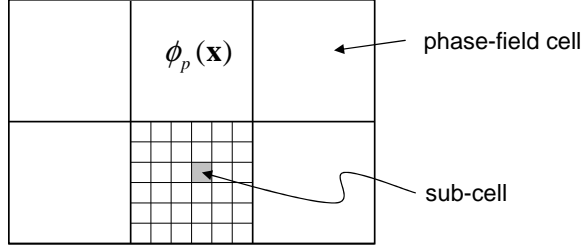


Figure 3.3: Mesoscale phase field cells and the uniformly divided sub-cells of size similar to a critical nucleus.

For the first question, a phase-field cell is uniformly divided into sub-cells of the size similar to the critical nucleus (Fig. 3.3). The physical properties (characterized by the phase fields  $\phi_p$ ) inside the phase-field cell are considered to be uniform so that all sub-cells therein are identical. The rate at which a sub-cell is transformed to the precipitate phase equals the nucleation rate

$$J = J(\{\phi_p(\mathbf{x}, t)\}) \quad (3.1)$$

Here  $\{\phi_p(\mathbf{x}, t)\}$  denotes the configuration of the phase fields  $\{\phi_p : p = 1, 2, \dots\}$  at the phase-field cell  $\mathbf{x}$  and at time  $t$ . The probability of a sub-cell being transformed in a time step,  $1/\beta$ , is

$$p = J\Delta v/\beta \quad (3.2)$$

Here  $\beta$  is the frequency at which atoms attach the surface of a critical nucleus,  $\Delta v$  is the volume of the sub-cell. The probability of transformation over a longer time step,  $\Delta\tau$ , is

$$p' = 1 - (1 - p)^{\Delta\tau\beta} = 1 - (1 - J\Delta v/\beta)^{\Delta\tau\beta} \quad (3.3)$$

If the transformations of sub-cells are considered as independent events and any single event subsequently transforms the whole phase-field cell, the probability of

transformation of a phase-field cell in a time step  $\Delta\tau$  is

$$P = 1 - (1 - p')^\nu = 1 - (1 - J\Delta v/\beta)^{\Delta\tau\beta\Delta V/\Delta v} \quad (3.4)$$

where  $\nu$  is the number of sub-cells in a phase field cell and  $\Delta V \equiv \nu\Delta v$  is the volume of the phase-field cell. Notice  $\lim_{x \rightarrow 0}(1 - x)^{1/x} = e^{-1}$ , Eq.(3.4) becomes

$$P \cong 1 - e^{-J\Delta V \Delta \tau} \quad (3.5)$$

at small value of  $p = J\Delta v/\beta$ . This condition is in fact not stringent. With typical values,  $J = 10^{20} m^{-3} s^{-1}$ ,  $\Delta v = 10^{-25} m^3$ , and  $\beta = 10^{15} s^{-1}$ ,  $p$  is only about  $10^{-20}$ .

Since the probability  $P$  is assessed upon the local phase field configurations  $\phi_p(\mathbf{x}, t)$ , it is a function of the spatial coordinate and varies with time. To actuate the nucleation event, at each time step a random number,  $r$ , with uniform distribution between 0 and 1 is generated for each phase-field cell. A phase-field cell is considered to transform only if  $r > P$ . With a sufficiently large number of phase-field cells, the nucleation rate (Eq.(3.1)) will be statistically reproduced by such sampling operations. After a phase-field cell is determined to transform, a predefined profile will be assigned to the phase field variables at that position, which resembles that of an equilibrated nucleus.

It should be pointed out that Eq.(3.1) does not assume any model for the nucleation rate. The explicit nucleation algorithm in fact receives the local conditions from phase field model, computes the local nucleation rate from a selected nucleation model, and generates nucleation events in the phase field. Separating the details of nucleation from the algorithm allows flexible incorporation of data from theories or experiments when dealing with various nucleation mechanisms, such as homogeneous or heterogeneous nucleation.

It is meanwhile worth noticing that the nucleation rate  $J$  in Eq.(3.2) is the rate of formation of *critical nuclei*, which could be more relevant to theoretical computation. The nucleation rate measured in experiment is often counted on the precipitates that already grew from or coalesced by critical nuclei. Such effects should be taken into account to make the use of Eq.(3.2) self consistent. In particular, if a given nucleation rate ( $J'$ ) is measured at the same mesoscale level as of phase field model,

$$P = J' \Delta V \Delta \tau \quad (3.6)$$

should be used instead of Eq.(3.5). The actual difference is negligible if  $J' \Delta V \Delta \tau \ll 1$ .

As mentioned earlier, the scales of time and length are coupled in the phase field model. Specifically, in a mesoscale model the time scale is associated with the variation of the phase field over a mesoscopic distance. This time scale, however, could happen to be too large at a relatively high nucleation rate that many nuclei are generated as apparently independent events in one time step, regardless of the actual correlation among these nuclei if they were allowed to occur in a naturally finer time step. This could considerably alter the later microstructure, especially in the presence of long-range interaction among nuclei. To prevent this artifact the explicit nucleation algorithm confines the time step,  $\Delta\tau$  (may be called nucleation time step), to a sufficiently small value that in each step only a few nucleation events occur. This time step, calculated dynamically upon the instant average nucleation rate, could be smaller than the phase field time step but still considerably larger than the characteristic time of thermal fluctuations. The actual simulation time step is chosen as the smaller one of these two time steps.

### 3.3 Computation of nucleation rate

Critical nuclei in solids are transient and typically about nanometer (or smaller) in size. Hence direct measurement for the nucleation rate, even for homogeneous nucleation, is usually difficult. In practice, nucleation is always interfered by immediate growth of nuclei, which reduces matrix supersaturation and causes local coarsening [74]. Thus most reported data in fact were obtained when the coarsening regime is already reached [75]. Due to these difficulties nucleation rate in simulations are mostly computed from theoretical models.

The classical nucleation theory [76, 77] considers vapor-liquid transitions and treats nuclei as spherical droplets with the bulk phase property and atomically sharp surfaces. The free energy of a nucleus of radius  $R$  is therefore

$$\Delta F = -\frac{4\pi R^3}{3} \Delta f + 4\pi R^2 \sigma \quad (3.7)$$

Here  $\Delta f \equiv f_v - f_l$  is the difference between the free energy of the vapor phase ( $f_v$ ) and that of the liquid phase ( $f_l$ ),  $\sigma$  is the surface energy per area. A critical nucleus corresponds to the maximum of the energy (by  $d\Delta F/dR = 0$ ) because any larger nucleus will have a smaller energy and spontaneously grow. The size and energy of the critical nucleus are then

$$R^c = \frac{2\sigma}{\Delta f} \quad (3.8)$$

$$\Delta F^c = \Delta F(R^c) = \frac{16\pi}{3} \frac{\sigma^3}{\Delta f^2} \quad (3.9)$$

The nucleation rate is considered in cluster dynamics, in which an  $m$ -mer cluster (cluster with  $m$  atoms) may gain (or loose) an atom to become an  $m+1$ -mer (or  $m-1$ -mer) cluster and results in a flow of the population among these cluster groups. At a

steady-state flow and by assuming the equilibrium (Boltzmann) distribution for each cluster group, the steady-state nucleation rate is obtained as

$$J = J_0 e^{-\Delta F^c / k_B T} \quad (3.10)$$

where  $k_B$  is Boltzmann constant and  $T$  is temperature. The prefactor

$$J_0 = Z\beta N \quad (3.11)$$

where  $Z$  is the Zeldovich factor,  $\beta$  the frequency factor, and  $N$  the number of nucleation site per unit volume [78].

Extension of the classical nucleation theory to solid-solid transitions requires additional consideration for the effects of crystallography. For example, the interfacial energy  $\sigma$  may depend on the interface orientation. Elastic stress should generally arise if the precipitated phase has different composition and/or crystal structure. Nuclei may develop non-spherical shapes due to interfacial and/or elastic anisotropy. The free energy of the nucleus (Eq.(3.7)) hence may be modified to

$$\Delta F = -V\Delta f + A\bar{\sigma} + E^{el} \quad (3.12)$$

where  $V$  is the volume of the nucleus and  $A$  the area of the interface.  $\bar{\sigma}$  may be regarded as an effective interfacial energy averaged over all orientations.  $E^{el}$  is traditionally considered as a volume strain energy and is directly incorporated into the bulk energy  $V\Delta f$ . This treatment however is not generally valid for elastically anisotropic medium, where the elastic energy does not rigorously show a simple linear dependence on the volume of nucleus. Section 3.5 will derive an approximate solution with the linear term of  $V$ , so that the anisotropic elastic energy can still be conveniently incorporated into the classical theory.

Despite the conceptual intuitiveness of Eq.(3.7) of the classical theory, assigning the bulk phase properties to nano-size nucleus is obviously doubtful. Moreover, the use of  $\sigma$  of a planar surface (or interface) is questionable when the radius of the curved interface is about its width, which is exactly the situation for a critical nucleus [1]. The non-classical nucleation theory due to Cahn and Hilliard [79] instead considers the total free energy of an inhomogeneous system(Eq.(2.1)) that contains a nucleus in an infinite matrix. The nucleation barrier is obtained at the saddle point of the total energy subject to the constraint of mass conservation

$$\frac{\delta}{\delta c} \left[ \mathcal{F}[c(\mathbf{x})] + \mu \int_{-\infty}^{+\infty} c(\mathbf{x}) d\mathbf{x} \right] = 0 \quad (3.13)$$

Here we explicitly use composition as the phase field variable.  $\mu$  is the Lagrangian multiplier for the constraint. The solution to Eq.(3.13) is

$$\frac{\partial f}{\partial c} - \kappa_c \nabla^2 c = \mu \quad (3.14)$$

The unknown  $\mu$  is determined by the boundary condition at infinite: recall the composition gradient far from the nucleus vanishes,  $\mu = \partial f / \partial c|_\infty$ . The composition profile of the critical nucleus,  $c^c(\mathbf{x})$ , is obtained by integrating Eq.(3.14) from infinite to the center of the nucleus. Correspondingly the free energy of the critical nucleus is

$$\Delta F^c = \mathcal{F}[c^c(\mathbf{x})] - \mathcal{F}[c = c^c(\infty)] \quad (3.15)$$

At the limit of vanishing supersaturation the non-classical theory is found to converge to the classical theory in terms of the size, profile, and energy of the critical nucleus; while at the high supersaturation side the non-classical theory predicts a spatially extended nucleus with composition significantly lower than that of the bulk phase. The non-classical theory does not address the dynamics of nucleation and thus the prefactor  $J_0$  is usually provided by cluster dynamic theories.

The Cahn-Hilliard theory exhibits a continuous transition of the mechanism of phase separation between nucleation and spinodal decomposition. On the other hand, as pointed out by Binder [68], the uncertainties in a precise determination of the coarsen-grained free energy  $f(c)$  and the gradient coefficient  $\kappa_c$  as well as their dependence on the coarse-graining cut-off still cause difficulties in the general accuracy of the theory. Moreover, the nucleation barrier in solids at some low temperature (or high supersaturation) can typically be around a few  $k_B T$  where the thermal fluctuations with same energy are abundant, thus the system may never settle down to a metastable state before undergoing the phase transition [5]. A similar circumstance is expected near the metastability limit (i.e., the spinodal line) where a critical nucleus exhibits a spatially extended configuration of which the evolution depends on long-range diffusion. Thus system may adopt a different kinetic path via nuclei with some higher energy but less extended configuration [63]. In fact the profile of a critical nucleus predicted in the Cahn-Hilliard non-classical nucleation theory decays asymptotically to infinite, which in a strict sense would require infinitely long time to achieve. With these and other concerns, microscopic theories of nucleation based on statistical mechanics have been developed [32, 80, 68, 69].

While the nucleation theories are evolving to be more fundamental nevertheless more complex, simulations for real materials often looks for a relatively simple and flexible model. In fact the apparently crudest classical nucleation theory has worked unexpectedly well in many material systems [81] (see also reviews [73, 78]).

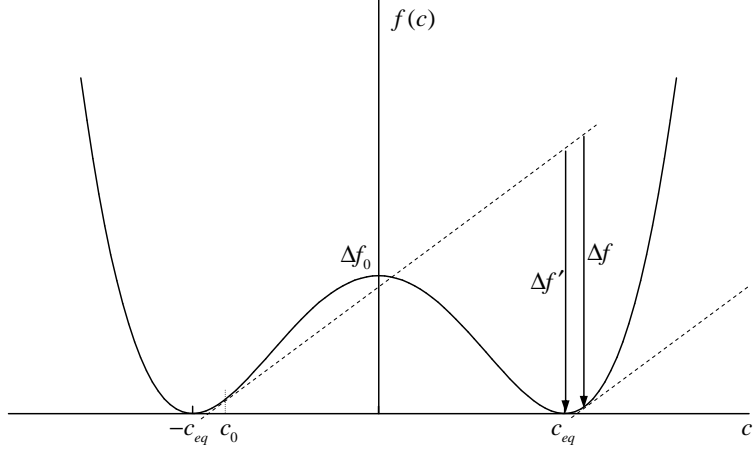


Figure 3.4: Double-well free energy given by Eq.(3.16). The nucleation driving force  $\Delta f$  at composition  $c_0$  is obtained by the parallel tangent construction. Shown also is the approximated driving force  $\Delta f'$  used in the simulation.

### 3.4 Simulation of nucleation, growth, and coarsening under isothermal condition

In this section we demonstrate the explicit nucleation algorithm in a simple two-dimensional (2D) phase field model. We consider a binary alloy with the chemical free energy,  $f$  in Eq.(2.1), described by a double-well function of composition  $c$

$$f(c) = \Delta f_0 c_{eq}^{-4} (c^2 - c_{eq}^2)^2 \quad (3.16)$$

As shown in Fig. 3.4,  $\Delta f_0$  is the height of the energy barrier, and  $\pm c_{eq}$  are the two local minima, corresponding to the equilibrium compositions <sup>9</sup>. By assuming the

<sup>9</sup>Here we use a generic form of free energy despite that real compositions are between 0 and 1.

mobility is independent of position, Eq.(2.3) is simplified to

$$\begin{aligned}\frac{\partial c}{\partial t} &= M\nabla^2 \left( \frac{\partial f}{\partial c} - \kappa_c \nabla^2 c \right) \\ &= M \frac{1}{l_0^2} \nabla^{*2} \left( \frac{\partial f^*}{\partial c} \Delta f_0 - \kappa_c \frac{1}{l_0^2} \nabla^{*2} c \right)\end{aligned}\quad (3.17)$$

Here the asterisk denotes dimensionless quantities defined by  $f^* \equiv f/\Delta f_0$  and  $\nabla^* \equiv l_0 \nabla$ , where  $l_0$  is the phase field grid size. With further substitution  $\kappa_c^* \equiv \kappa_c/(l_0^2 \Delta f_0)$  and  $t^* \equiv t M \Delta f_0 / l_0^2$ , the kinetic equation (Eq.(3.17)) is reduced to a dimensionless one

$$\frac{\partial c}{\partial t^*} = \nabla^{*2} \left( \frac{\partial f^*}{\partial c} - \kappa_c^* \nabla^{*2} c \right) \quad (3.18)$$

Nucleation is considered by the classical theory. The energy barrier in 2D, similar to Eq.(3.9), is  $\Delta F^c = \pi \sigma^2 / \Delta f$ . Substitution into Eq.(3.10) gives the nucleation rate

$$J = J_0 e^{-\pi \sigma^2 / k_B T \Delta f} \quad (3.19)$$

The driving force for nucleation  $\Delta f$  at a composition  $c_0$  is the vertical distance between the two parallel tangential lines on the free energy curve (Fig. 3.4). For simplicity we approximate it by measuring only to the local minimum of the precipitate phase as shown in the figure, which is found to be

$$\Delta f \cong \Delta f' = \Delta f_0 c_{eq}^{-4} (c + c_{eq}) (3c - c_{eq}) (c - c_{eq})^2 \quad (3.20)$$

The dimensionless nucleation rate can be written in the same way as before

$$J^* = J_0^* e^{-s^*/\Delta f^*} \quad (3.21)$$

with the substitution  $\Delta f^* \equiv \Delta f / \Delta f_0$  and  $s^* \equiv \pi \sigma^2 / (k_B T \Delta f_0)$ .

The simulation is performed in a  $1024 \times 1024$  mesh with initial composition  $c_0 = -0.77$ . Periodic boundary conditions are applied to the system. The dimensionless

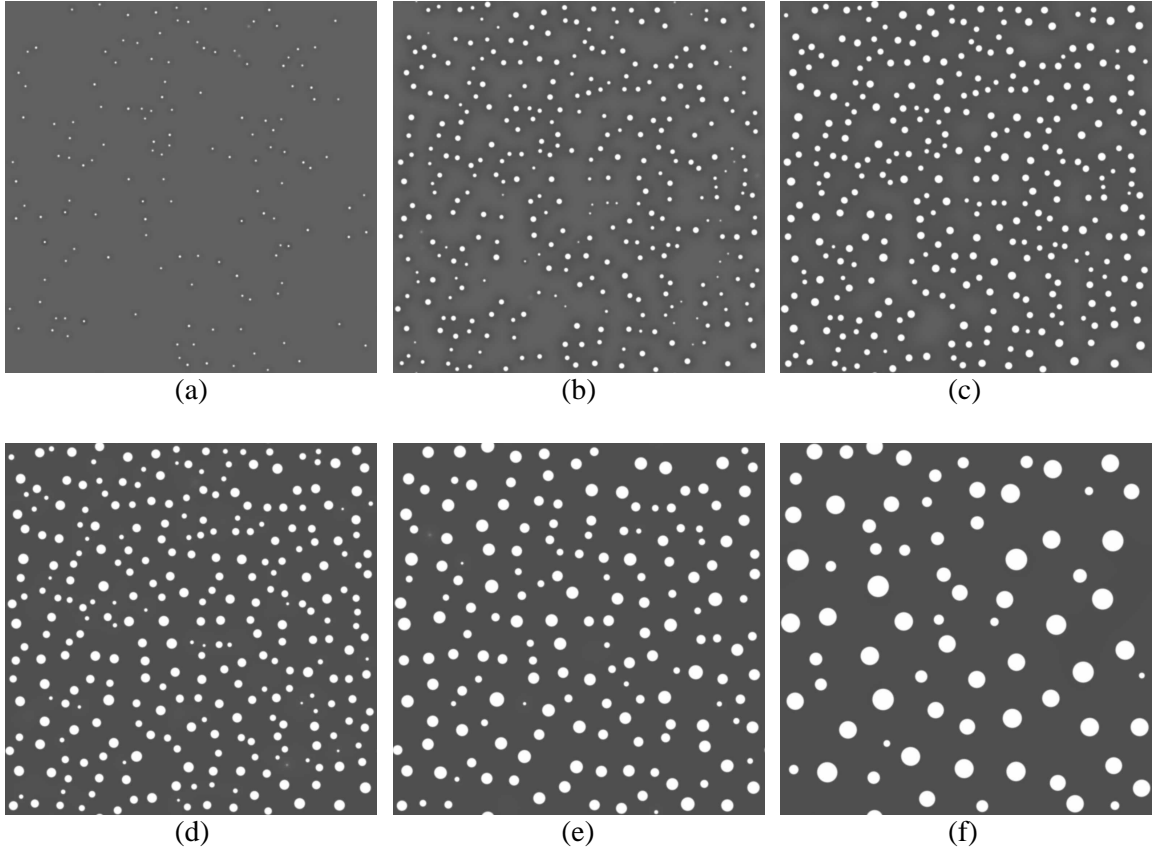


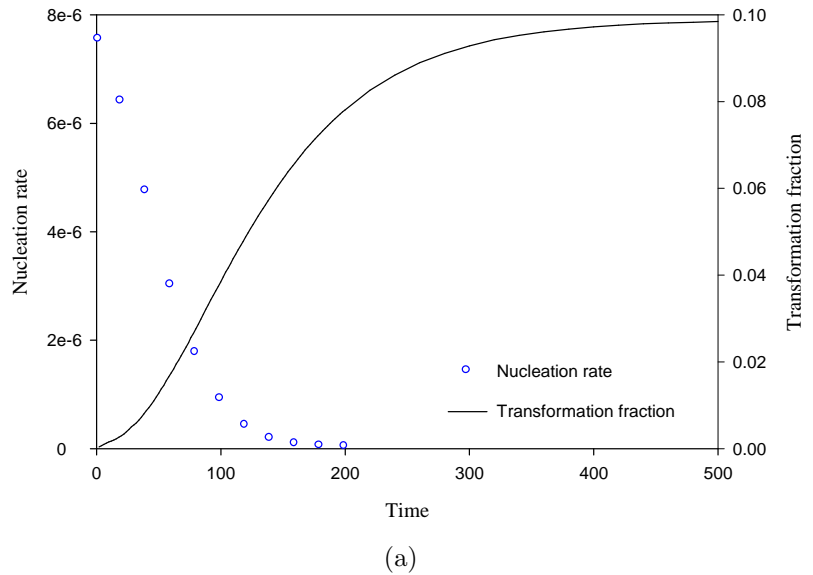
Figure 3.5: Simulated microstructures of concurrent nucleation, growth, and coarsening at reduced time (a)  $t^* = 20$ , (b)  $t^* = 100$ , (c)  $t^* = 200$ , (d)  $t^* = 1000$ , (e)  $t^* = 4000$ , (f)  $t^* = 20000$ .

parameters are chosen as  $c_{eq} = 1.0$ ,  $\kappa^* = 5.0$ ,  $J_0^* = 7403$ , and  $s^* = 47.70$ . The choice of  $s^*$  let the initial nucleation barrier around  $20k_B T$ . In each time step the nucleation routine is called and followed by phase field routines that describe growth and coarsening.

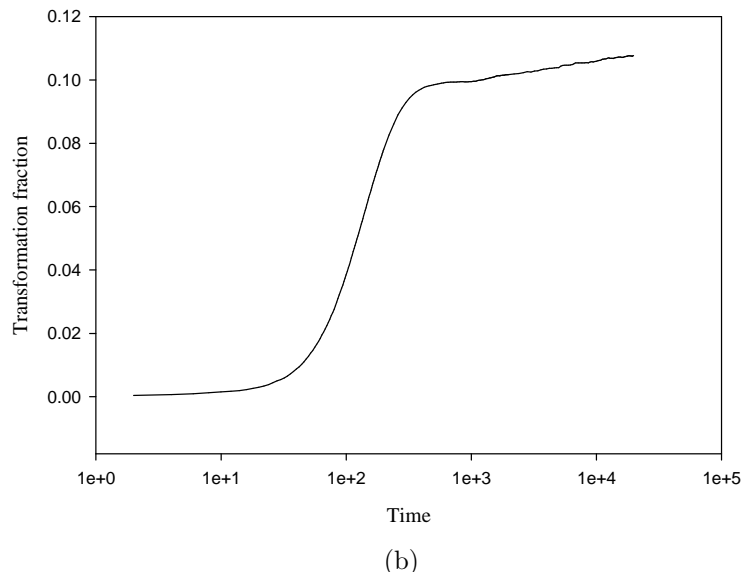
Figure 3.5 shows the simulated microstructures. At the early stages (Fig. 3.5(a)-(c)) nucleation and growth are seen to occur simultaneously. Solute depletion in the matrix during growth is revealed by the contrast in the gray scale. Local coarsening

is also seen in Fig. 3.5(c) where some small particles diminish. The reaction proceeds to the coarsening stage (Fig. 3.5(d)-(f)) where matrix composition approaches the equilibrium value and the number of particles starts to decrease with time.

The stages of nucleation, growth, and coarsening can also be identified from the plot of average nucleation rate and the transformed fraction in Fig. 3.6. The nucleation rate is lowered by an order of magnitude at  $t^* = 100$ . By the time  $t^* = 500$  the transformation fraction curve almost reaches saturation, indicating the beginning of a coarsening-dominant stage. A close look at the transformed fraction over a larger time range (Fig. 3.6(b)) indicates that the curve does not quickly converge to the equilibrium fraction 11.5%. This is evident, for example, by a continuous increase in a log-time scale at the stage of coarsening. By calculation the fraction is found consistent with the matrix composition, which decreases with time in accord with the particles' mean curvature (i.e., the Gibbs-Thomson effect). The mean radius of precipitates are found to follow a  $t^{1/2}$  law in the stage of growth and a  $t^{1/3}$  law in coarsening (Fig. 3.7(a)). During the nucleation stage it behaves similar to the growth stage but with slight variation. A transition region is found between the growth-dominant and coarsening-dominant stages, where the slope of the data in a log-log scale changes from  $1/2$  to below  $1/3$  and then back to  $1/3$ . This region is also seen to coincide with the plateau in the transformation fraction curve between  $t^* = 500$  and  $1000$  (Fig. 3.6(b)). The region corresponds to a necessary period of time in which the precipitate size distribution at the end of growth stage transforms to that for steady-state coarsening. In an extreme case where all precipitates are equal in size at the end of growth, the system reaches an unstable equilibrium state. A small perturbation to the size distribution initiates the coarsening but requires finite time to achieve a

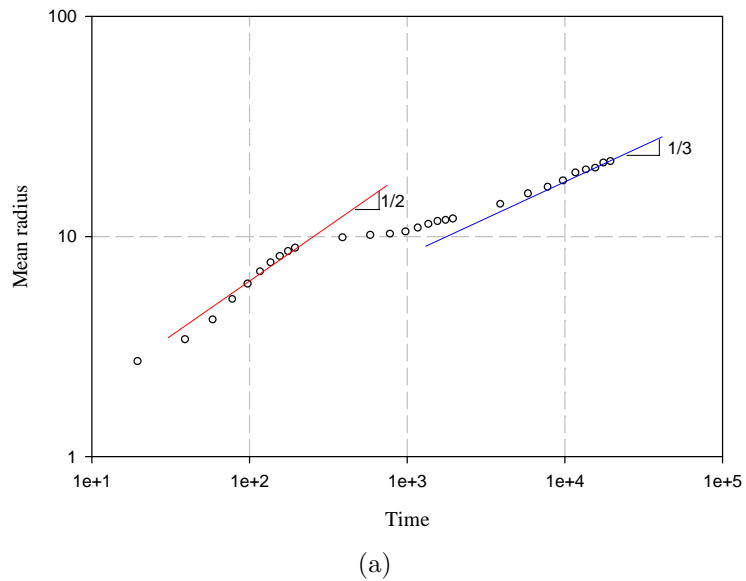


(a)

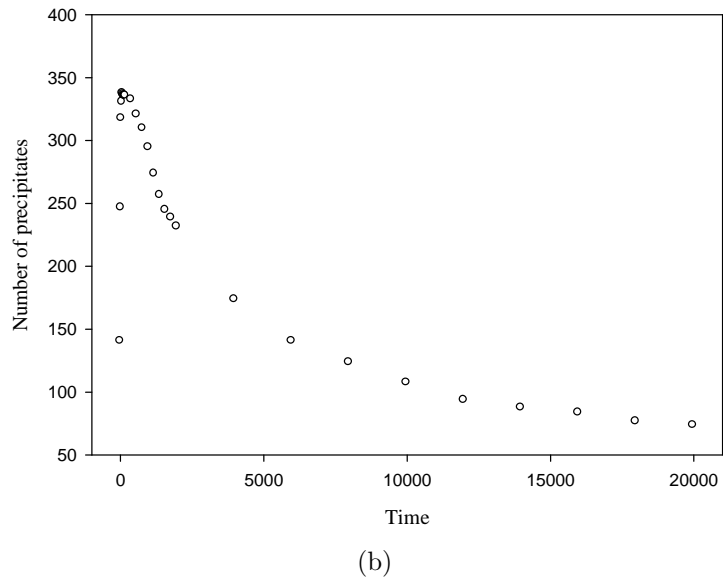


(b)

Figure 3.6: (a) Average nucleation rate and area fraction of the transformed phase.  
(b) The transformation fraction plotted in a larger time range.



(a)



(b)

Figure 3.7: (a) Mean radius of precipitates and (b) the number of precipitates.

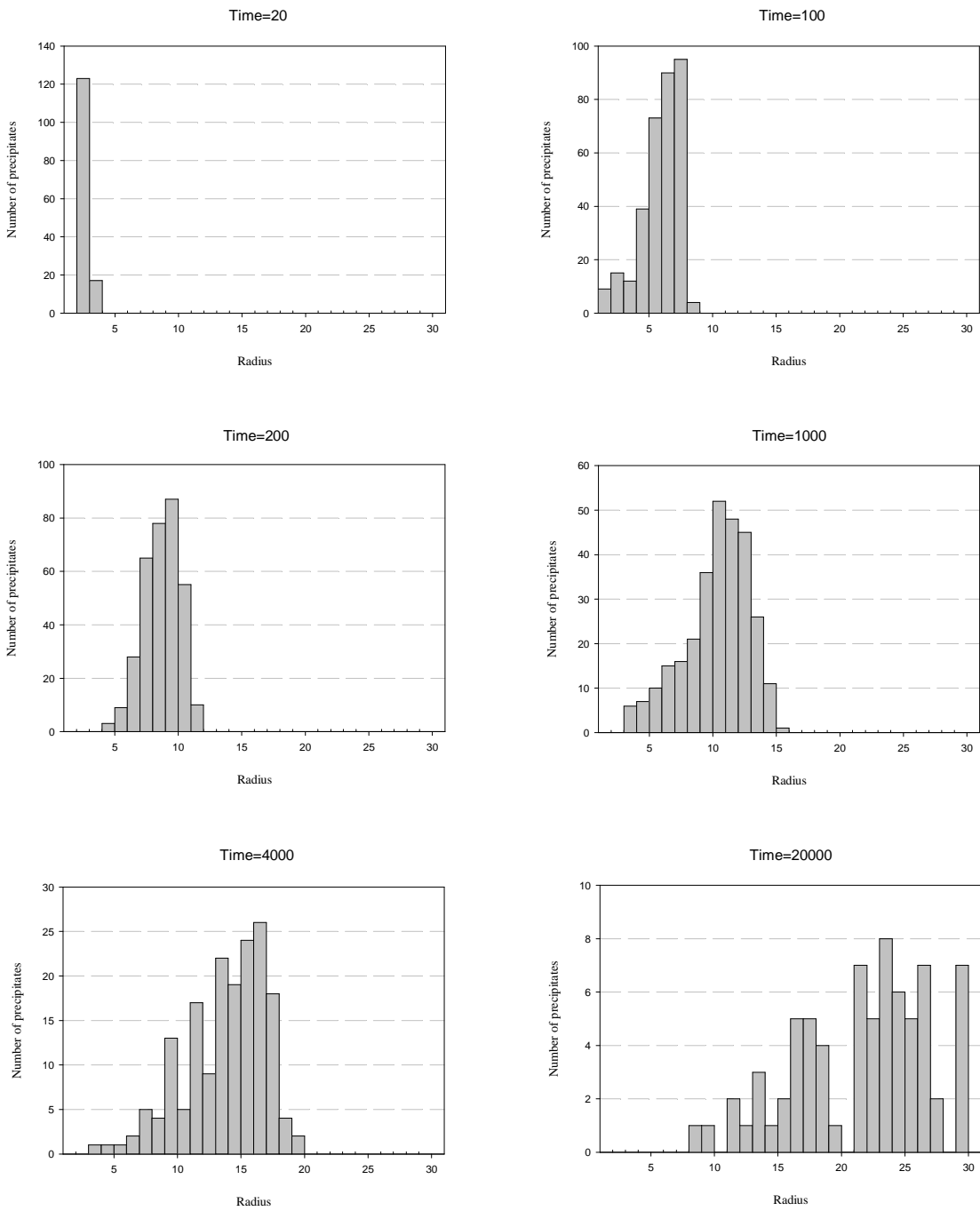


Figure 3.8: Size distribution of precipitates at stages of nucleation, growth, and coarsening.

new steady state. The number of precipitates increases during nucleation and then monotonically decreases during coarsening (Fig. 3.7(b)).

Finally, the precipitate size (radius) distributions are plotted in Fig. 3.8 at different time. In the stage of nucleation the precipitates are distributed in a very narrow size range, indicating a majority population of equal size. The size distribution is broadened during growth and coarsening. However, in the growth stage the envelope of the distribution remains almost constant but translates to the large size end (see  $t^* = 100$  and  $200$  for example). During coarsening the distribution is continuously broadened with the increase of the mean radius: it extends to both small and large size ends. All profiles exhibit an asymmetric shape.

### 3.5 Modeling coherent nucleation

Nucleation in crystalline solids is more complex than in liquids owing to crystallography. The difference in composition and/or crystal structure between precipitate and matrix generally causes lattice distortion in both. As the fluctuations associated with nucleation are typically small in dimension, their crystal lattices are often forced by the surrounding material to be close to that of the matrix. Such kinds of fluctuations are known as coherent fluctuations. Since the formation of a coherent interface typically costs less energy by order of magnitude than the formation of an incoherent interface, the former may significantly lower the energy barrier for nucleation. As a price, the stress to maintain the coherency (the coherency stress) causes a positive energy and partially cancels the chemical driving force for nucleation. Thus a phase transition prescribed by a conventional phase diagram, often measured with incoherent phases, may actually be suppressed due to the coherency strain energy [63], unless

the chemical driving force for the transition is sufficiently large (e.g. at a large undercooling). In other words, the phase boundary in the phase diagram will shift to the low temperature end for the coherent nucleation. Incoherent fluctuations usually cost too high interfacial energy and are less likely to exist. There are, however, examples of formation incoherent precipitates due to large lattice mismatch with the matrix phase. In these situations intermediate phases are often observed that reduce the initial barrier for nucleation. A typical example is the nucleation of  $\Theta$  precipitates in  $\alpha$ -Al-Cu solid solutions, where metastable coherent phases (GP I, GP II ( $\Theta''$ ) and  $\Theta'$ ) are observed at beginning and later develop to the stable incoherent  $\Theta$  phase [74].

Coherency elastic stress may considerably influence the process of nucleation by modifying the driving force [63, 82, 83]. In elastically isotropic and elastically homogeneous (i.e., equal elastic moduli) materials there is no interaction energy between dilatational coherent inclusions. This is evident if one rewrites Eq.(2.73) in an equivalent form [52]:

$$E^{el} = \frac{1}{2} \int \frac{d\mathbf{g}}{(2\pi)^3} B(\mathbf{n}) \tilde{\phi}(\mathbf{g}) \tilde{\phi}^*(\mathbf{g}) \quad (3.22)$$

where  $B(\mathbf{n}) \equiv C_{ijkl}^0 \epsilon_{ij}^{T0} \epsilon_{kl}^{T0} - n_i \sigma_{ij}^{T0} \Omega_{jk}^0(\mathbf{n}) \sigma_{kl}^{T0} n_j$ , and  $\sigma_{ij}^{T0} \equiv C_{ijkl}^0 \epsilon_{kl}^{T0}$ . For isotropic elastic modulus,  $B(\mathbf{n}) \rightarrow B$ , so it can be moved out from the integral. With Parseval's relation Eq.(3.22) becomes

$$E^{el} = \frac{B}{2} \int d\mathbf{x} [\phi(\mathbf{x}) - \bar{\phi}]^2 \quad (3.23)$$

where  $\bar{\phi} \equiv V^{-1} \int d\mathbf{x} \phi(\mathbf{x})$  is the mean value of  $\phi$ . Clearly the integral is invariant under any spatial rearrangement of the existing inclusions described by the phase field  $\phi$ . The coherency strain energy therefore is an additive quantity and only depends on the volume of each nucleus. Therefore, the strain energy in the classical nucleation

theory can be treated by simply adding to the chemical driving force (e.g.,  $\Delta f$  in Eq.(3.12)) [82].

The situation in the elastically anisotropic materials, however, is quite different and much more complex. The strain energy will depend on the shape of the nuclei as well as their mutual arrangement in the space. The elastic stress induced by an existing precipitate may promote nucleation in certain directions while suppresses it in the others, which results in preferential nucleation sites and contributes to the formation of microstructural patterns during further evolution. The increase of the nucleation rate due to a neighboring nucleus may induce formation of a second one, thus produces a phenomenon that nuclei are successively triggered one by one, known as the strain-induced autocatalytic nucleation [84]. To account for these important phenomena, the strain energy that describes the interaction between nuclei and existing microstructure due to elastic anisotropy must be appropriately included in the total free energy. Even with elastic homogeneity the interaction energy is not a simple function of the volume of the nucleus itself, but has a general dependence on the entire microstructure. This makes it a difficult task to treat the anisotropic coherency strain energy in the classical nucleation theory.

### 3.5.1 Coherency strain energy in nucleation driving force

The objective of this section is to derive a useful approximate solution that takes into account the interaction with microstructure while still preserves the form of a volume energy. To specify the problem in the context of phase field model, we may consider a system described by  $N$  independent phase fields  $\{\phi_p : p = 1, 2, \dots, N\}$ , among which the first  $M$  fields are transformed inside a nucleus:  $\{\phi_p \rightarrow \phi_p + \Delta\phi_p :$

$p = 1, 2, \dots, M\}$ . The coherency strain energy associated with formation of a nucleus is given by

$$\Delta E^{el} = E^{el}(\{\phi_p + \Delta\phi_p\}) - E^{el}(\{\phi_p\}) \quad (3.24)$$

Our goal is to obtain an appropriate form of  $\Delta E^{el}$ .

Substituting Eq.(3.22) into Eq.(3.24) yields

$$\Delta E^{el} = \Delta E_{int}^{el} + \Delta E_{self}^{el} \quad (3.25)$$

$$\Delta E_{int}^{el} = \text{Re} \left[ \sum_{p=1}^N \sum_{q=1}^M \int \frac{d\mathbf{g}}{(2\pi)^3} B_{pq}(\mathbf{n}) \tilde{\phi}_p(\mathbf{g}) \Delta \tilde{\phi}_q^*(\mathbf{g}) \right] \quad (3.26)$$

$$\Delta E_{self}^{el} = \frac{1}{2} \sum_{p=1}^M \sum_{q=1}^M \int \frac{d\mathbf{g}}{(2\pi)^3} B_{pq}(\mathbf{n}) \Delta \tilde{\phi}_p(\mathbf{g}) \Delta \tilde{\phi}_q^*(\mathbf{g}) \quad (3.27)$$

$\text{Re}[\dots]$  is the real part of the term inside. It is noted that  $\Delta\phi_p(\mathbf{x})$  represents a localized configuration of the nucleus and vanishes in the matrix. The coupling of the phase fields of the nucleus,  $\Delta\phi_p$ , and the microstructure,  $\phi_p$ , in the reciprocal space in Eq.(3.26) represents the interaction between the nucleus and the existing microstructure.  $\Delta E_{self}^{el}$  depends only on the nucleus itself, thus is regarded as a self energy. It can be shown that  $\Delta E_{self}^{el}$  is directly connected to the self energy  $E_{self}^{el}$  in Eq.(2.94). For a particular configuration that a point nucleus is embedded in a uniform matrix,  $\phi_p$  becomes constant and  $\Delta\phi_p$  reduces to a  $\delta$ -function.  $E^{el}(\{\phi_p\})$  in Eq.(3.24) and  $\Delta E_{int}^{el}$  thus vanish and

$$\Delta E^{el} = E^{el}(\{\phi_p + \Delta\phi_p\}) = \Delta E_{self}^{el}$$

Meanwhile,  $E_{int}^{el}(\{\phi_p + \Delta\phi_p\})$  vanishes in Eq.(2.95), leading to

$$E^{el}(\{\phi_p + \Delta\phi_p\}) = E_{self}^{el}(\{\phi_p + \Delta\phi_p\})$$

Therefore we find  $\Delta E_{self}^{el} = E_{self}^{el}$ . Practically, this result holds as long as the nucleus is much smaller than the size of the system, rather than at a strictly point nucleus. If the

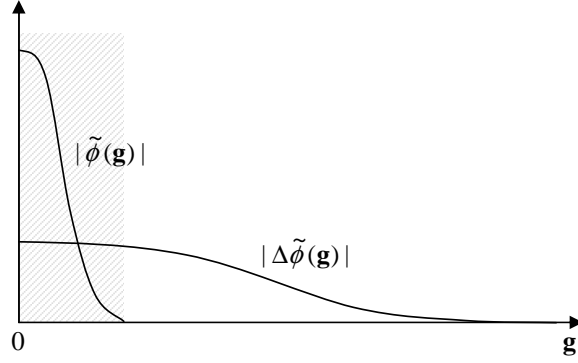


Figure 3.9: A mesoscale microstructure has a narrower spectrum than a critical nucleus in the reciprocal space.

chemical free energy of a given system is a coherent free energy, the self energy  $\Delta E_{self}^{el}$  is included in the “chemical” part of the nucleation driving force correspondingly, hence only the interaction energy,  $\Delta E_{int}^{el}$ , should present in the “mechanical” part of the nucleation driving force.

The integration in Eq.(3.26) over the reciprocal space is equivalent to counting the interaction of the nucleus with the microstructure over the entire range of length scales in the real space. Since microstructures responsible for material properties mostly exist at a mesoscopic scale while a critical nucleus is about a microscopic dimension, one can expect that the microstructure in the reciprocal space ( $\tilde{\phi}_p$ ) has a narrower spectrum than the nucleus ( $\Delta\tilde{\phi}_q$ ), with each bandwidth determined by the reciprocal of their respective characteristic dimensions (Fig. 3.9). Eq.(3.26) can be significantly simplified by taking the integration only up to the cut-off of the microstructure in the reciprocal space as indicated by the range in shadow in Fig. 3.9. For convenience we may use a local coordinate  $\mathbf{x}' \equiv \mathbf{x} - \mathbf{x}_s$  for a nucleus centered at position  $\mathbf{x} = \mathbf{x}_s$ ,

which yields

$$\Delta\tilde{\phi}_p(\mathbf{g}) = e^{-i\mathbf{g}\cdot\mathbf{x}_s} \int d\mathbf{x}' \Delta\phi_p(\mathbf{x}') e^{-i\mathbf{g}\cdot\mathbf{x}'}, \quad (p = 1, 2, \dots, M) \quad (3.28)$$

If  $\phi_p(\mathbf{x})$  is a smooth function, Eq.(3.28) can be expanded as a Taylor series near  $\mathbf{g} = 0$ :

$$\begin{aligned} \Delta\tilde{\phi}_p(\mathbf{g}) &= \Delta\tilde{\phi}_p(0) + \frac{d\Delta\tilde{\phi}_p(\mathbf{g})}{d\mathbf{g}} \Big|_{\mathbf{g}=0} \mathbf{g} + \frac{1}{2} \frac{d^2\Delta\tilde{\phi}_p(\mathbf{g})}{d\mathbf{g}^2} \Big|_{\mathbf{g}=0} \mathbf{g}^2 + \dots \\ &= e^{-i\mathbf{g}\cdot\mathbf{x}_s} \left[ \int d\mathbf{x}' \Delta\phi_p(\mathbf{x}') - i\mathbf{g} \cdot \int d\mathbf{x}' \mathbf{x}' \Delta\phi_p(\mathbf{x}') - \frac{\mathbf{g}^2}{2} \int d\mathbf{x}' \mathbf{x}'^2 \Delta\phi_p(\mathbf{x}') + \dots \right] \end{aligned} \quad (3.29)$$

If  $\Delta\phi_p(\mathbf{x}')$  possesses a central symmetry, all odd-order terms in Eq.(3.29) vanish. We now approximate the configuration of the nucleus as (1) spherical shape with radius  $r_0$ , and (2) the phase field  $\phi_p(\mathbf{x})$  inside nucleus equals to the constant  $\phi_{p,2}$ , where  $p = 1, 2, \dots, M$ , i.e.,

$$\Delta\phi_p(\mathbf{x}) \equiv \begin{cases} \phi_{p,2} - \phi_p(\mathbf{x}_s), & |\mathbf{x} - \mathbf{x}_s| \leq r_0 \\ 0, & |\mathbf{x} - \mathbf{x}_s| > r_0 \end{cases} \quad (3.30)$$

Substituting into Eq.(3.29) and retaining up to the second lowest non-vanishing term yield

$$\Delta\tilde{\phi}_p(\mathbf{g}) = e^{-i\mathbf{g}\cdot\mathbf{x}_s} [\phi_{p,2} - \phi_p(\mathbf{x}_s)] (1 - 3r_0^2 g^2 / 10) V \quad (3.31)$$

where  $V = 4\pi r_0^3/3$  is the volume of the nucleus. As discussed earlier, the upper limit of  $g$  is the cut-off of the microstructure in the reciprocal space, i.e.,  $g \leq 2\pi/L$ , where  $L$  is the characteristic length scale of the microstructure. The second term in the parenthesis in Eq.(3.31) becomes much smaller than unity if the nucleus is much smaller than the dimension of the microstructure, i.e.,  $r_0/L \ll 1$ . Accordingly Eq.(3.31) may keep only the first term, i.e.,

$$\Delta\tilde{\phi}_p(\mathbf{g}) \cong e^{-i\mathbf{g}\cdot\mathbf{x}_s} [\phi_{p,2} - \phi_p(\mathbf{x}_s)] V \quad (3.32)$$

Substituting into Eq.(3.26) gives the volume dependent interaction energy

$$\Delta E_{int}^{el} \cong V \sum_{p=1}^N \sum_{q=1}^M [\phi_{q,2} - \phi_q(\mathbf{x}_s)] \operatorname{Re} \left[ \int \frac{d\mathbf{g}}{(2\pi)^3} B_{pq}(\mathbf{n}) \tilde{\phi}_p(\mathbf{g}) e^{i\mathbf{g} \cdot \mathbf{x}_s} \right] \quad (3.33)$$

The self energy  $\Delta E_{self}^{el}$  is generally proportional to the volume  $V$ . Analytical expressions are available for some special geometries. For complex geometries it can be calculated numerically from Eq.(3.27).

For a spherical nucleus in a cubic crystal, if the stress-free transformation strain (SFTS) is a dilatational type,  $\epsilon_{ij}^T(\mathbf{x}) = \epsilon^{T0} \delta_{ij} [c(\mathbf{x}) - \bar{c}]$ , where  $c$  is composition, Eq.(3.33) becomes

$$\Delta E_{int}^{el} \cong V[c_2 - c(\mathbf{x}_s)] \operatorname{Re} \left[ \int \frac{d\mathbf{g}}{(2\pi)^3} B(\mathbf{n}) \tilde{c}(\mathbf{g}) e^{i\mathbf{g} \cdot \mathbf{x}_s} \right] \quad (3.34)$$

Here  $c_2$  denotes the equilibrium composition of the precipitate phase. The self energy equals the strain energy of an embedded coherent sphere, of which an analytical but approximate solution is given by [85]

$$\Delta E_{self}^{el} \cong V[c_2 - c(\mathbf{x}_s)]^2 (\epsilon^{T0})^2 \frac{\beta}{c_{11}} \left[ c_{11} - c_{12} - \frac{2\beta\Delta}{5(2c_{11} - \Delta)} - \frac{9\beta\Delta^2}{105(2c_{11} - \Delta)(3c_{11} - 2\Delta)} \right] \quad (3.35)$$

where  $\beta = c_{11} + 2c_{12}$ ,  $\Delta = c_{11} - c_{12} - 2c_{44}$ ,  $c_{11} = C_{iiii}^0$ ,  $c_{12} = C_{iiji}^0$ , and  $c_{44} = C_{ijij}^0$ .

The energy can also be calculated numerically by directly using Eq.(3.27).

Table 3.1 lists the calculated values of  $\Delta E_{self}^{el}$  and  $\Delta E_{int}^{el}$  near an embedded cubic coherent particle with the elastic constants  $c_{11}, c_{12}, c_{44}$  chosen as 231, 149, and 117GPa, respectively. The edge length of the particle is about 1/6 of that of the system, and near the particle the image stress due to the periodic boundary condition is negligible. Since  $\Delta E_{self}^{el}$  and  $\Delta E_{int}^{el}$  are not constant in the space, we only present their maximum or minimum values. The maximum (positive) values of  $\Delta E_{int}^{el}$  are located

near the corners of the particle, which in this case tend to suppress nucleation, and the minimum (negative) values are near the face-centers of the particle, which tend to promote nucleation.  $\Delta E_{self}^{el}$  is always positive. The typical driving force,  $\Delta f$  in Eq.(3.9) (for a spherical nucleus), that corresponds to a barrier of  $50k_B T$  for nucleation is also listed. The calculation shows when  $\epsilon^T \equiv \epsilon^{T0}(c_2 - c_1) = 1.6\%$ , where  $c_1$  is the equilibrium composition of the matrix phase, the elastic interaction (represented by  $\Delta E_{int}^{el}$ ) can have quite significant contribution to the nucleation driving force  $\Delta f$ , and thus the influence on the spatial positions of the nuclei.

Table 3.1: Elastic energies near a cubic precipitate calculated by Eqs.(3.34) and (3.35) and the volume driving force for nucleation calculated from  $16\pi\sigma^3/3\Delta f^2 = 50k_B T$ .

	$\epsilon^T = 0.5\%$	$1.6\%$	$5\%$
$\Delta E_{int}^{el}/V$ (J/m <sup>3</sup> )	$8.1 \times 10^5$ / $-1.0 \times 10^6$	$8.7 \times 10^6$ / $-1.1 \times 10^7$	$8.5 \times 10^7$ / $-1.1 \times 10^8$
$\Delta E_{self}^{el}/V$ (J/m <sup>3</sup> )	$5.9 \times 10^6$	$5.9 \times 10^7$	$5.9 \times 10^8$
$\Delta f$ (J/m <sup>3</sup> )	$4.7 \times 10^6$ (for $\sigma = 0.01$ J/m <sup>2</sup> ) or $5.3 \times 10^7$ (for $\sigma = 0.05$ J/m <sup>2</sup> )		

The approximate form of the interaction energy in Eq.(3.33) has the explicit dependence on the volume of the nucleus. The total coherency strain energy therefore can be combined directly with the chemical driving force for nucleation as a volume energy. The computation for the nucleation barrier will then follow the same procedures as for elastically isotropic materials in the classical nucleation theory.

### 3.5.2 Simulation of strain induced nucleation

Incorporation of the above formulations to the explicit nucleation algorithm presented in Section 3.2 allows for a study of the effect of coherency strain energy on microstructural evolution from the nucleation stage. Without loosing generality, we

consider a binary system for which the chemical free energy (per volume) is given by a regular solution model:

$$f^{ch}(c) = V_m^{-1} \{ c\mu_A^0 + (1-c)\mu_B^0 + RT[c \ln c + (1-c) \ln(1-c)] + \Omega c(1-c) \} \quad (3.36)$$

Here  $V_m$  is the molar volume,  $c$  is the composition (mole fraction) of the solute species ( $A$ ),  $R$  is gas constant,  $T$  is the absolute temperature, and  $\Omega$  is the interaction coefficient. The total free energy of the coherent system is given by Eq.(2.92), i.e., the sum of the total chemical free energy,  $\mathcal{F}^{ch}$ , and the coherency strain energy,  $E^{el}$ . The use of the regular solution model for the chemical free energy  $f^{ch}$  here does not make fundamental difference from the previous polynomial one (Eq.(3.16)) in Section 3.4. In this example it gives the convenience for using directly thermodynamic parameters. In addition, since we are considering a generic material system,  $f^{ch}$  can be considered as either an incoherent or a coherent free energy. In this example, we arbitrarily choose it as a coherent free energy. Correspondingly, since the configuration-independent part of the coherency strain energy is included in the coherent chemical free energy,  $E^{el}$  should contain only the configuration-dependent part, i.e, from Eq.(2.95):

$$E^{el} = E_{int}^{el} = \frac{1}{2} \int \frac{d\mathbf{g}}{(2\pi)^3} B'(\mathbf{n}) \tilde{c}(\mathbf{g}) \tilde{c}^*(\mathbf{g}) \quad (3.37)$$

where

$$B'(\mathbf{n}) = - \left[ n_i \sigma_{ij}^{T0} \Omega_{jk}^0(\mathbf{n}) \sigma_{kl}^{T0} n_l - \langle n_i \sigma_{ij}^{T0} \Omega_{jk}^0(\mathbf{n}) \sigma_{kl}^{T0} n_l \rangle_{\mathbf{g}} \right] \quad (3.38)$$

and  $\sigma_{ij}^{T0} \equiv C_{ijkl}^0 \epsilon_{ij}^{T0}$ . Here  $\epsilon_{ij}^{T0}$  is given by Eq.(2.75) for a linear dependence of the transformation strain on composition  $c$  apart from the average composition  $\bar{c}$ . In applying Eq.(2.95) we have substituted  $\phi_p$  with the composition field  $c(\mathbf{x}) - \bar{c}$ . The dynamic equation for our system with single composition field is reduced from Eq.(2.3)

$$\frac{\partial c}{\partial t} = M \nabla^2 \frac{\delta \mathcal{F}}{\delta c} = M \nabla^2 \left[ \frac{\partial f^{ch}}{\partial c} - \kappa_c \nabla^2 c + \{ B'(\mathbf{n}) \tilde{c}(\mathbf{g}) \}_{\mathbf{x}} \right] \quad (3.39)$$

$\{\dots\}_{\mathbf{x}}$  stands for an inverse Fourier transform of the term inside. Equations (3.36)-(3.39) give a complete description of our system except for nucleation.

The driving force for nucleation now includes the contributions from both the chemical free energy,  $\Delta f^{ch}$ , and the coherency strain energy,  $\Delta f^{el}$ :

$$\Delta f = \Delta f^{ch} + \Delta f^{el} \quad (3.40)$$

$\Delta f^{ch}$  is directly measured on the  $f^{ch}$ - $c$  free energy curve by the parallel line construction (e.g., Fig. 3.4) as we have applied in Section 3.4. To obtain  $\Delta f^{el}$  we need modify Eqs.(3.34) and (3.35) to their 2D counterparts

$$\Delta E_{int}^{el,2D} \cong A[c_2 - c(\mathbf{x}_s)] \operatorname{Re} \left[ \int \frac{d\mathbf{g}}{(2\pi)^3} B(\mathbf{n}) \tilde{c}(\mathbf{g}) e^{i\mathbf{g} \cdot \mathbf{x}_s} \right] \equiv A \Delta f_{int}^{el} \quad (3.41)$$

$$\Delta E_{self}^{el,2D} \cong A[c_2 - c(\mathbf{x}_s)]^2 (\epsilon^{T0})^2 \frac{\beta}{c_{11}} \left[ c_{11} - c_{12} - \frac{\beta \Delta}{4(2c_{11} - \Delta)} \right] \equiv A \Delta f_{self}^{el} \quad (3.42)$$

where  $A$  is the area of the nucleus. The dimension of  $\Delta E_{int}^{el,2D}$  and  $\Delta E_{self}^{el,2D}$  is energy per unit length. The form of  $\Delta E_{int}^{el,2D}$  remains unchanged except for the substitution of  $V$  by  $A$ . Instead, the change to 2D configuration is reflected in the composition field  $\tilde{c}(\mathbf{g})$ . The derivation of  $\Delta E_{self}^{el,2D}$  is given in Appendix A. Since our chemical free energy,  $f^{ch}$ , is chosen as a coherent one, as discussed earlier  $\Delta f^{el}$  should contain only the interaction energy:

$$\Delta f^{el} = \Delta f_{int}^{el} \quad (3.43)$$

Accordingly, the nucleation rate (Eq.(3.19)) is modified to

$$J = J_0 e^{-\pi\sigma^2 L/k_B T (\Delta f - \Delta f_{int}^{el})} \quad (3.44)$$

Different than the previous simulation for concurrent nucleation, growth, and coarsening (Section 3.4), we here use the driving forces and interfacial energy in real units,

Table 3.2: Dimensionless variables.

Length	Elastic constants	Energies	Time
$\mathbf{x}^* = \mathbf{x}/l_0$	$C_{ijkl}^{0*} = C_{ijkl}^0/\Delta f_0$	$f^{ch*} = f^{ch}/\Delta f_0$	$t^* = t(M\Delta f_0/l_0^2)$
$\mathbf{g}^* = \mathbf{g}l_0$	$B^* = B/\Delta f_0$	$\Delta f^{ch*} = \Delta f^{ch}/\Delta f_0$	
$\tilde{c}^*(\mathbf{g}^*) = \tilde{c}(\mathbf{g})/l_0^3$	$B'^* = B'/\Delta f_0$	$\Delta f^{el,i*} = \Delta f^{el,i}/\Delta f_0$	
$\nabla^* = l_0 \nabla$		$\kappa^* = \kappa/(\Delta f_0 l_0^2)$	

$J/m^3$  and  $J/m^2$ , respectively. Accordingly an artificial parameter of dimension of length,  $L$ , is added in Eq.(3.44) to maintain a correct dimension of the equation. In a qualitative simulation this alternation should not bring fundamental difference to the results.

In the simulation all parameters are used in dimensionless forms (Table 3.2).  $\Delta f_0$  and  $l_0$  are the scaling factors for energies and length, respectively. Accordingly, Eq.(3.39) is modified to a dimensionless form

$$\frac{\partial c}{\partial t^*} = \nabla^{*2} \left[ \frac{\partial f^{ch*}}{\partial c} - \kappa_c^* \nabla^{*2} c + \{B'^*(\mathbf{n})\tilde{c}^*(\mathbf{g}^*)\}_{\mathbf{x}^*} \right] \quad (3.45)$$

and Eq.(3.44) becomes

$$J^* = J_0^* e^{-s^*/(\Delta f^* - \Delta f_{int}^{el*})} \quad (3.46)$$

where  $s^* \equiv \pi\sigma^2 L/\Delta f_0 k_B T$ .

The material parameters employed in the simulation are  $\mu_A^0 = \mu_B^0 = 0$ ,  $\Omega = 2 \times 10^4 \text{J/mol}$ ,  $V_m = 10^{-5} \text{m}^3/\text{mol}$ ,  $\sigma = 0.05 \text{J/m}^2$ ,  $c_{11} = 231 \text{GPa}$ ,  $c_{12} = 149 \text{GPa}$ ,  $c_{44} = 117 \text{GPa}$ . The chemical free energies at 1000K and 1085K are plotted in Fig. 3.10. The chemical driving force for nucleation,  $\Delta f^{ch}$ , is calculated numerically for 1000K with the parallel tangent construction on the free energy curve. For convenience, the data is fitted by a quadratic function (Fig. 3.11),  $\Delta f^{ch} = a(c - 0.1696) + b(c - 0.1696)^2$ , with the coefficients  $a = 1.156 \times 10^9 \text{J/m}^3$  and  $b = -5.650 \times 10^9 \text{J/m}^3$ . The gradient

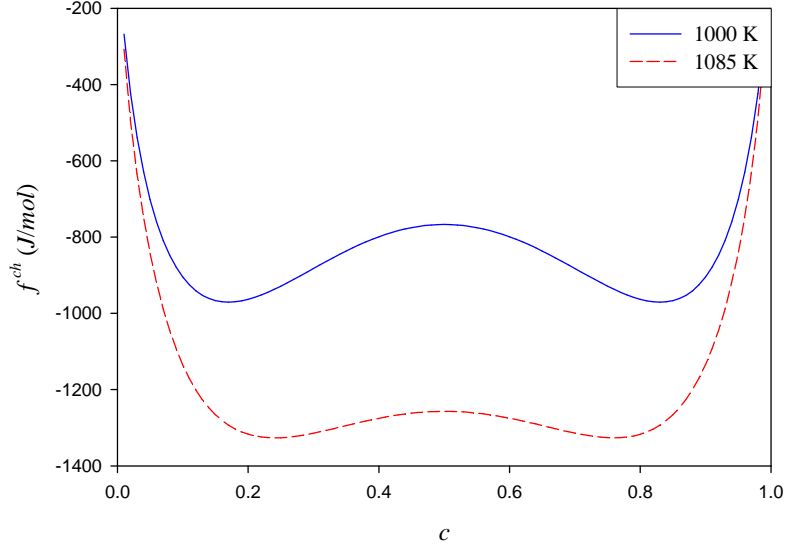


Figure 3.10: The chemical free energies (regular solution model, Eq.(3.36)) at  $1000K$  and  $1085K$ .

coefficient is chosen as  $\kappa_c = 3.03 \times 10^{-10} \text{ J/m}$  by fitting to the interfacial energy. The parameters for nucleation are  $J_0^* = 2.5 \times 10^6$  and  $s^* = 132.5$ . The latter produces approximately a nucleation barrier of  $50k_B T$  at composition 0.24. The scaling factors are chosen as  $\Delta f_0 = 2 \times 10^7 \text{ J/m}^3$  and  $l_0 = 5.5 \text{ \AA}$ . The system is discretized to a uniform  $1024 \times 1024$  mesh.

With the chosen grid size, the system considered is about  $560\text{nm} \times 560\text{nm}$ , which is rather small for the study of the effect of existing mesoscale microstructure on nucleation. To increase the system size without further increasing the number of mesh points, we employ the method proposed in [19] (see Chapter 6) to scale up phase field simulation length scale, i.e., by chosen  $\kappa_c^{simul} = 100\kappa_c$ , which yields a grid size of  $5.5\text{nm}$ . According to [19], such a treatment does not alter the driving

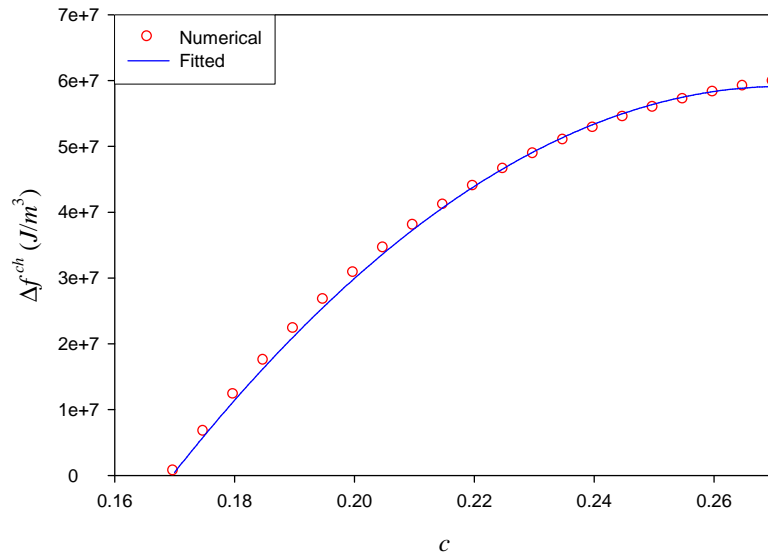


Figure 3.11: The chemical driving force for nucleation at 1000K.

force for growth, but will overestimate the Gibbs-Thomson effect during precipitate growth and coarsening. Since the main focus of the current study is on the effect of elastic interactions between a nucleating particle and an existing microstructure on rate and location of nucleation, and the nucleation process is treated in a separate subroutine by the explicit algorithm, such a scaling should not affect the calculation of the nucleation rates. After the scaling, the system size is about  $5.6\mu\text{m} \times 5.6\mu\text{m}$  and precipitates introduced by the explicit nucleation algorithm is  $\sim 60\text{nm}$  ( $\sim 10$  grids) in diameter, which is much larger than the size of a critical nucleus (smaller than a single cell in the phase field mesh). As will be shown later, the error in  $E_{int}^{el}$  due to the truncation of the expansion series of  $\Delta\phi$  in Eq.(3.32) is less than 1%.

To simulate the effect on nucleation by the coherency strain of a pre-existing particle, we set up an initial microstructure with a coherent particle of reduced size  $100 \times 100$  at the center. The particle and the matrix are relaxed to near equilibrium at 1085K, where the equilibrium compositions are approximately 0.24 and 0.76, respectively. We then quench the system to 1000K where the equilibrium compositions are 0.17 and 0.83. This produces a small supersaturation in the matrix and the driving force for nucleation. In Fig. 3.12 we compare the microstructures formed by nucleating coherent precipitates at two different transformation strains:  $\epsilon^T = 0.5\%$  and  $1.6\%$ . Precipitates formed at the small transformation strain (Fig. 3.12(a)-(c)) are almost randomly distributed. At the larger transformation strain (Fig. 3.12(d)-(f)), precipitates are formed preferably along the elastically soft directions (the horizontal and vertical directions of the figures). Nucleation not only exhibits strong spatial correlation due to the anisotropic elastic interaction, but is significantly promoted in the elastically soft directions because of the high sensitivity of the nucleation rate on the driving force. The effect of the coherent strain can be more clearly seen in the profiles of the chemical driving force,  $\Delta f^{ch}$ , and the coherency energy,  $\Delta f^{el}$ , along the soft directions (Fig. 3.13). Since the coherency energy is proportional to the square of the transformation strain, it is approximately 10 times smaller with  $\epsilon^T = 0.5\%$  than  $\epsilon^T = 1.6\%$ . Due to the stronger elastic interaction, at  $\epsilon^T = 1.6\%$  there is considerable solute segregation and thus the increase in  $\Delta f^{ch}$  near the pre-existing particle, where it promotes nucleation as the coherency energy (Fig. 3.13b).  $\Delta f^{ch}$  at  $\epsilon^T = 0.5\%$  is almost uniform (Fig. 3.13b).

To study the spatial correlation between the nucleating precipitates due to their mutual anisotropic elastic interactions, we simulate concurrent nucleation and growth

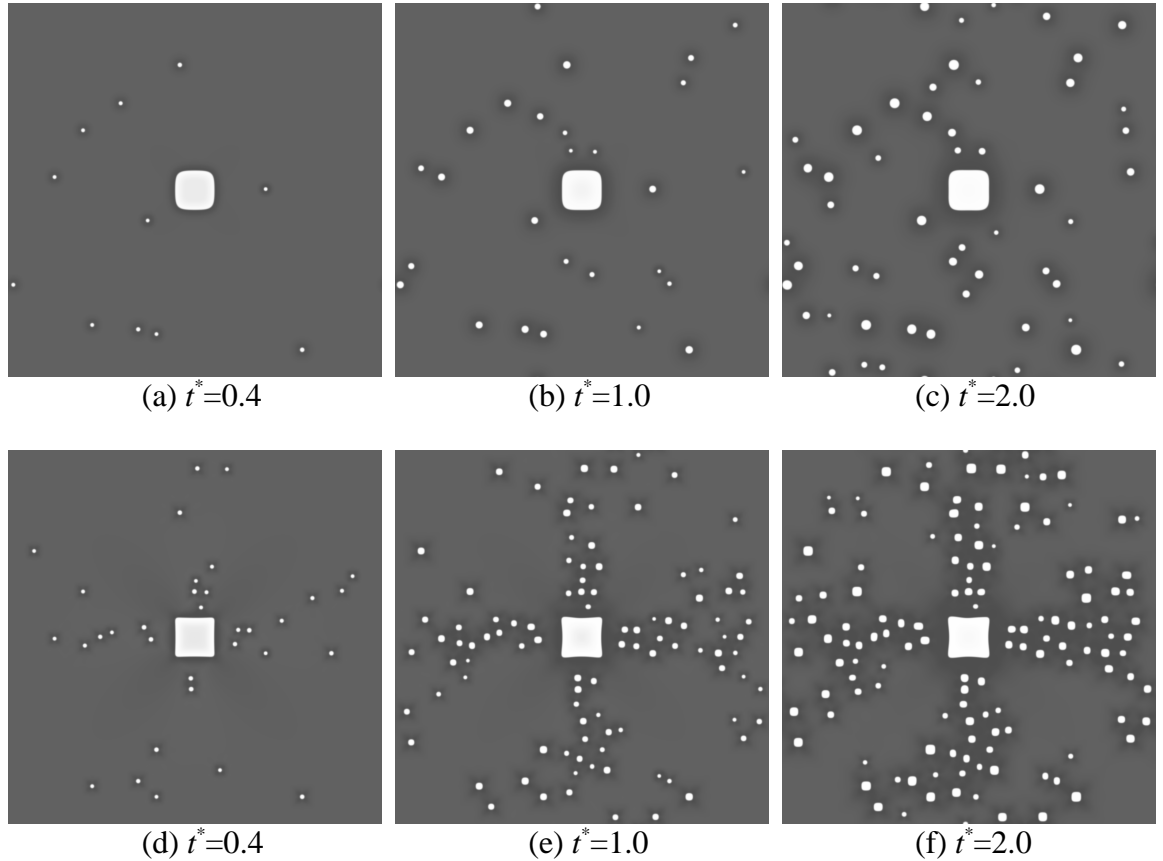
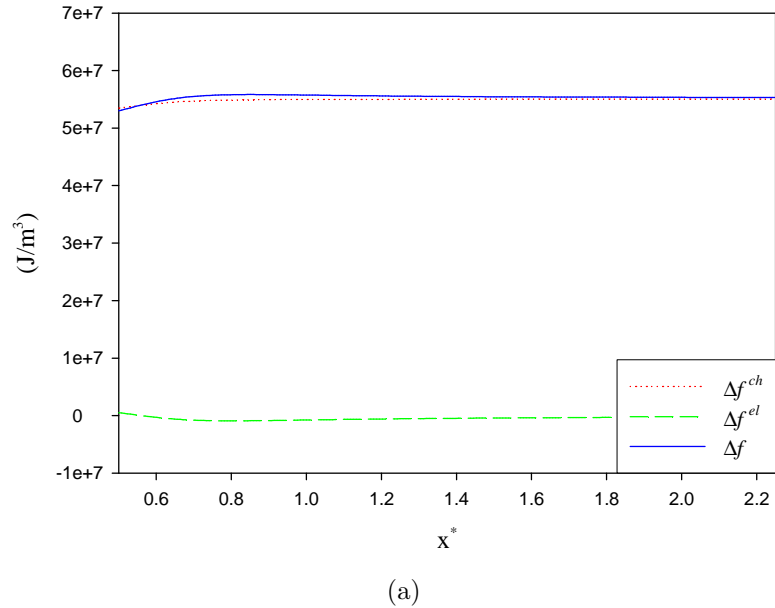
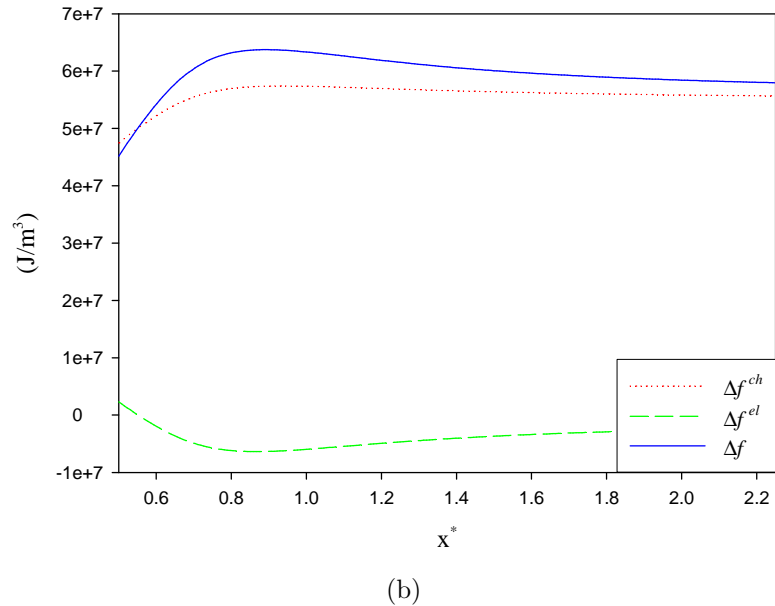


Figure 3.12: Simulated coherent nucleation near a pre-existing particle formed and equilibrated at a higher temperature in an elastically anisotropic medium. (a)-(c)  $\epsilon^T = 0.5\%$ , (d)-(f)  $\epsilon^T = 1.6\%$ .



(a)



(b)

Figure 3.13: Nucleation driving forces along the elastically soft direction at (a)  $\epsilon^T = 0.5\%$  and (b)  $\epsilon^T = 1.6\%$ . The profiles are taken from the precipitate:matrix interface (left end of the x-axis). The distance  $x^*$  is normalized by the edge length of the particle.

from a uniform matrix at 1000K. The initial matrix composition is  $c = 0.24$ . Figures 3.14(a)-(c) show the simulated microstructures at  $\epsilon^T = 1.6\%$ . Different than the microstructures displayed in the preceding example with the same  $\epsilon^T$  (Fig. 3.12(d)-(f)), without the influence from the large coherent particle the nuclei are formed nearly randomly in the matrix. Increase the transformation strain to 3.2%, however, the microstructures (Fig. 3.14(d)-(f)) exhibit much stronger mutual correlation between the nuclei. Not only new particles are formed directly near the previously formed particles in the soft directions, but many of them are triggered one by one along the same direction with time. Such consecutive formation of nuclei is clearly caused by the strong elastic interaction. As expected, due to the stronger elastic interaction the number densities of nuclei at each moment are also higher in the case with the larger  $\epsilon^T$ . In addition, some nuclei coalesce during subsequent growth and form a microstructure consisting of stripes oriented in the soft directions (Fig. 3.14(f)).

The truncation in the reciprocal space in Eq.(3.32) enables us to express the coherency strain energy as a linear function of the nucleus' volume. This brings immediately the benefit of combining the coherency strain energy with the chemical driving force,  $\Delta f^{ch}$ , for nucleation, so that the activation energy of nucleation in the classical nucleation theory includes the long-range and highly anisotropic elastic interactions. This truncation to the zero<sup>th</sup> order term in the expansion is in fact equivalent to an approximation that the stress field generated by the existing microstructure is uniform within the nucleus. As the characteristic dimension of microstructure decreases to a level comparable to that of nuclei, its stress field can no longer be considered uniform inside the nucleus and deviation must arise. Figure 3.15 plots the calculated relative error in  $\Delta E_{int}^{el}$  for a typical configuration of a nucleus near a particle (shown

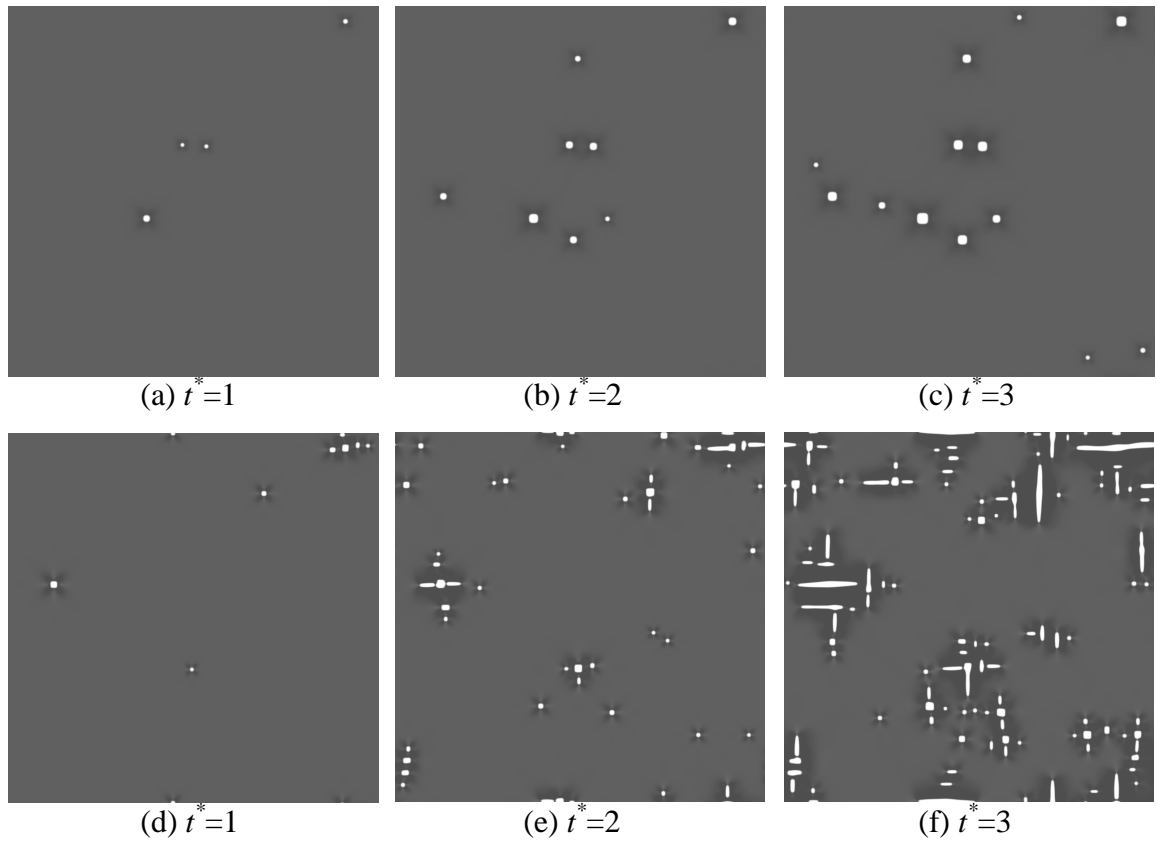


Figure 3.14: Simulated microstructures during a concurrent nucleation and growth process in a uniform matrix with  $\epsilon^T = 1.6\%$  ((a)-(c)) and  $\epsilon^T = 3.2\%$  ((d)-(f)).  $t^*$  is reduced time.

by the inset), as a function of the ratio of their radii,  $r_0$  and  $R_0$ , respectively. The relative error is seen to reduce rapidly to 1% as the radius of the big particle is 7 times larger than that of the nucleus. Different values of  $r_0$  as well as the system size  $L_0$  are used so as to ensure no numerical artifacts would arise from them.

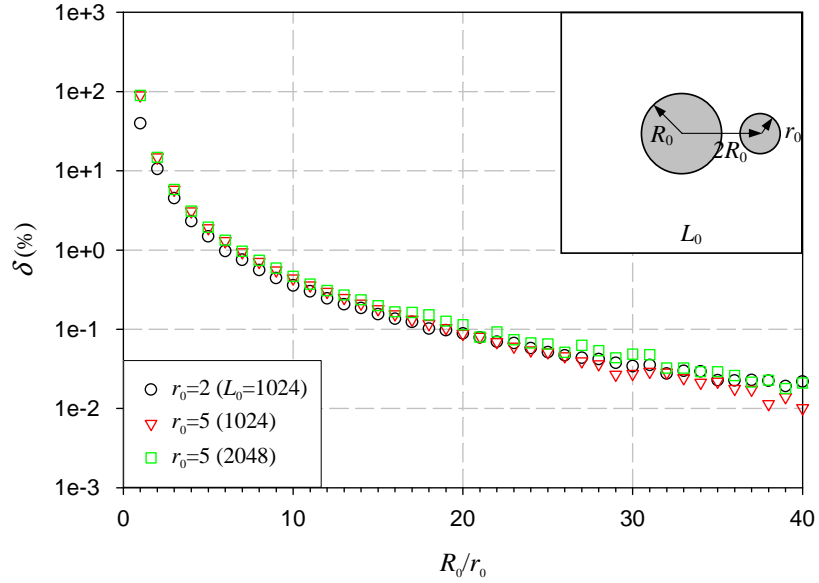


Figure 3.15: The relative error  $\delta = |\Delta E_{int}^{el} - \Delta E_{int,approx}^{el}|/\Delta E_{int}^{el}$  vs. ratio of the radii of the particle ( $R_0$ ) and the nucleus ( $r_0$ ), where  $\Delta E_{int}^{el}$  is calculated numerically from Eq.(3.26) and  $\Delta E_{int,approx}^{el}$  is from the approximate solution Eq.(3.42). The particular configuration for the calculation is shown by the inset.

During the derivation of the coherency strain energy we have assumed a spherical (circular in 2D) shape for nuclei. This assumption nevertheless does not enter the final form of  $\Delta E_{int}^{el}$  (Eq.(3.34)) because the interaction of a nucleus with a nearly uniform stress field of microstructure is independent of its shape. However, the self energy  $\Delta E_{self}^{el}$  in general depends on the shape. Since  $\Delta E_{self}^{el}$  is always proportional to the volume of a nucleus, for general cases with arbitrary shapes the per-volume

factor can be computed numerically using Eq.(3.27). In general the shape of a nucleus could be a function of the local stress state where it is seeded. In this case, the self energy needs to be expressed as a function of both the volume and the shape, with the latter being determined by minimizing the total free energy of the system.

### 3.6 Comparison to JMAK theory with soft impingement

The theory of the overall kinetics of phase transformations involving concurrent nucleation and growth is due to Kolmogorov [86], Johnson-Mehl [87], and Avrami [88, 89, 90], known as the JMAK theory. Based on the assumptions of (1) random formation of point nuclei in an infinite matrix, (2) isotropic growth of nuclei at a constant rate ( $dR/dt$ ,  $R$  being the radius), and (3) stop of growth at any point the nucleus impinges other nuclei (hard impingement), the theory relates the volume fraction of the transformed region,  $X$ , to an extended volume fraction,  $X_{ex}$ , in which each nucleus is hypothetically formed and grow in an untransformed matrix. Despite the sophisticated mathematical derivation involving the use of statistics and functional expansion in terms of multiple overlapping regions [88], the final expression is surprisingly simple:

$$X(t) = 1 - \exp(-X_{ex}(t)) \quad (3.47)$$

where  $t$  is time. The extended volume fraction is contributed by both nucleation and growth without impingement. Mathematically it is a convolution of the nucleation rate,  $J$ , and the volume of a nuclei,  $V$ , formed at time  $\tau$

$$X_{ex}(t) = \int_0^t J(\tau)V(t-\tau)d\tau \quad (3.48)$$

According to the assumption (2),  $V(t-\tau)$  is simply  $G(t-\tau)^d$ , where  $G$  is a constant and  $d$  is the dimensionality.

An important utility of the JMAK theory is to analyze the mechanisms of nucleation and growth from a measured transformation fraction curve. To do this, Eq.(3.48) can be rewritten in a form of power law of time

$$X_{ex}(t) = kt^n \quad (3.49)$$

The time exponent,  $n$ , known as the Avrami exponent, is the slope of a plot  $\ln(-\ln(1-X))$  versus  $\ln t$  since the combination of Eqs.(3.47) and (3.49) gives

$$\ln(-\ln(1-X(t))) = \ln k + n \ln t \quad (3.50)$$

The Avrami exponent has constant values for several special kinetic modes. For example, if all nuclei are formed at  $t = 0$  (i.e., the site-saturation limit), the nucleation rate is  $J(\tau) = I_0\delta(\tau)$  where  $I_0$  is the number of nuclei divided by the volume of the system and  $\delta$  is the Dirac delta function. Substitution into Eq.(3.48) gives

$$X_{ex}(t) = I_0V(t) = I_0Gt^d \quad (3.51)$$

and therefore  $n = d$ . Another example is that if the nucleation rate does not vary with time, i.e.,  $J(t) = J_0$ , Eq.(3.48) yields

$$X_{ex}(t) = J_0 \int_0^t V(\tau)d\tau = J_0 \left( \frac{G}{d+1} \right) t^{d+1} \quad (3.52)$$

and  $n = d + 1$ . In a general case where the nucleation rate depends on time, the Avrami exponent is not necessarily a constant. Table 3.3 summarizes the values of Avrami exponent for some typical kinetic modes. Note that dimensionality  $d = 2$  and  $d = 1$  may be considered equivalent to the thickening of very large plates and very long cylinders in experimental conditions, respectively.

Table 3.3: Values of Avrami exponent (from ref. [1]).  $d$  is the spatial dimensionality.

(a) Homogeneous nucleation.

Description	Avrami exponent $n$			Site saturation
	Increasing $J$	Constant $J$	Decreasing $J$	
Constant growth rate	$n > d + 1$	$d + 1$	$d + 1 > n > d$	$d$
Parabolic growth rate	$n > d/2 + 1$	$d/2 + 1$	$d/2 + 1 > n > d/2$	$d/2$

(b) Heterogeneous nucleation.

Description	Avrami exponent $n$
Grain edge nucleation after saturation	2
Grain boundary nucleation after saturation	1
Precipitation on dislocations (very early stages)	$\sim 2/3$

The extension of the JMAK theory to diffusion-controlled precipitation often takes the assumption that the relation between the transformation fraction and the extended fraction (Eq.3.47) still holds if the constant growth rate is simply replaced by the parabolic growth law. Meanwhile, since the final volume of the precipitates is only a fraction of the total volume, Eq.(3.47) is modified to

$$X(t)/X^{eq} = 1 - \exp(-X_{ex}(t)/X^{eq}) \quad (3.53)$$

where  $X^{eq}$  is the equilibrium volume fraction of the precipitates. The resultant values of Avrami exponent are listed in Table 3.3.

Doubts on this extension are mostly cast on the statistical validity associated with the impingement mode. The growth of precipitates depletes the matrix through long-range diffusion. The expansion of diffusion fields from each precipitate overlap and reduce their further growth rate. Rather than an immediate halt of growth upon impingement the growth of a precipitate is gradually slowed down until the matrix is completely depleted (reaching the equilibrium composition) and thus is called soft impingement. Consequently the impingements are no longer localized events but

are correlated among all nearby precipitates. Clearly these characteristics are very different from those considered in the original JMAK theory.

Since validation of JMAK theory in experiment is often interfered by complicating factors such as transient and/or heterogeneous nucleation, non-spherical growth, and multiple phase formation, etc [91], the task is often considered along a theoretical path. The first theoretic treatment for soft impingement was due to Wert and Zener [92]. Given a low supersaturation, the concentration fields near particles were approximated by the steady-state solution of an isolated particle of same dimension and with the far-field concentration scaled by the average concentration in the matrix. The exact solution to the diffusion problem was derived by Ham for a periodic array of isotropically growing precipitates [93]. The derivation employed eigenfunction expansion at a limit of low supersaturation (small volume fraction). At small  $t$  the untransformed fraction was derived to a form of  $\exp(-kt^n)$  and  $n$  had the values of  $\frac{3}{2}$  for spheroids and 1 for cylinders, which coincided the Avrami exponent for the corresponding precipitate geometries at site-saturation limit (Table 3.3). Ham also found that the results remained unchanged for dissimilar and irregularly arranged particles at small supersaturation, where the particles were well separated and could be treated individually.

Various numerical models have emerged recently for the study of soft impingement. Crespo and Pradell *et al.* [94, 95] explicitly calculated the extended volume fraction in Eq.(3.48). Instead of using the parabolic growth law for the diffusion-controlled growth, they used the steady-state solution of diffusion equation with the far-field composition approximated by the instantaneous average matrix composition. The growth was assumed isotropic. In addition, interface-controlled growth

was implemented for the initial stage of growth, and was then explicitly switched to the diffusion-controlled mode when a nucleus reached a pre-determined radius. The model tested both hard and soft impingement, as well as various nucleation rate. The calculated transformation fraction with soft impingement was best fit to the experiment data. The Avrami exponent was found to decrease with time owing to soft impingement rather than the decreasing nucleation rate. Along a different line, Yu *et al.* [96] derived the time dependent transformation fraction by evaluating the survival probability of individual sites<sup>10</sup>. Parabolic growth law was employed in the expression of the transformation fraction, from which the time exponent was found in agreement with the JMAK predictions except for final stages. The approach, however, was only applicable to one dimension (1D) and site saturation.

Both the theoretical and numerical approaches summarized above assume low supersaturation and small volume fraction of precipitates, at which the precipitates are separated far from one another with the mutual distance much greater than the radius of each. This is equivalent to embedding particles in a matrix with uniform composition except in the vicinity of a particle the composition is replaced by the local steady-state diffusion field. The assumption makes solving the growth equation significantly simpler, however, is not anticipated in many realistic situations. The difficulty is that description of a general composition distribution dramatically increases the number of degrees of freedom and the complexity of the treatment. Moreover, whereas the nucleation rate may be well approximated by constant in the classical JMAK models, it often varies considerably from place to place in diffusion-controlled growth due to the non-uniform composition. Being lack of a complete description of

<sup>10</sup>The approach is resemble to the one employed in the dynamic theory of expanding inhibitory fields by Armstrong *et al.* [97]

composition distribution also restricts the evaluation of nucleation rate. A typical approximation is to assign a constant value to nucleation rate in a narrow region surround each particle and another constant value to the remaining portion of the matrix [98, 99].

The field description by the phase field approach gives certain advantages. Composition is characterized by the position dependent phase fields and is solved in a generalized diffusion equation. The matrix composition is not restricted to mean-field type approximations, nor the growth has to be isotropic. With incorporation of the explicit nucleation algorithm introduced in Section 3.2, nucleation can be evaluated upon instantaneous local conditions in a self-consistent manner and can be applied directly to non-isothermal conditions. These characters can considerably relief the restrictions in the previous approaches. In this section, we apply the phase field method to the soft impingement problems and compare results with JMAK theory.

We will continue to use simple double-well chemical free energy Eq.(3.16) and dynamic equation Eq.(3.18). The latter is essentially a diffusion equation. In the beginning, however, we shall analyze in some detail how it is related to the standard form of diffusion equation

$$\frac{\partial c}{\partial t} = -\nabla \cdot \mathbf{J} \quad (3.54)$$

where the flux is  $\mathbf{J} = -D\nabla c$  and  $c$  is concentration. Compared with the flux from phase field method

$$\mathbf{J} = -M\nabla \frac{\delta \mathcal{F}}{\delta c} \cong -M\nabla \frac{df}{dc} = -M \frac{d^2 f}{dc^2} \nabla c \quad (3.55)$$

the phase field kinetic coefficient  $M$  is found to relate to the diffusivity by [63]

$$D = M \frac{d^2 f}{dc^2} \quad (3.56)$$

In Eq.(3.55) we have neglected the contribution from concentration gradient. Thus the relation in Eq.(3.56) is strictly valid at zero concentration gradient limit.

### 3.6.1 Growth of single precipitate

To compare the growth kinetics we shall solve the phase field equations and the diffusion equation individually. We restrict the comparison to isotropic growth of a single precipitate in a 2D matrix. The diffusion equation (Eq.(3.54)) correspondingly reduces to

$$\frac{\partial c}{\partial t} = \frac{1}{r} \frac{d}{dr} \left( D r \frac{dc}{dr} \right) \quad (3.57)$$

Eq.(3.57) is usually solved as a moving boundary problem: precipitate and matrix regions are solved separately and concentrations on the interface are specified as boundary conditions. The velocity of the moving interface is given according to mass conservation

$$v \equiv \frac{dR}{dt} = \frac{-1}{c^{0+} - c^{0-}} \left( J^{0+} - J^{0-} \right) \quad (3.58)$$

Here  $0^+$  and  $0^-$  denote the matrix side and the precipitate side of the interface, respectively. By applying the previous approach to reduce each variable to dimensionless one, i.e.,  $r \equiv r^* l_0$ ,  $f \equiv f^* \Delta f_0$ , and  $t \equiv t^* l_0^2 / (M \Delta f_0)$ , Eq.(3.57) becomes

$$\frac{\partial c}{\partial t^*} = \frac{1}{r^*} \frac{d}{dr^*} \left( D^* r^* \frac{dc}{dr^*} \right) \quad (3.59)$$

with  $D^* \equiv D / (M \Delta f_0)$ . We further assume concentration in the precipitate is always uniform. Both phase field and diffusion equation computations are performed on a 1D mesh with 128 grids. Periodic condition is applied at the outer boundary, by which the precipitate interacts with all its images through soft impingement.

Initially we let the concentrations on the interface at the precipitate and matrix sides,  $c^{0-}$  and  $c^{0+}$ , equal the bulk equilibrium concentrations,  $+c_{eq}$  and  $-c_{eq}$ , respectively. Let  $c_{eq} = 1$ ,  $\kappa^* = 5.0$ , and  $M = \text{constant}$ . Diffusivity  $D$ , given by Eq.(3.56), is a function of position through  $d^2f/dc^2$ . Matrix concentration is initially  $-0.77$  and the equilibrium area fraction is  $11.5\%$  accordingly. Since phase field model requires a finite particle to start with, we set the initial radius of precipitate  $3$  grids for all cases. Figure 3.16 compares the transformed area fractions from phase field equation (interface identified by  $c = 0$ ) and diffusion equation, and the time evolution of each concentration profile. The initially linear increase of the area fraction with time indicates the parabolic growth law for the both solutions (see also Sec. 2.4). The curve of the diffusion equation (red dotted curve), however, yields a faster initial growth rate and higher final area fraction, compared with the curve of the phase field equation (black solid curve). A detailed analysis on the concentration profiles indicates that the interface concentrations are not strictly the bulk equilibrium values due to the interface curvature. The concentrations at interface may be approximated by (Appendix B)

$$c^{0+} \cong c_{eq}^{0+} = -\frac{2}{\sqrt{3}} \cos\left(\frac{\varphi - \pi}{3}\right) \quad (3.60)$$

$$c^{0-} \cong c_{eq}^{0-} = \frac{2}{\sqrt{3}} \cos\left(\frac{\varphi}{3}\right) \quad (3.61)$$

where

$$\varphi \equiv \cos^{-1}\left(\frac{3\sqrt{3}\sigma}{16\Delta f_0} \frac{1}{R}\right) = \cos^{-1}\left(\frac{3\sqrt{3}\sigma^*}{16} \frac{1}{R^*}\right)$$

and  $\sigma^*$  and  $R$  are the dimensionless interfacial energy and precipitate radius, respectively. The selected phase field parameters yields  $\sigma^* \equiv \sigma/(\Delta f_0 l_0) = 4.22$ . The diffusion equation with this correction (green dashed curves in Fig. 3.16) shows good

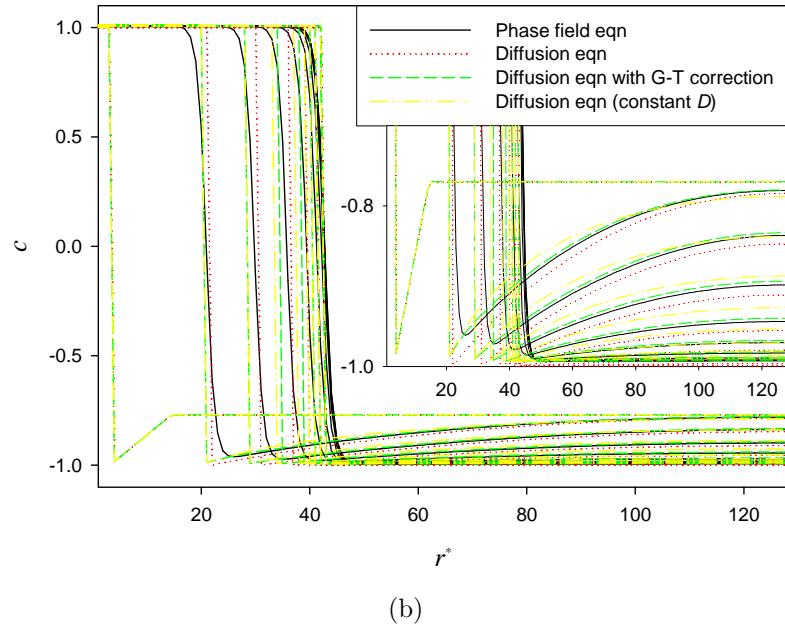
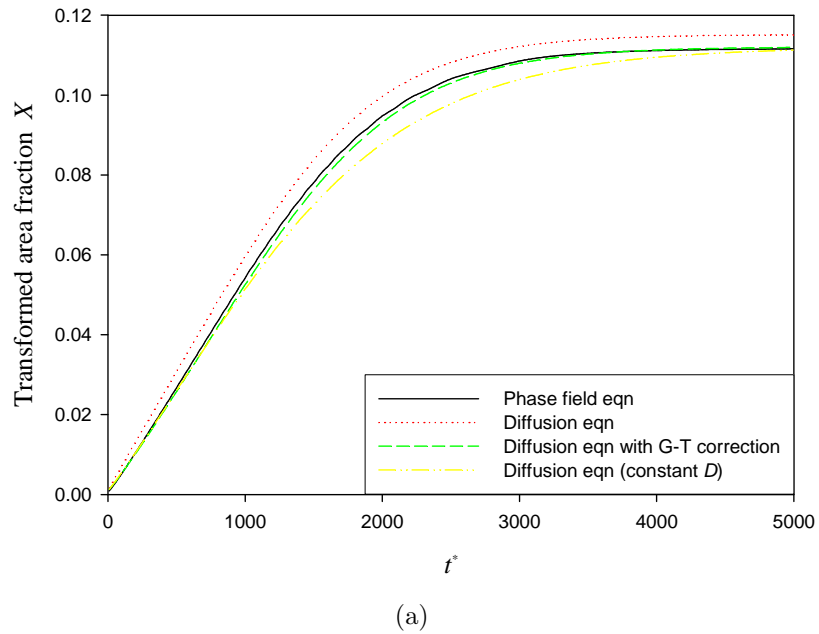


Figure 3.16: Comparison of (a) area fraction and (b) concentration profiles from the phase field equation, diffusion equation with constant  $M$ , with Gibbs-Thomson correction, and with constant  $D$ .

agreement with the phase field approach. Lastly, since diffusion equation is often solved with constant  $D$  instead of  $M$ , we also compare the result with the phase field solution. Arbitrarily we choose  $D^* = 5.56$  for Eq.(3.59) so that the initial slope of the transformed fraction curve matches that of the phase field solution. The curvature correction for concentrations at interface is also applied. The results are the yellow dash-dot curves in Fig. 3.16. The kinetic curve shows an earlier deviation from the parabolic growth law (i.e., the onset of soft impingement) compared with the case of constant  $M$ . This is also evident by comparing the concentration profiles of these two: the profile with constant  $M$  is in general less curved (convex) than that with constant  $D$  because of a decreasing  $D$ , determined by  $d^2f/dc^2$ , away from the interface into the matrix. Since at same particle size the amount of solute depleted in matrix is equal for the two cases, the one with more convex profile (constant  $D$ ) extends the diffusion field farther to the matrix and thus initiates soft impingement earlier. Note that in the moving boundary problem described here the shape of the concentration profile depends on the spatial distribution, rather than the magnitude, of  $D$ .

Finally, we make a plot for the Avrami exponent, given by  $-d \ln \ln(1 - X/X^{eq})/d \ln t$ , where the equilibrium fraction is  $X^{eq} = 11.5\%$ . Despite that in a strict sense our single particle growth is not a JMAK type kinetics, the plot can still reveal some general behavior related to the soft impingement, which will help to interpret the later tests for JMAK. Figure 3.17 shows the plot for all the four cases we tested above. All curves are seen to start with approximately unity, the theoretical value <sup>11</sup>, except for the very early stage, and continuously increase for a certain period of time. The increase of the Avrami exponent is sensible because the growth prior to soft impingement is

<sup>11</sup>With the area fraction  $X/X^{eq} = At$ ,  $n = -d \ln \ln(1 - At)/d \ln t = At/[(1 - At) \ln(1 - At)]$ . Applying l'Hôpital's rule gives  $\lim_{t \rightarrow 0} n = 1$ .

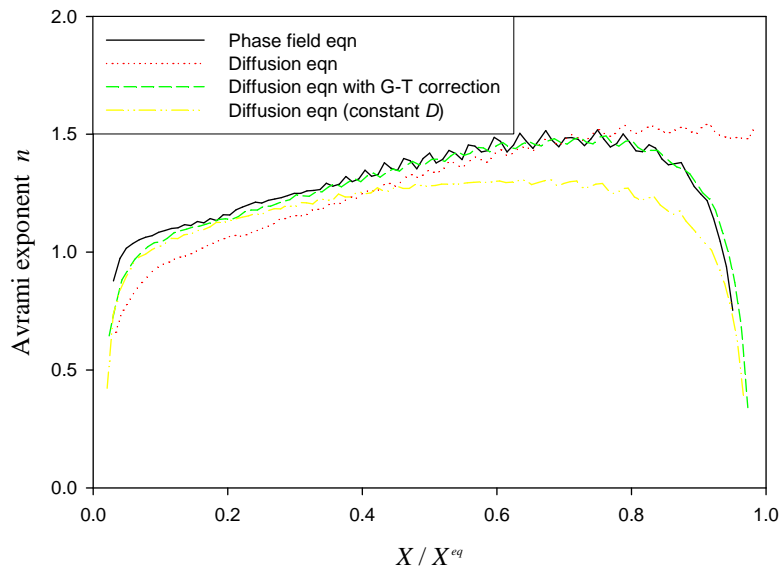


Figure 3.17: Plot of the Avrami exponent for single precipitate growth.

faster and not subject to continuously slow down due to impingement, while the latter corresponds to a constant value of  $n$ . As diffusion fields between the neighboring particles start to overlap due to the periodic boundary condition, the curves tend to bend down, which happens first for the case with constant  $D$  (yellow dash-dot curve) because of the earlier onset of soft impingement. The curve of the diffusion equation solution without considering the Gibbs-Thomson effect continues to reach an almost constant value 1.5 at the end of growth, while other curves decrease toward zero. The deviation from the theoretic value of unity at the beginning is found to relate to the finite initial size of the precipitate. Figure 3.18 plots three curves, with initial radius

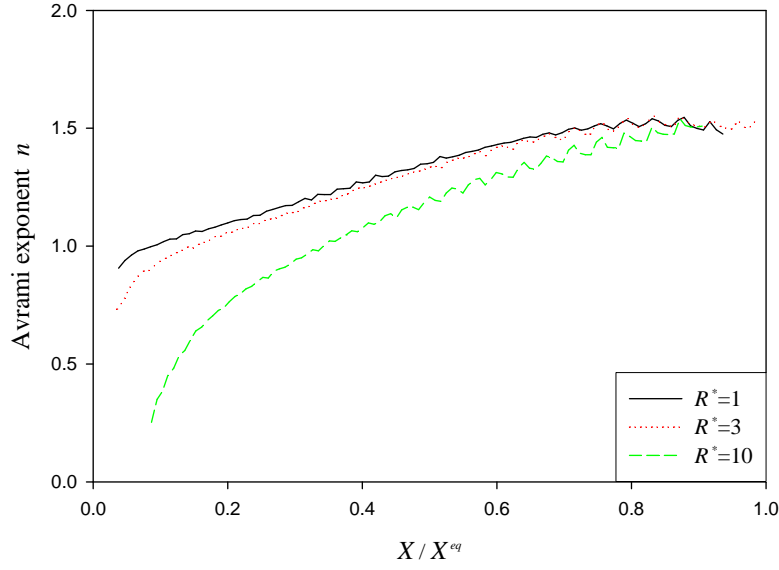


Figure 3.18: Effect of finite initial precipitate size on the Avrami exponent.

1, 3, and 10 grids, calculated by diffusion equation without Gibbs-Thomson correction. The beginning of the curves progressively falls below unity with the increase of initial radius.

### 3.6.2 Periodic versus random array of precipitates

Ham's analysis shows that, at small supersaturations, deviation of precipitate distribution from a periodic array will not change the growth kinetics [93]. This result is reasonable in a sense that since the characteristic distance of diffusion is much greater than the spacing between precipitates the matrix can be approximated well by a uniform field. Each precipitate, regardless of the location of its neighboring precipitates, will experience more or less similar environment. For a *random* distribution of precipitates, however, this scenario does not seem true because regardless of the

precipitate density there is always a fraction of precipitates that are close to each other. At a relatively high supersaturation, on the other hand, the diffusion distance decreases and the matrix concentration will become non-uniform, e.g., the matrix is more depleted where precipitates are denser. As a result, the overall growth kinetics may tend to be considerably influenced by the spatial distribution of precipitates.

To investigate these situations, we compare the growth of two groups of precipitates of the same number. One group forms a periodic array and the other is distributed randomly (Fig. 3.19). We consider three cases with the number of precipitates  $N=16$ , 64, and 256, respectively. All precipitates are introduced at  $t^* = 0$  as small nuclei. The matrix has the size  $1024 \times 1024$  and initially is uniform with concentration -0.77. The equilibrium area fraction is accordingly 11.5%.

The growth kinetics for each case is shown in Fig. 3.20 by the plot of the transformed area fraction with time. In all cases the growth rate of the random precipitates is identical to the growth rate of the periodic precipitates at the early stage and both follow the parabolic law. This corresponds to the time that the diffusion fields from each particle have not yet significantly overlapped. Gradually, deviation from the parabolic law is observed owing to the soft-impingement, while it occurs relatively earlier among the random precipitates. This is consistent to the fact that the periodic precipitates are always separated by the maximal distance, which postpones the onset of soft-impingement. Because the growth rate of the random groups is reduced earlier they also take longer time to complete the transformation. A close look indicates that in all cases the final area fraction is smaller than the theoretical value 11.5%, in particular, the case with more precipitates (or smaller final size) has larger deviation. This is found due to the Gibbs-Thomson effect, which raises the matrix concentration

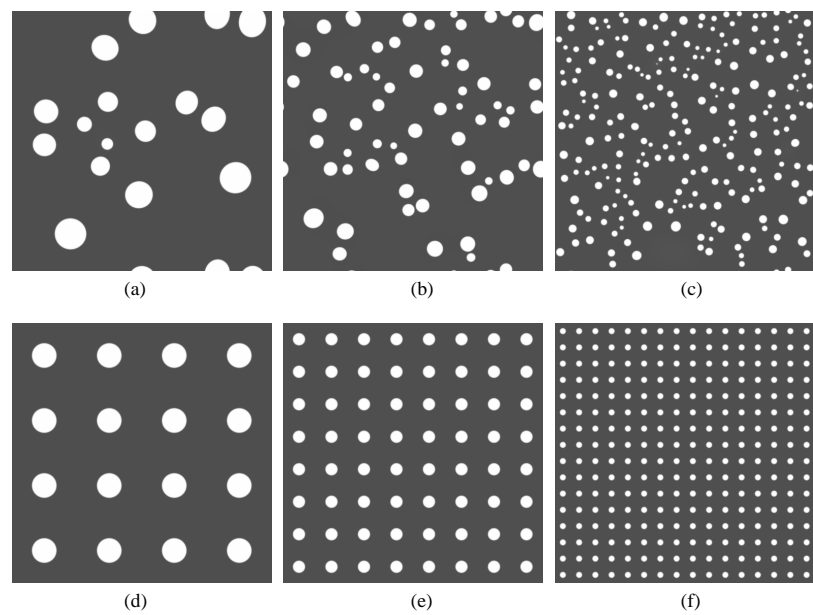


Figure 3.19: Final microstructures of the randomly (a-c) and the periodically (e-f) arranged precipitates. Different numbers of precipitates are used: (a,d)  $N=16$ , (b,e) 64, and (c,f) 256. The initial precipitates are equal in size.

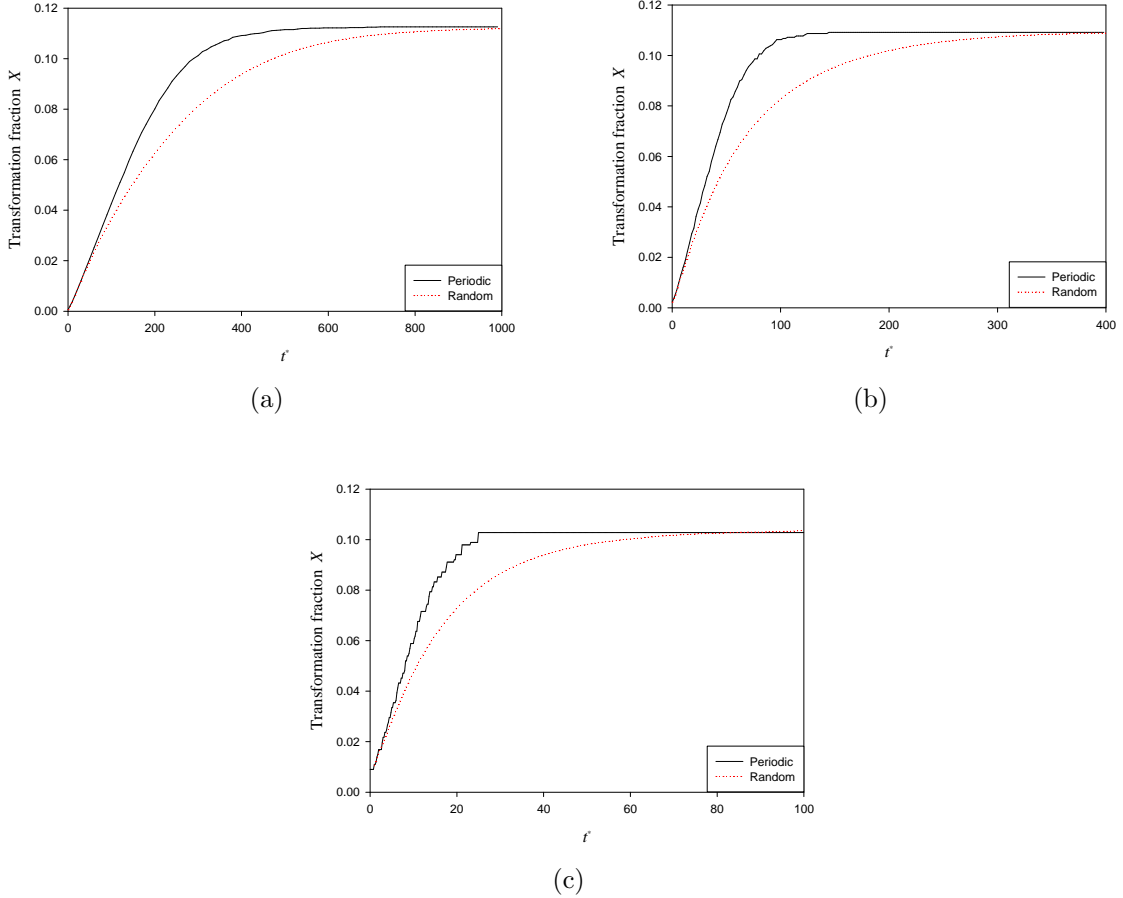


Figure 3.20: Transformed area fractions of the periodic and the random precipitates with different number: (a)  $N=16$ , (b) 64, and (c) 256.

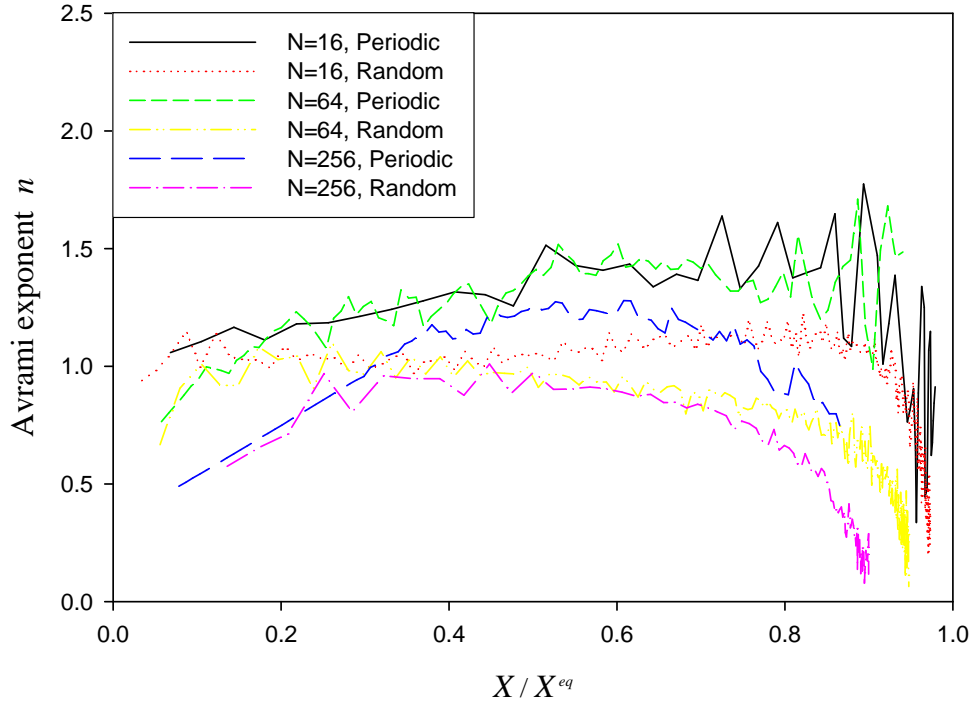


Figure 3.21: Plot of the Avrami exponent for growth of periodic and random precipitates.

and lowers the final transformed fraction, as we once encountered in the growth of single precipitate in Section 3.4.

Figure 3.21 gives the plot of Avrami exponent,  $n$ , with respect to the reduced transformed fraction,  $X/X^{eq}$ , for each case. All curves are seen to start from approximately  $n = 1$  (the two curves with 256 precipitates are somewhat lowered due to the finite precipitate size effect). The growth of the periodic precipitates, which in fact is identical to the previous case of single precipitate, shows a continuous increase in the Avrami exponent up to about 1.5 before decay. The curves of the random

precipitates, however, stay at  $n = 1$  for a long period of time. The curve of 16 precipitates shows some increase, nevertheless much insignificant compared to its periodic counterpart. This could be caused by uncertainties in statistics due to the very limited number of precipitates. Approaching the completion of the transformation all curves seem to decay toward zero. Moreover the final area fractions are shifted to the low end. These features are found to relate to the Gibbs-Thomson effect and will be discussed in more detail in Section 3.6.3.

### 3.6.3 Nucleation, growth, and coarsening

We now introduce nucleation into the kinetics. Being consistent to the chemical free energy model the nucleation rate is given by Eqs.(3.21) and (3.20). A relatively large mesh,  $2048 \times 2048$ , is used for eliminating the system size effects on the statistics associated with the randomness of nucleation, especially at a low nucleation rate. The starting matrix is always chosen to be uniform with concentration -0.77. Since the major portion of the phase transformation will be the interplay between nucleation and growth, we shall include a number of different nucleation rates to observe the influence from the relative strengths of the two processes. To do so, we vary the prefactor  $J^*$  in Eq.(3.21) so that the initial (i.e.,  $t^*=0$ ) dimensionless nucleation rates will vary from  $1.5 \times 10^{-7}$  to  $7.5 \times 10^{-4}$  nuclei per phase field grid per unit phase field time. The lower limit corresponds to a rate of forming less than 1 nucleus in the entire matrix per unit time and the latter is over 3000 nuclei. Accordingly the time step is dynamically determined to ensure that at most 2 nuclei can be formed in each step. In addition to the magnitude of nucleation rate, we also vary the dimensionless parameter  $s^*$  in Eq.(3.21) to change the degree of sensitivity of nucleation rate to the

supersaturation. The parameter  $s^*$  in fact is associated with the interfacial energy. Two values are used that correspond to an initial nucleation activation energy  $20k_B T$  and  $50k_B T$ , respectively. All the parameters are summarized in Table 3.4.

Table 3.4: The parameters employed in the nucleation rate (Eq.(3.21)).

Test number	1	2	3	4	5	6
$J^*(t^* = 0)$	$1.5 \times 10^{-7}$		$1.5 \times 10^{-6}$		$1.5 \times 10^{-5}$	
$\Delta G^*(t^* = 0)$	50	20	50	20	50	20
$J^*$	74.03	$7.911 \times 10^{14}$	740.3	$7.911 \times 10^{15}$	7403	$7.911 \times 10^{16}$
$s^*$	47.70	119.3	47.70	119.3	47.70	119.3
Test number	7	8	9	10		
$J^*(t^* = 0)$	$1.5 \times 10^{-4}$		$7.5 \times 10^{-4}$			
$\Delta G^*(t^* = 0)$	50	20	50	20		
$J^*$	$7.403 \times 10^4$	$7.911 \times 10^{17}$	$3.702 \times 10^5$	$3.956 \times 10^{18}$		
$s^*$	47.70	119.3	47.70	119.3		

$$\Delta G^* \equiv -\pi\sigma^2/k_B T \Delta f \equiv -s^*/\Delta f^*.$$

Figure 3.22 gives the final microstructures of each test. As nucleation becomes successively dominant from Fig. 3.22(a) to (j) the final precipitate density increases while the size decreases. Difference between the tests with same  $J^*$  but different  $s^*$  seems negligible. The transformed area fraction of each test is recorded with time, from which the Avrami exponent is extracted and plotted against the reduced transformation fraction  $X/X^{eq}$  in Fig. 3.23.

It is seen in Fig. 3.23 that with the increase of  $J^*$  the Avrami exponents generally shift to lower values. In particular, when  $J^*$  is between  $1.5 \times 10^{-7}$  and  $1.5 \times 10^{-5}$ , the Avrami exponent curves are very close to one another up to 70% equilibrium fraction ( $X^{eq}$ ) despite that their actual transformation time differ in order of magnitude. This range corresponds to a low nucleation rate regime where the growth process is dominant. Accordingly, nuclei are formed at a low rate in a large matrix, and at

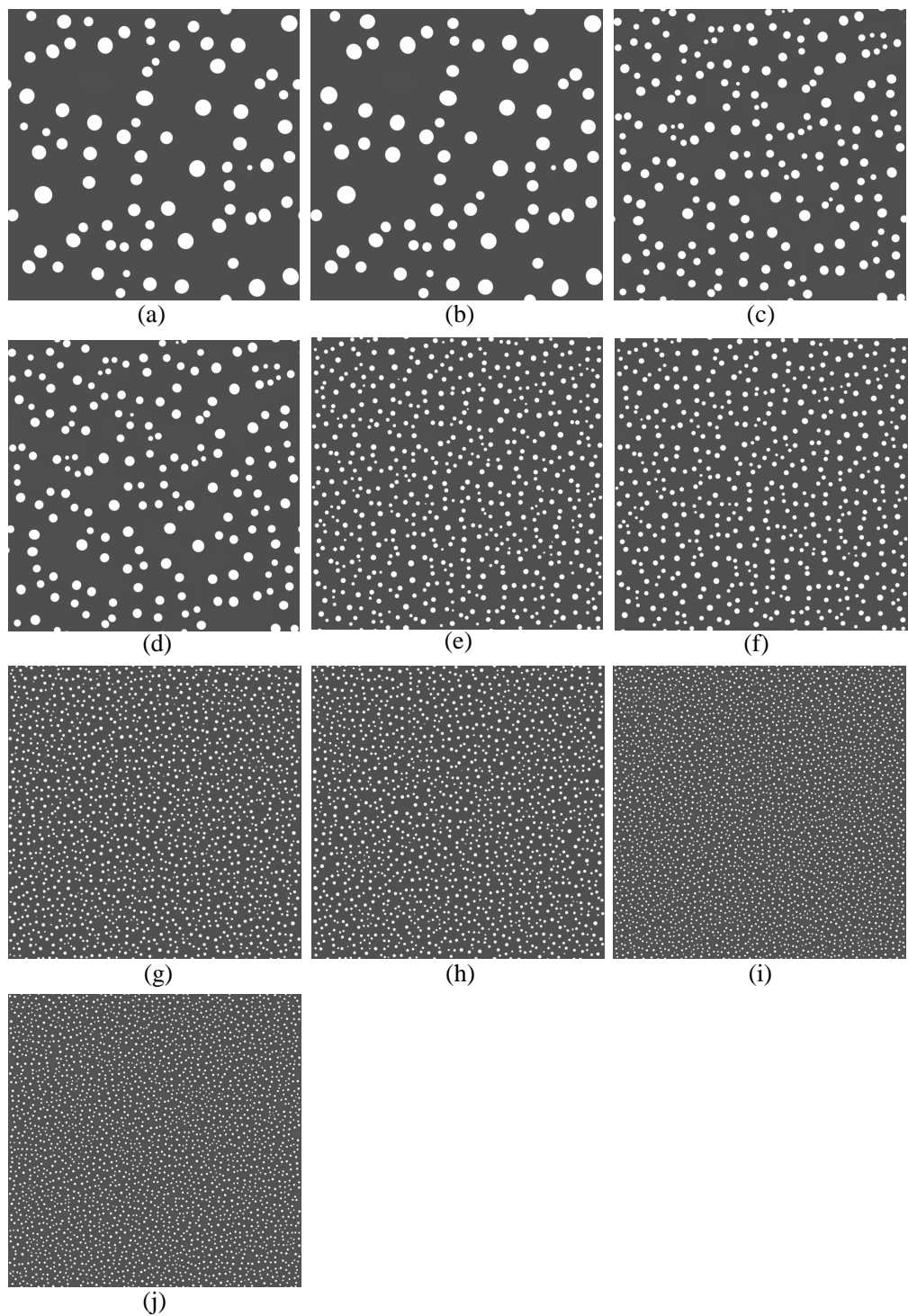


Figure 3.22: Final microstructures: (a-j) correspond to the tests 1 to 10 in Table 3.4.

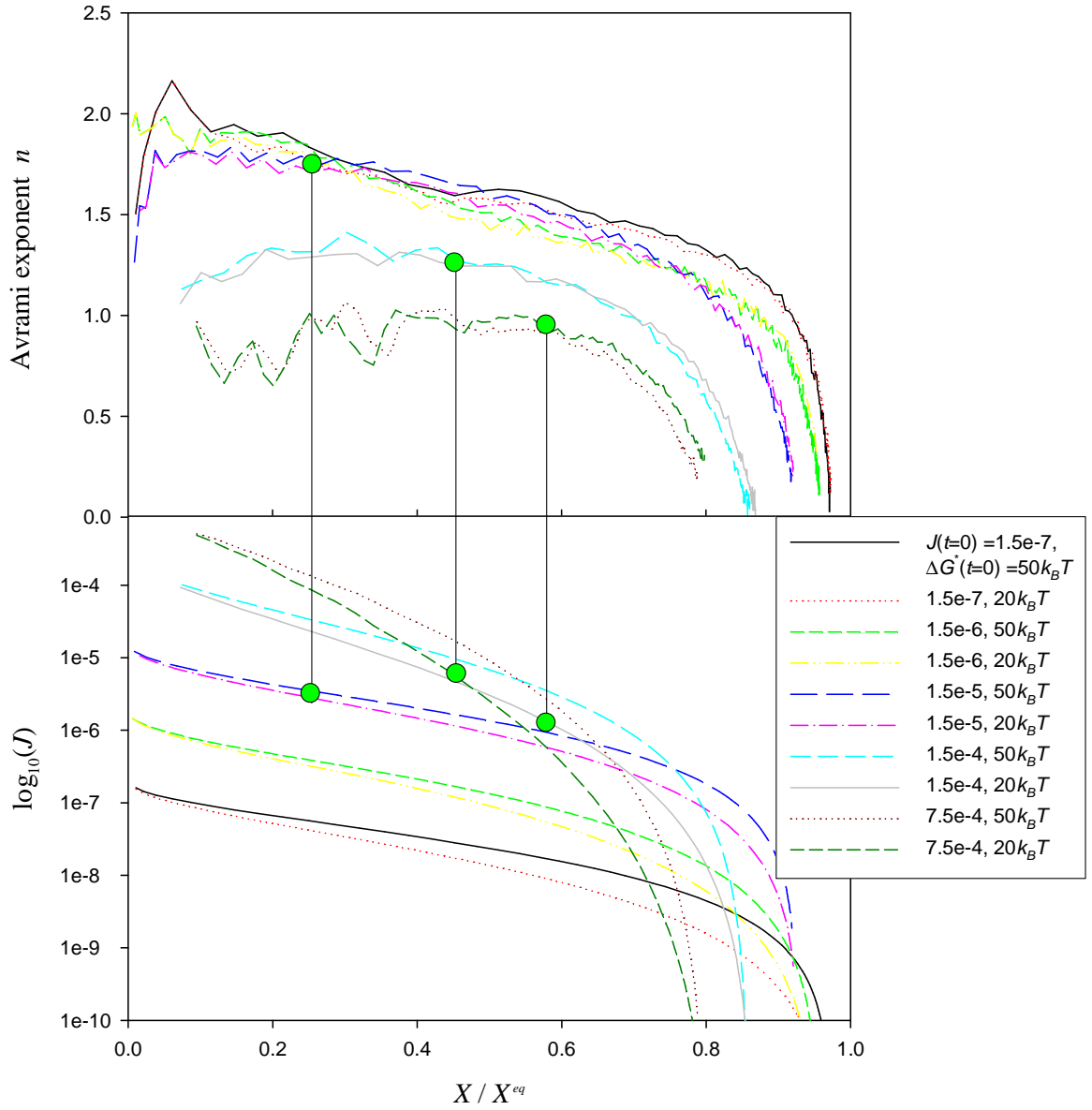


Figure 3.23: Plot of the Avrami exponent for concurrent nucleation, growth and coarsening (upper panel) and the nucleation rate (lower panel).

very early stages a large area of untransformed and undepleted matrix is available for nucleation. Thus nucleation may be considered to occur at a nearly constant rate. The theoretical Avrami exponent for such situation is 2 (see Table 3.3). The curves in Fig. 3.23 seem to agree with this value well. Unlike in massive transformations or recrystallizations that typically applicable to the original JMAK theory, nucleation in precipitation reactions can seldom achieve a constant rate because of concentration depletion in the matrix. Thus except for very early stages the nucleation within our consideration is always a decaying process. This is confirmed by the continuous decrease in the simulated Avrami exponent with time. The curves at  $J^* = 1.5 \times 10^{-4}$  correspond to a moderate nucleation rate regime. It is considerably lower than the previous curves and their starting values are between 2 and 1. Finally,  $J^* = 7.5 \times 10^{-4}$  corresponds to a high nucleation rate regime. The curves appear to maintain a constant value 1 from the beginning and up to about  $0.6X^{eq}$ . The site saturation limit in Table 3.3 produces the same value. However, an analysis of the data shows nucleation occurs up to  $0.5X^{eq}$ . Thus the plateau of the curves must involve the contributions from nucleation. Plateau is also observed in other curves while each lasts for different period of time from the beginning. By taking the moment it ends and mapping to the nucleation rate curves (indicated by the green dots in Fig. 3.23), we find the corresponding nucleation rate is typically between  $5.5 \times 10^{-6}$  and  $1 \times 10^{-5}$ . It appears that the Avrami exponent curves will start to decay whenever the nucleation rate drops below this limit. In addition, for the two low nucleation rate cases ( $J^* = 1.5 \times 10^{-6}$  and  $1.5 \times 10^{-7}$ , which are below this limit), the Avrami exponent curves decay from the very beginning. These features seem to indicate that the constant Avrami exponents may be due to nucleation.

To gain better understanding on the shift of the Avrami exponent curves with the nucleation rate, we may consider a simpler nucleation and growth problem described by Eq.(3.48). During the precipitation process two particular things may be expected for the decay of the matrix concentration. First, the background (or the average) matrix concentration keeps decreasing with the increase of the transformed fraction, which reduces the overall driving forces for nucleation and growth; Second, the spatial distribution of precipitates influences local concentration and local nucleation and growth rates. The latter seems to relate to the concept of impingement described in the original JMAK theory. According to the former we assume in the extended volume a decaying form for the nucleation rate

$$J(t) = J_0 \frac{e^{-t/t_n}}{t_n} \quad (3.62)$$

and the growth rate

$$V(t) = V_0 (1 - e^{-t/t_g}) \quad (3.63)$$

where  $t_n$  and  $t_g$  are the characteristic time for nucleation and growth, respectively.  $J_0$  and  $V_0$  are two constants. We should keep in mind that  $t_n$  and  $t_g$  are in fact correlated to  $J_0$  and  $V_0$  here. For example, if  $J_0$  is larger, nuclei will be formed more rapidly, which depletes the matrix faster and thus  $t_g$  should decrease. Substitute into Eq.(3.48) gives

$$\begin{aligned} X_{ex}(t) &= J_0 V_0 \int_0^t \frac{e^{-\tau/t_n}}{t_n} (1 - e^{-(t-\tau)/t_g}) d\tau \\ &= J_0 V_0 \left[ 1 - \frac{t_n}{t_n - t_g} e^{-t/t_n} - \frac{t_g}{t_g - t_n} e^{-t/t_g} \right] \end{aligned} \quad (3.64)$$

To retrieve the Avrami exponent, the extended fraction needs to be written in a form  $X_{ex} \propto t^n$ , and

$$n = \frac{d \ln X_{ex}}{d \ln t} = \frac{e^{-t/t_n} - e^{-t/t_g}}{\frac{t_n}{t} (1 - e^{-t/t_n}) - \frac{t_g}{t} (1 - e^{-t/t_g})} \quad (3.65)$$

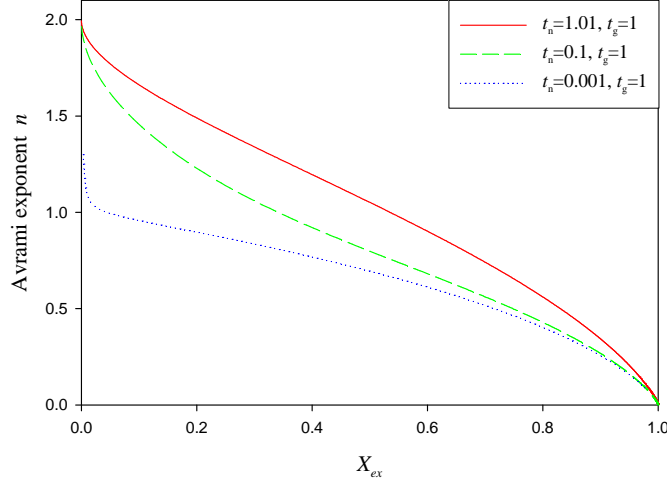


Figure 3.24: Plot of the Avrami exponent vs. the extended transformed fraction from a simple analytic model with exponentially decaying nucleation rate and growth rate.

$n$  is plotted in Fig. 3.24 for three sets of  $t_n$  and  $t_g$ . For a given  $t_g$ , decreasing  $t_n$  corresponds to a faster decay of nucleation rate with time, which can be caused by a larger initial rate of nucleation that depletes the matrix. In this trend the Avrami exponent curves are seen to shift downwards, which agrees with the previous observations in Fig. 3.23. Eq.(3.65) also indicates that the initial Avrami exponent is always between 1 and 2, although the rigorous  $t = 0$  value is 2. The low end of  $t_n$  is equivalent to an extremely fast decay of nucleation rate, or a site saturation limit. Indeed the corresponding curve starts approximately at the theoretical value 1. It is also interesting to notice that  $t_n$  and  $t_g$  have an interchangeable role in Eq.(3.65). This implies that an opposite extreme case, with large nucleation rate while almost frozen growth rate, will produce the same result as the site saturation limit (i.e., frozen nucleation). This may provide the explanation to the previous cases with

$J^*(t^* = 0) = 7.5 \times 10^{-4}$  in Fig.3.23. We may also notice that the analytic model in fact assumes a spontaneous decay of nucleation rate during growth, while in reality, especially at a relatively low nucleation rate, the reach of diffusion field to another precipitate may require finite time, thus the nucleation rate in the untouched area does not immediately drop. Therefore the current analytic model may overestimate the effect of soft-impingement. In contrary, the extension of JMAK theory with simple parabolic growth law neglects the contribution from the matrix depletion due to impingement, and thus produces an underestimate. A more realistic situation, such as described by the microstructure-based simulation shown in Fig. 3.23, should predict results between these two limits.

Finally, we have seen that all curves in Fig. 3.23 reduces to zero near the completion of the transformation. Since the Gibbs-Thomson effect has the same physical origin as precipitate coarsening, here we combine the coarsening kinetics to explain this phenomenon. First, the transformed fraction can be written as

$$X(R) = \frac{c_0 - c_1(R)}{c_2(R) - c_1(R)} \quad (3.66)$$

where  $c_0$  is the average concentration of the system (including the precipitates),  $c_1$  and  $c_2$  are the concentrations of the matrix and the precipitates.  $R$  is the average radius of precipitates. The concentration deviation due to the curvature (for 2D) is given by

$$\delta c(R) \cong \frac{\delta\mu}{(\partial\mu/\partial c)} = \frac{\sigma/R}{f''}$$

Here  $\mu$  is the chemical potential and  $f'' = \partial^2 f^{ch}/\partial c^2 = \partial\mu/\partial c$ . Correspondingly,

$$c_1(R) = c_1(\infty) + \delta c_1 = c_1(\infty) + \frac{\sigma/R}{f_1''}$$

$$c_2(R) = c_2(\infty) + \delta c_2 = c_2(\infty) + \frac{\sigma/R}{f_2''}$$

Subscripts 1 and 2 are used to denote the matrix and the precipitate.  $\infty$  stands for the property at zero curvature. Substitution into Eq.(3.66) yields

$$\begin{aligned} X(R) &= \left[ c_0 - c_1(\infty) - \frac{\sigma}{R} \frac{1}{f''_1} \right] \left[ c_2(\infty) - c_1(\infty) + \frac{\sigma}{R} \left( \frac{1}{f''_2} - \frac{1}{f''_1} \right) \right]^{-1} \\ &\approx \frac{c_0 - c_1(\infty)}{c_2(\infty) - c_1(\infty)} - \left[ \frac{1}{c_2(\infty) - c_1(\infty)} \frac{1}{f''_1} - \frac{c_0 - c_1(\infty)}{(c_2(\infty) - c_1(\infty))^2} \left( \frac{1}{f''_2} - \frac{1}{f''_1} \right) \right] \frac{\sigma}{R} \\ &\equiv X(\infty) - \frac{\beta}{R} \end{aligned}$$

Note here  $X(\infty) = X^{eq}$ . By taking  $R^3 = R_0^3 + kt$ , the transformed fraction becomes

$$X(R(t)) = X^{eq} - \beta(R_0^3 + kt)^{-\frac{1}{3}} \quad (3.67)$$

The Avrami exponent is given by Eq.(3.50), i.e.,

$$\begin{aligned} n &= \frac{d \ln \ln(1 - X/X^{eq})^{-1}}{d \ln t} \\ &= \frac{-t}{(1 - X/X^{eq}) \ln(1 - X/X^{eq})} \frac{dX/X^{eq}}{dt} \\ &= \frac{-1}{3(R_0^3 + kt)^{-\frac{1}{3}} \ln[(\beta/X^{eq})(R_0^3 + kt)^{-\frac{1}{3}}]} \frac{kt}{(R_0^3 + kt)^{\frac{4}{3}}} \end{aligned} \quad (3.68)$$

where the last step has taken Eq.(3.67). At  $t \rightarrow \infty$ , the Avrami exponent is

$$\lim_{t \rightarrow \infty} n = \lim_{t \rightarrow \infty} (\ln t)^{-1} = 0$$

This proves that, due to the Gibbs-Thomson effect the Avrami exponent in soft-impingement always converges to zero at the end of the transformation.

### 3.7 Summary

Characterization of real microstructures often requires treating nucleation, growth, and coarsening as concurrent processes. Despite that Langevin noise terms in phase field equations can self-consistently model nucleation according to the fluctuation-dissipation theorem, its use at *mesoscales* causes problem both theoretically, due to

the neglect of microscopic fluctuations by coarse-graining, and practically, due to the time scale limitation, and thus cannot characterize nucleation quantitatively. The explicit nucleation algorithm provides a phenomenological alternative that introduces nuclei in microstructure according to local driving force. Relying on the particular model for the evaluation of nucleation rate it introduces quantitative feature to nucleation. More importantly, nucleation can be treated as a simultaneous process with growth and coarsening, instead of being constrained to the site-saturation limit previously.

Integration of the algorithm to phase field model is demonstrated firstly under isothermal condition, where nucleation driving force is evaluated instantaneously during growth and coarsening. Generic material parameters, such as chemical free energy and interfacial energy, are shared by both phase field model and nucleation algorithm. Microstructural evolution is predicted from the beginning of nucleation stage, from which precipitate number and size distribution are extracted. The  $t^{1/2}$  and  $t^{1/3}$  kinetic laws are reproduced at growth and coarsening stages, respectively.

For nucleation in solids involving lattice mismatch, the coherency strain energy is derived and incorporated into the local nucleation driving force. The formulation considers nucleation in mesoscale microstructure and takes into account elastic anisotropy of the material. The final form separates the volume of the nucleus and the contributions from microstructure, and therefore can be directly combined with the volume chemical free energy in the classical nucleation theory. Through simulations we illustrate that depending on the interplay between the chemical free energy and the elastic interaction energy the existing microstructure may considerably influence nucleation process in both nucleation sites and rate. In addition, elastic interaction

among nucleating precipitates is also found to contribute to microstructure patterning that often observed during growth and coarsening.

The advantage of the explicit nucleation algorithm is seen more clearly in the study of the overall kinetics by the phase field method. Consistent with the predictions by the JMAK theory, the kinetics of concurrent nucleation and growth is very different from that of the site-saturation limit where all nuclei are form at the beginning. In a 2D simulation of diffusion-controlled precipitation, the former at a low nucleation rate yields the initial Avrami exponent as 2 while the latter gives 1. More detailed analysis indicates that, different from the conventional adoption of JMAK theory for diffusion-controlled phase transformation and many other analyses, the Avrami exponent is in general a decaying function with time. It is found that the soft-impingement of the diffusion fields from each precipitate reduces the Avrami exponent. Both simulation and analytical derivation show that due to the Gibbs-Thomson effect the Avrami exponent will converge to zero approaching the equilibrium transformation fraction. Nucleation rate in diffusion-controlled transformation generally decays exponentially due to matrix depletion. In the simulation it seems to correlate to the width of the initial plateau on the Avrami exponent ( $n-X/X^{eq}$ ) curve. The exact reason, however, needs more detailed study. Regardless of these deviations, the JMAK analysis seems applicable to predicting various transformation mechanisms if only the initial portion of the transformation data is used.

## CHAPTER 4

### PHASE FIELD MODEL FOR DISLOCATIONS

Dislocation reactions and dynamics have become the basis for explaining and improving mechanical properties of crystalline materials. In engineering practice, for instance, various approaches to make stronger materials, such by solid solution treatment, cold work, introducing dispersion particles and grain boundaries, are rooted in the reactions of dislocation with various crystalline defects. Interactions of dislocations with other defects involve both short-range reactions at the interrupted lattice planes in dislocation cores and long-range reactions through elastic distortion of crystal lattice. The roles that a large assembly of dislocations play in a macroscopic material body thus generally span a wide spectrum of length scales, from lattice parameter to meso- or even macroscopic scales, and raise challenges to theoretic analyses. Since the early 1990s this difficulty has been actively attacked at multiple length scales, mostly owing to the breakthrough in computer technology [100]. At atomic level, quantum mechanical calculations [101, 102, 103, 104, 105, 106] and molecular dynamics [107, 108, 109, 110] are employed to study the energetics and interatomic processes. The Peierls-Nabarro model [111, 112, 2] as the continuum alternative and its generalizations [113, 103, 114, 115, 116, 117] are applied to analyze dislocation core structure, recombination energy, and Peierls stress (lattice friction), which determine

dislocation mobility and the barrier for cross-slip. Mesoscale dislocation dynamics models mostly adopt line segment description for dislocations under Peach-Koehler forces and have been successfully applied to very sophisticated 3D dislocation configurations [118, 119, 120, 121] and to thin films [122, 123, 124, 125, 126]. While the models at each level are under extensive development, multiscale models that aim to provide a hierarchical yet complete description of plasticity problems are also in active progress [127, 128].

The newly developed phase field model of dislocation [129, 130, 131, 132], as essentially a 3D generalization of Peierls-Nabarro model, fit itself in between the atomic scale and mesoscale. With the capability of describing an *arbitrary* microstructure as illustrated previously, the model can conveniently treat complex 3D dislocation structures in an elastically anisotropic and/or inhomogeneous material at a mesoscopic level. With more general energy formulations the model is extended [14] to allow appropriate descriptions of dislocation nodal reactions, which leads to a flexible model for treating complex dislocation networks. In the meantime, in the same framework the generalized stacking fault energy ( $\gamma$ -surface) [133] is introduced into the phase field model and the traditional Peierls-Nabarro type analysis for dislocation core structures is extended to 3D arbitrary configurations [15]. In addition, various reactions such as dislocation core dissociation as well as formation and annihilation of various planar faults can be studied [18].

In this chapter we first review the energy terms introduced in the original phase field method [129, 131] and demonstrate the need for a more appropriate formulation. We then introduce new expressions according to the equivalence of representing a dislocation by multiple slip modes. Various simulation results obtained using these

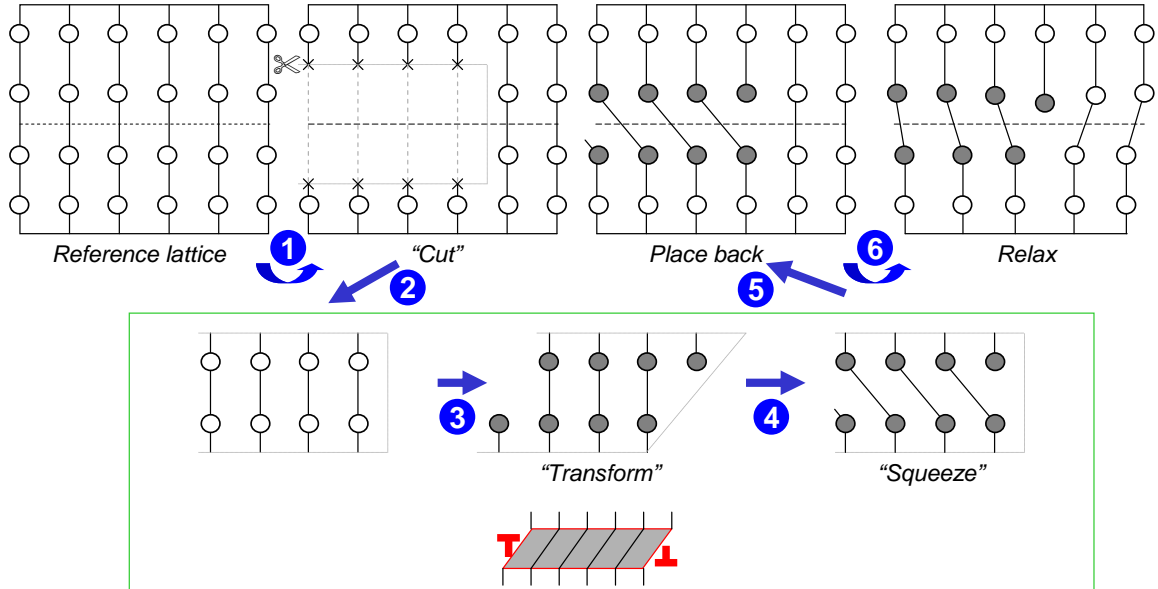


Figure 4.1: Lattice correspondence between an edge dislocation and a sheared thin plate.

new expressions for reactions among perfect dislocations and partial dislocations in fcc crystal are then presented, together with discussions on some general features about the crystalline and gradient energies and particular features associated with the new formulation.

## 4.1 Field description of dislocations

The equivalence between the atomic lattices around a dislocation line and around a sheared plate of one atomic layer thick makes it possible to describe a glide dislocation loop in the traditional way in phase field method. Figure 4.1 sketches such a picture for an edge dislocation. Start from a perfect crystal, we (1) cut a portion of two atomic layers and (2) hypothetically take it out without “disturbing” the lattice of either itself

or the remaining part of the crystal; (3) the cut portion then undergoes a “phase transformation” that results in a relative shear between the two layers of atoms in a stress-free state; we then (4) “squeeze” the transformed crystal to restore its original shape and (5) place it back into the crystal; (6) finally the entire lattice is allowed to relax to reduce the strain energy stored in the transformed crystal. The procedure described is essentially an Eshelby’s process for computing the elastic energy of a coherent inclusion [43, 44] if the volume that occupied by the dark circles is imagined as a continuum coherent thin plate. Nevertheless in this context it produces the lattice configuration of an edge dislocation. Step (3) also defines the transformation strain associated with the dislocation

$$\epsilon_{ij}^T = \mathbf{b} \otimes \mathbf{n}/2d = (b_i n_j + b_j n_i)/2d \quad (4.1)$$

where  $\mathbf{b}$  and  $\mathbf{n}$  are the shear displacement (Burgers vector) and the normal of the plate (slip plane), respectively.  $d$  is the thickness of the plate (interplanar distance of the slip plane). It should be noted that whereas a plate under simple shear is equivalent to a glide dislocation loop, a plate with tensile strain along the normal can correspond to a Frank-type dislocation loop.

This analog between a platelet inclusion and a dislocation loop, recognized by Nabarro in 1951 [134], is the basis of the phase field description of dislocation loops in terms of martensitic platelets [135, 136]. In a way similar to the latter, a plate (or a dislocation loop) is described by a phase field,  $\eta(\mathbf{x})$ , with the value 1 inside the plate and 0 in the remaining 3D crystal (Fig. 4.2). In a general situation the values of  $\eta$ , not necessarily to be 1, characterize the amount of shear with respect to a defect free crystal, in the unit of  $b/d$ , caused by sweeping of dislocations of the same slip system [14].

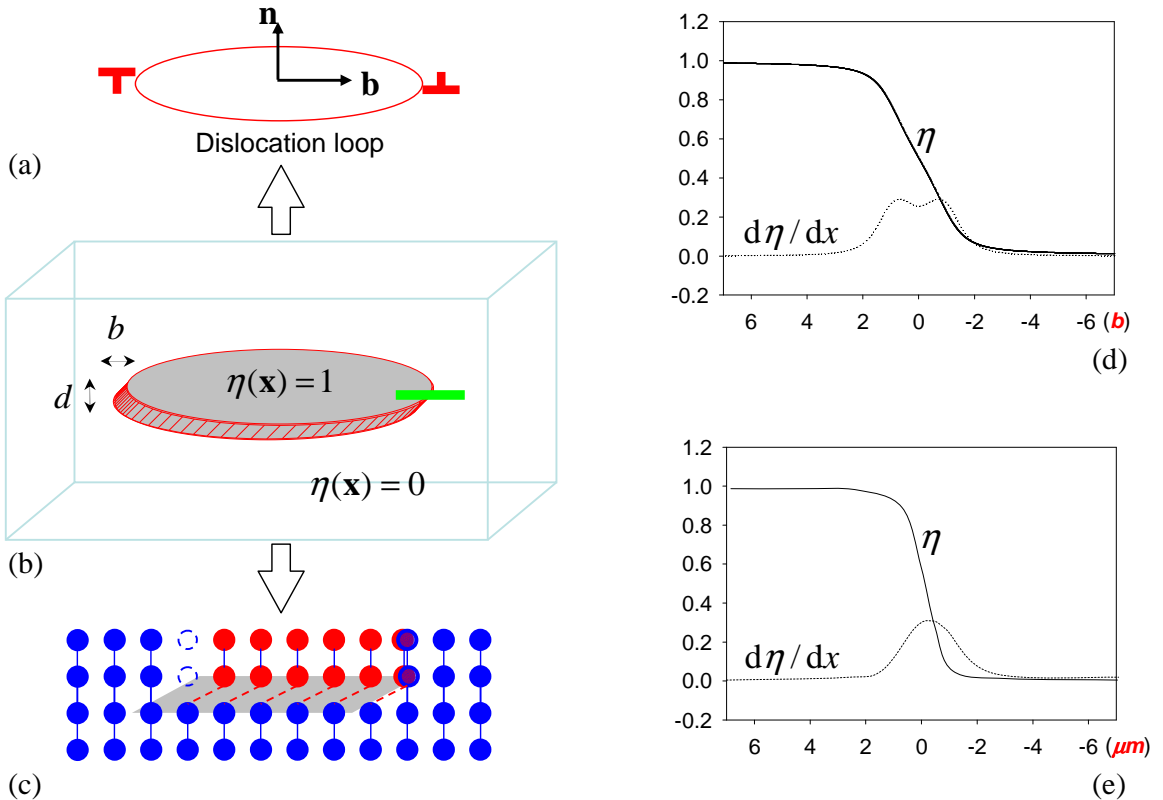


Figure 4.2: Field description of (a) a dislocation loop in terms of (b) a thin platelet by phase field  $\eta$ , corresponding to (c) the atomic lattice picture. Typical profiles of  $\eta$  across a dislocation line (the green bar in (b)) are plotted at (d) microscopic and (e) mesoscopic scales, depending on the choice of model parameters.

A complex dislocation configuration may consist of more than one slip system and evolve with time. Accordingly, the notation of phase field is modified to  $\eta(\alpha, m_\alpha, \mathbf{x}, t)$  where the indices  $\alpha$  and  $m_\alpha$  denote the slip plane and the slip directions on that plane. For example, the 12 slip systems in a fcc crystal can be denoted by  $\alpha = 1, 2, 3, 4$  for each of the four  $\{111\}$  slip planes and  $m_\alpha = 1, 2, 3$  for each of the three  $\langle 1\bar{1}0 \rangle$  slip directions. The transformation strain is a linear combination of each contributing slip system defined in Eq.(4.1) [131]:

$$\epsilon_{ij}^T(\mathbf{x}, t) = \sum_{\alpha, m_\alpha} \epsilon_{ij}^T(\alpha, m_\alpha) \eta(\alpha, m_\alpha, \mathbf{x}, t) \quad (4.2)$$

where,

$$\epsilon_{ij}^T(\alpha, m_\alpha) = [b_i(\alpha, m_\alpha)n_j(\alpha) + b_i(\alpha, m_\alpha)n_j(\alpha)] / 2d(\alpha) \quad (4.3)$$

## 4.2 Formulation of energies and equation of motion

In the dislocation language, the field description present in the preceding section treats a dislocation line as a boundary between two different slipped regions on a particular slip plane. The total energy of a dislocation consists of a long-range elastic energy associated with the lattice distortion by dislocation and a short-range periodic potential energy associated with the relative slip between two infinite crystal halves above and below the slip plane, known as *crystalline energy* in phase field model [129]. In the extended model [14] the latter is generalized to an energy associated with a general plastic strain produced by linear combinations of all individual slips. In addition, the conventional gradient term energy of phase field model is retained in the dislocation model to account for additional short-range core reactions and to produce a diffuse core in a mesoscale simulation of moving dislocations. The total

energy of a dislocation system is thus

$$E = E[\eta(\alpha, m_\alpha, \mathbf{x}, t)] = E^{crys} + E^{grad} + E^{el} + W \quad (4.4)$$

where  $E^{crys}$ ,  $E^{grad}$ , and  $E^{el}$  represent the crystalline, gradient, and elastic energy, respectively. These energies depend on and are functionals of *arbitrary* dislocation configuration represented by the phase fields  $\eta(\alpha, m_\alpha, \mathbf{x}, t)$ .  $W = \int d\mathbf{x} \sigma_{ij}^{app} \epsilon_{ij}^T(\mathbf{x})$  is the mechanical work under applied stress  $\sigma_{ij}^{app}$ .

The time evolution of dislocations is described by the dynamic equation for non-conserved fields (Eq.(2.4)) in the absence of thermal fluctuations

$$\frac{\partial \eta(\alpha, m_\alpha, \mathbf{x}, t)}{\partial t} = -L \frac{\delta E}{\delta \eta(\alpha, m_\alpha, \mathbf{x}, t)} \quad (4.5)$$

with  $L$  being the kinetic coefficient.

#### 4.2.1 Original formulations

The crystalline energy was initially proposed as a general Fourier expansion series whose degenerated minima are located at the crystal lattice sites [129]

$$E^{crys} = \int d\mathbf{x} \sum_{\mathbf{H}} A(\mathbf{H}) (1 - \exp(i2\pi \mathbf{H} \cdot \mathbf{b}(\mathbf{x}))) \quad (4.6)$$

where

$$\mathbf{b}(\mathbf{x}) = \sum_{\alpha, m_\alpha} \mathbf{b}(\alpha, m_\alpha) \eta(\alpha, m_\alpha, \mathbf{x}) \quad (4.7)$$

is the total Burgers vector,  $\mathbf{H}$  are reciprocal lattice vectors of the host lattice and  $A(\mathbf{H})$  are positive coefficients. In the subsequent phase field modeling [131, 137], a simplified approximation was employed

$$E^{crys} = \int d\mathbf{x} \sum_{\alpha, m_\alpha} A \sin^2 \pi \eta(\alpha, m_\alpha, \mathbf{x}) \quad (4.8)$$

where  $A \equiv \mu(b/d)^2/2\pi^2$  is a constant and is obtained by fitting at small strain limit to the shear modulus,  $\mu$ , for the corresponding slip system <sup>12</sup>.

The gradient energy was proposed as [131]

$$E^{grad} = \frac{1}{2} \int d\mathbf{x} \sum_{\alpha_1, \alpha_2} \left[ \beta(\alpha_1, \alpha_2)_{ijkl} \frac{\partial b(\alpha_1, \mathbf{x})_i}{\partial x_j} \frac{\partial b(\alpha_2, \mathbf{x})_k}{\partial x_l} \right] \quad (4.9)$$

where  $\beta(\alpha_1, \alpha_2)_{ijkl}$  are the components of a multi-dimensional fourth-rank tensor which provides the vanishing surface energy of the slipped regions along interfaces parallel to the slip planes and  $\mathbf{b}(\alpha, \mathbf{x})$  is the total Burgers vector in the slip plane of  $\alpha$ . In [131], Eq.(4.9) has been approximated for an fcc crystal as

$$E^{grad} = \frac{\beta}{2} \int d\mathbf{x} \Phi(\mathbf{x}) \quad (4.10)$$

where  $\beta$  is a positive constant and  $\Phi(\mathbf{x})$  is given by

$$\begin{aligned} \Phi(\mathbf{x}) = & \left( \mathbf{n}_{(111)} \times \nabla \eta_{(111)}^{[\bar{1}\bar{1}0]} + \mathbf{n}_{(\bar{1}\bar{1}1)} \times \nabla \eta_{(\bar{1}\bar{1}1)}^{[\bar{1}\bar{1}0]} \right)^2 + \left( \mathbf{n}_{(111)} \times \nabla \eta_{(111)}^{[0\bar{1}\bar{1}]} + \mathbf{n}_{(1\bar{1}\bar{1})} \times \nabla \eta_{(1\bar{1}\bar{1})}^{[0\bar{1}\bar{1}]} \right)^2 \\ & + \left( \mathbf{n}_{(111)} \times \nabla \eta_{(111)}^{[10\bar{1}]} + \mathbf{n}_{(\bar{1}1\bar{1})} \times \nabla \eta_{(\bar{1}1\bar{1})}^{[10\bar{1}]} \right)^2 + \left( \mathbf{n}_{(1\bar{1}\bar{1})} \times \nabla \eta_{(1\bar{1}\bar{1})}^{[\bar{1}\bar{1}0]} + \mathbf{n}_{(\bar{1}1\bar{1})} \times \nabla \eta_{(\bar{1}1\bar{1})}^{[\bar{1}\bar{1}0]} \right)^2 \\ & + \left( \mathbf{n}_{(1\bar{1}\bar{1})} \times \nabla \eta_{(1\bar{1}\bar{1})}^{[101]} + \mathbf{n}_{(\bar{1}\bar{1}1)} \times \nabla \eta_{(\bar{1}\bar{1}1)}^{[101]} \right)^2 + \left( \mathbf{n}_{(\bar{1}1\bar{1})} \times \nabla \eta_{(\bar{1}1\bar{1})}^{[0\bar{1}\bar{1}]} + \mathbf{n}_{(\bar{1}\bar{1}1)} \times \nabla \eta_{(\bar{1}\bar{1}1)}^{[0\bar{1}\bar{1}]} \right)^2 \end{aligned} \quad (4.11)$$

In the above equation  $\eta(\alpha, m_\alpha, \mathbf{x})$  is specified for each slip system and  $\mathbf{x}$  is omitted for short notation. Eqs.(4.10) and (4.11) show that the gradient energy is associated with the gradient of  $\eta$ , which assumes significant values only within the core regions where  $\eta$  changes from one integer to another. Thus the gradient energy is part of the core energy. Although the use of gradient energy for characterizing dislocation cores is, in principle, similar to the way that interfaces are described in the gradient thermodynamics of phase transformations, two essential new ingredients have been

<sup>12</sup>Take  $\lim_{\eta \rightarrow 0} d^2(A \sin^2 \pi \eta)/d\epsilon^2 \equiv \mu$ , where  $\epsilon^0 \equiv b/d$

introduced in Eq.(4.10). First of all, it is proportional to the length of the dislocation lines rather than to the area of the slipped regions. This is achieved by the  $(\mathbf{n} \times \nabla\eta)^2$  terms in Eq.(4.11) ( $\mathbf{n} \times \nabla\eta$  in fact gives the direction of the dislocation line, i.e., the sense vector). Secondly, it takes into account the rules of core-core interactions such as the cancellation of two dislocations of identical Burgers vector but opposite sense. However, as will be shown later, Eq.(4.11) is insufficient to account for all the core-core interactions among dislocations in an fcc crystal, for instance, it does not describe the core-core interactions among perfect dislocations on the same slip plane.

The elastic energy associated with long-range elastic interactions among dislocations of arbitrary configurations is calculated using the linear elasticity theory of Khachaturyan and Shatalov reviewed in Section 2.5. The theory was formulated for an arbitrary distribution of precipitates of arbitrary geometry in an elastically anisotropic media. To apply it to dislocations, one needs just to replace the stress-free transformation strain by the eigenstrain of dislocations given by Eq.(4.2) [131].

Among the three constituent terms in the total energy (Eq.(4.4)), the crystalline and gradient energies assume significant values only within the core regions while the elastic energy (from linear elasticity) has finite values throughout the entire crystal. The equilibrium profile of  $\eta$  across the core region defines the core structure and width. It is determined by minimization of the total energy of the system.

### 4.2.2 Limitations

The general framework of the phase field approach to dislocation plasticity formulated in [129, 131] provides new opportunities for computer modeling of the collective

motion of dislocations of arbitrary configurations and dislocation-precipitate interactions. However, the general form of the crystalline energy proposed in [129] does not include all necessary degrees of freedom. For a given crystal (and thus  $\mathbf{H}$ ) the integrand in Eq.(4.6) is formulated as a function of the total local Burgers vector,  $\mathbf{b}(\mathbf{x})$ . This implies that slip operations between two crystal halves on *any* slip plane that parallel to a given Burgers vector are indistinguishable in the crystalline energy, which is physically unjustified. Specifically, if we consider two field variables,  $\eta_1$  and  $\eta_2$ , that correspond to two slip systems with identical Burgers vector. The crystalline energy will remain identical for any combination of  $\eta_1$  and  $\eta_2$  as long as their sum (and therefore the total Burgers vector, given by Eq.(4.7)) is constant. This problem, for example, results in a failure in simulating dislocation cross-slip. In examining the simplified form of the crystalline energy, Eq.(4.8), we find the same problem does not exist. Thus Eqs.(4.6) and (4.8) do not constitute a rigorous relation as general/special forms. They clearly contain different assumptions.

The particular forms of the crystalline energy and the gradient energy, i.e., Eqs.(4.8) and (4.10), also have certain limitations. They do not always correctly describe reactions among dislocations. Consider in Fig. 4.3, for example, two dislocations gliding on a (111) plane in an fcc crystal with Burgers vectors  $\mathbf{b}_1 = a[0\bar{1}1]/2$  and  $\mathbf{b}_2 = a[10\bar{1}]/2$ , respectively ( $a$  being the lattice parameter). If two segments (labeled 1 and 2 in Fig. 4.3) from the two dislocation lines run into each other, they should react and form a single dislocation segment with Burgers vector  $-\mathbf{b}_3 = \mathbf{b}_1 + \mathbf{b}_2$  (segment 3) because this results in a lower energy ( $\mu b_3^2 < \mu b_1^2 + \mu b_2^2$ ). The line energy of segment 3 should be identical to the line energy of either segment 1 or 2 since  $b_1^2 = b_2^2 = b_3^2$ . According to Eq.(4.8) and Eq.(4.10), however, the gradient energy and

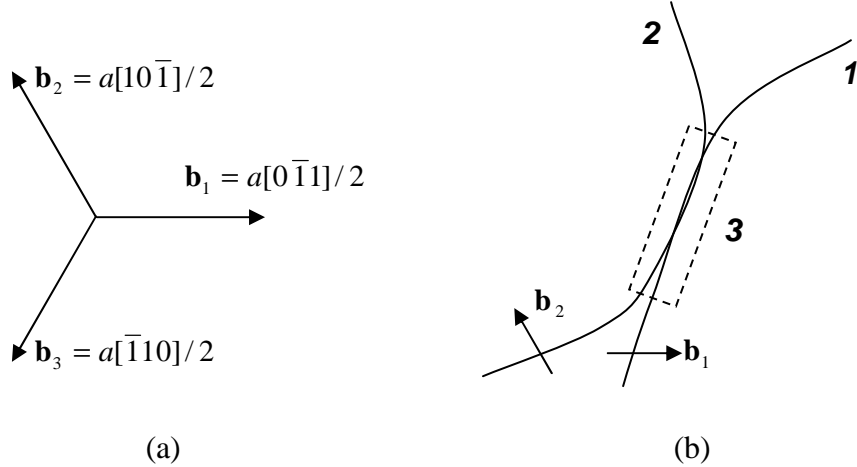


Figure 4.3: (a) Burgers vector relationship among perfect dislocations on (111) slip planes in an fcc crystal; (b) As two dislocations with  $\mathbf{b}_1$  and  $\mathbf{b}_2$  encounter (in the dashed box) they form a new dislocation with  $-\mathbf{b}_3$ , which follows the Burgers vector relationship in (a).

the crystalline energy do not meet this condition. The gradient energy of segment 3 is given by

$$\Phi(\mathbf{x}) = \left( \mathbf{n}_{(111)} \times \nabla \eta_{(111)}^{[0\bar{1}1]} \right)^2 + \left( \mathbf{n}_{(111)} \times \nabla \eta_{(111)}^{[10\bar{1}]} \right)^2$$

which is twice of that of either segment 1 or 2. Similarly, the crystalline energy for segment 3 is, according to Eq.(4.8), given by

$$E^{crys} = \int d\mathbf{x} A \left( \sin^2 \pi \eta_{(111)}^{[0\bar{1}1]} + \sin^2 \pi \eta_{(111)}^{[10\bar{1}]} \right)$$

which is also twice of the crystalline energy of either segment 1 or 2.

It is clear that both the crystalline energy and the gradient energy of segment 3 yield twice as much of the values that they are supposed to be. As a consequence, this will result in a different reaction as two dislocation lines with  $\mathbf{b}_1$  and  $\mathbf{b}_2$  meet

each other. Below we derive new expressions to account for such reactions. Although the approach is general, we choose an fcc crystal for the convenience of discussion.

### 4.2.3 Extension and generalization

The difficulty encountered in the original general form of the crystalline energy, Eq.(4.6), is owing to the fact that a slip operation described previously requires four degrees of freedom, among which two define the slip plane normal and the remaining two define the Burgers vector in the plane, in contrast to the three degrees of freedom solely provided by the Burgers vector in Eq.(4.6). For this reason, Eq.(4.6) is only valid when the missing one degree of freedom (belonging to the slip plane) is specified. Pursuing along the same line, we imagine that a general deformation to the crystal due to dislocations may consist of more than one slip operation, for example, near two intersected dislocations from different slip planes. The consequence, however, may not necessarily be possible to describe in terms of an equivalent slip operation, because superposition of two slips (simple shears) does not always give a third slip (simple shear). Therefore it appears that a general form of the crystalline energy may require even more degrees of freedom in its parameter. One apparently suitable solution is to express it as a function of a strain tensor

$$E^{crys} = \int d\mathbf{x} f(\boldsymbol{\varepsilon}^s(\mathbf{x})) \quad (4.12)$$

where the general strain tensor is a sum of the simple shear strains associated with all contributing slip systems, i.e.,

$$\varepsilon_{ij}^s(\mathbf{x}) = \sum_{\alpha, m_\alpha} \varepsilon_{ij}^{ss}(\alpha, m_\alpha) \eta(\alpha, m_\alpha, \mathbf{x}) \quad (4.13)$$

and the simple shear strain tensor,  $\boldsymbol{\varepsilon}^{ss}(\alpha, m_\alpha)$  is given by

$$\varepsilon_{ij}^{ss}(\alpha, m_\alpha) \equiv n_i(\alpha) b_j(\alpha, m_\alpha) / d(\alpha) \quad (4.14)$$

The exact mathematical expression of this construction for a general case remains unsolved at this moment. Nevertheless two properties of Eq.(4.12) can be briefly described here. First,  $f(\boldsymbol{\varepsilon}^s(\mathbf{x}))$  is a periodic function and reaches a local minimum when  $\boldsymbol{\varepsilon}^s$  possess some special crystallographic value – for simple shear when the slip displacement coincides lattice translation and the slip plane is on a rational plane. The energy degeneracy coincides the crystal symmetry. Second, when the deformation reduces to a simple shear (or slip) the crystalline energy is projected to the corresponding slip plane, where it collapses to a  $\gamma$ -surface (divided by the interplanar distance).

To detail this idea we may consider a simpler case in which dislocations glide and react on the  $\{111\}$  slip planes in an fcc crystal. We limit our discussion on the crystalline energy to the specific form involving only the  $\{111\}$  slip planes. Since any arbitrary linear combination of simple shears on the same slip plane is still a simple shear, the crystalline energy for this particular slip plane can be formulated as a function of the total Burgers vector on that slip plane.

As mentioned earlier, the field variable,  $\eta(\alpha, m_\alpha, \mathbf{x})$ , represents the amount of relative shear of the two parts of a crystal above and below a slip plane at an arbitrary position  $\mathbf{x}$ . However this description is not unique. As shown in Fig.4.4, for example, there are three types of perfect dislocations on a  $(111)$  plane characterized by their Burgers vectors  $\mathbf{b}_1$ ,  $\mathbf{b}_2$  and  $\mathbf{b}_3$ . Let us use  $\eta_1$ ,  $\eta_2$ , and  $\eta_3$  to represent each of them. Since the sum of the Burgers vectors of any two dislocations equals to the negative of the Burger vector of the remaining one, a slip characterized by  $-\mathbf{b}_3$  can be represented

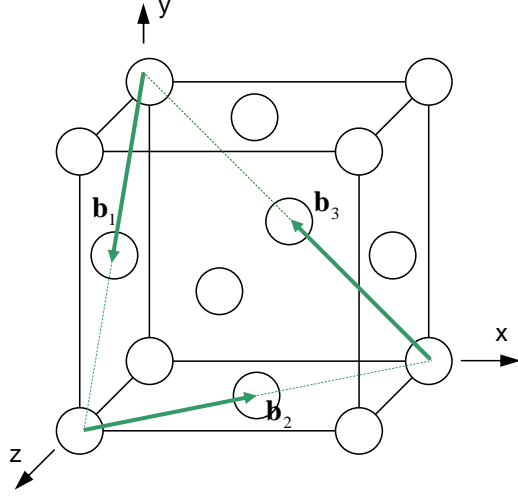


Figure 4.4: The Burgers vectors of the three types of perfect dislocations on the (111) slip plane of an fcc crystal.

either by  $(\eta_1 = \eta_2 = 0, \eta_3 = -1)$ , or equivalently by  $(\eta_1 = \eta_2 = 1, \eta_3 = 0)$ . In the specific form given by Eq.(4.8) such degeneration is not considered, e.g., there is no coupling among different  $\eta_i$ . This limitation can be removed if one considers the total Burgers vector resulted from all  $\eta$ , as defined in Eq.(4.7), rather than the individual Burgers vectors characterized by  $\eta_i$  as the independent variable.

For the convenience of discussion, we consider the Burgers vector field at  $\mathbf{x}$ . Its value differs from the shear strain by the interplanar distance that is constant for  $\{111\}$  planes. It is characterized by a combination of  $\eta$  and its Burgers vector. For example, according to Eq.(4.7) the total Burgers vector,  $\mathbf{b}(\mathbf{x})$ , cause by glide of perfect dislocations on the (111) plane shown in Fig. 4.4 is given by

$$\mathbf{b}(\mathbf{x}) = \eta_1(\mathbf{x})\mathbf{b}_1 + \eta_2(\mathbf{x})\mathbf{b}_2 + \eta_3(\mathbf{x})\mathbf{b}_3 \quad (4.15)$$

Substituting into Eq.(4.15) the Burgers vectors

$$\mathbf{b}_1 = (a/2)(\hat{\mathbf{z}} - \hat{\mathbf{y}}), \quad \mathbf{b}_2 = (a/2)(\hat{\mathbf{x}} - \hat{\mathbf{z}}), \quad \mathbf{b}_3 = (a/2)(\hat{\mathbf{y}} - \hat{\mathbf{x}})$$

which are expressed in the coordinate system defined in Fig. 4.4, where  $\hat{\mathbf{x}}, \hat{\mathbf{y}}, \hat{\mathbf{z}}$  are unit vectors of the coordinate system, one finds

$$\mathbf{b}(\mathbf{x}) = [(\eta_2(\mathbf{x}) - \eta_3(\mathbf{x}))\hat{\mathbf{x}} + (\eta_3(\mathbf{x}) - \eta_1(\mathbf{x}))\hat{\mathbf{y}} + (\eta_1(\mathbf{x}) - \eta_2(\mathbf{x}))\hat{\mathbf{z}}]a/2 \quad (4.16)$$

A simple continuum function that bears the fcc crystal symmetry can be formulated from the periodical potential given by Eq.(4.6). Consider, for example, only the nearest reciprocal lattice vector of an fcc lattice,  $\{111\}$ , and express the continuum total Burgers vector as  $\mathbf{b} = (ax, ay, az)$  where  $a$  is the lattice parameter, one obtains

$$f(\mathbf{b}) = f(x, y, z) = (1 - \cos 2\pi x \cos 2\pi y \cos 2\pi z)/2$$

where  $f(x, y, z)$  is normalized to  $[0, 1]$  and its minima are located at the fcc lattice sites. Substituting  $x, y$  and  $z$  by the corresponding components of the total Burgers vector in Eq.(4.16), i.e.,  $x = \eta_2 - \eta_3$ ,  $y = \eta_3 - \eta_1$ ,  $z = \eta_1 - \eta_2$ , and adding an appropriate leading coefficient in order to fit to the shear modulus at small strain limit, one obtains the crystalline energy for the  $(111)$  slip plane

$$E^{crys} = \int d\mathbf{x} A [1 - \cos \pi(\eta_2 - \eta_3) \cos \pi(\eta_3 - \eta_1) \cos \pi(\eta_1 - \eta_2)] \quad (4.17)$$

It is readily to verify that Eq.(4.17) gives the identical crystalline energy of a dislocation in the two equivalent representations ( $\eta_1 = \eta_2 = 1, \eta_3 = 0$ ) and ( $\eta_1 = \eta_2 = 0, \eta_3 = -1$ ). It reduces to Eq.(4.8) if the dislocation is expressed by a single  $\eta$ , e.g., ( $\eta_1 = \eta_2 = 0, \eta_3 = -1$ ).

Figure 4.5 shows a contour plot of the integrand in Eq.(4.17) on the  $(111)$  plane. As

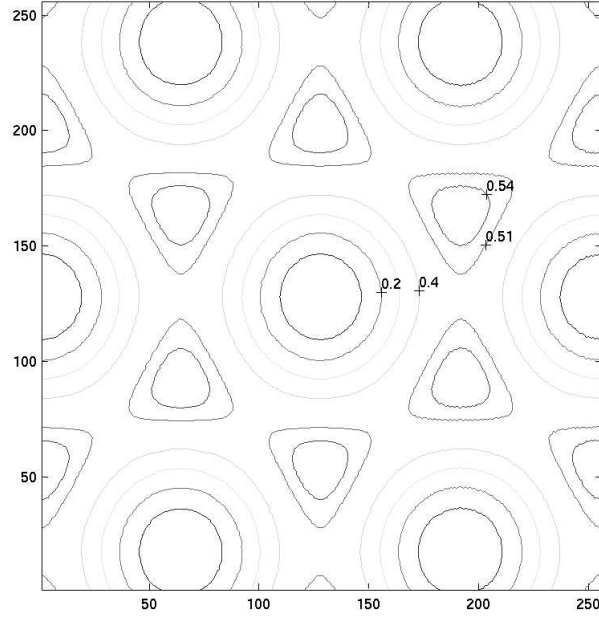


Figure 4.5: A contour plot of the crystalline energy density (given by the integrand in Eq.(4.17)) projected on the (111) plane. The minima are located at the centers of the circular contours and they correspond to the lattice sites of an fcc crystal. This construction reflects the equivalence of representing a slip by either  $(\eta_1 = \eta_2 = 1, \eta_3 = 0)$  or  $(\eta_1 = \eta_2 = 0, \eta_3 = -1)$ .

can be seen, the particular crystalline energy given by Eq.(4.17) does not correspond to a typical  $\gamma$ -surface of the (111) plane of fcc crystal. In fact the maximum and the minimum are reversed in Fig. 4.5. The purpose is purely to simplify our problem by avoiding dissociation of a perfect dislocation. Using  $\gamma$ -surface for the crystalline energy will be demonstrated in Section 4.4 in simulation of partial dislocation.

Note that the crystalline energy given by Eq.(4.17) is formulated for a single (111) slip plane. To derive a more general expression including all 12 slip systems of an fcc crystal, one has to consider the contribution from interplanar potentials of all relevant slip planes and their mutual coupling. As the simplest approximation, we employ the following linear superposition

$$E^{crys} = \int d\mathbf{x} A [4 - \cos \pi(\eta_{(111)}^{[01\bar{1}]} - \eta_{(111)}^{[\bar{1}01]}) \cos \pi(\eta_{(111)}^{[\bar{1}01]} - \eta_{(111)}^{[1\bar{1}0]}) \cos \pi(\eta_{(111)}^{[1\bar{1}0]} - \eta_{(111)}^{[01\bar{1}]}) \\ - \cos \pi(\eta_{(1\bar{1}\bar{1})}^{[0\bar{1}1]} - \eta_{(1\bar{1}\bar{1})}^{[\bar{1}0\bar{1}]}) \cos \pi(\eta_{(1\bar{1}\bar{1})}^{[\bar{1}0\bar{1}]} - \eta_{(1\bar{1}\bar{1})}^{[110]}) \cos \pi(\eta_{(1\bar{1}\bar{1})}^{[110]} - \eta_{(1\bar{1}\bar{1})}^{[0\bar{1}1]}) \\ - \cos \pi(\eta_{(\bar{1}1\bar{1})}^{[011]} - \eta_{(\bar{1}1\bar{1})}^{[10\bar{1}]}) \cos \pi(\eta_{(\bar{1}1\bar{1})}^{[10\bar{1}]} - \eta_{(\bar{1}1\bar{1})}^{[\bar{1}10]}) \cos \pi(\eta_{(\bar{1}1\bar{1})}^{[\bar{1}10]} - \eta_{(\bar{1}1\bar{1})}^{[011]}) \\ - \cos \pi(\eta_{(\bar{1}\bar{1}1)}^{[0\bar{1}\bar{1}]} - \eta_{(\bar{1}\bar{1}1)}^{[\bar{1}01]}) \cos \pi(\eta_{(\bar{1}\bar{1}1)}^{[\bar{1}01]} - \eta_{(\bar{1}\bar{1}1)}^{[\bar{1}10]}) \cos \pi(\eta_{(\bar{1}\bar{1}1)}^{[\bar{1}10]} - \eta_{(\bar{1}\bar{1}1)}^{[0\bar{1}\bar{1}]})] \quad (4.18)$$

It can be verified that energy barriers exist in Eq.(4.18) for dislocation cross-slip owing to the simple linear superposition. A quantitative description of this barrier, nevertheless, may require high order terms that characterize the coupling among the interplanar potential of intersecting slip planes.

As part of the core energy, the gradient energy term is required to obey all the rules for core-core interactions. Even though a general definition of the gradient term has been given in Eq.(4.9), it appears difficult to determine for a specific case all the coefficients of the forth-rank tensor,  $\beta(\alpha_1, \alpha_2)_{ijkl}$ . These coefficients should

characterize all the Burgers vector relationships following Frank's rule. There is no discussion in [129, 131] on how to construct such a forth-rank tensor in general, nor on how to link the explicit form of the gradient energy term for fcc crystals given by Eq.(4.10) to this general definition in particular. Below we derive a more detailed general form of the gradient energy from a different point of view, e.g., we consider the total Burgers vector dependence of dislocation line energy.

Again, let's consider the equivalence of the phase field representations of an identical dislocation by either  $(\eta_1 = \eta_2 = 1, \eta_3 = 0)$  or  $(\eta_1 = \eta_2 = 0, \eta_3 = -1)$  as mentioned earlier. The gradient energy must yield the same value for these representations. According to the Burgers vector relationship:  $\mathbf{b}_1 + \mathbf{b}_2 = -\mathbf{b}_3$  and taking into account the fact that the energy depends on  $b^2$ , we may express the gradient energy by either  $(\mathbf{b}_1 + \mathbf{b}_2)^2$  or  $(\mathbf{b}_3)^2$ , depending on the choice of the representation. Because the characteristics of a dislocation is determined by both its Burgers vector and its sense vector, a full expression of the gradient term should include the sense vector, i.e.,  $\mathbf{n} \times \nabla \eta$  as well. As a result, the gradient energy term involving two dislocations can be written as

$$\Phi(\mathbf{x}) = \mathbf{b}_1^2(\mathbf{n}_1 \times \nabla \eta_1)^2 + \mathbf{b}_2^2(\mathbf{n}_2 \times \nabla \eta_2)^2 + 2\mathbf{b}_1 \cdot \mathbf{b}_2(\mathbf{n}_1 \times \nabla \eta_1) \cdot (\mathbf{n}_2 \times \nabla \eta_2) \quad (4.19)$$

It is straightforward to verify that this equation satisfies the annihilation condition of two dislocations with the same Burgers vector but opposite sense vector. In the case shown in Fig. 4.3, where  $\mathbf{b}_1 + \mathbf{b}_2 \rightarrow -\mathbf{b}_3$  takes place, the last term in Eq.(4.19) cancels one of the first two terms and results in an identical energy if the configuration were represented in terms of  $-\eta_3$  instead.

A formulation including reactions among all three Burgers vectors in the (111) plane can be written as

$$\begin{aligned}\Phi(\mathbf{x}) = & \mathbf{b}_1^2(\mathbf{n} \times \nabla \eta_1)^2 + \mathbf{b}_2^2(\mathbf{n} \times \nabla \eta_2)^2 + \mathbf{b}_3^2(\mathbf{n} \times \nabla \eta_3)^2 \\ & + 2\mathbf{b}_1 \cdot \mathbf{b}_2 (\mathbf{n} \times \nabla \eta_1) \cdot (\mathbf{n} \times \nabla \eta_2) + 2\mathbf{b}_2 \cdot \mathbf{b}_3 (\mathbf{n} \times \nabla \eta_2) \cdot (\mathbf{n} \times \nabla \eta_3) \\ & + 2\mathbf{b}_3 \cdot \mathbf{b}_1 (\mathbf{n} \times \nabla \eta_3) \cdot (\mathbf{n} \times \nabla \eta_1)\end{aligned}\quad (4.20)$$

Finally Eq.(4.20) can be simply extended to include all 12 Burgers vectors in an fcc crystal

$$E^{grad} = \frac{1}{2} \int d\mathbf{x} \left\{ \sum_{\alpha, m_\alpha} \sum_{\alpha', m_{\alpha'}} \xi(\alpha, m_\alpha, \alpha', m_{\alpha'}) \frac{\mathbf{b}(\alpha, m_\alpha) \cdot \mathbf{b}(\alpha', m_{\alpha'})}{b(\alpha, m_\alpha)b(\alpha', m_{\alpha'})} \right. \\ \left. [\mathbf{n}(\alpha) \times \nabla \eta(\alpha, m_\alpha)] \cdot [\mathbf{n}(\alpha') \times \nabla \eta(\alpha', m_{\alpha'})] \right\} \quad (4.21)$$

where  $\xi(\alpha, m_\alpha, \alpha', m_{\alpha'})$  is a parameter associated with slip systems and reduces to  $\beta$  in Eq.(4.10).

#### 4.2.4 Dimensionless form of energies and equation of motion

As usual, we use dimensionless parameters in phase field simulations. The derivation of the dimensionless parameters from their dimensional counterparts is summarized in Table 3. Note that when the mesh size,  $l_0$ , is chosen other than the interplanar distance of the slip plane, proper modification on each energy term will be necessary [131]. Here we give some more detailed explanation. As shown in Fig. 4.6, a cell filled with  $\eta = 1$  indicates, by definition, a stress-free shear strain in a magnitude of  $b/d$ . When the mesh size equals to the interplanar distance  $d$ , this corresponds to a relative displacement of the top and bottom of the cell by  $l_0 b/d = b$ , and thus the cell marked by  $C$  in Fig. 4.6 contains a single dislocation with Burgers vector  $b$ .

Table 4.1: Scaling factors that reduce each physical parameter into a dimensionless quantity.

Length	Strain/Stress	Energy	Time
$\mathbf{x} = \mathbf{x}^* l_0$	$\epsilon = \epsilon^* b/d$	$f = f^* \mu (b/d)^2$	$t = t^* / [L \mu (b/d)^2]$
$\mathbf{g} = \mathbf{g}^* / l_0$	$C_{ijkl} = C_{ijkl}^* \mu$	$\xi = \xi^* \mu (b/d)^2 l_0^2$	
$\mathbf{b} = \mathbf{b}^* l_0$	$\sigma = \sigma^* \mu b/d$		
$d = d^* l_0$			
$\tilde{\eta}(\mathbf{g}) = \tilde{\eta}^*(\mathbf{g}^*) l_0^3$			
$\nabla = \nabla^* / l_0$			
$\delta/\delta\eta = l_0^{-3} \delta^*/\delta^*\eta$			

If the mesh size is other than  $d$ , the relative displacement becomes  $l_0 b/d \neq b$ , thus the cell  $C$  contains equivalently  $l_0/d$  dislocations each with Burgers vector  $b$ , which is inconsistent to that implied by the definition of  $\eta$ . To resolve this discrepancy,  $E^{crys}$  and  $E^{grad}$  should be divided by  $l_0/d$ . Meanwhile  $E^{elast}$  should be divided by  $(l_0/d)^2$  because it depends on the square of the stress-free strain. After such normalization, the effective number of dislocations in a cell is consistent with the value of  $\eta$ . With these modifications Eq.(4.5) can be written in a dimensionless form

$$\frac{\partial \eta(\alpha, m_\alpha, \mathbf{x}^*, t^*)}{\partial t^*} = -\frac{\delta^*}{\delta^* \eta} \left[ \varphi E^{crys*} + \varphi E^{grad*} + \varphi^2 E^{elast*} + \varphi^2 W^* \right] \quad (4.22)$$

where  $\varphi \equiv d/l_0$ .

### 4.3 Simulation of dislocation networks

Formation of networked dislocations is an important process during plastic deformation of crystalline solids. The characteristic length scale associated with a given dislocation substructure in general depends on the applied stress, temperature, and the history of deformation. Extensive reviews on dislocation patterning can be found in [138, 139]. In particular, the coarsening behavior of dislocation substructures is critical for understanding recovery kinetics and formulating constitutive creep laws [140].

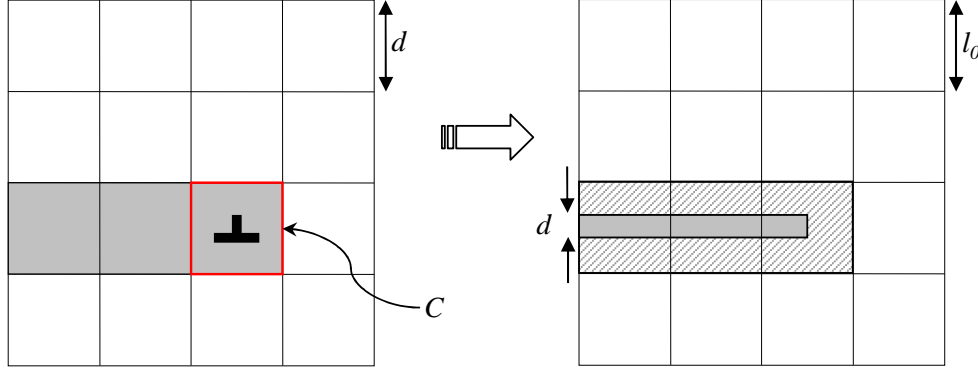


Figure 4.6: Distribution of  $\eta$  values on the cross-section plane of an edge dislocation, where the gray area ( $\eta = 1$ ) represents the slipped region and the white area ( $\eta = 0$ ) represents the unslipped region. Cell  $C$  contains the dislocation core. The right figure corresponds to a larger scale meshing ( $l_0 > d$ , where  $d$  is the interplanar spacing of the slip plane). The shadowed region is the ‘resolvable’  $\eta$  distribution while the actual distribution is indicated by the solid gray region.

Typical phenomena observed in the evolution of a dislocation substructure include the formation and decomposition of nodal points in a dislocation network as a result of mutual interaction among dislocation cores. Below we apply the new formulations of the crystalline and gradient energies to describe dislocation reactions and node formation and decomposition. Following the rules described in Table 4.1 The coefficient in the crystalline energy becomes  $A^* \equiv A/[\mu(b/d)^2] = 1/(2\pi^2)$ . In the following simulations, the gradient coefficient is chosen as  $\xi = 0.4$ , we employ isotropic elastic constants  $c_{11} = 2\mu(1 - \nu)/(1 - 2\nu)$ ,  $c_{12} = 2\mu\nu/(1 - 2\nu)$ , and  $c_{44} = \mu$ , where  $\nu = 0.3$  is the Poisson’s ratio.

### 4.3.1 Two coplanar dislocation loops

Two dislocation loops, with Burgers vector  $\mathbf{b}_1 = a[0\bar{1}1]/2$  and  $\mathbf{b}_3 = a[\bar{1}10]/2$  respectively, are initially placed on a (111) plane and aligned along the [10\bar{1}] direction (Fig. 4.7(a)). Both loops expand under an applied shear stress that is parallel to (111) plane and along the [1\bar{2}1] direction. Fig. 4.7(b) shows the results obtained from the new expressions of the crystalline energy and gradient energy (Eqs.(4.18) and (4.21)). It is shown that when the two dislocation loops meet, the two neighboring segments react and produce a third type dislocation of  $\mathbf{b}_2 = a[10\bar{1}]$ . Simultaneously, two nodal points are formed. Since the applied stress has no resolved component on  $\mathbf{b}_2$ , the new segment remains stationary. These results are different from the ones (Fig. 4.7(c)) following the corresponding equations used in [131] (i.e. Eqs.(4.8), (4.10) and (4.11)). In the latter case, each dislocation loop expands as if the other does not exist. This is not surprising because there is no coupling between the two dislocation loops in these equations.

### 4.3.2 Two dislocation loops from intersecting slip planes

We consider all six Burgers vectors on the (111) and ( $\bar{1}\bar{1}\bar{1}$ ) planes. This allows for any possible interactions among the six slip systems. The initial configuration consists of two loops, one with Burgers vector  $\mathbf{b}_1 = a[0\bar{1}1]/2$  lying on the (111) plane and one with  $\mathbf{b}_2 = a[\bar{1}\bar{1}0]/2$  lying on the ( $\bar{1}\bar{1}\bar{1}$ ) plane (Fig. 4.8(a)). Apply a shear stress

$$\boldsymbol{\tau}^{app} = \tau_0^{app} \begin{pmatrix} 1 & -0.5 & 1 \\ -0.5 & -2 & 0.5 \\ 1 & 0.5 & 1 \end{pmatrix}$$

so that the resolved shear stress on the two loops are identical ( $\tau_0^{app} = 0.04\mu b/d$ ). The two loops expand until their neighboring segments meet at the intersection line of the

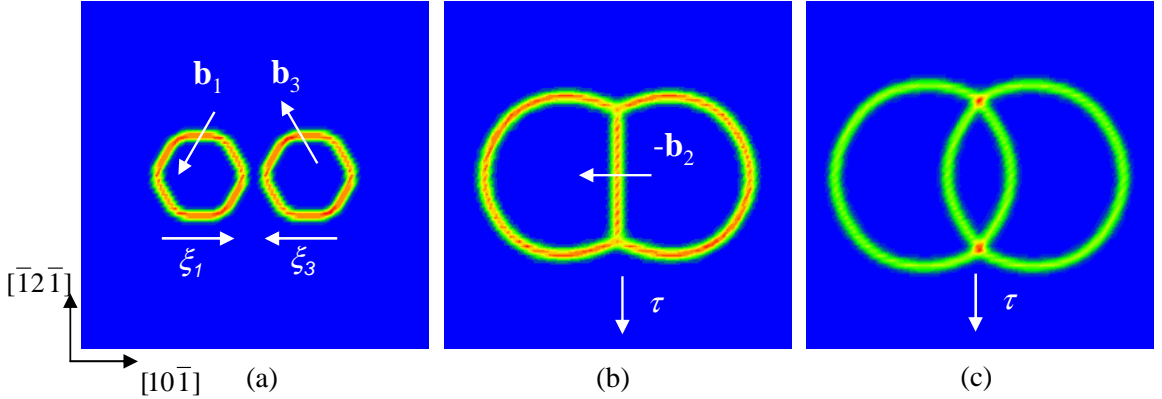


Figure 4.7: Reaction between two dislocation loops on a (111) plane of an fcc crystal: (a) the initial configuration of the loops and their Burgers vectors and sense vectors; (b) the loops expand by the applied shear stress  $\tau$ , react and form a new dislocation segment of Burgers vector  $\mathbf{b}_2$ ; (c) result obtained from the original model, no interaction taking place between the two expanding loops. The relation among the Burgers vectors is defined in Fig.4.4.

two slip planes (oriented in the  $[1\bar{1}0]$  direction). The reaction of the two Burgers vectors (with opposite sense) gives  $a[0\bar{1}1]/2 - a[\bar{1}\bar{1}0]/2 \rightarrow a[101]/2$ .

Since the new Burgers vector formed lies in neither of the two original slip planes, it stays immobile unless the applied stress is sufficiently large to dissociate it into two mobile dislocations. Fig. 4.8(b) shows the formation of the immobile dislocation segment together with two nodal points. Again, the result obtained from the formulations given in [131] does not yield such a reaction between the two loops, as shown in Fig. 4.8(c).

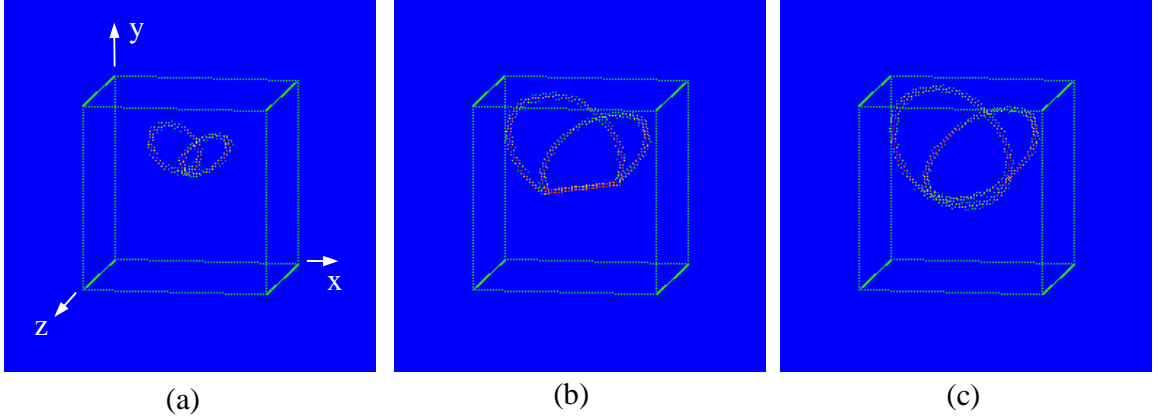


Figure 4.8: Reaction between two dislocation loops from different slip planes: (a) initial configuration with one loop placed on the (111) plane with  $\mathbf{b}_1 = [0\bar{1}1]/2$  and the other on the ( $\bar{1}\bar{1}\bar{1}$ ) plane with  $\mathbf{b}_2 = [\bar{1}\bar{1}0]/2$ ; (b) under the applied stress the two loops expand and react, forming an immobile dislocation segment with  $\mathbf{b}_3 = [101]/2$  which belongs to neither of the initial slip plane; (c) result obtained using the original phase field model, no reaction taking place.

### 4.3.3 Dislocation networks on a single slip plane

A simple dislocation network shown in Fig. 4.9(a) is considered to explore the possible reactions (formation and decomposition of nodes) among different dislocations and the corresponding effect on the network coarsening. It consists of two sets of parallel dislocations with Burgers vectors  $\mathbf{b}_1 = a[0\bar{1}1]/2$  and  $\mathbf{b}_2 = a[10\bar{1}]/2$  lying in a (111) plane. Both are near screw type dislocations. Their sense vectors are indicated in Fig. 4.9(a). The configuration is composed of two identical parts in the horizontal direction due to the use of the periodic boundary condition. According to the schematic diagram shown in Fig. 4.10(a), there are basically two types of nodes (A and B) in the initial network (the other two nodes C and D are equivalent to A and B respectively except that their sense direction is reversed). The reaction at each

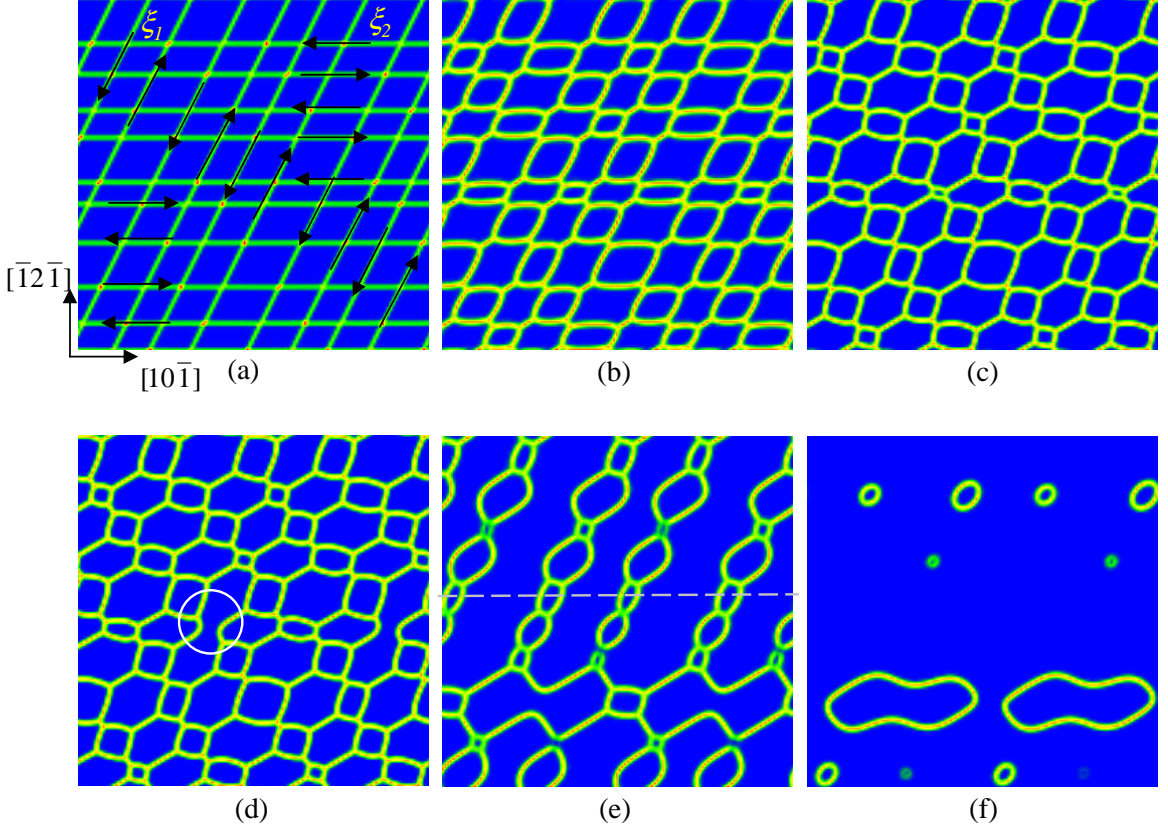


Figure 4.9: Evolution of a dislocation network on a (111) plane. The network consists of two arrays of near screw dislocations of  $\mathbf{b}_1$  and  $\mathbf{b}_2$  that defined in Fig. 4.4. (a) Initial configuration with the sense vectors specified, (b)-(f) the evolution of the network (b)  $t^* = 5$ , (c)  $t^* = 15$ , (d)  $t^* = 18$ , (e)  $t^* = 40$ , (f)  $t^* = 75$ . Note in (d) decomposition of the network starts to occur (see the circle).

node leads to the decomposition of a quadruple junction into two triple junctions, with the formation of a new dislocation segment of Burgers vector  $\mathbf{b}_3 = -\mathbf{b}_1 + \mathbf{b}_2$ ). Geometrically there are two possible reactions at each node, i.e.,  $\mathbf{b}_1 + \mathbf{b}_2$  or  $\mathbf{b}_1 - \mathbf{b}_2$ . However, only the former is energetically favorable. The reactions taking place at the nodes A and B are sketched in Fig. 4.10(b) and 4.10(c), respectively. The temporal evolution of the network produced by the simulation is shown in Fig. 4.9(b-f). Besides

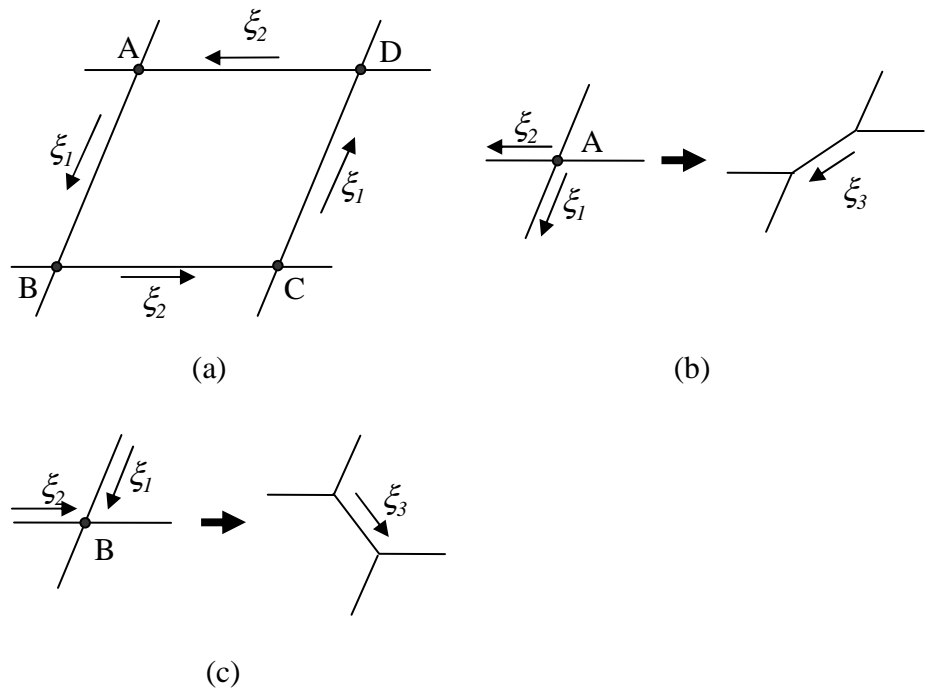


Figure 4.10: The schematic drawing (a) illustrates the two types of the node (A and B) presented in the network in Fig. 4.9. The nodes C and D are equivalent to A and B respectively, except that their sense directions are reversed. (b) and (c) show the nodal reaction at the nodes A and B.

the nodal reactions discussed above, the network appears to be unstable. Destruction of nodal points in a local region (see the circle in Fig.4.9(d)) breaks the network that further decomposes into individual loops and eventually disappears. Fig. 4.11 presents another configuration of the network with the Burgers vectors shown in Fig. 4.11(f). A similar behavior is observed. The decomposition of the networks is attributed to the fact that in both configurations the net Burgers vector of the dislocation network (sum of all Burgers vectors) is zero. This means that a dislocation segment can always find from its neighborhood other segments that cancel its Burgers vector. Stable dislocation networks that frequently observed in experiment (for example, Ref. [141]) may be formed by interaction among arrays of dislocations that yield non-zero net Burgers vector, as well as by various pinning defects, such as dislocation jogs, grain boundaries, precipitates, etc. A difficulty in setting up a network configuration with non-zero net Burgers vector is due to the employed periodic boundary condition, which effectively makes an infinite medium with all dislocation loops confined in each periodically repeated block. A possible solution will be presented in the next section with introduction of free surfaces to the system.

In contrast to the original model where field variables  $\eta(\alpha, m_\alpha)$  within a slipped region away from dislocation cores are integers, corresponding to the lattice displacement being multiples of the Burgers vector, individual  $\eta$  in the extended model may possess non-integral values as seen in Fig. 4.12. Nevertheless the total Burgers vector given by their linear combination (Eq.(4.7)) still equals a multiple of the lattice translation. This characteristic is consistent to the essential idea underlying our extended model that the local densities of  $E^{cryst}$  and  $E^{grad}$  should be given upon a definite physical state determined by all non-zero  $\eta$ s as a whole, rather than the individual

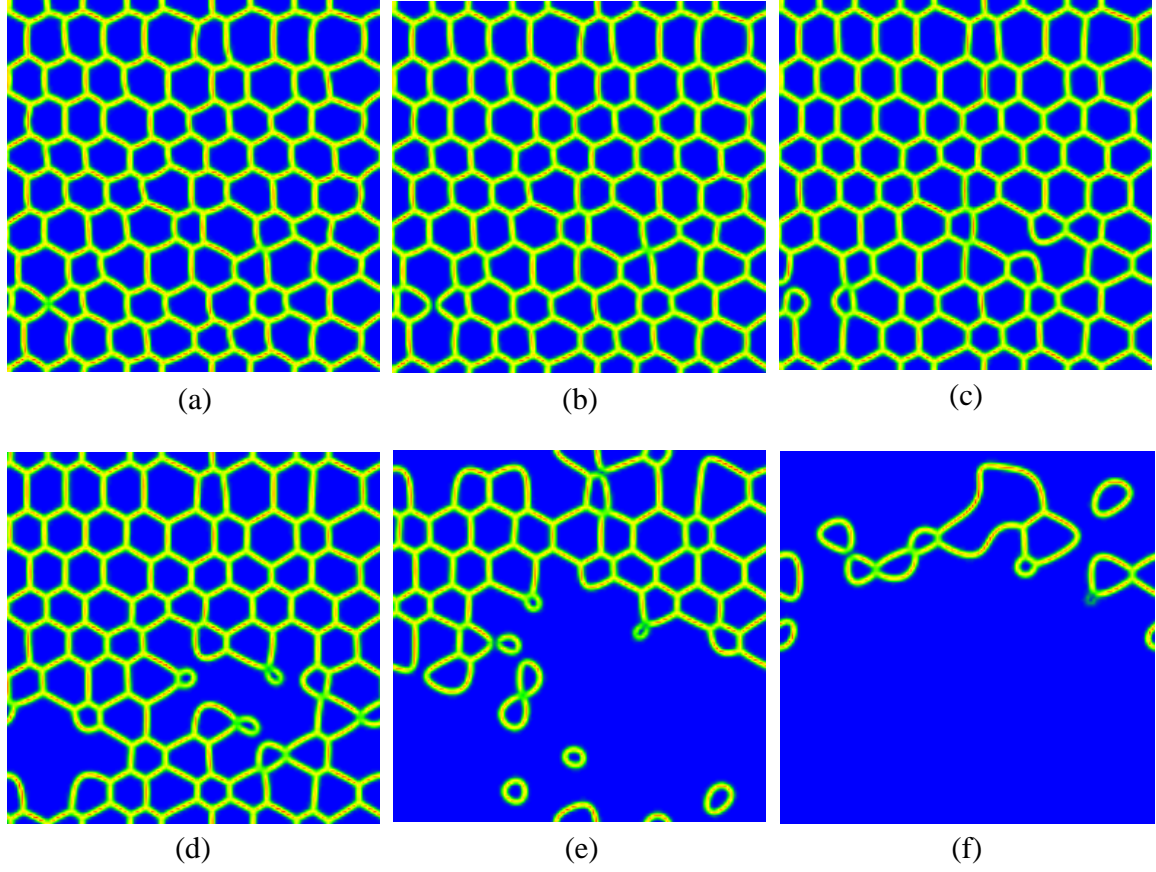


Figure 4.11: Time evolution of a dislocation network on (111) plane consisting of three types of dislocations loops of  $\mathbf{b}_1$ ,  $\mathbf{b}_2$  and  $\mathbf{b}_3$ . (a)  $t^* = 2.5$ , (b)  $t^* = 54$ , (c)  $t^* = 12.5$ , (d)  $t^* = 25$ , (e)  $t^* = 50$ , (f)  $t^* = 75$ , the sense vectors in the same color have the same Burgers vectors.

ones separately. It is also interesting to note in Fig. 4.12 that sharp boundaries exist (marked  $\mathbf{I}$ ) since usually interfaces in the phase field model have to be diffuse in order to have the appropriate interface mobility. A close comparison of the profiles to the total energy density map as shown in Fig. 4.9(e) indicates that these sharp boundaries do not produce any excess energy. Indeed, they are only the boundaries between the two *equivalent* representations of slip, which are physically indistinguishable. Being sharp is dominated by the requirement of vanishing total energy; each energy terms (crystalline, gradient, and elastic) are perfectly cancelled on these boundaries. This is again a manifestation of the fact that the forms of the crystalline and gradient energies introduced in Section 4.2.3 describe correctly the equivalent representations of slip. The boundary marked by  $\mathbf{I}$  in Fig. 4.12 is in fact the initial position of the dislocation (as in Fig. 4.9(a)), and its current position is marked by  $\mathbf{I}'$ .

#### 4.3.4 Dislocation network with free surface

In Section 2.5 we have seen that calculation of elastic energy is considerably simplified with the use of Fourier transforms since the double integral of convolution in real space reduces to a single integral in the reciprocal space, i.e.,

$$\iint_{-\infty}^{+\infty} d\mathbf{x}d\mathbf{x}' W(\mathbf{x} - \mathbf{x}') \phi(\mathbf{x}) \phi(\mathbf{x}') \xrightarrow{\text{Fourier transform}} \int_{-\infty}^{+\infty} d\mathbf{g} \tilde{W}(\mathbf{g}) \tilde{\phi}(\mathbf{g}) \tilde{\phi}^*(\mathbf{g})$$

The current model for dislocation inherits this benefit by employing the phase field microelasticity theory for the elastic interactions among dislocations. Meanwhile, however, the periodic boundary condition necessary to Fourier transform has limited our dislocation configurations. For example, Fig. 4.13 illustrates that three parallel dislocations of same type can be produced by successively increasing the value of  $\eta$  (amount of slip) from left to right. Because of the periodic boundary condition, there

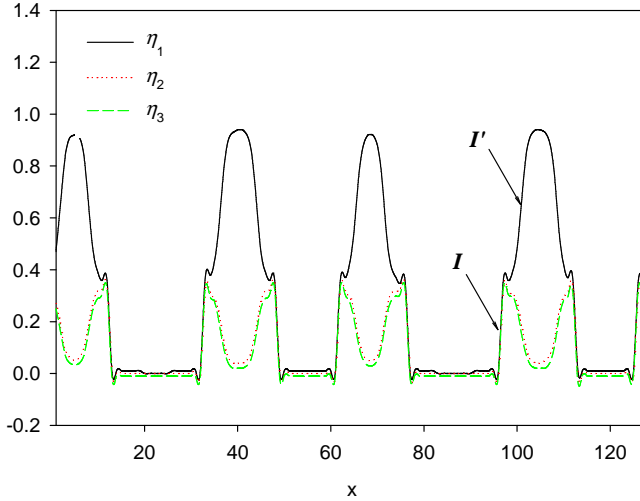


Figure 4.12: Profiles of  $\eta_1$ ,  $\eta_2$ , and  $\eta_3$  along the dashed line in Fig. 4.9(e) indicate the existence of sharp interfaces (marked by  $I$ ). These interfaces are actually the boundary between two equivalent representations of slip and also the initial location of the dislocation lines. The actual present locations are marked by  $I'$ .

is a discontinuity of  $\eta$  at the right hand side boundary, where it changes from 3 to 0. This results in a dislocation of  $3b$  with the opposite sense at the boundary. The much higher line energy ( $9b^2$ ) thus quickly forces the dislocation to decompose into three dislocation each with  $b$  and opposite sense compared to the former three dislocations. Eventually the six dislocations will attract to each other and restore the matrix into an unslipped region.unity of  $\eta$  at the right hand side boundary, where it changes from 3 to 0. This results in a dislocation of  $3b$  with the opposite sense at the boundary. The much higher line energy ( $9b^2$ ) thus quickly forces the dislocation to decompose into three dislocation each with  $b$  and opposite sense compared to the former three dislocations. Eventually the six dislocations will attract to each other and restore the matrix into an unslipped region.

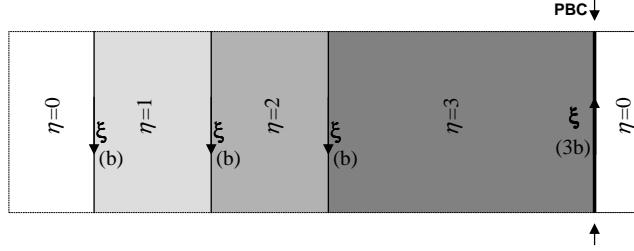


Figure 4.13: A particular distribution of  $\eta$  produces three parallel dislocations of  $b$  in the matrix, while due to the periodic boundary condition, an opposite dislocation of  $3b$  at the right hand side boundary.

Such a process is not unnatural because dislocation never ends inside a crystal, except at various incoherent defects or free surfaces. Nevertheless, since we have been using the coherent microelasticity theory under homogeneous elasticity (constant elastic modulus) assumption, the periodic boundary condition in fact results in an infinite medium and eliminates the possibility for dislocations ending at either internal incoherent defects or the external surface of the crystal. Fortunately, the most recently extension of the microelasticity theory to inhomogeneous elastic modulus [59] enables us to introduce free surfaces, being equivalent for the elasticity, by assigning zero modulus to a certain internal volume.

To explore this possibility, we set up dislocation network with all three slip systems on a (111) plane in a  $256 \times 256 \times 32$  matrix (Fig. 4.14(a)). The initial dislocation network is produced by randomly depositing non-zero  $\eta$ , with progressively higher value from one side of the system to the other, which yields a configuration with non-zero net Burgers vector. To produce free surfaces, we assign zero elastic modulus to a thin layer of 4 grids at the lateral boundaries and a layer of 1 grid at the top and bottom boundaries. Accordingly Eq.(2.91) is used for calculating the elastic energy,

in which the virtual strain field  $\epsilon_{ij}^0(\mathbf{x})$ , treated as a non-conserved field, is obtained through phase field iteration, by following the procedure described in Ref. [59]. The simulated evolution of the random dislocation network is shown in Fig. 4.14(b)-(d). Initially the regions with high energy density are relaxed very quickly. At the later stage (Fig. 4.14(d)) the dislocations develop into a nearly uniform hexagonal network.

#### 4.4 Introducing $\gamma$ -surface to crystalline energy

As proposed in Section 4.2.3, the crystalline energy characterizes the potential energy subject to a general plastic strain produced by arbitrary linear combinations of localized simple shear (slip) associated with all possible slip systems characterized by the corresponding field variables,  $\eta(\alpha, m_\alpha, \mathbf{x}, t)$ . As projected to a particular slip plane, the crystalline energy reduces to the interplanar potential which can be described by the  $\gamma$ -surface from various energetic calculations. Accordingly, the crystalline energy can be simply fitted to the  $\gamma$ -surface data so that, similar to the Peierls-Nabarro model, the phase field model can make quantitative analysis on dislocations at atomic scales. A simple way to fit the  $\gamma$ -surface is, by recognizing that the crystalline energy reflects the symmetry of the crystal, to perform Fourier expansion on the corresponding reciprocal vectors. For  $\{111\}$  planes in an fcc crystal for example, by considering the three-fold rotational symmetry the expansion can be

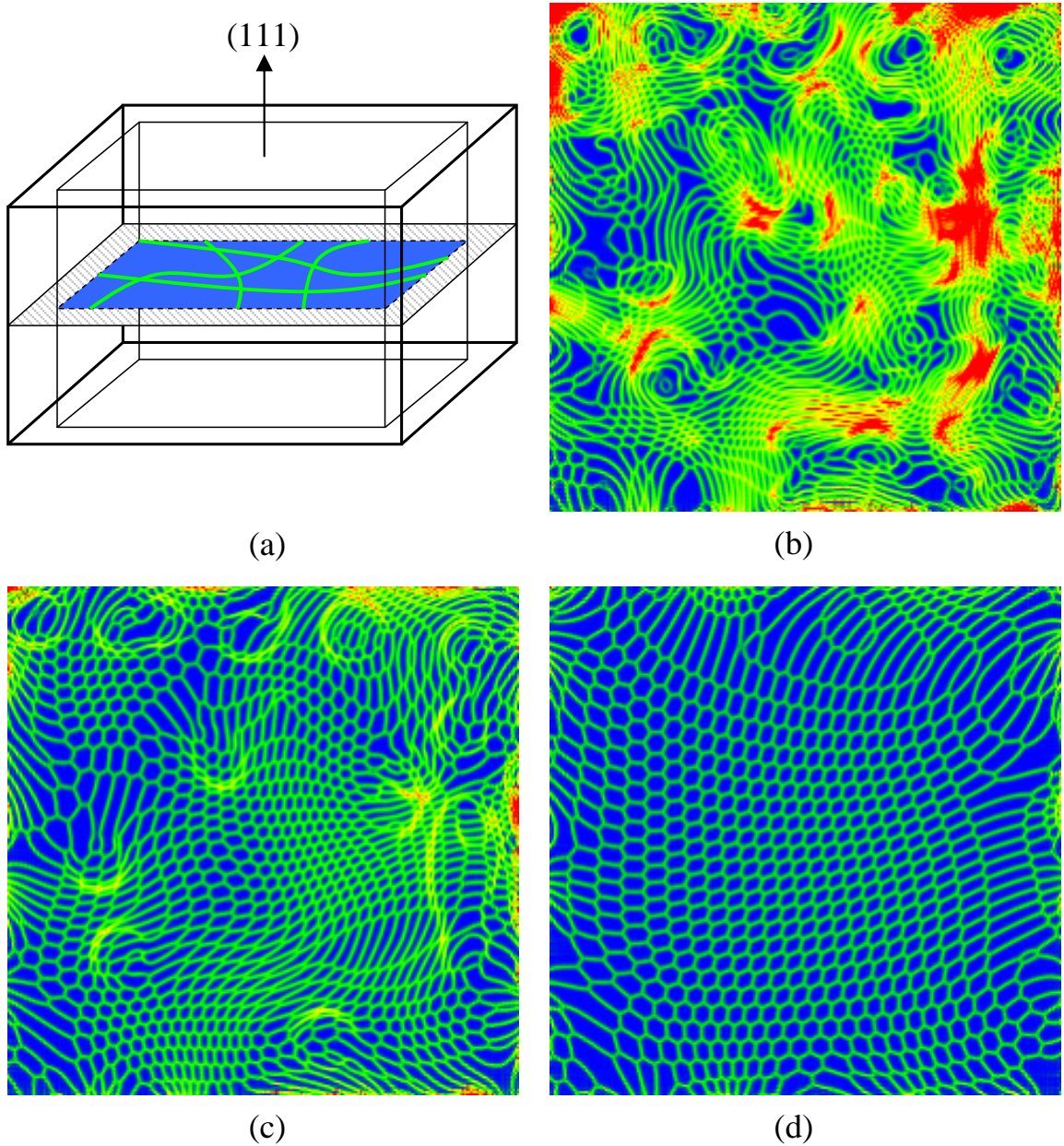


Figure 4.14: Evolution of a random dislocation network with non-zero net Burgers vector. The boundaries are set as free surfaces where elastic stress is zero. The initial configuration is given in (a), and (b)-(d) correspond to reduced time  $t^* = 10, 50, 300$ . The colors from blue, green, to red represent the increasingly higher energy density.

expressed as [116]

$$\begin{aligned}
f(y, z) = & \{ c_0 + c_1 [\cos 2py + \cos(py + qz) + \cos(py - qz)] \\
& + c_2 [\cos 2qz + \cos(3py + qz) + \cos(3py - qz)] \\
& + c_3 [\cos 4py + \cos(2py + 2qz) + \cos(2py - 2qz)] \\
& + c_4 [\cos(py + 3qz) + \cos(-py + 3qz) + \cos(4py + 2qz) + \\
& \quad \cos(-4py + 2qz) + \cos(5py + qz) + \cos(5py - qz)] \\
& + a_1 [\sin 2py - \sin(py + qz) - \sin(py - qz)] \\
& + a_3 [\sin 4py - \sin(2py + 2qz) - \sin(2py - 2qz)] \} / d
\end{aligned} \tag{4.23}$$

where  $y$  and  $z$  are the displacement components along  $[\bar{1}\bar{2}\bar{1}]$  and  $[10\bar{1}]$ , respectively (Fig. 4.15),  $p = 2\pi/(\sqrt{3}b)$ ,  $q = 2\pi/b$ ,  $b = a/\sqrt{2}$  ( $a$  being the lattice parameter) and  $d$  is the interplanar distance. If the field variables  $\eta_1$ ,  $\eta_2$ , and  $\eta_3$  are chosen to correspond to the Burgers vectors  $\mathbf{b}_1$ ,  $\mathbf{b}_2$ , and  $\mathbf{b}_3$  respectively, the latter can be expressed as

$$\mathbf{b}_1 = (-\hat{\mathbf{z}} - \sqrt{3}\hat{\mathbf{y}})b/2, \quad \mathbf{b}_2 = \hat{\mathbf{z}}b, \quad \mathbf{b}_3 = (-\hat{\mathbf{z}} + \sqrt{3}\hat{\mathbf{y}})b/2$$

where  $\hat{\mathbf{y}}$  and  $\hat{\mathbf{z}}$  are the unit vectors along  $[\bar{1}\bar{2}\bar{1}]$  and  $[10\bar{1}]$ , respectively. Again, we can write the total Burgers vector due to the three individual Burgers vectors as

$$\begin{aligned}
\mathbf{b} &= \eta_1 \mathbf{b}_1 + \eta_2 \mathbf{b}_2 + \eta_3 \mathbf{b}_3 \\
&= b \left[ \hat{\mathbf{z}}(-\eta_1/2 + \eta_2 - \eta_3/2) + \hat{\mathbf{y}}(-\sqrt{3}\eta_1/2 + \sqrt{3}\eta_3/2) \right]
\end{aligned}$$

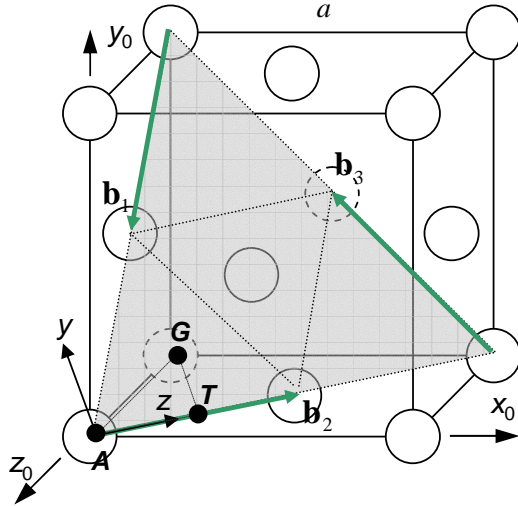


Figure 4.15: The coordinate system  $(y, z)$  chosen on the  $(111)$  slip plane for the  $\gamma$ -surface and its relation to the coordinate system  $(x_0, y_0, z_0)$  of the fcc lattice.  $\mathbf{b}_1$ ,  $\mathbf{b}_2$ , and  $\mathbf{b}_3$  are the three Burgers vectors on the  $(111)$  plane and  $a$  is the lattice parameter. The fitting points  $A$ ,  $G$ , and  $T$  are marked in the graph. Point  $G_1$  is located in the middle of  $A$  and  $G$ . Points  $T_{1-3}$  are uniformly located between  $A$  and  $T$ .

and obtain

$$\begin{aligned} z &= (-\eta_1 + 2\eta_2 - \eta_3)b/2 \\ y &= (-\eta_1 + \eta_3)\sqrt{3}b/2 \end{aligned} \tag{4.24}$$

Substituting Eq.(4.24) into Eq.(4.23) one finds the interplanar potential for a single (111) plane as a function of the field variables,  $\eta_i$

$$\begin{aligned}
f(\eta_1, \eta_2, \eta_3) = & \{ c_0 \\
& + c_1[\cos 2\pi(\eta_1 - \eta_2) + \cos 2\pi(\eta_2 - \eta_3) + \cos 2\pi(\eta_3 - \eta_1)] \\
& + c_2[\cos 2\pi(2\eta_1 - \eta_2 - \eta_3) + \cos 2\pi(2\eta_2 - \eta_3 - \eta_1) + \cos 2\pi(2\eta_3 - \eta_1 - \eta_2)] \\
& + c_3[\cos 4\pi(\eta_1 - \eta_2) + \cos 4\pi(\eta_2 - \eta_3) + \cos 4\pi(\eta_3 - \eta_1)] \\
& + c_4[\cos 2\pi(3\eta_1 - \eta_2 - 2\eta_3) + \cos 2\pi(3\eta_1 - 2\eta_2 - \eta_3) + \\
& \quad \cos 2\pi(3\eta_2 - \eta_3 - 2\eta_1) + \cos 2\pi(3\eta_2 - 2\eta_3 - \eta_1) + \\
& \quad \cos 2\pi(3\eta_3 - \eta_1 - 2\eta_2) + \cos 2\pi(3\eta_3 - 2\eta_1 - \eta_2)] \\
& + a_1[\sin 2\pi(\eta_1 - \eta_2) + \sin 2\pi(\eta_2 - \eta_3) + \sin 2\pi(\eta_3 - \eta_1)] \\
& + a_3[\sin 4\pi(\eta_1 - \eta_2) + \sin 4\pi(\eta_2 - \eta_3) + \sin 4\pi(\eta_3 - \eta_1)]\} / d
\end{aligned} \tag{4.25}$$

The corresponding crystalline energy in the phase field model is then given by

$$E^{crys} = \int d\mathbf{x} f(\eta_1(\mathbf{x}), \eta_2(\mathbf{x}), \eta_3(\mathbf{x})) \tag{4.26}$$

Note that  $\eta_i$  are functions of position  $\mathbf{x}$ . The expansion coefficients  $c_{0-4}$  and  $a_{1,3}$  are obtained by fitting to seven selected points on the  $\gamma$ -surface [116]. The coordinates and the energies are listed in Table 4.2. The coefficients are given in Table 4.3.

## 4.5 Simulation of dislocation dissociation

### 4.5.1 Dissociation of a straight perfect dislocation into two Shockley partials

In this section we calculate the equilibrium core profiles of a straight edge dislocation and a straight screw dislocation for both Al and Pd, with the crystalline energy

Table 4.2: The coordinates of the selected fitting points (Fig. 4.15) on the  $\gamma$ -surface and the corresponding energy.

Point	$(y, z)$	$(\eta_1, \eta_2, \eta_3)$	$f_{\text{Al}}$ (mJ/m <sup>2</sup> )	$f_{\text{Pd}}$ (mJ/m <sup>2</sup> )
$A$	$(0, 0)$	$(0, 0, 0)$	0	0
$T_1$	$a/\sqrt{2}(0, 1/4)$	$(0, 1/4, 0)$	220.0	356.8
$T$	$a/\sqrt{2}(0, 1/2)$	$(0, 1/2, 0)$	378.0	583.7
$G_1$	$a/\sqrt{2}(\sqrt{3}/24, 1/8)$	$(0, 1/6, 1/12)$	79.94	128.4
$G_2$	$a/\sqrt{2}(\sqrt{3}/12, 1/4)$	$(0, 1/3, 1/6)$	172.3	255.8
$G_3$	$a/\sqrt{2}(\sqrt{3}/8, 3/8)$	$(0, 1/2, 1/4)$	176.8	239.4
$G$	$a/\sqrt{2}(\sqrt{3}/6, 1/2)$	$(0, 2/3, 1/3)$	141.7	176.0

The values are given for both the  $(y, z)$  and  $(\eta_1, \eta_2, \eta_3)$ . The energies in the last two columns are for Al and Pd, respectively, obtained from Ref. [102].

Table 4.3: The fitted expansion coefficients in Eq.(4.26) (in unit of mJ/m<sup>2</sup>).

	$c_0$	$c_1$	$c_2$	$c_3$	$c_4$	$a_1$	$a_3$
Al	242.5	-51.65	-39.71	13.68	-1.572	-30.40	-13.72
Pd	374.1	-71.01	-69.62	21.22	-2.644	-54.80	-27.13

for the (111) plane fitted to the corresponding *ab initio* data of the  $\gamma$ -surfaces [102].

The 3D system is uniformly divided into  $1024 \times 128 \times 2$  cubic cells. The initial configuration is a straight perfect dislocation located at the center of the system and oriented along the third dimension. With periodic boundary condition applied in all three dimensions the dislocation extends to infinity. Doubling the first two dimensions yields negligible variation of the profiles of  $\eta(\alpha, m_\alpha, \mathbf{x})$ , indicating that the given system size is sufficiently large that the boundary effect can be practically neglected.  $l_0$  is set to be the interplanar distance  $d$ . Since the variation of the core profiles typically occurs within a few Burgers vectors from the center of the core, to keep the profiles continuous on the discrete grids, the mesh is refined by a factor of 10 along the direction perpendicular to the dislocation line in the slip plane. The energies are normalized accordingly as discussed above. The equilibrium profile of  $\eta(\alpha, m_\alpha, \mathbf{x})$  is

obtained by iteratively solving the kinetic equation (Eq.(4.5)) until the variation of the field variables is no longer observed. This corresponds to the minimum energy state within the accuracy of the simulation. The elastic constants employed are listed in Table 4.4.

Table 4.4: Elastic constants of Al [2] and Pd<sup>1</sup> [3], Pd<sup>2</sup> [4], in unit of ( $\times 10^{10}$ Pa).

	Al	Pd <sup>1</sup>	Pd <sup>2</sup>
$c_{11}$	10.82	22.7	29.28
$c_{12}$	6.13	17.6	19.36
$c_{44}$	2.85	7.17	12.64

Figures 4.16 and 4.17 show the simulated core profiles of Al and Pd, respectively. In both cases the screw dislocations are less dissociated as compared to the edge dislocations. This is because the core profile of a dislocation is determined by the interplay between the elastic energy and the stacking fault energy (SFE) determined by the crystalline energy. While the SFE remains the same for edge and screw dislocations, the relatively smaller elastic energy associated with a screw dislocation (due to the Poisson's ratio) or, equivalently, the relatively weaker repulsive force between the two partials from a screw dislocation results in a less extended core. For the same reason, the core dissociation is more significant in Pd because Pd has smaller value of the normalized SFE than Al. The SFE corresponds to the energy at point  $G$  (Fig. 4.15), normalized by the effective shear modulus that can be calculated from the elastic constant in Table 4.4. For the edge dislocations, the distance between the two dissociated partials is found to be  $2.2b$  for Al and  $3.8b$  for Pd ( $b$  is the magnitude of the Burgers vector of the perfect dislocation), which agree with the estimations by Hartford *et al.* ( $2.15b$  and  $3.85b$ , respectively) using a force-balance equation [102].

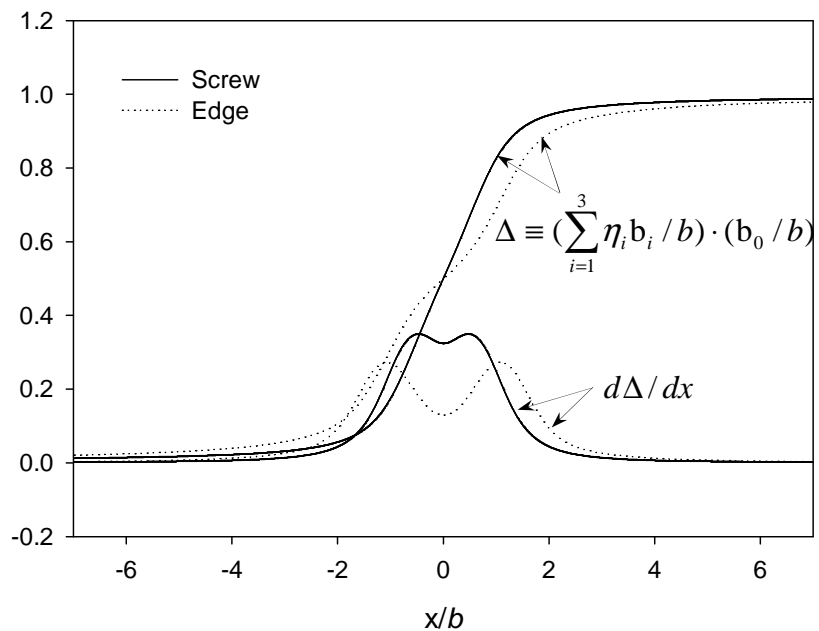


Figure 4.16: The equilibrium core profiles of infinitely long straight dislocations in Al obtained by the phase field simulation. The dotted lines are for an edge dislocation and the solid lines for a screw dislocation.  $\mathbf{b}_0$  is the Burgers vector of the perfect dislocation.

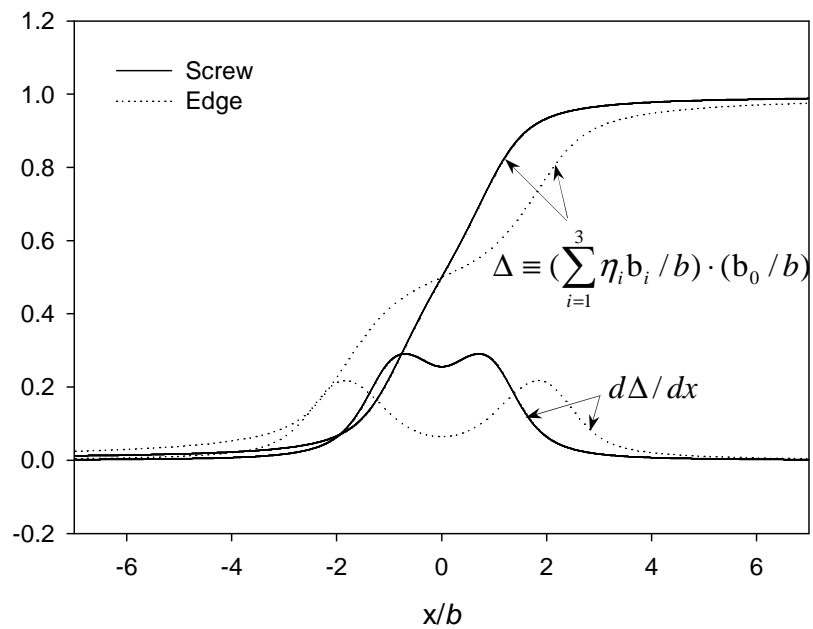


Figure 4.17: The equilibrium core profiles of infinitely long dislocations in Pd obtained by the phase field simulation. The dotted lines are for an edge dislocation and the solid lines for a screw dislocation.  $\mathbf{b}_0$  is the Burgers vector of the perfect dislocation.

More recently von Sydow *et al.* reported a splitting distance of  $17.6\text{\AA}$  (approximately  $6.38b$ ) [4] for Pd. The discrepancy with the value reported in [102] is mainly due to the use of a different set of elastic constants for Pd ( $\text{Pd}^2$  in Table 4.4). This has been confirmed in the phase field simulation, which yields a distance of  $6b$  when the second set of the elastic constants given in Table 4.4 is used.

There are few computational results available in literature for the dissociation of screw dislocations. The phase field model predicts splitting distances of  $0.98b$  for Al and  $1.8b$  for Pd. Teutonico [142] derived a ratio of the splitting distance of an edge dislocation to that of a screw dislocation for a number of pure fcc metals based on the balance between the forces associated with the stacking fault and the elastic interaction. His calculation treats the two partials as line defects and results in a ratio of 2.3 for Al and a ratio of 2.6 for Pd. The phase field results are 2.2 and 2.1, respectively.

The effects of the gradient-energy coefficient  $\xi$  on the core structure are studied for an edge dislocation in Pd. Figure 4.18 shows the difference between the core profiles when the dimensionless values of 0.1 and 0.01 are used for  $\xi^*$ . It can be seen that the change of  $\xi^*$  does modify the profile (both the width and height of the peaks), nevertheless the splitting distance is not altered significantly. This indicates that the splitting distance is mainly determined by the SFE and the elastic interaction, while the gradient term has only local influence on the core profile (e.g., the sharpness of the peaks on the profile).

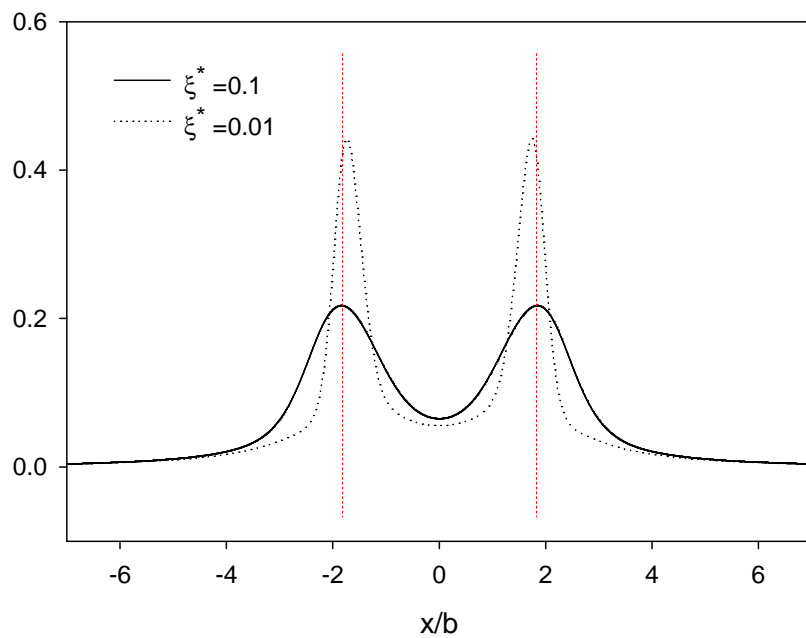


Figure 4.18: Effect of the gradient-energy coefficient  $\xi^*$  on the dislocation core profile. The vertical dashed lines indicate the position of the two partial peaks for  $\xi^* = 0.1$ . Reducing  $\xi^*$  does change the core profile but has little influence on the peak spacing.

#### 4.5.2 Dissociation of dislocation nodes

As shown in Fig. 4.19 three perfect dislocations are initially placed on a (111) plane of Pd. They intersect at a node at the center of the plane. The Burgers vectors are given as  $\mathbf{b}_1 = a[01\bar{1}]/2$ ,  $\mathbf{b}_2 = a[\bar{1}01]/2$ , and  $\mathbf{b}_3 = a[1\bar{1}0]/2$ . Their sense vectors point toward the node. The configuration leads to a dissociation of the three perfect dislocations into three pairs of Shockley partials. Each partial is identified by Thompson's notation [2]. In this configuration each partial has the same Burgers vector as its neighboring partials dissociated from another perfect dislocation. They therefore coalesce and form a single dislocation line, resulting in a stacking fault enclosed by three partial dislocations. Note in the final configuration that the two partials ( $\delta B$  and  $C\delta$ ) dissociated from the dislocation of  $\mathbf{b}_2$  have a smaller spacing than that of the other two pairs. As has been discussed earlier, this is because  $\mathbf{b}_2$  is a screw dislocation and has relatively smaller elastic energy.

The other nodal configuration considered (Fig. 4.20(a)) develops into a contracted node of the three pairs of partials. The line tension tends to pull the partials away from the central nodal point to reduce the total length of the dislocation lines. This reduces the spacing between the dissociated partial pair as compared to the previous case. However a close-up view at the junction (Fig. 4.20(b)) indicates that detachment of the partials from the junction develops a region with a stacking sequence of higher energy. Figures 4.19 and 4.20(a)-(b) actually give a mapping of the crystalline energy density on the slip plane. Figure 4.20(b) shows that the energy at the junction is higher than that in the surrounding stacking faults. This can be verified if one examines the stacking sequence in the individual region (Fig. 4.20(c)). The stacking sequence at the junction become  $acb|bac$  and the associated high stacking fault

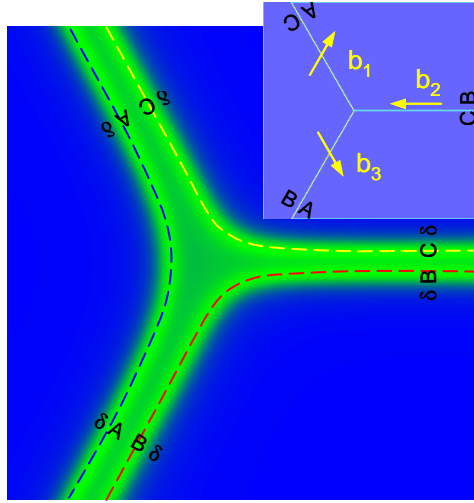


Figure 4.19: Three perfect dislocations initially joined at a node as shown in the inset dissociate into an extended node with partial dislocations enclosing a stacking fault. Thompson notation is used in identifying the partial dislocations. The shade of gray in the plot corresponds to the crystalline energy density ( $f$  in Eq.(4.26)).

energy prevents the partials to move by line tension further away from the junction and therefore stabilizes the entanglement at the junction. Depending on the energy balance, there could be a possibility that this region be replaced by stacking faults with lower energies via nucleation mechanism.

#### 4.5.3 Dissociation of a bent dislocation on two intersecting planes

Stair-rod partial dislocations [143] can be formed by dissociation of a perfect dislocation that bends over two intersecting slip planes. They are highly immobile because of the creation of high-energy fault [2]. This becomes one of the important mechanisms that resist to dislocation motion in fcc crystals. Depending on the two intersecting slip planes and their mutual angles there are various types of stair-rod

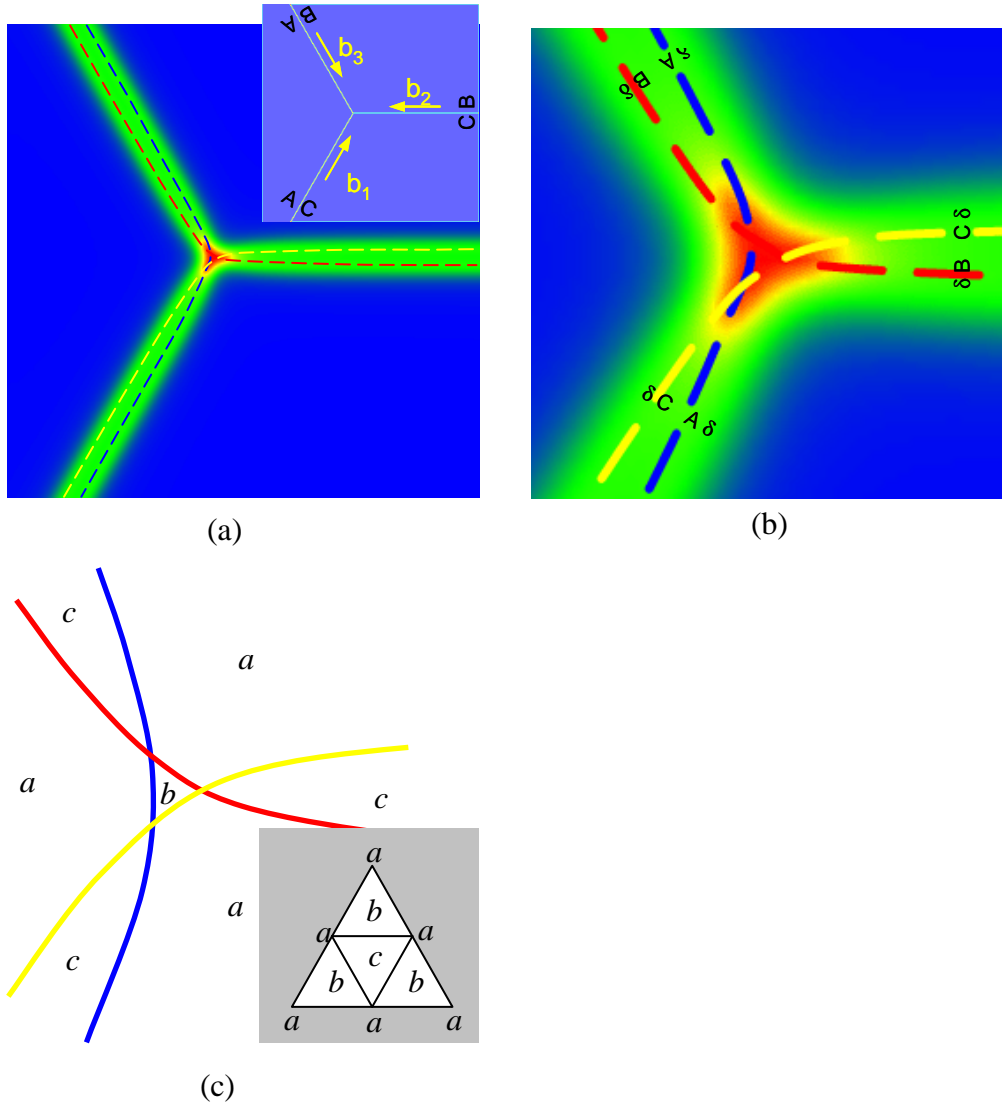


Figure 4.20: Three perfect dislocations initially joined at a node as shown in the inset dissociate into a contracted node (a). Thompson notations are used for the perfect and partial dislocations. A close look at the node (b) reveals a high-energy stacking fault region at the node (e.g., a-c-b-b-a-c stacking sequence), as schematically shown in (c). The size of the node is determined by the balance between the stacking fault energy and the line tension of the partials.

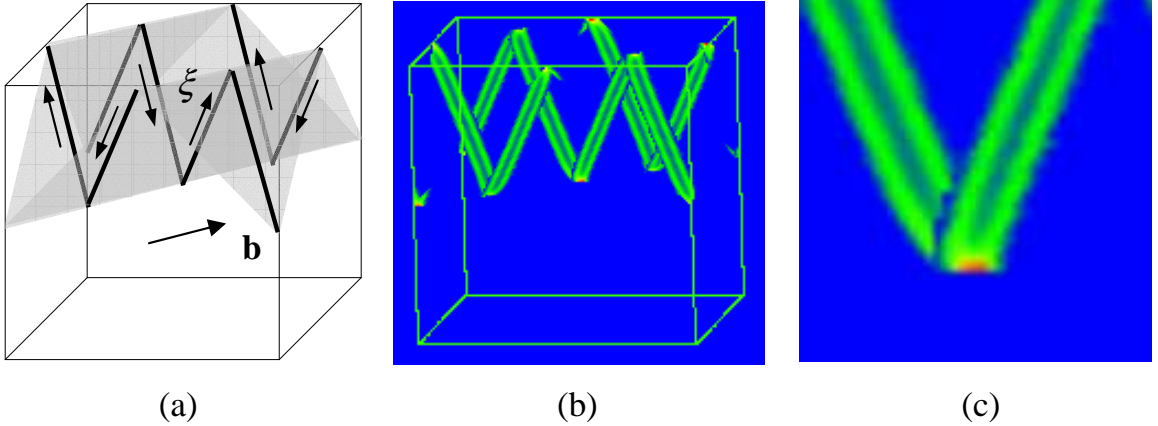


Figure 4.21: A periodic array of perfect dislocations originally lie on the (111) and ( $\bar{1}\bar{1}1$ ) slip planes (a). They have the same Burgers vector  $a[\bar{1}10]/2$  and alternating sense vectors. The dislocations dissociate into Shockley partials (b) and result in stair-rod segments as shown by the enlarged image in (c).

dislocations. The four types of stable configurations are given, for example, by Hirth and Lothe [2]. The first configuration (Fig. 4.21(a)) is chosen for simulation using the phase field model, in which an array (because of the periodic boundary condition) of bent perfect dislocations are placed on the two glide planes (111) and ( $\bar{1}\bar{1}1$ ) with equal spacing. All dislocations have the same Burgers vector  $a[\bar{1}10]/2$  but alternatively opposite sense direction required by the periodic boundary conditions. Figure 4.21(b) gives the configuration after the perfect dislocations are dissociated into partials. A stair-rod partial is formed at the intersection of the two glide planes. The magnified image is shown in Fig. 4.21(c).

## 4.6 Summary

The vision of a glide dislocation loop as a sheared platelet on the slip plane extends the success of phase field description of complex microstructures to dislocations. A

complex dislocation assembly is simply a superposition of individual dislocation loops (or sheared plates). From the original phase field dislocation model we extend and generalize the energy formulations. Crystal symmetry is introduced to both crystalline energy and gradient energy, which is necessary for correctly describing nodal reactions among perfect or partial dislocations. Without any explicit rules, the nodal reactions are driven by the reduction of the total energy of the dislocation system. The form of the crystalline energy as a function of a *general strain tensor* is proposed in recognizing that the “stress-free” part of the deformation by a glide dislocation is given by a simple shear strain, and that a collective contribution from multiple dislocations is a general strain. This is different than the original formulation of the crystalline energy, as a function of the total Burgers vector, because the degrees of freedom in the independent variable of the former is necessarily more. Although the exact mathematical expression has not been given yet, the properties of the crystalline energy is discussed. A more detail and general form of the gradient energy is also derived from the consideration of the total Burgers vector dependence of dislocation line energy.

For fcc crystal, a particular form of such a crystalline energy is formulated by simple linear superposition of the interplanar potential of each individual {111} slip plane. Examples of applications are presented for interactions between two dislocation loops expanding on either a single slip plane or two intersecting slip planes, as well as for more complex reactions taking place in dislocation networks. It is shown that the generalized expressions are able to handle self-consistently reactions among dislocations of all slip systems in accord with Frank’s rule. Some network configurations considered tend to decompose completely owing to the vanishing net Burgers

vector under periodic boundary condition. Thin layers of zero elastic modulus are then introduced at the system's boundary to mimic free surfaces that stabilize dislocation network. These extensions are necessary steps toward advanced applications of the phase field method to dislocation substructure formation and coarsening.

The proposed crystalline energy reduces to  $\gamma$ -surface when the deformation is a simple shear on a slip plane. Incorporation of accurate  $\gamma$ -surfaces from energetic calculations allows quantitative characterization of core structures of extended dislocations of arbitrary configuration. The model is validated against the generalized Peierls-Nabarro model for dissociation of straight edge and screw dislocations in Al and Pd using the same set of  $\gamma$ -surface data and elastic constants. Dissociation of dislocation nodes and a bent dislocation gliding on two intersecting  $\{111\}$  planes are investigated. The former leads to either an extended or a contracted node, depending on the direction of the sense vectors of the perfect dislocations that join the node, while the latter leads to a stair-rod dislocation at the intersection of the two planes.

The extended phase field dislocation model is shown to treat both mesoscale dislocation network structures and microscopic dislocation core structures in a same framework. While only fcc crystals are considered in the examples, the model is directly applicable to other crystal systems.

## CHAPTER 5

### DISLOCATION-MICROSTRUCTURE INTERACTION IN NI-BASED SUPERALLOYS

Interaction between dislocations and multiphase microstructures has long been recognized as an important factor that influences the mechanical properties of metals. In Ni-based alloys, for example, the creep resistance of  $\gamma/\gamma'$  alloys is much higher than that of the bulk form of either  $\gamma$  or  $\gamma'$  phase [144]. The increase of the strength was found to arise from, in addition to dislocation mutual interactions, the confined dislocation motion due to  $\gamma'$  precipitates. Specifically, these alloys consist of  $\gamma'$  precipitates (ordered intermetallics of  $L1_2$  structure) coherently embedded in a  $\gamma$ -phase (fcc) matrix. The  $\gamma'$  particles have cuboidal shapes and are aligned strongly along the elastically soft directions (the  $\langle 100 \rangle$  directions). Depending on the applications (such as single crystal turbine blades), the volume fraction of the  $\gamma'$  precipitates could be as high as 60 – 70%. In this case, plastic deformation and strengthening of the alloys are believed to begin with the “filling” of the softer  $\gamma$ -matrix channels (which are typically about 50 – 100nm wide) by  $1/2\langle 110 \rangle$ -type dislocations [144]. The  $\gamma'$  precipitates may also be sheared under certain conditions which include large local stress and availability of appropriate matrix channel dislocations. Moreover, the coherency stress due to the lattice misfit between  $\gamma$  and  $\gamma'$  is also considered as an important

factor, especially at the initial stages of the deformation when dislocations start to fill in the defect-free  $\gamma$  channels.

A theoretical study that is aimed to confirm and exchange with experiments the understanding of these processes is obviously very difficult in considering the interaction between dislocations and microstructure as an overall and collective effect to the macroscopic strength, instead of sole

In spite that the current dislocation model is still under intensive extension from a theoretical formulation to a more practical tool, we provide in this chapter a study of several simple yet typical problems of dislocation interacting with microstructure. We will only focus on the glide motion of dislocations in all examples.

## 5.1 Dislocation glide in $\gamma$ channels

To study the migration of dislocations in the  $\gamma$  channels, we first investigate the critical shear stress that drives a dislocation line into the channel and its dependence on the channel width. Figure 5.1(a) shows the tested configuration for an fcc system, where a dislocation loop is initially placed on a (111) slip plane in the  $\gamma$  layer. The periodic boundary condition is applied in all three dimensions. Thus the microstructure is equivalent to alternating layers of  $\gamma$  and  $\gamma'$ , and the dislocation loop is repeated in the space accordingly. a  $64 \times 64 \times 64$  mesh is used for the system. The width of the  $\gamma$  layer,  $S$ , is chosen to be 9, 11, 13, and 17 grids. For simplicity, no lattice misfit between  $\gamma$  and  $\gamma'$  layers is introduced. In order to confine the dislocation loop within the  $\gamma$  channel, we let the crystalline energy ten times greater in the  $\gamma'$  layer than in the  $\gamma$  layer. The critical stress may be estimated, as shown in Fig. 5.2 , by equating the work done by the applied shear stress over the swept area,  $W = \tau S dx$ , and the

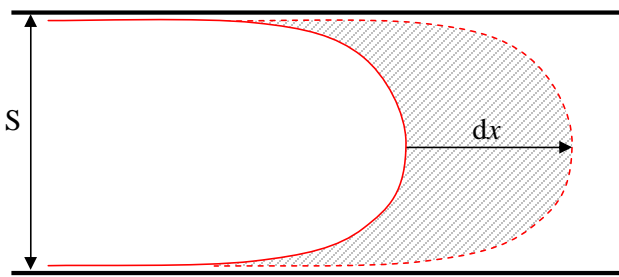


Figure 5.2: The migration of dislocation is approximated by a translation from the solid line to the dashed line over a distance of  $dx$ . The swept area, denoted by the shadow lines, is  $Sdx$ .

energy for creating two dislocation segments at the interface,  $E = 2Tdx$ , where  $T$  is the line energy of the dislocation per unit length. This gives the critical stress  $\tau = 2T/S$ . If  $T$  is not a strong function of the distance between the two dislocations  $S$ , the critical stress is simply inversely proportional to the  $\gamma$  channel width. In the simulation, for each choice of the channel width we apply several different stresses and obtain the corresponding velocity of the leading dislocation. Interpolation at the zero velocity gives the critical stress. The simulated critical stresses plotted in Fig. 5.1(b) shows a good agreement to the  $1/S$  dependence.

A more realistic geometry is considered in Fig. 5.3(a) which consists of a periodic array of cuboidal  $\gamma'$  precipitates under the applied periodic boundary condition. The system is represented in a  $64 \times 64 \times 64$  mesh with edge length  $1\mu\text{m}$ . The particle size is 800nm and channel width is 200nm. The volume fraction of the  $\gamma'$  phase is about 50%. Dislocations are considered to glide on a (111) plane, with Burgers vector along  $[\bar{1}01]$ . Frank-Read sources are introduced in one type of the  $\gamma$  channels (Fig. 5.3(a)) and the multiplication and propagation of dislocations in different  $\gamma$  channels under an applied shear stress (parallel to the glide plane and along the Burgers vector direction) are simulated using the phase field model. The amplitude of the applied stress is  $4 \times 10^{-3}\mu$  ( $\mu$  is the shear modulus), about 20% higher than the critical stress estimated in the previous case without lattice misfit. The stress on a dislocation in  $\gamma$  channels consists of contributions from dislocations present in the system, misfit stress and applied stress. The evolution of the dislocation structure and local stresses in the  $\gamma$  channels is quite complicated because the same matrix dislocations may either compensate or add to the misfit, depending upon the orientation of the matrix channel.

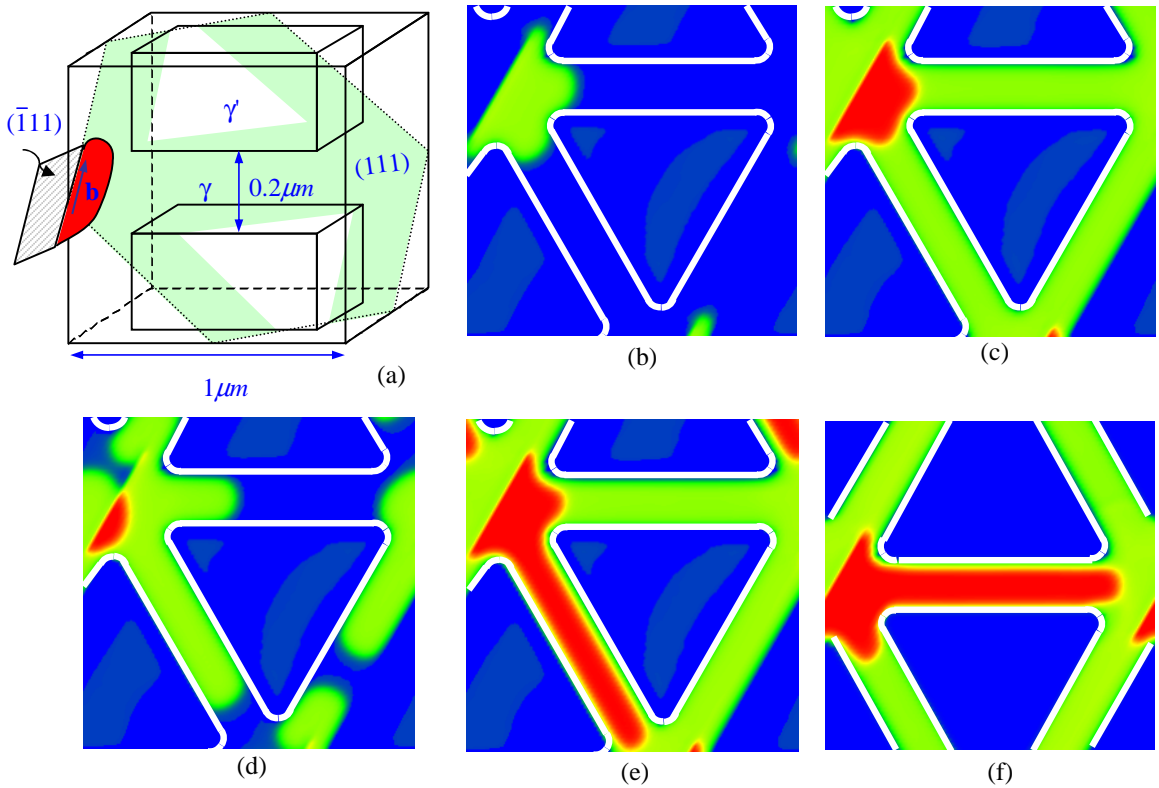


Figure 5.3: A  $1/2\langle 110 \rangle$  type screw dislocation enters  $\gamma$  channels in a cuboidal  $\gamma/\gamma'$  microstructure. (a) schematic drawing of the  $\gamma/\gamma'$  microstructure. Periodic boundary condition is used in all three directions. The glide plane in the  $\gamma$  channel is shown by the shaded area. (b)-(f) Channel filling processes by the matrix dislocations at different lattice misfit (only the glide plane is shown). The dislocation lines are given by the boundaries between regions of different colors. The two segments in the horizontal and the  $60^\circ$  channels appear symmetrical in (b, c) where  $\gamma/\gamma'$  misfit strain is small ( $\epsilon^T = 0.56\%$ ). It becomes non-symmetrical in (d, e) where  $\epsilon^T = 5.6\%$  and in (f) where  $\epsilon^T = -5.6\%$ .

The simulation results are presented in Fig. 5.3(b)-(f), in which a number of matrix dislocations (represented by different colors) are driven through the  $\gamma$  channel. The elastic anisotropy is also considered. The first dislocation line (boundary between green and blue) generated by the Frank-Reed source enters into both the horizontal and  $60^\circ$   $\gamma$  channels, but with different velocities. When the lattice mismatch is small, the difference in the velocities is almost negligible (Fig. 5.3(b)-(c)). When the lattice mismatch is large, however, this difference becomes significant and the second dislocation line (boundary between red and green) can only enter into the  $60^\circ$  channel under the same applied stress when the mismatch is positive (Fig. 5.3(d)-(e)). This result is confirmed by a contour plot of the misfit stress that is resolved to the slip plane and along the Burgers vector direction (Fig. 5.4(a)). It is readily seen that different stress state exists in the channels. When the lattice mismatch is positive, the resolved misfit stress on the dislocation is positive in the  $60^\circ$  channel and therefore increases the local applied stress. In the horizontal channel the resolved misfit stress is negative, which partially cancels the applied stress. It can also be seen that the misfit stress does not affect the other  $60^\circ$  channel. When the mismatch is negative, the channel filling process is reversed: the second dislocation loop can now only enter the horizontal channel (Fig. 5.3(f)). This is also consistent with the contour plot of the misfit stress in Fig. 5.4(b). The misfit stress with positive misfit and isotropic elastic moduli is shown in Fig. 5.4(c), which indicates that the elastic anisotropy does not result in qualitative difference for the given configuration.

In all cases as the leading dislocation propagates through the channel, it deposits two segments on the two sides of the channels. In the absence of dislocation climb these segments are piled up and their elastic stress effectively reduces the width of

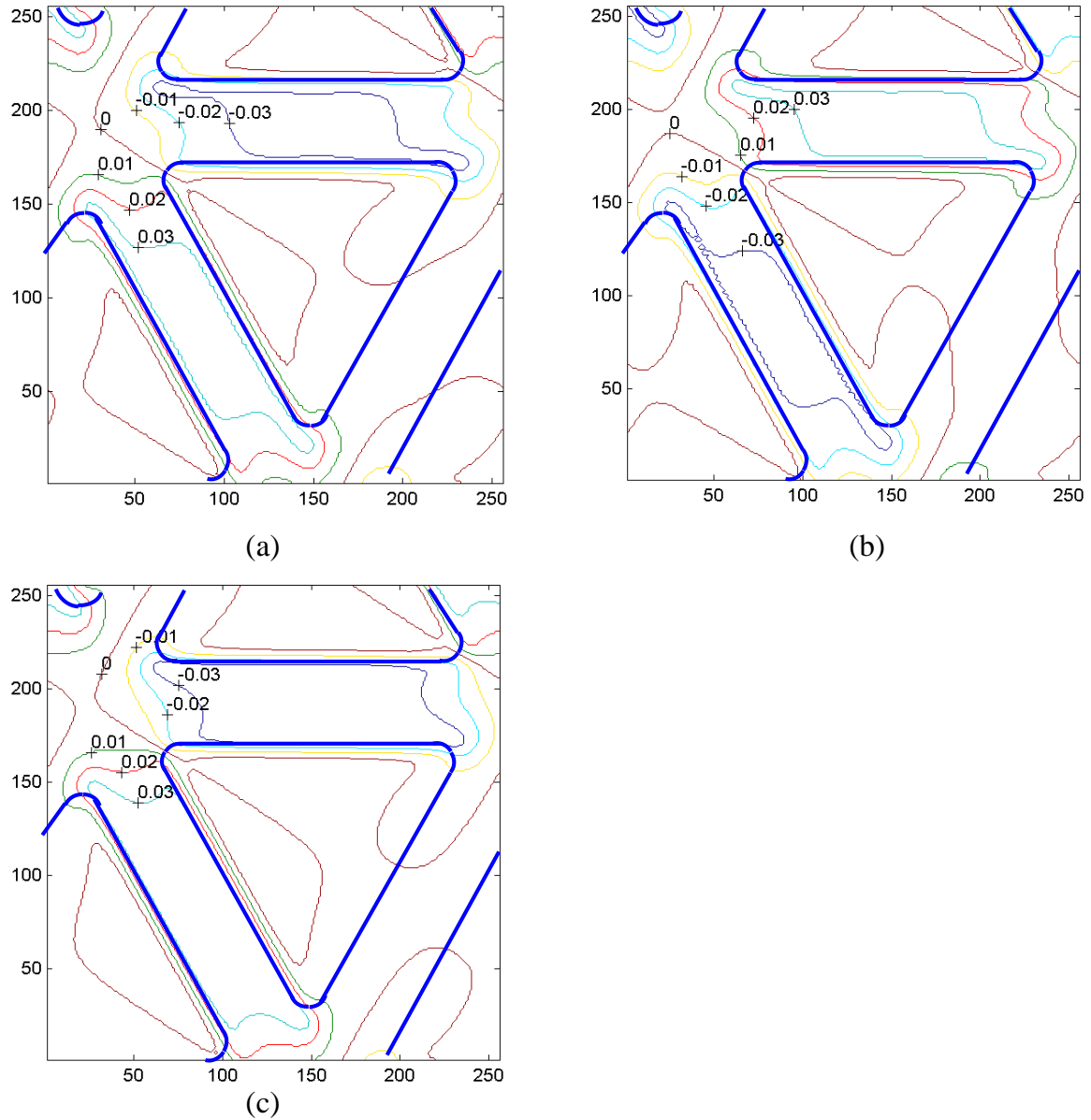


Figure 5.4: Contour plot of the resolved misfit stress (in reduced unit) on the dislocation, (a) with positive misfit (lattice parameter of  $\gamma'$  is greater than that of  $\gamma$ ), (b) with negative misfit, and (c) with positive misfit and isotropic elastic moduli.

the channel. Eventually no more dislocation can enter the channel, which provides one of the strengthening mechanisms for Ni-based superalloys.

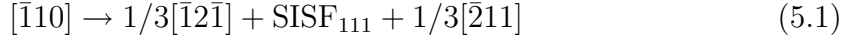
## 5.2 Threading dislocation in multilayer $\gamma/\gamma'$ thin film

Superior plastic strength has been found in thin films of multilayer microstructures [145] mainly due to the existence of the misfit stress that confines the motion of the threading dislocations. To understand the prevailing deformation mechanisms in multilayer thin films, Li and Anderson [146] applied a newly developed 3D discrete model that discretizes a slip plane into small triangular patches with dislocation segments residing on the edges of the patches. Slip of a dislocation is determined by whether or not there is an energy reduction in doing so. It was found that the deformation behavior of the thin film changes from a confined layer slip mode at large lattice mismatch, in which dislocation slip is only confined in individual layer, to a co-deformation mode at smaller lattice mismatch, in which dislocation threads the layers. To validate these simulation predictions, we performed phase field modeling by using the same geometry, elastic properties and lattice mismatch [147]. In the simulation a pair of screw dislocations with opposite Burgers vector are introduced into the multilayered structure. Each layer has equal thickness ( $75b$ ,  $b$  being the length of the Burgers vector). A resolved shear stress ( $7.5 \times 10^{-3} \mu$ ) is applied to the dislocation. The lattice friction is considered by comparing the actual local stress to the Peierls stress. If the stress is lower than the Peierls stress, which in the simulation is chosen as  $4.7 \times 10^{-3}$ , the kinetic coefficient  $L$  in Eq.(4.5) (proportional to the mobility of dislocation) is set to zero, otherwise it is a positive constant. The local stress is a sum of the misfit stress, the applied stress, and the elastic stress of dislocation. Misfit stress

is assumed compressive in the  $\gamma'$  layers and tensile in the  $\gamma$  layers. The response of the threading dislocations to the applied stress under different conditions is shown in Fig. 5.5. Quantitative agreement has been obtained among the two methods. In the confined layer slip mode, the dislocation segments in the  $\gamma'$  layers become stationary as a result of lattice friction.

### 5.3 Dislocation dissociation and cutting of $\gamma'$ precipitates

Superdislocations in the  $\gamma'$  phase are usually observed in complex dissociated configurations. The dissociation of a  $\langle 110 \rangle$  type dislocation can occur by



at room temperature or below, and by



at high temperature [148](Fig. 5.6). In the above CSF, APB, and SISF stand for the *complex stacking fault*, *antiphase boundary*, and *superlattice intrinsic stacking fault*, respectively. Non-planar configurations for APB dissociated dislocation have also been reported [148, 149]. Because the ordering of  $\gamma'$  phase doubles the lattice parameter of  $\gamma$  phase, a perfect dislocation in the latter will change its character to a Shockley partial as it enters the former, and will create a CSF joined with an APB along the path. From an energetic point of view, for dislocations to enter the  $\gamma'$  phase sufficiently high driving force is required to overcome the interfacial barrier and to compensate the energies associated with the creation of APB and CSF. As a second dislocation passes through the swept area, the relative displacement of the upper and lower crystal halves will restore to a full lattice translation in  $\gamma'$  and therefore the

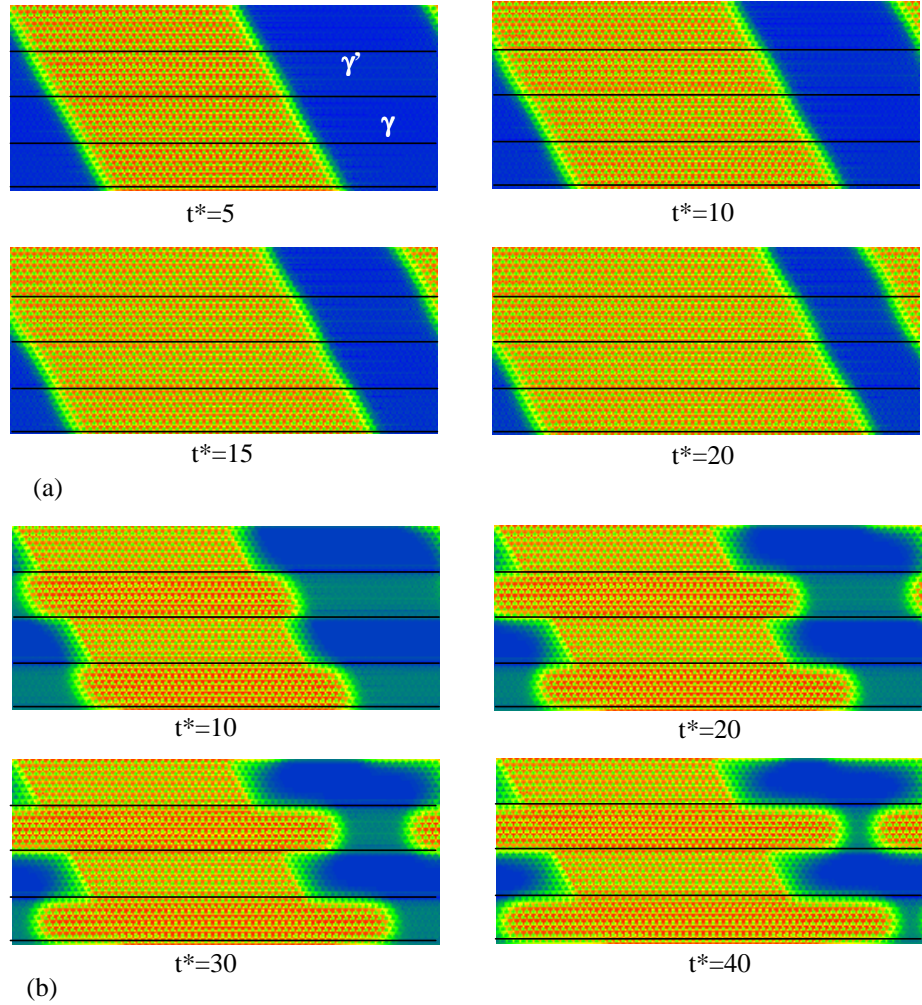


Figure 5.5: Phase field modeling of threading dislocations propagating in multilayer  $\gamma/\gamma'$  thin film. (a) Co-deformation across layers at small lattice mismatch (0.2%) and (b) confined layer slip at larger lattice mismatch (1%).  $t^*$  is the reduced time. The crystalline energies of the  $\gamma$  and  $\gamma'$  phases are assumed the same in these simulations, which is different from the simulations shown in Fig. 5.3.

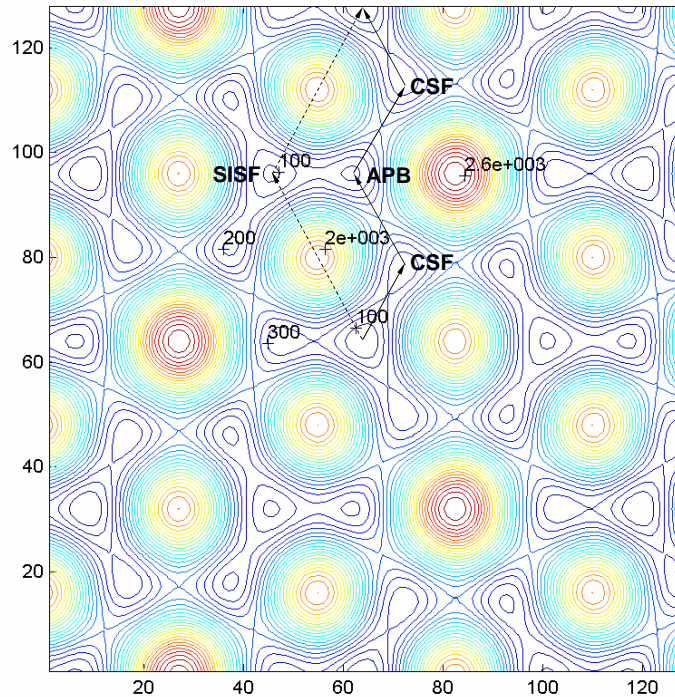


Figure 5.6: Contour plot of the  $\gamma$ -surface of (111) slip plane of  $\text{Ni}_3\text{Al}$  (in  $\text{mJ/m}^2$ ). The two types of dislocation dissociation given in Eqs.(5.1) and (5.2) are represented by the dashed and the solid lines, respectively.

stacking fault diminishes. Moreover, the coherency stress due to lattice misfit between the  $\gamma$  and  $\gamma'$  phases will be superimposed on the applied stress, either increasing or decreasing the effective local stress.

The extended phase field model introduced in Section 4.2.3 can naturally describe such kind of processes without additional complexity. This is in principle done by assigning specific  $\gamma$ -surface to each phase. The similar idea was actually employed, however in a rather rough way, in our previous examples of dislocation migration in  $\gamma$  channels, where the crystalline energy in the  $\gamma'$  precipitate was given by an artificially high value to prevent the dislocations cutting in. In this section we demonstrate the more self-consistent description of dislocation migration in both disordered  $\gamma$  and ordered  $\gamma'$  phases.

For dislocations on a (111) slip plane we may keep the same convention of  $\eta_1$ ,  $\eta_2$ , and  $\eta_3$  as in Section 4.4. Any dislocation on the slip plane, including both perfect and partial dislocations, can be described by a linear combination of the three  $\eta$ s. Similarly, the  $\gamma$ -surfaces of the two phases can be expressed in a form of Fourier series

by considering the three-fold symmetry of the slip plane

$$\Gamma = c_0$$

$$\begin{aligned}
& + c_1[\cos m\pi(\eta_1 - \eta_2) + \cos m\pi(\eta_2 - \eta_3) + \cos m\pi(\eta_3 - \eta_1)] \\
& + c_2[\cos m\pi(2\eta_1 - \eta_2 - \eta_3) + \cos m\pi(2\eta_2 - \eta_3 - \eta_1) + \cos m\pi(2\eta_3 - \eta_1 - \eta_2)] \\
& + c_3[\cos 2m\pi(\eta_1 - \eta_2) + \cos 2m\pi(\eta_2 - \eta_3) + \cos 2m\pi(\eta_3 - \eta_1)] \\
& + c_4[\cos m\pi(2\eta_1 - 3\eta_2 + \eta_3) + \cos m\pi(3\eta_1 - 2\eta_2 - \eta_3) + \cos m\pi(2\eta_2 - 3\eta_3 + \eta_1) + \\
& \quad \cos m\pi(3\eta_2 - 2\eta_3 - \eta_1) + \cos m\pi(2\eta_3 - 3\eta_1 + 2\eta_2) + \cos m\pi(3\eta_3 - 2\eta_1 - \eta_2)] \\
& + c_5[\cos 3m\pi(\eta_1 - \eta_2) + \cos 3m\pi(\eta_2 - \eta_3) + \cos 3m\pi(\eta_3 - \eta_1)] \\
& + c_6[\cos 4m\pi(\eta_1 - \eta_2) + \cos 4m\pi(\eta_2 - \eta_3) + \cos 4m\pi(\eta_3 - \eta_1)] \\
& + a_1[\sin m\pi(\eta_1 - \eta_2) + \sin m\pi(\eta_2 - \eta_3) + \sin m\pi(\eta_3 - \eta_1)] \\
& + a_3[\sin 2m\pi(\eta_1 - \eta_2) + \sin 2m\pi(\eta_2 - \eta_3) + \sin 2m\pi(\eta_3 - \eta_1)] \\
& + a_4[\sin m\pi(2\eta_1 - 3\eta_2 + \eta_3) + \sin m\pi(3\eta_1 - 2\eta_2 - \eta_3) + \sin m\pi(2\eta_2 - 3\eta_3 + \eta_1) + \\
& \quad \sin m\pi(3\eta_2 - 2\eta_3 - \eta_1) + \sin m\pi(2\eta_3 - 3\eta_1 + \eta_2) + \sin m\pi(3\eta_3 - 2\eta_1 - \eta_2)] \\
& + a_5[\sin 3m\pi(\eta_1 - \eta_2) + \sin 3m\pi(\eta_2 - \eta_3) + \sin 3m\pi(\eta_3 - \eta_1)] \\
& + a_6[\sin 4m\pi(\eta_1 - \eta_2) + \sin 4m\pi(\eta_2 - \eta_3) + \sin 4m\pi(\eta_3 - \eta_1)] \tag{5.3}
\end{aligned}$$

where the coefficients for both  $\gamma$  and  $\gamma'$  are given in Table 5.1. Note that the coefficient  $m$  corresponds to a lattice translation in  $\gamma'$  being twice in the  $\gamma$ . The crystalline energy is simply

$$E^{crys} = \int d\mathbf{x} \Gamma / d \tag{5.4}$$

The elastic energy and gradient energy formulations are identical to those presented in Section 4.2.3. The elastic constants are assumed to be the same for both  $\gamma$  and

Table 5.1: The fitted expansion coefficients in Eq.(5.3) (in unit of mJ/m<sup>2</sup>).

	$c_0$	$c_1$	$c_2$	$c_3$	$c_4$	$c_5$	$c_6$
Ni <sub>3</sub> Al <sup>§</sup>	878.1	-78.0	16.4	-226.9	3.9	-1.3	-10.7
Ni(Al) <sup>†</sup>	516.9	-108.9	-82.2	20.6	-0.9	0	0
	$a_1$	$a_3$	$a_4$	$a_5$	$a_6$	$m$	
Ni <sub>3</sub> Al <sup>§</sup>	138.7	-385.9	-13.3	1.8	4.4	1	
Ni(Al) <sup>†</sup>	-114.2	-28.0	0	0	0	2	

<sup>§</sup> Fitted to *ab initio* results by Kohlhammer [150].

<sup>†</sup> At this moment it is difficult, however, not essential to have the  $\gamma$ -surface data for the disordered  $\gamma$  phase. We therefore made a generic data which is scaled from the  $\gamma$ -surface date of Al [102] and Ni [151].

$\gamma'$  phases and the following values are employed:  $c_{11}=224.3\text{GPa}$ ,  $c_{12}=148.6\text{GPa}$ , and  $c_{44}=125.8\text{GPa}$  [152]. The dimensionless gradient coefficient is chosen as  $\xi^*=0.1$ .

A set of separate phase fields are used to distinguish the  $\gamma$  and  $\gamma'$  phases for a general microstructure. The coefficients in the crystalline energy are chosen at each position according to the identified phase. Figure 5.7 illustrates such a “stitched”  $\gamma$ -surface. At this moment we let the  $\gamma$ -surface of each phase extend up to the two phase interface. Possible transition from one  $\gamma$ -surface to the other at the interface is left to the future study when the corresponding physical picture is understood.

### 5.3.1 Dissociation of superdislocation in $\gamma'$ phase

A perfect  $\langle 110 \rangle$  type straight screw dislocation is initially placed on a  $(111)$  plane in the  $\gamma$  phase. After relaxation it dissociates into a complex configuration consisting of two CSFs and an APB in between as described by Eq.(5.2). Figure 5.8 shows a profile of the crystalline energy density ( $\Gamma/d$  in Eq.(5.4) in dimensionless form) across the dissociated dislocation. The values characterize the energy along the relaxed displacement path on the  $\gamma$ -surface. The flat region in the middle of the profile in Fig. 5.8 corresponds to the APB energy divided by  $d$ . Similarly the two local minima

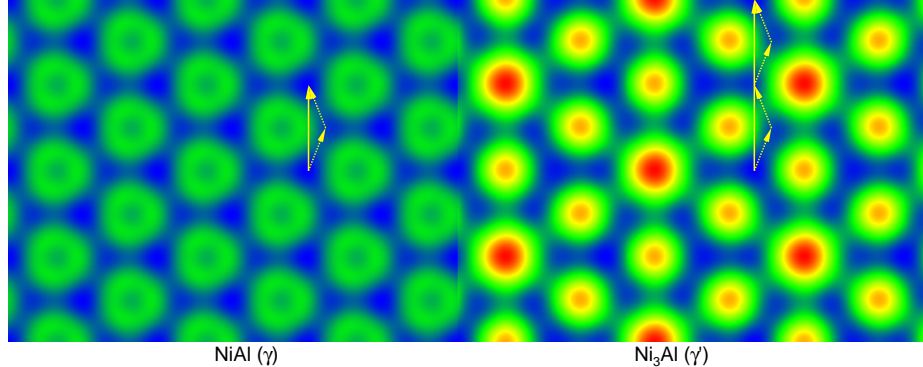


Figure 5.7: A combined  $\gamma$ -surface of  $\gamma$  and  $\gamma'$  phases each given by Eq.(5.3). Also shown are Burgers vectors of perfect (solid lines) and partial dislocations (dashed lines) in each phase.

correspond to the CSF energy. The distance between the two large peaks is found to be  $9.2b$  and between the adjacent large and small peaks is  $2.3b$ . As compare to the results obtained by Schoeck *et al.* [153] ( $13.07b$  and  $2.48b$ , respectively), the former is significantly smaller.

### 5.3.2 Straight screw dislocation cutting a flat $\gamma/\gamma'$ interface

The configuration considered is shown in Fig. 5.9. The  $\gamma'$  phase is located at the left and  $\gamma$  phase at the right. They are separated by a flat coherent interface indicated by the dashed line. For simplicity, no lattice mismatch is considered. Two perfect  $1/2\langle 110 \rangle$  straight screw dislocations are initially placed in the  $\gamma$  phase. Each develops into an extended dislocation with a stacking fault connecting two Shockley partials (Fig. 5.9(a)). The two extended dislocations move toward the  $\gamma/\gamma'$  interface under an applied stress. Figures 5.9(a)-(c) show the snap shots of the crystalline energy profiles at three consecutive moments. In Fig. 5.9(a) the dislocations are moving toward the

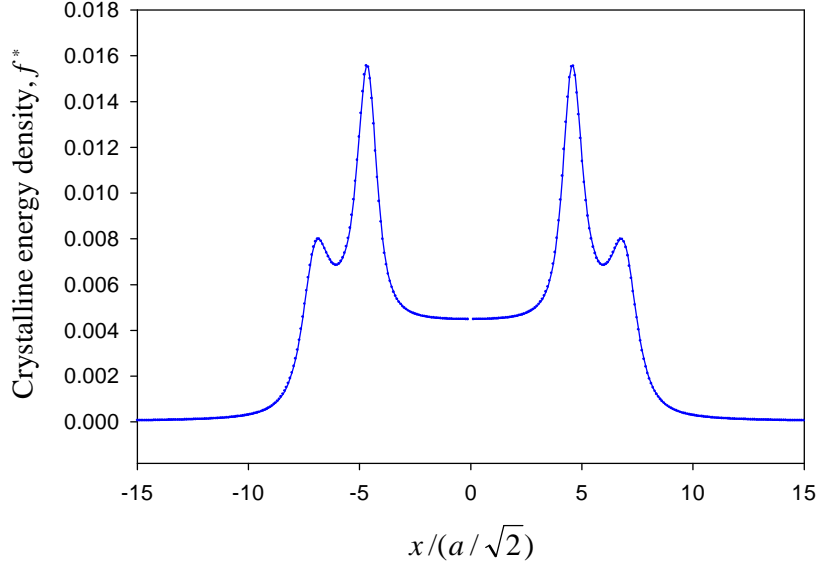


Figure 5.8: Energy profile of the dissociated dislocation in  $\gamma'$  phase after relaxation.  $a$  is the lattice parameter of  $\gamma$  phase. The flat region in the middle corresponds to the APB energy. The other two local minima correspond to the CSF energy.

interface and, at the same time, the spacing between the two extended dislocations keeps increasing (not shown) due to the mutual elastic repulsion. In Fig. 5.9(b) one extended dislocation cuts through the interface and creates a CSF (between the large and the small peak) and an APB (represented by the higher plateau) in the  $\gamma'$  phase. As the second extended dislocation enters the  $\gamma'$  phase (Fig. 5.9(c)), another CSF is created and the APB behind it is removed. The distance between the two extended dislocations decreases, reducing the APB area between them. The stress applied in this case is about 1.2 of the APB energy divided by the Burgers vector.

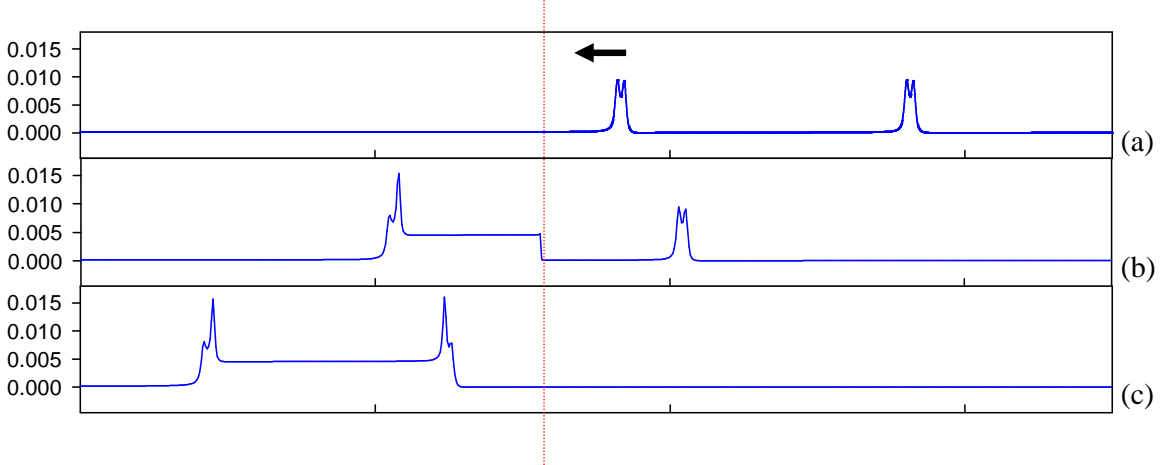


Figure 5.9: Snap shots of profiles of two extended dislocations at consecutive moments from (a) to (c). The left side is in  $\gamma'$  phase and the right side in  $\gamma$  phase. The  $\gamma/\gamma'$  interface is marked by the dashed line. Dislocations move toward the left side under an applied stress. At moment (b) one dislocation enters the  $\gamma'$  phase, leaving an APB behind. At moment (c) a similar configuration to Fig. 5.8 is formed when the second extended dislocation enters the  $\gamma'$  phase.

### 5.3.3 Dislocation interactions with $\gamma'$ particles

We start with a configuration consisting of two spherical  $\gamma'$  particles embedded in a 3D  $\gamma$  phase matrix. The particles have different sizes, as shown in Fig. 5.10 by their intersections with a (111) slip plane (the lighter regions). A straight screw dislocation is placed in the  $\gamma$  matrix at the top in the beginning. The dissociated core is not resolved in this case because of the mesoscopic length scale presented in Fig. 5.10. The applied stress is approximately 70% of the APB energy divided by the Burgers vector. The effects of the misfit coherency stress are ignored at this moment. The simulation results show that the dislocation cannot enter the big particle, it bypasses the particle and deposits a dislocation loop around it. However, the dislocation does

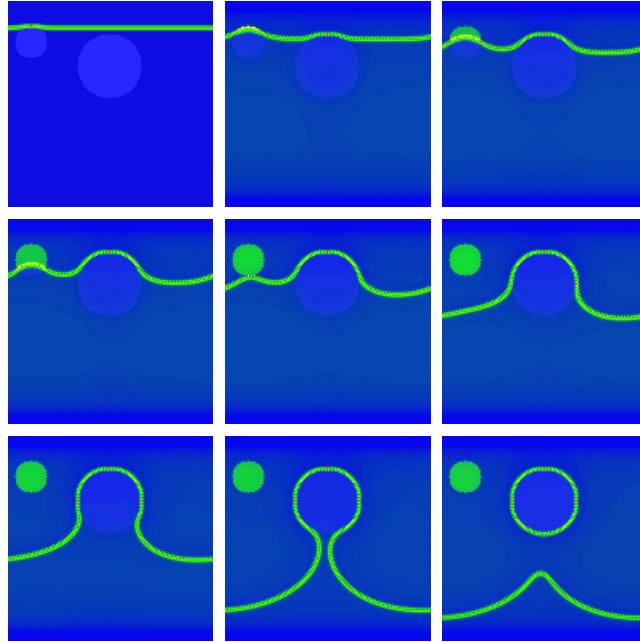


Figure 5.10: A screw dislocation with Burgers vector  $1/2\langle 110 \rangle$  moves from the top to the bottom of the (111) slip plane under an applied stress, encountering two  $\gamma'$  particles of different sizes. The dislocation bypasses the large particle while cuts through the small one. An APB is left in the small particle as the dislocation cuts through. The contrast in the figure reflects the relative value of the crystalline energy density.

cut through the small particle and leaves an APB inside (indicated by the brighter shade in the figures). This is because when the dislocation line is impeded by the particles, curvatures are developed which provide an additional effective stress that superimposes on the applied stress.

## CHAPTER 6

### LENGTH SCALE AND QUANTITATIVE PHASE FIELD MODELING

#### 6.1 The length scales of a phase field model

In chapter 2 we have discussed that the coarse-graining process for a physical system must choose the length scale no greater than the microstructural elements of importance to the physical process. Otherwise the important features will be averaged and neglected in the derived coarse-grained free energy. This may be considered as the first place that a length scale constraint appears. Thus in nucleation, for example, the length scale has to be associated with the critical fluctuations that make a small portion of the initial phase unstable with respect to an infinitesimal perturbation to the size. In growth of finite microstructural domains, such as grains, precipitates, or slipped regions by dislocations, it is the typical distance over which the microstructure domains vary from one to another, which can often be equivalent to the width of the domain boundaries. In this sense, the length scale of a phase field model could differ considerably from that of the microstructure it describes.

When the field variables and energies in a given phase field model are defined as physical quantities, the gradient energy is the first non-vanishing term in the

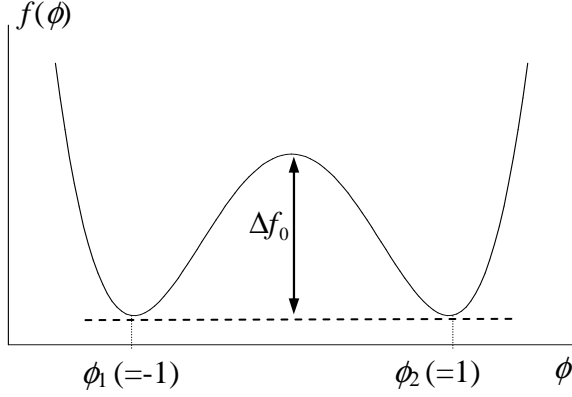


Figure 6.1: A double-well free energy with two minima at  $\phi_1$  and  $\phi_2$ .  $\Delta f_0$  is defined as the maximum height from the common tangent to the free energy curve.

expansion of the free energy of an inhomogeneous system with respect to the spatial non-uniformity. Combined with the leading term that describes the uniform phases, it gives a physical description of the variation of the material properties over the space, in particular, across the domain boundaries or interfaces. For example, as shown by Cahn and Hilliard [21], the energy of a flat interface can be obtained by minimization of the total energy functional, such as in a simplest form given by Eq.(2.1)

$$\sigma = 2 \int_{\phi_1}^{\phi_2} d\phi \sqrt{\Delta f(\phi) \kappa / 2} \quad (6.1)$$

and accordingly the width of the interface is

$$\lambda = (\phi_2 - \phi_1) \sqrt{\kappa / (2 \Delta f_0)} \quad (6.2)$$

Here  $\Delta f$  is the difference between  $f(\phi)$  and the common tangent line the the range between  $\phi_1$  and  $\phi_2$  (Fig. 6.1), and  $\Delta f_0$  is the maximum of  $\Delta f(\phi)$ . On the other hand, in a discrete mesh based simulation evaluation of the gradient term requires a sufficient sampling of the grid points on a non-uniform microstructure. The minimal spatial

frequency of the sampling is constrained by the interface, where the microstructure varies most rapidly. Thus in a numerical implementation based on a uniform mesh, the grid spacing must be chosen smaller than the width of the interface. We can regard this grid spacing as *simulation length scale*. Clearly the simulation length scale is limited by the boundary width in a phase field model.

Except at very high temperature or near critical point, interfaces and domain boundaries encountered in materials are often found around nanometers in width. This can also be confirmed by Eqs.(6.1) and (6.2). For example, at 1300K, using the following values for a Ni-Al alloy:  $c_\gamma = 16.0$  and  $c_{\gamma'} = 22.9$ at% Al,  $\Delta f_0 = 1.5 \times 10^7 \text{J/m}^3$ ,  $\sigma = 0.01 \text{J/m}^2$ , the interface thickness  $\lambda$  turns out to be approximately  $4.7 \text{\AA}$ <sup>13</sup>. If five grid points are kept on the interface, the grid spacing, or the simulation length scale, has to be around  $1 \text{\AA}$ . In this case a 3D mesh of 512 cells in each direction corresponds to a physical length of about 50nm, which corresponds to the typical size of one relatively small  $\gamma'$  particle observed in the Ni-base superalloys. Then, it would not be affordable to treat thousands of particles in a phase field modeling even with the use of state-of-the-art parallel computers. Since  $\Delta f_0$ ,  $\sigma$ , and  $\kappa$  are material parameters, the interface width  $\lambda$  is uniquely determined for a given system. In other words, there is no degrees of freedom for adjusting  $\lambda$  without altering at least one of these materials parameters in Eqs.(6.1) and (6.2).

It should be noted that there is another important kind of phase field modeling which introduces the gradient term as, instead of a physical expansion term, solely a numerical technique to avoid boundary tracking. This idea was first proposed by Langer [154] for the study of complex pattern formation such as in solidification.

<sup>13</sup>Here we take Eq.(6.1) approximately as  $\sigma \cong (c_{\gamma'} - c_\gamma)\sqrt{\Delta f_0 \kappa}$  and substitute  $\kappa$  into Eq.(6.2).

The parameters in such a phase field model are determined by matching the moving boundary equations (Eq.(2.57)-(2.59)) via [154, 36]

$$d_0 = a_1 W / \chi, \quad \beta = a_1 \tau / (\chi W) \quad (6.3)$$

or in a less stringent condition by a recent thin-interface approach [40]

$$d_0 = a_1 W / \chi, \quad \beta = a_1 [\tau / (\chi W) - a_2 W / D] \quad (6.4)$$

where  $d_0$  and  $\beta$  are the capillary length and the kinetic coefficient in Eq.(2.59), respectively.  $W$  and  $\chi$  are related to the two phase field parameters  $\kappa$  and  $\Delta f_0$ .  $D$  is diffusivity,  $a_1$  and  $a_2$  are two constants of order unity. Detailed discussion for this category of phase field models is beyond the scope of this chapter and can be found in Ref.[40, 37]. It is worth pointing out that Eq.(6.3) or (6.4) involves less moving boundary parameters at the left hand side than the phase field parameters at the right hand side. The extra degree of freedom is thus left to adjusting the width of the phase field boundary without violating Eq.(6.3) or (6.4), and a larger grid spacing may be achieved. Nevertheless, the actual boundary width is still considerably limited by the assumptions for deriving Eqs.(6.3) or (6.4).

## 6.2 Increase simulation length scale for individual processes

From the above analyses, it is clear that if material-specific parameters for the free energy and interfacial energy are employed in the phase field modeling, system sizes that can be simulated are fixed. The only choice within a uniform mesh finite difference scheme is to increase the interface thickness. As can be seen in Eq.(6.2), this has to be done by increasing the ratio  $\kappa / \Delta f_0$ . Because there are no degrees of freedom for adjusting either  $\kappa$  or  $\Delta f_0$ , modify these material parameters will inevitably end up

with a *different* material system. In a less stringent situation that a material modeling is interested only in a particular feature of microstructural evolution, we may seek an equivalent system that behaves identically in the interested feature by maintaining only the controlling parameters. This less stringent approach thus gives the hope to gain the extra degrees of freedom for adjusting the interface width. As will be seen below, in simple cases this can be achieved by keeping either  $\kappa$  or  $\Delta f_0$ , or their product  $\kappa\Delta f_0$  unchanged, depending on the specific problem under consideration.

Throughout the following examples we choose to use the free energy (Fig. 6.1)

$$f(\phi) = \Delta f_0(\phi^2 - 1)^2$$

and the kinetic equation simplified from Eqs.(2.3) and (2.4)

$$\frac{\partial\phi}{\partial t} = \boldsymbol{\Gamma} \frac{\delta\mathcal{F}}{\delta\phi}$$

where  $\boldsymbol{\Gamma} = -M$  for non-conserved field and  $\boldsymbol{\Gamma} = M\nabla^2$  for conserved field.  $M$  is chosen as unity.

### 6.2.1 Anti-phase domain (APD) coarsening and grain growth

These processes involve no long-range transport of atoms and are purely curvature driven. Allen and Cahn [28] have shown that the growth rate (or the normal velocity of the boundary motion) depends only on  $\kappa$  but not  $\Delta f$  in Eq.(6.1). An important consequence is that the velocity of boundary motion is independent of the interface thickness and interfacial energy. This was in agreement with their experimental observations in Fe-Al alloys and, independently, was confirmed in an experiment by Pindak *et al.* [155] where the boundary thickness of orientational domains in freely suspended dipolar smectic-*C* liquid crystal films was controlled precisely by external

electrical fields. Pindak *et al.* have found that, in accordance with Allen and Cahn, the motion of the domain boundary is independent of boundary width, provided  $\lambda/R \ll 1$ , where  $R$  is the domain size. Considering these theoretical and experimental results, we should be able to diffuse arbitrarily the domain or grain boundaries by decreasing  $\Delta f$  without changing the kinetics of the boundary motion. Figure 6.2(a) shows the growth rates in a set of three 2D phase field simulation tests, in which  $\kappa$  is maintained as a constant ( $\kappa = 5$ ) while  $\Delta f_0$  is varied by two orders of magnitude. In changing  $\Delta f_0$  here and in the examples that will follow, the free energy functional is rescaled simply by a constant factor in accord with  $\Delta f_0$ . Excellent agreement in growth kinetics is obtained although the boundary thickness in the three tests differs significantly from each other (Fig. 6.2(b)).

Even though altering  $\Delta f$  does not affect the kinetics of domain coarsening, it changes the boundary energy according to Eq.(6.1). When reporting the interfacial energy for a particular simulation result, the one calculated directly from the simulation,  $\sigma^{simul}$ , using an altered  $\Delta f_0^{simul}$  should be converted back to the real value corresponding to the unaltered  $\Delta f_0$  by  $\sigma = \sigma^{simul} \sqrt{\Delta f_0 / \Delta f_0^{simul}}$ .

It is interesting to note that the results obtained by Allen and Cahn are different from Turnbull's analysis [156] of boundary migration where boundary velocity is proportional to interfacial energy and inversely proportional to boundary thickness. According to Cahn and Novick-Cohen [157], the discrepancy could be attributed to the difference in the characteristic movement of atoms that fulfills the motion of the interfaces: atoms are only required for a local re-arrangement instead of moving across the boundary during the motion of anti-phase domain boundaries and grain

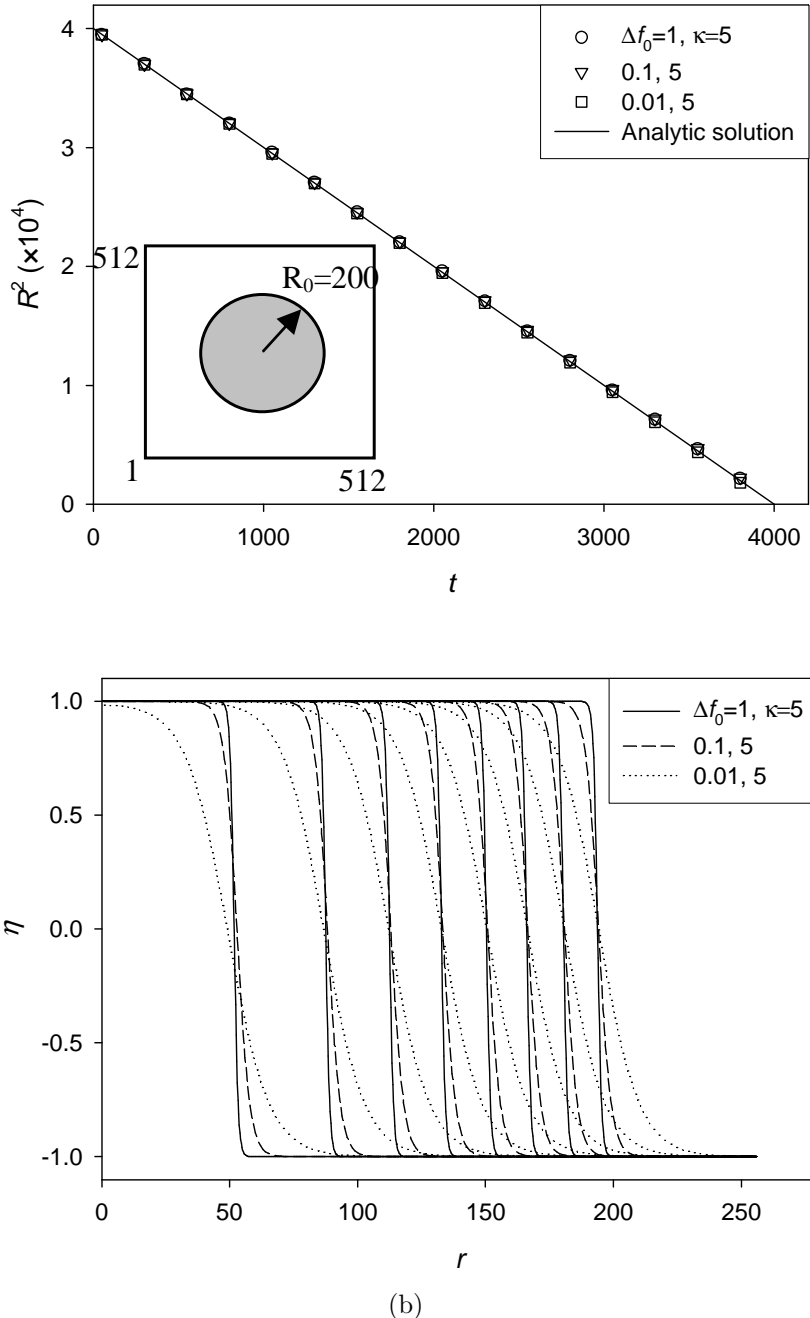


Figure 6.2: (a) Simulated shrinkage rate of an island antiphase domain. The inset shows the initial configuration ( $\eta = 1$  in the island and -1 in the matrix). The solid line is the analytic solution,  $R_0^2 - R^2(t) = 2M\kappa t$ , by integrating Eq.(2.50) at  $H = 0$ . Domain boundary profiles across the interface ( $\eta = 0$ ) at different sizes are shown in (b) in three cases with  $\kappa$  fixed and  $\Delta f_0$  varied by two orders of magnitude.

boundaries, which is different from the motion of an inter-phase interface considered by Turnbull.

### 6.2.2 Precipitate growth

Precipitate growth requires long-range diffusion. The driving force is provided by chemical potential gradients. If precipitates are not so small that the Gibbs-Thomson effect can be neglected, their growth will depend only on the  $f(c) - c$  curve (e.g.,  $\partial f(c)/\partial c$  where  $c$  is composition) and is independent of  $\kappa$ . Figure 6.3 shows the results of phase field simulations of 1D precipitate growth in a supersaturated matrix where the value of  $\Delta f_0$  is kept constant ( $=1$ ) while  $\kappa$  is changed by two orders of magnitude. The growth rates obtained from different cases are almost identical (Fig. 6.3(a)) and agree well with the numerical solution to the moving-boundary diffusion equation (solid curve) described in Section 3.6. At early stages the area of the particle increases linearly with time, indicating a parabolic growth law that is expected for diffusion-controlled growth. At later stages, the growth slows down because of the overlap of the diffusion fields (soft-impingement) of the growing particles from different computational cells produced by the homogeneous Neumann (zero-flux) boundary conditions.

These simulation results have demonstrated that the growth kinetics of a precipitate will be the same as long as  $f(c)$  is unaltered. Therefore in the absence of a strong Gibbs-Thomson effect one can increase the value of  $\kappa$  to diffuse the interface without altering the growth kinetics. In this case, the interfacial energy will also be altered and the real value can be calculated by the relation  $\sigma = \sigma^{simul} \sqrt{\kappa/\kappa^{simul}}$ .

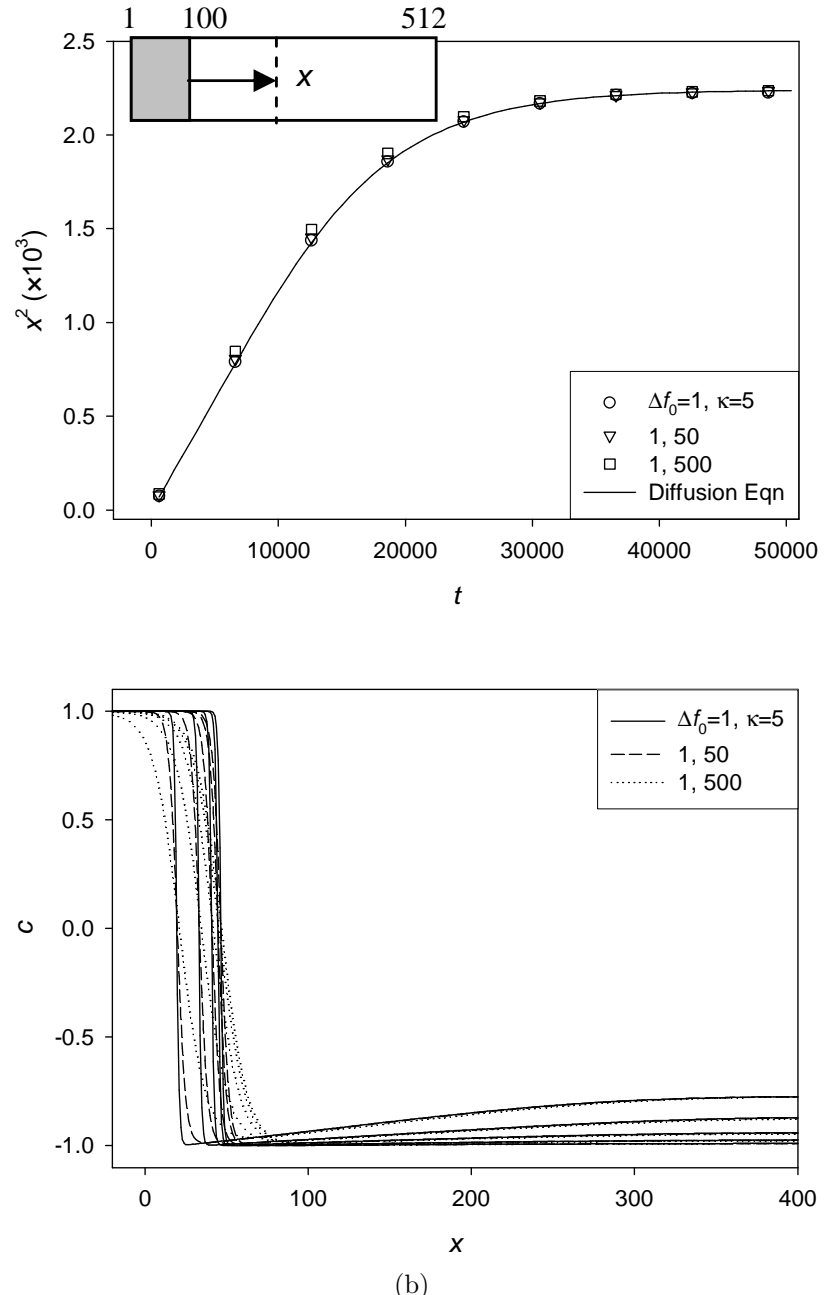


Figure 6.3: Simulated growth kinetics of a 1D precipitate (a) with the initial configuration shown in the inset ( $c=1$  in the precipitate (in gray) and  $-0.77$  in the matrix (in white)). The solid curve is the solution from the corresponding sharp-interface model. Concentration profiles across the interface at a particular moment are given in (b) for three cases with  $\Delta f_0$  fixed and  $\kappa$  varied by two orders of magnitude. The positions of interfaces are determined by the intersections of the concentration profiles with  $c=0$ .

### 6.2.3 Coarsening

The kinetics of coarsening depends on the interfacial energy, which is a function of both  $\Delta f$  and  $\kappa$  in the phase field model (Eq.(6.1)). To keep the kinetics unaltered, one should adjust the ratio of  $\kappa/\Delta f_0$  to diffuse the interface while keeping their product constant in this case. Similar to the previous two cases, direct phase field simulation tests are made by fixing the product of  $\kappa\Delta f_0$  while increasing successively the ratio of  $\kappa/\Delta f_0$ . The configuration considered in the tests is shown in the inset of Fig. 6.4(a). The coarsening kinetics from the simulation (Fig. 6.4(a)) is shown consistent with the solution to the coupled moving-boundary diffusion equation and Gibbs-Thomson equation (see SectionJMAK.sec). The chemical potential change inside the precipitate as a function of particle radius (the Gibbs-Thomson effect) during the coarsening process also agrees well with the theoretical predictions (Fig. 6.4(c)). However, considerable departure is observed in both cases at later stages when the particle radius becomes commensurable with the interface thickness and the departure occurs earlier for the wider interface. It is clear from these results that as long as the condition of  $\lambda/R \ll 1$  (where  $R$  is particle radius) is satisfied, the coarsening kinetics is independent of the ratio  $\kappa/\Delta f_0$  and one can diffuse the interface to increase system size by increasing the ratio of  $\kappa/\Delta f_0$  while maintaining the product  $\kappa\Delta f_0$  constant.

### 6.2.4 Development of coherent microstructures

The presence of coherency misfit strain may have two effects on the microstructure development. First, in an elastically anisotropic material the equilibrium shape of a precipitate is determined by the minimization of the sum of coherency strain energy and interfacial energy [52]. Similar to the role of bulk free energy in nucleation, the

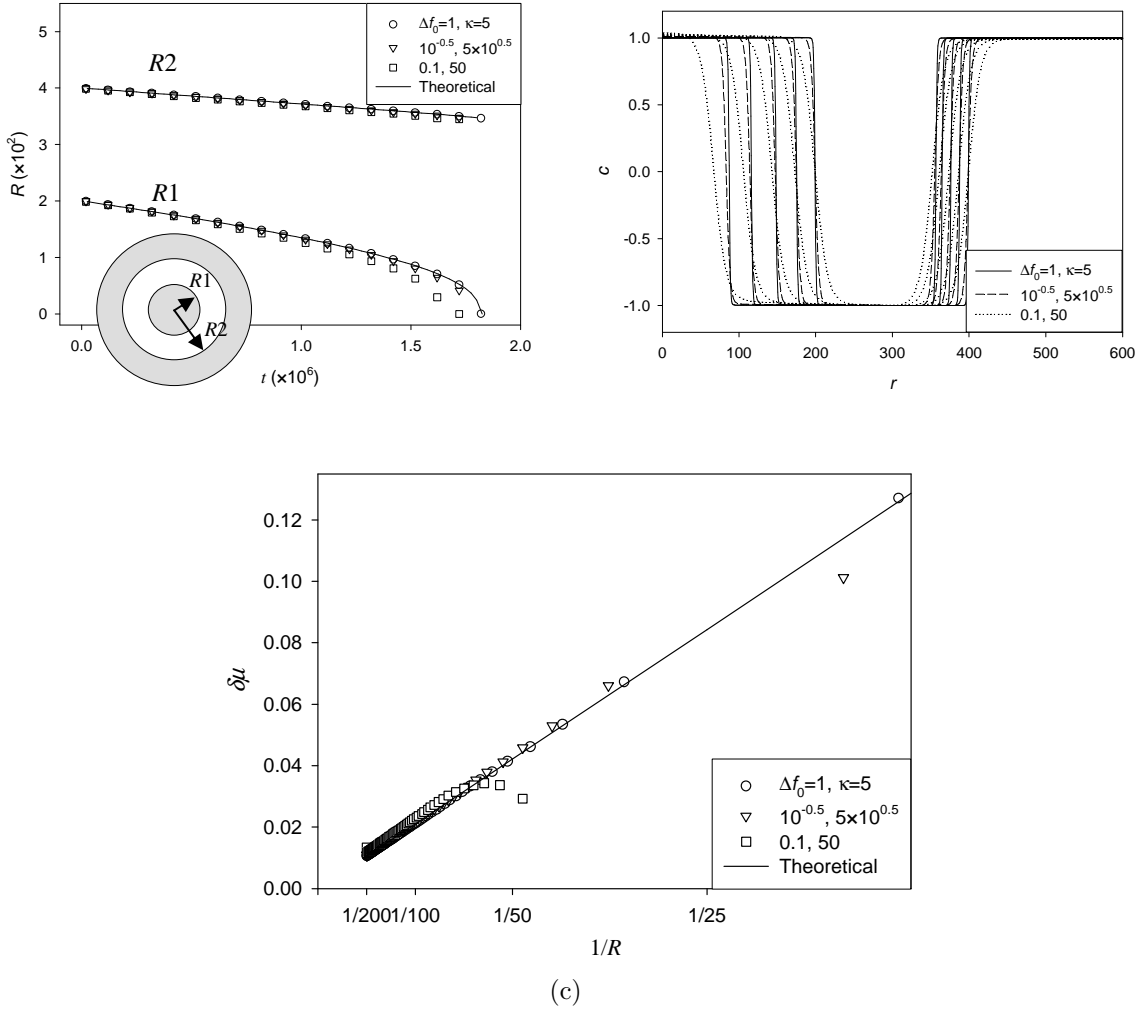


Figure 6.4: Simulated (a) coarsening kinetics for the configuration shown in the inset and (b) concentration profiles across the interface in three cases with  $\kappa\Delta f_0$  fixed while  $\kappa/\Delta f_0$  varied by two orders of magnitude.  $R_1$  and  $R_2$  are the positions of interface identified by  $c=0$ . (c) The deviation of chemical potential  $\delta\mu$  at different particle radii agrees with the predictions by the Gibbs-Thomson equation (solid line). Note that deviations occur as the particle radius becomes commensurate with the interface thickness.

coherency strain energy is scaled with the volume of precipitate, and thus the equilibrium shape of a precipitate will be a function of its size. Therefore to simulate precipitate morphology at a large length scale, the approach to achieve the correspondingly wide interface should be same as that for coarsening in order to maintain the interfacial energy.

Second, the coherency strain field influences chemical potential in the matrix. The interplay between coherency strain energy and bulk chemical free energy determines the driving force for diffusion and thus for precipitate growth in a strained matrix. In addition, as discussed in Section 2.6, the coherency strain energy is combined with the chemical free energy to form a coherent phase diagram, which determines the two-phase equilibrium in a coherent system, including equilibrium compositions and volume fraction of the constituent phases. The approach to correctly describe these situations at a large scale thus has to be the same as that for precipitate growth, where the bulk chemical free energy is fixed. However, since the approach modifies the interfacial energy, precipitate will appear in different shapes.

### 6.3 Increase simulation length scale for concurrent processes

In the preceding section we have shown that with material-specific parameters as inputs, one can diffuse the interface without altering the kinetics and paths of microstructural evolution by one of the following: (a) increasing  $\kappa$  (for precipitate growth); (b) reducing  $\Delta f_0$  (for antiphase domain coarsening and grain growth); (c) increasing the  $\kappa$  and reducing  $\Delta f_0$  simultaneously while keeping the product of the two unchanged (for precipitate coarsening). For processes with concurrent growth and coarsening, however, these approaches do not apply anymore because fixing the

driving forces for growth and coarsening requires to fix both  $\Delta f_0$  and  $\kappa$ , thus no degree of freedom left for adjusting the interface width. In this section we propose an approach for increasing the length scale of quantitative phase field modeling of concurrent growth and coarsening processes with neither growth nor coarsening kinetics altered. The approach is valid for phase transformations involving both composition and symmetry changes. In this case, the free energy is a function of both composition and long-range order (*lro*) parameter, and the driving force for precipitate growth and the free energy hump that determines interface thickness and interfacial energy are associated with different parts of the free energy surface. We will use the Ni-Al system as an example.

The non-equilibrium bulk chemical free energy of  $\gamma$  and  $\gamma'$  phases in the binary Ni-Al system has been modeled as a function of temperature and site fractions by Ansara *et al.* [158] using a four-sublattice model. A set of model parameters consistent with experimental phase diagram and thermodynamics has been obtained by using the so-called CALPHAD technique. Recently, it has been shown [159] that their formulation can be used directly in the phase field model for Ni-Al [160] by substituting the *lro*

parameters for the site fractions, which yields the chemical free energy per mole

$$\begin{aligned}
f(c, \eta_1, \eta_2, \eta_3) = & cg_{\text{Al}}^0 + (1 - c)g_{\text{Ni}}^0 + c(1 - c) \sum_{i=0}^3 L_i (2c - 1)^i \\
& + 4U_1 c^2 (\eta_1^2 + \eta_2^2 + \eta_3^2) + 12U_4 (1 - 2c) c^2 (\eta_1^2 + \eta_2^2 + \eta_3^2) - 48U_4 c^3 \eta_1 \eta_2 \eta_3 \\
& + (RT/4) \left\{ \right. \\
& c(1 + \eta_1 + \eta_2 + \eta_3) \ln c(1 + \eta_1 + \eta_2 + \eta_3) \\
& + [1 - c(1 + \eta_1 + \eta_2 + \eta_3)] \ln [1 - c(1 + \eta_1 + \eta_2 + \eta_3)] \\
& c(1 + \eta_1 - \eta_2 - \eta_3) \ln c(1 + \eta_1 - \eta_2 - \eta_3) \\
& + [1 - c(1 + \eta_1 - \eta_2 - \eta_3)] \ln [1 - c(1 + \eta_1 - \eta_2 - \eta_3)] \\
& c(1 - \eta_1 + \eta_2 - \eta_3) \ln c(1 - \eta_1 + \eta_2 - \eta_3) \\
& + [1 - c(1 - \eta_1 + \eta_2 - \eta_3)] \ln [1 - c(1 - \eta_1 + \eta_2 - \eta_3)] \\
& c(1 - \eta_1 - \eta_2 + \eta_3) \ln c(1 - \eta_1 - \eta_2 + \eta_3) \\
& \left. + [1 - c(1 - \eta_1 - \eta_2 + \eta_3)] \ln [1 - c(1 - \eta_1 - \eta_2 + \eta_3)] \right\} \quad (6.5)
\end{aligned}$$

where  $c$  is composition (mole fraction),  $\eta_i$  ( $i=1,2,3$ ) are the *lro* parameters. Quantities  $g_{\text{Al}}^0$ ,  $g_{\text{Ni}}^0$ ,  $L_i$ ,  $U_1$ , and  $U_4$  can be found in Ref. [158]. Figure 6.5 depicts a contour plot of the free energy surface at 1300K in a coordinate system of  $c$  and  $\eta$  ( $\eta_1 = \eta_2 = \eta_3 = \eta$ ). The two local minima correspond to the equilibrium  $\gamma$  and  $\gamma'$  phases. The temporal evolution of the composition and *lro* parameters in a non-equilibrium system is determined by solving, according to Eqs.(2.3) and (2.4)

$$\frac{1}{V_m} \frac{\partial c(\mathbf{x}, t)}{\partial t} = \nabla \cdot M \nabla \frac{\delta \mathcal{F}}{\delta c(\mathbf{x}, t)} \quad (6.6)$$

$$\frac{\partial \eta_i(\mathbf{x}, t)}{\partial t} = -L \nabla \frac{\delta \mathcal{F}}{\delta \eta_i(\mathbf{x}, t)} \quad (i = 1, 2, 3) \quad (6.7)$$

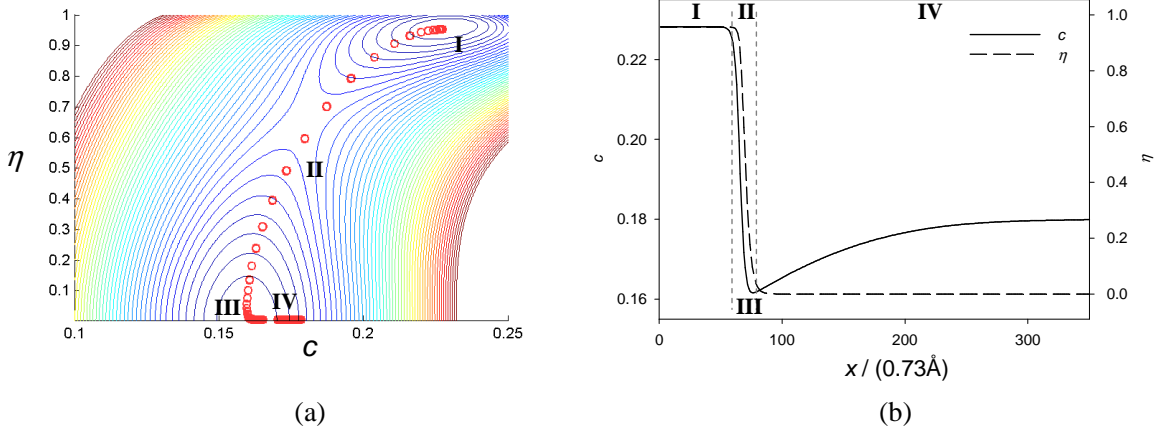


Figure 6.5: (a) Contour plot of the free energy surface given by Eq.(6.5) on  $\eta$ - $c$  plane. (b) Composition and Iro parameter profiles across an interface. The profiles in (b) are mapped onto the contour plot in (a) (open circles) to show the relaxation path of both  $c$  and  $\eta$  on the  $f$ - $c$ - $\eta$  surface during precipitate growth.

where  $V_m$  is the molar volume. The total chemical free energy of a non-uniform system,  $\mathcal{F}$ , is given by

$$\mathcal{F} = \int d\mathbf{x} \left\{ f[c(\mathbf{x}), \eta_1(\mathbf{x}), \eta_2(\mathbf{x}), \eta_3(\mathbf{x})] + \frac{\kappa_c}{2} |\nabla c(\mathbf{r})|^2 + \frac{\kappa_\eta}{2} \sum_{i=1}^3 |\nabla \eta_i(\mathbf{x})|^2 \right\} \quad (6.8)$$

where  $\kappa_c$  and  $\kappa_\eta$  are the gradient-energy coefficients.

In the limit of diffusion-controlled transformation, the  $\gamma$  phase is at local equilibrium with the  $\gamma'$  phase at their interface. Thus the diffuse interface (marked by II in Fig. 6.5(b)) bridges the equilibrium phases of  $\gamma'$  (marked by I) and  $\gamma$  (by III). The profiles of  $c$  and  $\eta$  across the interface shown in Fig. 6.5(b) are simulation results obtained using Eqs.(6.5)-(6.8). The gradient-energy coefficients are  $\kappa_c = 7.1 \times 10^{-15} \text{ Jm}^2/\text{mol}$  and  $\kappa_\eta = 3.6 \times 10^{-17} \text{ Jm}^2/\text{mol}$ , obtained by fitting the interfacial energy to experimental data, e.g., 14 mJ/m<sup>2</sup> [161]. The computational grid spacing is  $l_0 = 0.09 \text{ nm}$ .

As the values of  $c$  and  $\eta$  within the interface (Fig. 6.5(b)) are mapped onto the bulk free energy contour plot given in Fig. 6.5(a) (calculated from Eq.(6.5) with  $\eta_1 = \eta_2 = \eta_3 = \eta$ ), they are clearly seen to pass through the lowest energy path between  $\gamma$  and  $\gamma'$  and across the saddle point in between. This path on the  $f$ - $c$ - $\eta$  surface is fully responsible for the interface properties, such as energy and thickness. On the other hand, the values of  $c$  and  $\eta$  in the supersaturated  $\gamma$  phase (region IV in Fig. 6.5(b)) follow a separate path (IV) along the  $\eta = 0$  edge on the free energy surface (Fig. 6.5(a)). This path is responsible for the growth of  $\gamma'$  precipitates. These results thus suggest a possibility of adjusting the interface thickness with none of the drive forces for growth and coarsening (i.e., the chemical potential gradient and the interfacial energy) altered.

Instead of scaling down uniformly the entire free energy surface for a wider interface, as employed in the preceding section for single driving force processes, we may now suppress only the portion that is responsible for interface thickness while leaving the rest unaltered. In such a modification, we can produce a more diffuse interface and at the same time maintain the chemical potential gradient and interfacial energy. For example, we may replace the bulk free energy in Eq.(6.8) by a modified function at 1300K:

$$f^m(c, \eta_1, \eta_2, \eta_3) = f(c, \eta_1, \eta_2, \eta_3)g(c, \eta_1, \eta_2, \eta_3) \quad (6.9)$$

where

$$g(c, \eta_1, \eta_2, \eta_3) = 1 - 0.8 \exp[-2000(0.9972c' - 0.0748\eta')^2 - 2.5(0.0748c' + 0.9972\eta')^2]$$

$$c' = c - 0.18$$

$$\eta' = \frac{1}{3}(|\eta_1| + |\eta_2| + |\eta_3|) - 0.657$$

$g(c, \eta_1, \eta_2, \eta_3)$  is simply a function that has values between zero and one along and in the vicinity of the relaxation path related to the interface (Fig. 6.6(b)), and is almost unity elsewhere on the free energy surface. Multiplication of this term to the bulk free energy effectively reduces the energy hump along the relaxation path of the interface while leaving the free energy associated with the growth process unchanged (Figs. 6.6(a), (c), and (d)). Note that in general  $g$  should be also a function of temperature. To maintain the same interfacial energy and thus the coarsening kinetics, we need to increase the gradient-energy coefficients accordingly. Since none of the driving forces is altered in this approach, we expect the same kinetics for both growth and coarsening as that obtained by calculations with a direct use of the material parameters, nevertheless, of a much narrower interface.

Figure 6.7 compares the composition profiles across the interface produced by the original and the modified bulk free energies. In the modified case,  $\kappa_c = 2.2 \times 10^{-14} \text{ Jm}^2/\text{mol}$  and  $\kappa_\eta = 1.1 \times 10^{-16} \text{ Jm}^2/\text{mol}$  are used to maintain the same interfacial energy. The modification results in roughly a four-time increase in interface thickness (Fig. 6.7). Correspondingly, the grid spacing in the modified system can be four times greater if the same nodal density is kept within the interface.

To compare the growth kinetics, we consider 1D growth of a  $\gamma'$  precipitate in a supersaturated  $\gamma$  matrix. The mesh spacing is chosen as 0.09nm with the use of the original bulk free energy and 0.36nm with the use of the modified free energy. In both cases, the number of grid points within the interface is kept approximately the same. The length perpendicular to the interface is set as 92nm, which requires 1024 grid points in the former case and only 256 grid points in the latter. For a full-scale 3D simulation, the total amount of CPU time saving will be  $\sim 4^5$  (1024) times.

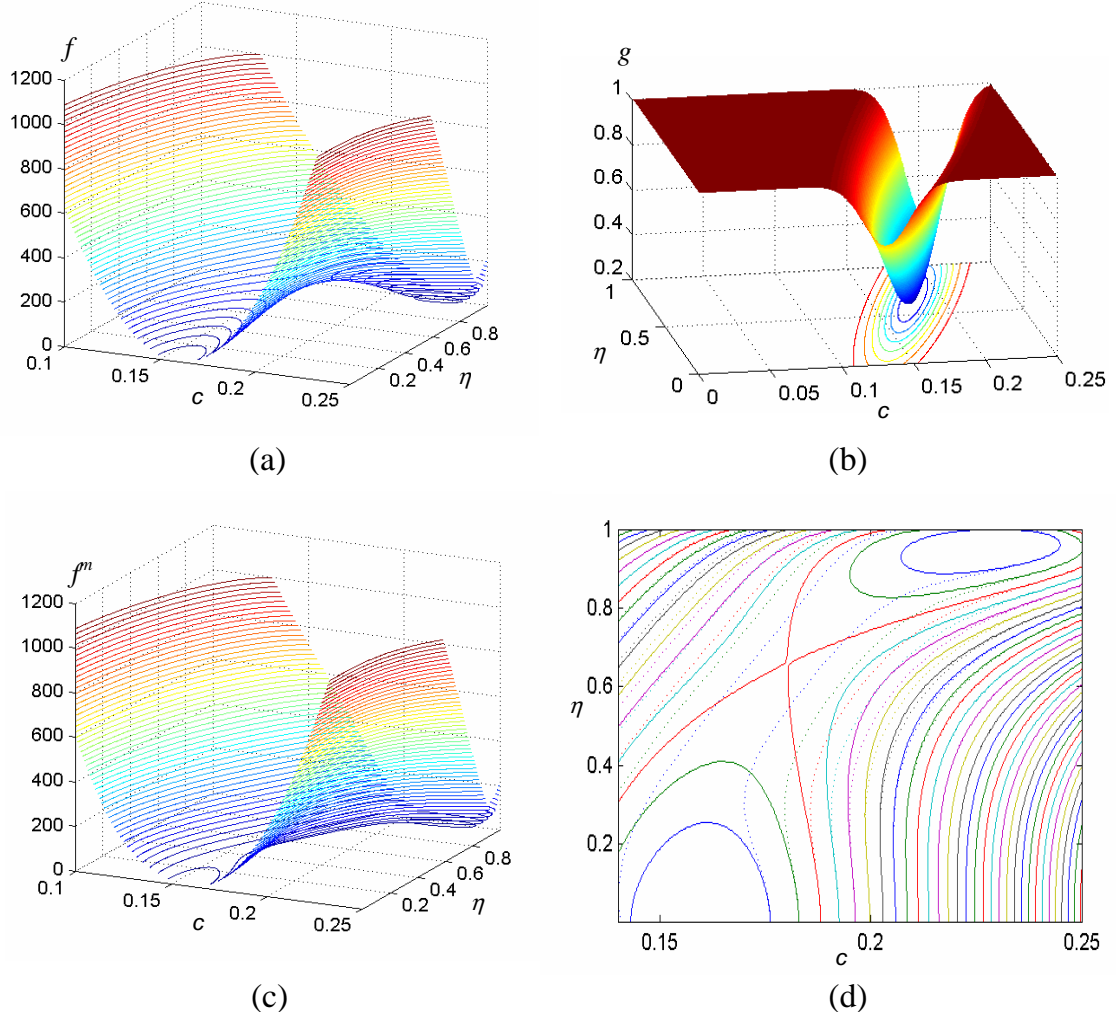


Figure 6.6: Modification of the  $f$ - $c$ - $\eta$  surface (a) by a specially constructed function (b) to lower locally the energy hump between the two equilibrium phases to widen the interface thickness. The  $f$ - $c$ - $\eta$  surface after the modification is shown in (c) and its contour plots on the  $c$ - $\eta$  plane is shown in (d) (dash lines). For comparison, the contours of the free energy surface shown in (a) are also plotted in (d) by the solid lines. It is readily seen that the free energy surface along the  $\eta = 0$  line that determines the growth kinetics is unchanged.

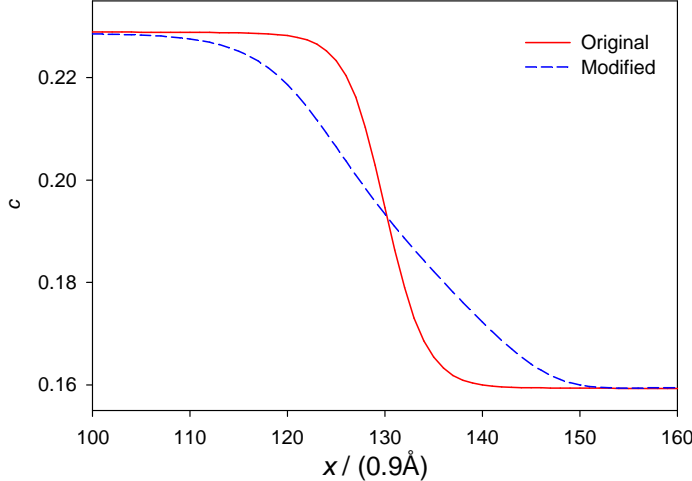


Figure 6.7: Comparison of composition profiles across an interface produced by the original and modified local free energy  $f(c, \eta_1, \eta_2, \eta_3)$ . The interfacial energies associated with the two profiles are the same.

Concentration and *lro* parameter profiles across the interface in the two cases are compared in Fig. 6.8 at different times. It is seen that the position of the interfaces match well at all times in the two cases.

It should be emphasized that in increasing the interface thickness the approach used previously [162, 159] for concurrent processes scales down the entire local free energy surface uniformly. In doing so the driving force for growth and hence the growth kinetics will be altered. This is clearly demonstrated by two parallel simulations performed with the same initial configuration consisting of 50 nuclei of  $\gamma'$  phase randomly distributed in a uniform supersaturated  $\gamma$  matrix. In one case, the modified free energy (Eq.(6.9)) is used to lower the energy hump and to increase the interface width, while in the other the free energy  $f(c, \eta_1, \eta_2, \eta_3)$  is divided by a factor of 4 and the gradient-energy coefficients are increased by 4 times in order to match

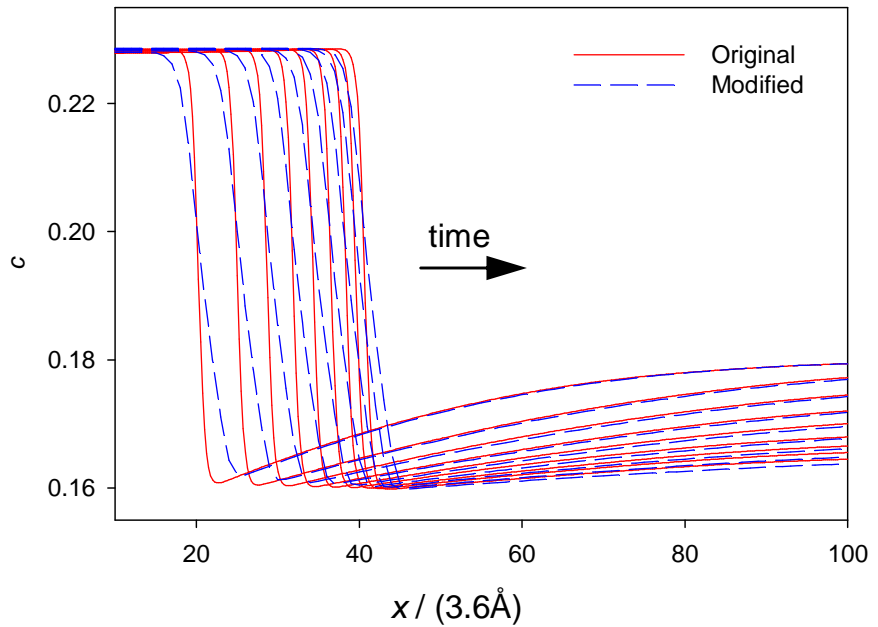


Figure 6.8: Composition profiles across the interface at different times obtained from the original (solid lines) and modified (dash lines) local free energy function. The well matched interface positions at all times indicate that the growth kinetics is the same in both cases even though the interface thickness is different.

the same interface thickness and interfacial energy. The simulation results obtained for the two cases are compared in Fig. 6.9, with the top row for the latter case and the bottom row for the former case, respectively. The system size is  $256l_0 \times 256l_0$  with  $l_0 = 0.36\text{nm}$ . The time scale is the same in both simulations. It is readily seen that particles in the top row grow more slowly. In fact, a close comparison of the particle sizes in Figs. 6.9(c) and (f) indicates that the growth rate is about 4 times slower in the top row. This becomes obvious if one recognizes that the driving force for growth has been reduced by 4 times when  $f(c, \eta_1, \eta_2, \eta_3)$  is divided by 4. However, the coarsening processes taking place at later stages in the two cases are about the same due to the same interfacial energy, leading to very similar microstructures at  $t=800$  (in reduced unit).

## 6.4 Summary and discussion

In quantitative phase field modeling using material-specific parameters as inputs, the affordable system sizes are limited by the actual interface thickness. For individual processes such as growth or coarsening, by modifying appropriate physical parameters of the system, one can diffuse the interface to the length scale of practical interests without altering the driving force. The approaches for each particular case are summarized in Table 6.1.

Such a degree of freedom is, however, not available in concurrent processes involving multiple driving forces such as simultaneous growth and coarsening. In this case the common practice of uniformly scaling down the bulk free energy function fails to produce correct growth kinetics. Considering the fact that additional degrees of freedom may exist in a multi-dimensional free energy surface, we have developed an

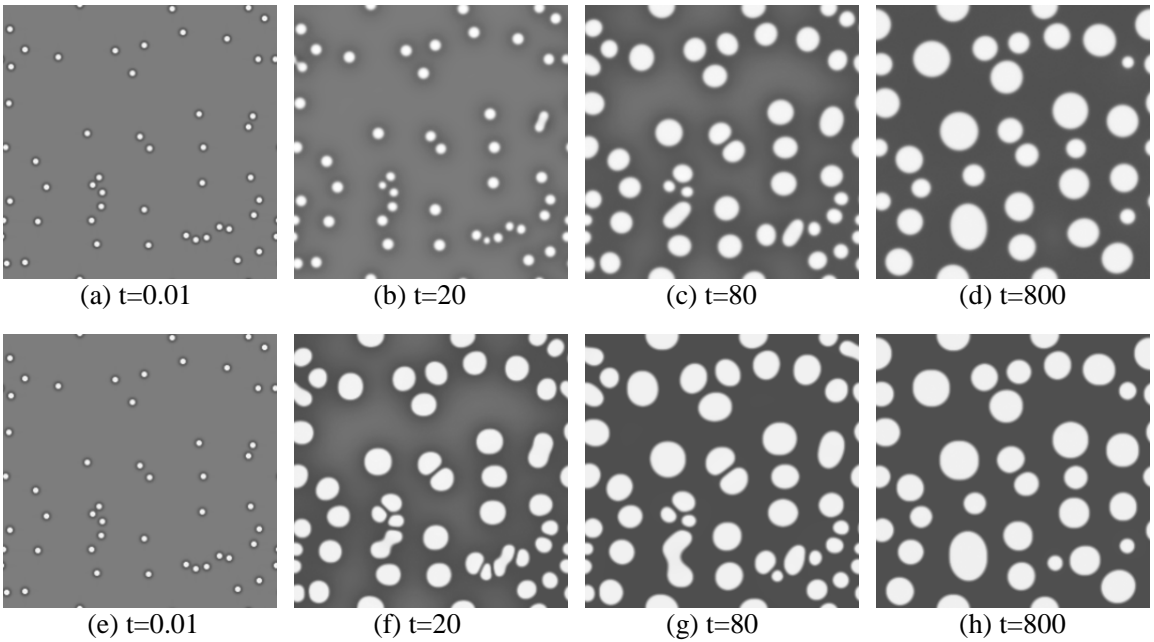


Figure 6.9: Microstructural evolutions predicted by the conventional approach (a-d) and the new approach (e-h), starting from the same initial configuration consisting of 50 randomly distributed nuclei. It is readily seen that the conventional approach predicts a much slower growth rate. The system size is 92nm×92nm.

Table 6.1: Summary of the treatments for individual processes to produce right kinetics at a wider interface.

Type of process	Variables	Rate	Approach	Required calibration
APD/grain growth	$\eta$	$\propto \kappa$	Fix $\kappa$ , reduce $\Delta f_0$	$\sigma \leftarrow \sigma^{simul} \sqrt{\kappa/\kappa^{simul}}$
Precipitate growth	$c$	$\propto \nabla (\propto \Delta f_0)$	Fix $\Delta f_0$ , increase $\kappa$	$\sigma \leftarrow \sigma^{simul} \sqrt{\kappa/\kappa^{simul}}$
Coarsening	$c$	$\propto \sigma (\propto \sqrt{\kappa \Delta f_0})$	Fix $\kappa \Delta f_0$ , increase $\kappa/\Delta f_0$	

approach for increasing the length scale of a concurrent process with none of the driving forces for each individual process altered. This is achieved by modifying locally the hump on the  $f$ - $c$ - $\eta$  surface between the two equilibrium phases, which determines the interface thickness but is not associated with the driving force for growth. The approach allows for quantitative modeling of microstructural evolution with multiple driving forces to take full advantage of critically assessed free energy and interfacial energy databases that are currently under active development. For the particular example considered, i.e., precipitation of  $\gamma'$  in a binary Ni-Al alloy, the total CPU time saving is  $\sim$ 64 times in 1D and 1024 times in 3D as compared to brute force calculations.

An artificially diffused interface in the phase field model may alter the non-equilibrium effects at interface from interface kinetics, solute trapping, interface stretching and surface diffusion, as have been discussed by Karma for quantitative phase field modeling of alloy solidification [163]. For individual processes discussed in Section 6.2 the kinetic effects can be proven negligible when the typical length scale of the microstructure (e.g., the domain or precipitate size) considerably exceeds the interface thickness. For precipitate growth, the condition becomes  $\lambda/\Lambda \ll 1$ , where  $\Lambda$  is the characteristic diffusion distance [37]. For concurrent processes discussed in Section 6.3, the interface kinetic effect is eliminated by adjusting the mobility of the  $lro$  parameters ( $L$ ) to ensure a diffusion-controlled process. This is similar to the approach of Karma and Rappel [40] who chose to adjust the diffusivity. Furthermore, since isotropic interface properties and constant diffusivity for the entire system are assumed in the current study, the other non-equilibrium effects vanish as well. Detailed discussions of various non-equilibrium effects can be found in [37, 163].

# CHAPTER 7

## CONCLUSIONS

### 7.1 Conclusions

Modeling real material microstructure often encounters three issues: (1) a coherent description of all contributing microstructure components (phases, grains, defects, etc.); (2) quantitativeness; and (3) computational efficiency. The first issue is concerned with a collective, non-additive contribution from microstructure components, for example, through long-range diffusion, elastic interactions, etc. It may also extend to the microstructure-property relationship. The second issue ensures appropriate relative contributions from the individual component, especially important in a complex system. The last one aims to fit all components in an affordable computational model. The major focus of the thesis work is to pursue a practical modeling framework at mesoscales with the three elements.

An explicit nucleation algorithm is developed to allow nucleation to be treated as a function of instantaneous local conditions, including composition, temperature, and stress state. It circumvents the previous difficulties in using Langevin noise where nucleation is constrained at site-saturation limit. Concurrent description of nucleation with growth and coarsening is necessary to simulation of microstructures

under many realistic conditions, such as high volume fraction and non-isothermal heat treatment. Coherency strain energy is incorporated to the nucleation driving force to account for elastic interactions with mesoscale microstructures as well as among nucleating precipitates in an elastically anisotropic solid. Both effects are observed in simulations as a result of the interplay between chemical free energy and elastic energy. The concurrent description of nucleation, growth, and coarsening is applied to study the overall kinetics of diffusion-controlled precipitation and to compare with the corresponding JMAK theory. The Avrami exponents, while agree with the JMAK predictions at early stages, in general decay with time due to both soft-impingement and Gibbs-Thomson effect.

Mesoscale dislocation networks and microscopic dislocation core structures are studied in an extended phase field dislocation model. With the necessary correction and generalization to the energy formulations according to crystal symmetry, the model is shown to handle self-consistently the dislocation nodal reactions and core dissociation. The latter, with accurate  $\gamma$ -surface as input, can quantitatively characterize dislocation core structures and various associated planar faults. Agreements are found in comparison with Peierls-Nabarro analyses for dissociation of straight dislocations in Al and Pd. In addition, the model provides the possibility to study dislocation structures in non-planar configuration. The study of dislocation interacting with  $\gamma/\gamma'$  microstructure aims to treat the both in a unified phase field model, where dislocations and precipitates are described by different field variables, and they enter the same elastic energy formulation. This provides an opportunity to bridge microstructure simulation and material property prediction in a same methodology.

The simulation length scale limit due to physical width of interface is discussed as a generic feature in phase field models. Conventional approaches to increase the length scale via artificially widening interface are quantitatively examined. Their applicability and limitations are analyzed for typical processes including APD/grain growth, precipitate growth, and coarsening. The criterion is to maintain the respective controlling driving force so as to ensure the right kinetics. Necessary corrections to the altered physical parameters are provided. For processes involving multiple driving forces, where the conventional treatments do not apply, novel approach with modification on the free energy surface is proposed to increase the length scale and thus the computational efficiency. These studies are necessary for quantitative phase field modeling at a mesoscopic length scale.

## 7.2 Directions for future research

The concurrent nucleation, growth, and coarsening model can be implemented to an engineering tool to predict microstructures for real material systems. For example, it can be applied to Ni-Al alloy to study the development of multi-modal precipitate size distribution under non-isothermal heat treatment. Temperature dependent material parameters, such as the chemical free energy, interfacial energy, and kinetic constants should be obtained first. Nucleation should be calibrated quantitatively, or semi-quantitatively, to experimental data. The simulation size necessary for observing the multi-modal precipitates should be determined according to experimental micrograph. The approach proposed in Section 6.3 for increasing simulation length scale may be applied with the modification function  $g$  extended to non-isothermal conditions. With a given heat treatment scheme the microstructures predicted by

the model need to be compared with the experimental results. Upon achieving an agreement, the model may explore alternate heat treatment curves and predict the optimal processing parameters.

The further extension of the dislocation model may be pursued along three lines. First, dislocation climb will be introduced. In a similar picture to a glide dislocation, the climb dislocation may be described by a platelet on a “climb” plane with a tensile stress-free strain. Since the “climb” plane is a non-physical plane, the choice of its orientation should be arbitrary and the dislocation motion should be independent of any particular choice. Energy formulation for the climb dislocations will be similar to that for the glide dislocations. The kinetic motion of the climb dislocation should follow the vacancy diffusion. In addition, the energy barrier for the cross-slip of screw dislocation may be calibrated to given experimental or theoretical value. With cross-slip and climb, evolution of 3D dislocation networks may be described quantitatively in the phase field model.

Dislocation cutting ordered  $\gamma'$  particle can be studied in more detail. The transition of the core structure as a  $\gamma$ -matrix dislocation enters the  $\gamma'$  particle and the corresponding energy changes can be studied in a similar manner as the Peierls-Nabarro model. Elastic modulus difference may be introduced to take into account the additional image force at  $\gamma/\gamma'$  interface. Energy barrier for a single dislocation to enter the  $\gamma'$  particle can be evaluated. Furthermore, lattice mismatch between  $\gamma$  and  $\gamma'$  may be introduced. The effect may be studied in conjunction with dislocation motion in  $\gamma$  channels.

Lattice friction is missing in the current phase field dislocation model because the energy formulation is invariant with respect to an arbitrary translation of a dislocation line. To take into account this necessary feature for dislocation kinetics, the model may be formulated on a real lattice of the given crystal. The total energy correspondingly becomes a discrete sum over all lattice points. In addition, the continuum elastic energy will be replaced by elastic energy based on the lattice Green's function formulation.

## APPENDIX A

### STRAIN ENERGY OF A TWO-DIMENSIONAL COHERENT PRECIPITATE

The strain energy of a 2D coherent precipitate in a “cubic” solid can be directly derived from the 3D solution of Khachaturyan *et al.* [85] if one dimension is extended to infinite (to zero in the reciprocal space). By assuming the (cross-section of) precipitate is circular and the transformation strain is  $\epsilon_{ij}^T = \epsilon^T \delta_{ij}$ , the approximate solution of the strain energy (per unit length) is

$$E^{el} = \frac{A\beta\epsilon^T}{c_{11}} \left[ (c_{11} - c_{12}) - \frac{2\beta\Delta I_1}{2c_{11} - \Delta} - \frac{9\beta\Delta^2 I_2}{(2c_{11} - \Delta)(3c_{11} - 2\Delta)} \right] \quad (\text{A.1})$$

where  $A = \pi r_0^2$  is the area and  $r_0$  the radius of the precipitate,  $\beta = c_{11} + 2c_{12}$ ,  $\Delta = c_{11} - c_{12} - 2c_{44}$ ,  $I_2 = 0$ , and  $I_1 = (\pi r^2)^{-1} \int d\mathbf{g}/(2\pi)^2 (\sin^2 \phi \cos^2 \phi) |\tilde{\theta}(\mathbf{g})|^2$ . Here  $\phi$  is the angle between the reciprocal vector  $\mathbf{g}$  and the real space vector  $\mathbf{x}$  (Fig. A.1).

The function  $\theta(\mathbf{x})$  describes the shape of the precipitate:

$$\theta(\mathbf{x}) = \begin{cases} 1, & |\mathbf{x}| \leq r_0 \\ 0, & |\mathbf{x}| > r_0 \end{cases}$$

and its Fourier transform is  $\tilde{\theta}(\mathbf{g}) = (2\pi r_0/g) J_1(gr_0)$ , where  $J_1$  is the Bessel function of the first kind for  $n = 1$ . With the substitution of  $\tilde{\theta}(\mathbf{g})$ ,  $I_1$  is reduced to

$$I_1 = \frac{1}{(2\pi)^2 A} \int_0^{2\pi} \sin^2 \phi \cos^2 \phi d\phi \int_0^\infty \frac{4\pi^2 r_0^2 J_1^2(gr_0)}{g^2} g dg = \frac{1}{8}$$

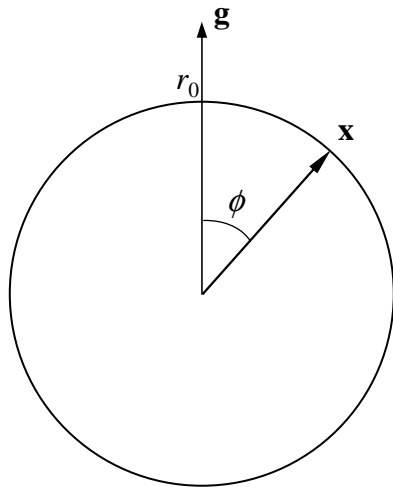


Figure A.1: Vectors in  $I_1$ .

By substituting into Eq.(A.1) we have

$$E^{el} = A \frac{\beta \epsilon^T 2}{c_{11}} \left[ (c_{11} - c_{12}) - \frac{\beta \Delta}{4(2c_{11} - \Delta)} \right] \quad (\text{A.2})$$

## APPENDIX B

### CONCENTRATIONS AT A CURVED INTERFACE

As discussed in Section 2.4.3, the departure from the equilibrium concentrations at interface in diffusion-controlled precipitate growth is determined by both interface curvature and velocity. At small velocity, characterized in a Cahn-Hilliard type phase field model by  $\xi/\Lambda \ll 1$  where  $\xi$  and  $\Lambda$  are the interface width and the diffusion distance in matrix respectively, the concentration deviation at interface is dominated by the curvature.

For a spherical  $\beta$  particle of interface area  $A$  and interfacial free energy  $\sigma$  in equilibrium with  $\alpha$  matrix, the molar free energy of the  $\beta$  phase is raised by  $\sigma(dA/dn^{(\beta)})$ , with respect to a flat interface [66], where  $n^{(\beta)}$  is the mole of  $\beta$ . In an A-B binary system, for example, the increase in the chemical potential can be expressed as (Fig. B.1)

$$\delta\mu = \delta\mu^{(\beta)} = \delta(\mu_B^{(\beta)} - \mu_A^{(\beta)}) \cong \frac{\sigma}{X_\infty^{(\beta)} - X_\infty^{(\alpha)}} \frac{dA}{dn^{(\beta)}} = \frac{1}{v^{(\beta)}} \frac{\sigma}{c_\infty^{(\beta)} - c_\infty^{(\alpha)}} \frac{dA}{dn^{(\beta)}} \quad (\text{B.1})$$

where  $X_\infty^{(\alpha)}$ ,  $X_\infty^{(\beta)}$  are the equilibrium mole fractions of the B component in  $\alpha$  and  $\beta$  phases at a flat interface, respectively, and  $c_\infty^{(\alpha)}$ ,  $c_\infty^{(\beta)}$  are the corresponding concentrations.  $v^{(\beta)}$  is molar volume of the  $\beta$  phase. For a sphere (3D),

$$V = \frac{4}{3}\pi R^3 = n^{(\beta)}v^{(\beta)}, \quad A = 4\pi R^2 = 4\pi \left(\frac{3V}{4\pi}\right)^{\frac{2}{3}}, \quad \frac{dA}{dn^{(\beta)}} = v^{(\beta)} \frac{dA}{dV} = \frac{2v^{(\beta)}}{R}$$

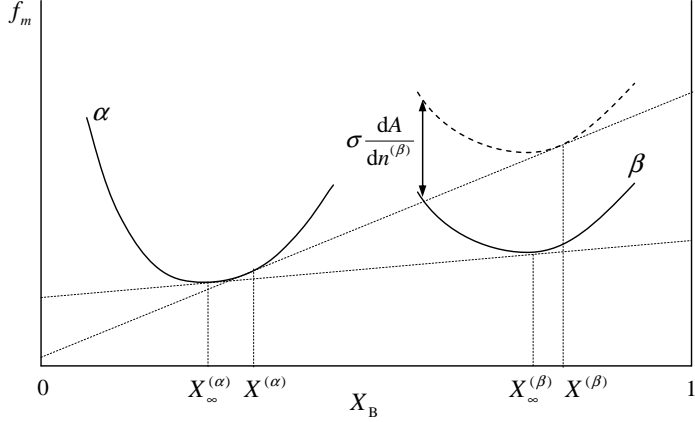


Figure B.1: Gibbs-Thomson effect on the molar free energy.

and for a cylinder (2D)

$$V = \pi R^2 L = n^{(\beta)} v^{(\beta)}, \quad A = 2\pi R L = 2\pi \left(\frac{V}{\pi}\right)^{\frac{1}{2}} L, \quad \frac{dA}{dn^{(\beta)}} = v^{(\beta)} \frac{dA}{dV} = \frac{v^{(\beta)}}{R}$$

Substitution into Eq.(B.1) yields

$$\delta\mu_{3D}^{(\beta)} = \frac{1}{c_\infty^{(\beta)} - c_\infty^{(\alpha)}} \frac{2\sigma}{R} \quad (B.2)$$

$$\delta\mu_{2D}^{(\beta)} = \frac{1}{c_\infty^{(\beta)} - c_\infty^{(\alpha)}} \frac{\sigma}{R} \quad (B.3)$$

which are identical to Eq.(2.53) derived from the diffusion interface approach.

The equilibrium concentrations at a curved interface are determined by the common tangent line between the  $\alpha$  phase and the raised  $\beta$  phase in the  $f_m$ - $X$  curve. Note chemical potential  $\mu^{(\beta)} = \partial f_m / \partial X = d(fv^{(\beta)}) / d(c^{(\beta)}v^{(\beta)}) = df / dc_B^{(\beta)}$ , where  $f$  is the per volume free energy, the analysis also applies to  $f$ - $c$  curves. By applying Eq.(B.3) to the free energy model (Eq.(3.16)) employed in Section. 3.6.1, the concentrations at interface are given by

$$\frac{df}{dc} = 4\Delta f_0 c_{eq}^{-4} (-c + c^3) = \delta\mu = \frac{d-1}{2c_{eq}} \frac{\sigma}{R}$$

where we have place the dimensionality  $d$  back into the equation. The solutions are

$$c^{(\alpha)}(R) = -\frac{2c_{eq}}{\sqrt{3}} \cos\left(\frac{\varphi - \pi}{3}\right) \quad (\text{B.4})$$

$$c^{(\beta)}(R) = \frac{2c_{eq}}{\sqrt{3}} \cos\left(\frac{\varphi}{3}\right) \quad (\text{B.5})$$

where

$$\varphi \equiv \cos^{-1} \left( \frac{3\sqrt{3}(d-1)\sigma}{16\Delta f_0} \frac{1}{R} \right)$$

## BIBLIOGRAPHY

- [1] J. Christian, *The theory of transformations in metals and alloys*, Pergamon, Amsterdam ; Boston, 2002.
- [2] J. Hirth and J. Lothe, *Theory of dislocations*, Wiley, New York, 2nd ed., 1982.
- [3] Landolt-Bornstein, *Numerical data and functional relationships in science and technology*, Vol. III/1, Springer-Verlag, Berlin, 1966.
- [4] B. von Sydow, J. Hartford, and G. Wahnström, *Computational materials science*, **15**, 367–79 (1999).
- [5] J. Langer, *Physica*, **73**, 61–72 (1974).
- [6] J. Cahn In *The mechanism of phase transformations in crystalline solids*; The Institute of Metals, London, 1969; page 1.
- [7] M. Kaufman, P. Voorhees, W. Johnson, and F. Biancaniello, *Metallurgical Transactions A.*, **20**, 2171–2175 (1989).
- [8] R. Cahn, *Artifice and Artefacts, 100 Essays in Materials Science*, Institute of Physics Publishing Ltd., Bristol and Philadelphia, 1992.
- [9] F. Abraham, *Philosophical transactions of the Royal Society of London. Series A*, **360**, 367–82 (2002).
- [10] J. Langer, M. Bar-on, and H. Miller, *Physical Review A*, **11**(4), 1417–29 (1975).
- [11] J. Simmons, C. Shen, and Y. Wang, *Scripta Materialia*, **43**, 935–942 (2000).
- [12] C. Shen, J. Simmons, and Y. Wang, *Acta Materialia* (submitted).
- [13] Y. Wen, J. Simmons, C. Shen, C. Woodward, and Y. Wang, *Acta Materialia*, **51**, 1123–32 (2003).
- [14] C. Shen and Y. Wang, *Acta Materialia*, **51**, 2595–2610 (2003).
- [15] C. Shen and Y. Wang, *Acta Materialia*, **52**, 683–691 (2004).

- [16] C. Shen, A. Kazaryan, P. Anderson, and Y. Wang In M. Laudon and B. Romanowicz, Eds., *The 2nd International Conference on Computational Nanoscience and Nanotechnology*, pages 259–262. Computational Publications, Cambridge, MA, 2002.
- [17] C. Shen and Y. Wang, *International Journal for Multiscale Computational Engineering*, **1**(1), 103–117 (2003).
- [18] C. Shen, M. Mills, and Y. Wang, *Materials Research Society Symposium Proceedings*, **753**, BB5.21.1 (2003).
- [19] C. Shen, Q. Chen, Y. Wang, Y. Wen, and J. Simmons, *Scripta Materialia*, **50**(7), 1023–1028 (2004).
- [20] C. Shen, Q. Chen, Y. Wang, Y. Wen, and J. Simmons, *Scripta Materialia*, **50**(7), 1029–1034 (2004).
- [21] J. Cahn and J. Hilliard, *Journal of Chemical Physics*, **28**(2), 258–267 (1958).
- [22] W. Boettinger, J. Warren, C. Beckermann, and A. Karma, *Annual review of materials research*, **32**, 163–194 (2002).
- [23] A. Khachaturyan, *Philosophical Magazine A*, **74**(1), 3–14 (1996).
- [24] K. Binder, *Reports on progress in physics*, **50**, 783–859 (1987).
- [25] P. Hohenberg and B. Halperin, *Reviews of Modern Physics*, **49**(3), 435–479 (1977).
- [26] J. Gunton, M. Miguel, and P. Sahni In *Phase transitions and critical phenomena*, C. Domb and J. L. Lebowitz, Eds., Vol. 8; Academic Press, New York, 1983.
- [27] J. Cahn, *Acta Metallurgica*, **9**, 795–801 (1961).
- [28] S. Allen and J. Cahn, *Acta Metallurgica*, **27**, 1085–1095 (1979).
- [29] N. Goldenfeld, *Lectures on phase transitions and the renormalization group*, Addison-Wesley Publishing Company, 1992.
- [30] R. Pathria, *Statistical Mechanics*, Butterworth-Heinemann, 2nd ed., 1996.
- [31] R. Zwanzig, *Nonequilibrium statistical mechanics*, Oxford University Press, Inc, New York, 2001.
- [32] J. Langer, *Annals of Physics*, **54**, 258–275 (1969).

- [33] J. Langer, *Annals of Physics*, **65**, 53–86 (1971).
- [34] J. Langer In *Solids far from equilibrium*, C. Godrche, Ed.; Cambridge University Press, New York, 1992.
- [35] A. Bray, *Advances in Physics*, **51**(2), 481–587 (2002).
- [36] G. Caginalp, *Physical Review A*, **39**(11), 5887–5896 (1989).
- [37] K. Elder, M. Grant, N. Provatas, and J. Kosterlitz, *Physical Review E*, **64**, 021604 (2001).
- [38] G. Caginalp and W. Xie, *Physical Review E*, **48**(3), 1879–1909 (1993).
- [39] A. Karma and W.-J. Rappel, *Physical Review E*, **53**(4), 3017–3020 (1996).
- [40] A. Karma and W.-J. Rappel, *Physical Review E*, **57**(4), 4323–4349 (1998).
- [41] R. Almgren, *SIAM Journal on Applied Mathematics*, **59**(6), 2086–2107 (1999).
- [42] G. McFadden, A. Wheeler, and D. Anderson, *Physica D*, **144**, 154–168 (2000).
- [43] J. Eshelby, *Proceedings of the Royal Society of London. Series A*, **241**(376-96) (1957).
- [44] J. Eshelby, *Proceedings of the Royal Society of London. Series A*, **252**, 561 (1959).
- [45] S. Sass, T. Mura, and J. Cohen, *Philosophical Magazine*, **16**, 679 (1967).
- [46] G. Faivre, *Physica status solidi*, **35**, 249 (1969).
- [47] R. Sankaran and C. Laird, *Journal of the Mechanics and Physics of Solids*, **24**, 251 (1976).
- [48] J. Lee and W. Johnson, *Physica status solidi*, **46**, 267 (1978).
- [49] J. Lee, D. Barnett, and H. Aaronson, *Metallurgical Transactions A*, **8**, 963 (1977).
- [50] A. Khachaturyan, *Fizika Tverdogo Tela*, **8**, 2710 (1966).
- [51] A. Khachaturyan, *Sov. Phys. Solid State*, **8**, 2163 (1967).
- [52] A. Khachaturyan, *Theory of Structural Transformations in Solids*, John Wiley & Sons, New York, 1983.
- [53] A. Onuki, *Journal of the Physical Society of Japan*, **58**, 3065–68 (1989).

- [54] Y. Wang, L. Chen, and A. Khachaturyan, *Scripta metallurgica et materialia*, **25**, 1387–92 (1991).
- [55] L. Chen, Y. Wang, and A. Khachaturyan, *Philosophical magazine letters*, **65**, 15–23 (1992).
- [56] W. Johnson and P. Voorhees, *Journal of Applied Physics*, **61**, 1610 (1986).
- [57] A. Khachaturyan, S. Semennovskaya, and T. Tsakalakos, *Physical Review B*, **52**, 15909 (1995).
- [58] S. Hu and L. Chen, *Acta Materialia*, **49**, 1879 (2001).
- [59] Y. Wang, Y. Jin, and A. Khachaturyan, *Journal of Applied Physics*, **92**(3), 1351–1360 (2002).
- [60] D. Li and L. Chen, *Acta Materialia*, **46**(2), 639–49 (1998).
- [61] D. Li and L. Chen, *Acta Materialia*, **45**(6), 2435–42 (1997).
- [62] W. Press, *Numerical recipes in fortran 77 : the art of scientific computing*, Cambridge University Press, New York, 2nd ed., 1996.
- [63] J. Cahn, *Acta Metallurgica*, **10**, 907–913 (1962).
- [64] J. Cahn, *Acta Metallurgica*, **10**, 179 (1962).
- [65] J. Cahn, *Acta Metallurgica*, **14**, 83 (1966).
- [66] J. Christian, *The theory of transformations in metals and alloys*, Pergamon Press, Oxford, 2nd ed., 1975.
- [67] E. Nembach and G. Neite, *Progress in Materials Science*, **29**, 177–319 (1985).
- [68] K. Binder and D. Stauffer, *Advances in Physics*, **25**(4), 343–396 (1976).
- [69] K. Binder, *Physical Review B*, **15**(9), 4425–4447 (1977).
- [70] J. Langer and A. Schwartz, *Physical Review A*, **21**(3), 948–958 (1980).
- [71] H. Wendt and P. Haasen, *Acta Metallurgica*, **31**, 1649 (1983).
- [72] R. Kampmann and R. Wagner In *Decomposition of alloys: the early stages*, P. Haasen, V. Gerold, R. Wagner, and M. F. Ashby, Eds.; Pergamon Press, Oxford, 1984; pages 91–103.
- [73] R. Wagner and R. Kampmann In *Materials Science and Technology: A Comprehensive Treatment*, R. W. Cahn, P. Haasen, and E. Kramer, Eds.; VCH, Weinheim; New York, 1991.

- [74] P. Haasen, *Physical metallurgy*, Cambridge university press, Cambridge; New York, 3rd ed., 1996.
- [75] H. Aaronson and F. LeGoues, *Metallurgical Transactions A.*, **23**, 1915 (1992).
- [76] M. Volmer and A. Weber, *Zeitschrift für physikalische Chemie*, **119**, 277 (1926).
- [77] R. Becker and W. Döring, *Annals of Physics*, **24**, 719 (1935).
- [78] H. Aaronson and J. Lee In *Lectures on the theory of phase transformations*, H. I. Aaronson, Ed.; The Minerals, Metals & Materials Society, 1999; pages 165–229.
- [79] J. Cahn and J. Hilliard, *Journal of Chemical Physics*, **31**, 688 (1959).
- [80] J. Langer and L. Turski, *Physical Review A*, **8**(6), 3230–3243 (1973).
- [81] J. Katz, C. Scoppa II, N. Kumar, and P. Mirabel, *Journal of Chemical Physics*, **62**, 448 (1975).
- [82] K. Russell In *Phase Transformations*, H. I. Aaronson, Ed.; American Society for Metals, Metals Park, OH, 1970; page 219.
- [83] F. Larché, *Annual review of materials science*, **20**, 83–99 (1990).
- [84] V. Perovic and G. Purdy, *Acta Metallurgica*, **29**, 889–902 (1981).
- [85] A. Khachaturyan, S. Semenovskaya, and J. Morris, J.W., *Acta Metallurgica*, **36**(6), 1563–1572 (1988).
- [86] A. Kolmogorov, *Izv Akad Nauk SSSR, Ser Matem* **3**, 355–359 (1937).
- [87] W. Johnson and R. Mehl, *TAIME*, **135**, 416–458 (1939).
- [88] M. Avrami, *Journal of Chemical Physics*, **7**, 1103–1112 (1939).
- [89] M. Avrami, *Journal of Chemical Physics*, **8**, 212–224 (1940).
- [90] M. Avrami, *Journal of Chemical Physics*, **9**, 177–184 (1941).
- [91] M. Weinberg, *Journal of Crystal Growth*, **82**, 779–780 (1987).
- [92] C. Wert and C. Zener, *Journal of Applied Physics*, **21**, 5–8 (1950).
- [93] F. Ham, *The Journal of physics and chemistry of solids*, **6**, 335–351 (1958).
- [94] D. Crespo, T. Pradell, M. Clavaguera-Mora, and N. Clavaguera, *Physical Review B*, **55**(6), 3435–3444 (1997).

- [95] T. Pradell, D. Crespo, N. Clavaguera, and M. Clavaguera-Mora, *Journal of Physics: Condensed Matter*, **10**, 3833–3844 (1998).
- [96] G. Yu, Y. Lai, and W. Zhang, *Journal of Applied Physics*, **82**(9), 4270–4276 (1997).
- [97] R. Armstrong, J. Jackson, and L. Glass, *Science*, **183**(4123), 444–446 (1974).
- [98] E. Pineda, T. Pradell, and D. Crespo, *Philosophical Magazine A*, **82**(1), 107–121 (2002).
- [99] E. Pineda and D. Crespo, *Journal of Non-Crystalline Solids*, **317**, 85–90 (2003).
- [100] L. Levine, L. Kubin, and R. Becker, *Materials Science and Engineering A*, **309-310**, ix (2001).
- [101] E. Kaxiras and M. Duesbery, *Physical Review Letters*, **70**(24), 3752–3755 (1993).
- [102] J. Hartford, B. Sydow, G. Wahnstrm, and B. Lundqvist, *Physical Review B*, **58**(5), 2487–2496 (1998).
- [103] G. Lu, N. Kioussis, V. Bulatov, and E. Kaxiras, *Physical Review B*, **62**(5), 3099–3108 (2000).
- [104] M. Mehl, D. Papaconstantopoulos, N. Kioussis, and M. Herbranson, *Physical Review B*, **61**(7), 4894–4897 (2000).
- [105] S. Ismail-Beigi and T. Arias, *Physical Review Letters*, **84**, 1499 (2000).
- [106] C. Woodward and S. Rao, *Physical Review Letters*, **88**, 216402 (2002).
- [107] S. Zhou, D. Preston, P. Lomdahl, and D. Beazley, *Science*, **279**, 1525–1527 (1998).
- [108] J. Chang, W. Cai, V. Bulatov, and S. Yip, *Materials Science and Engineering A*, **309-310**, 160–163 (2001).
- [109] D. Rodney, G. Martin, and Y. Brechét, *Materials Science and Engineering A*, **309-310**, 198–202 (2001).
- [110] F. Abraham, R. Walkup, H. Gao, M. Duchaineau, T. Diaz De La Rubia, and M. Seager, *Proceedings of National Academy of Sciences*, **99**, 5777–5782 (2002).
- [111] R. Peierls, *Proc. Phys. Soc.*, **52**, 23 (1940).
- [112] F. Nabarro, *Proc. Phys. Soc.*, **59**, 256 (1947).

- [113] G. Schoeck, *Philosophical Magazine A*, **69**(6), 1085–95 (1994).
- [114] G. Lu, N. Kioussis, V. Bulatov, and E. Kaxiras, *Philosophical magazine letters*, **80**, 675–682 (2000).
- [115] G. Lu, N. Kioussis, V. Bulatov, and E. Kaxiras, *Materials Science and Engineering A*, **309-310**, 142–7 (2001).
- [116] G. Schoeck, *Philosophical Magazine A*, **81**(5), 1161–1176 (2001).
- [117] G. Schoeck, *Materials Science and Engineering A*, **333**, 390–396 (2002).
- [118] B. Devincre and L. Kubin, *Materials Science and Engineering A*, **234**, 8–14 (1997).
- [119] R. Madec, B. Devincre, and L. Kubin, *Physical Review Letters*, **89**(25), 255081–255084 (2002).
- [120] R. Madec, B. Devincre, and L. Kubin, *Scripta Materialia*, **47**, 689–695 (2002).
- [121] R. Madec, B. Devincre, L. Kubin, T. Hoc, and D. Rodney, *Science*, **301**, 1879–1882 (2003).
- [122] K. Schwarz, *Journal of Applied Physics*, **85**(1), 108–119 (1999).
- [123] K. Schwarz, *Journal of Applied Physics*, **85**(1), 120–129 (1999).
- [124] X. Liu, F. Ross, and K. Schwarz, *Physical Review Letters*, **85**(19), 4088–4091 (2000).
- [125] P. Pant, K. Schwarz, and S. Baker, *Acta Materialia*, **51**, 3243–3258 (2003).
- [126] S. Groh, B. Devincre, L. Kubin, A. Roos, F. Feyel, and J.-L. Chaboche, *Philosophical magazine letters*, **83**(5), 303–313 (2003).
- [127] V. Bulatov, F. Abraham, L. Kubin, B. Devincre, and S. Yip, *Nature*, **391**, 669–672 (1998).
- [128] J. Broughton, F. Abraham, N. Bernstein, and E. Kaxiras, *Physical Review B*, **60**, 2391–2403 (1999).
- [129] A. Khachaturyan In *The Science of Alloys for the 21st Century: A Hume-Rothery Symposium Celebration*, P. Turchi, R. Shull, and A. Gonis, Eds.; TMS, St. Louis, MO, 2000; pages 293–308.
- [130] D. Rodney and A. Finel In M. Aindow, M. Asta, M. V. Glazov, D. L. Medlin, A. D. Rollet, and M. Zaiser, Eds., *MRS Symp Proc*, Vol. 652, pages Y4.9.1–Y4.9.6, Boston, 2000. MRS.

- [131] Y. Wang, Y. Jin, A. Cuitino, and A. Khachaturyan, *Acta Materialia*, **49**, 1847 (2001).
- [132] D. Rodney, Y. Le Bouar, and A. Finel, *Acta Materialia*, **51**, 17–30 (2003).
- [133] V. Vitek, *Philosophical Magazine*, **18**, 773 (1968).
- [134] F. Nabarro, *Philosophical Magazine*, **42**, 1224 (1951).
- [135] Y. Wang and A. Khachaturyan, *Acta Metallurgica Materialia*, **45**, 759 (1997).
- [136] Y. Jin, A. Artemev, and A. Khachaturyan, *Acta Materialia*, **49**, 2309–2320 (2001).
- [137] Y. Wang, Y. Jin, A. Cuitino, and A. Khachaturyan, *Philosophical Magazine*, **81**, 385 (2001).
- [138] L. Kubin In *Treatise in Materials Science and Technology*, H. Mughrabi, Ed., Vol. 6; VCH, D-Weinberg, 1993.
- [139] L. Kubin In *Stability of materials*, A. Gonis, P. Turchi, and J. Kudrnovski, Eds.; Plenum, New York, 1996; pages 99–135.
- [140] M. Przystupa and A. Ardell, *Metallurgical and materials transactions A*, **33A**, 231 (2002).
- [141] V. Lindroos and H. Miekk-OJA, *Philosophical Magazine*, **16**, 593 (1967).
- [142] L. Teutonico, *Acta Metallurgica*, **11**, 1283 (1963).
- [143] N. Thompson, *Proc. Phys. Soc.*, **66B**, 481 (1953).
- [144] T. Pollock and A. Argon, *Acta Metallurgica Materialia*, **40**(1), 1–30 (1992).
- [145] P. Anderson, *MRS Bulletin*, **Feb**, 27–33 (1999).
- [146] Q. Li and P. Anderson, private communications.
- [147] P. Anderson, Y. Wang, C. Shen, and Q. Li In *MRS Symposium on "Thin Films: Stresses and Mechanical Properties IX"*, Boston, MA, 2001.
- [148] F. Nabarro and M. Duesbery, *Dislocations in Solids*, Vol. 10, Elsevier, Amsterdam, 1996.
- [149] R. Srinivasan, G. Eggeler, and M. Mills, *Acta Materialia*, **48**(20), 4867–4878 (2000).
- [150] S. Kohlhammer Phd. thesis, University of Stuttgart, (2001).

- [151] J. Zimmerman, H. Gao, and F. Abraham, *Modelling Simul. Mater. Sci. Eng.*, **8**, 103–115 (2000).
- [152] F. Kayser and C. Stassis, *Phys. stat.*, **64**, 335–342 (1981).
- [153] G. Schoeck, S. Kohlhammer, and M. Fhnle, *Philosophical magazine letters*, **79**(11), 849–857 (1999).
- [154] J. Langer In *Direction in Condensed Matter*; World Scientific, Singapore, 1986; pages 165–186.
- [155] R. Pindak, C. Young, and R. Meyer, *Physical Review Letters*, **45**(14), 1193 (1980).
- [156] D. Turnbull, *Trans. AIME*, **191**, 661 (1951).
- [157] J. Cahn and A. Novick-Cohen, *Acta Materialia*, **48**, 3425 (2000).
- [158] I. Ansara, N. Dupin, H. Lukas, and B. Sundman, *Journal of Alloys and Compounds*, **247**, 20–30 (1997).
- [159] J. Zhu, Z. Liu, V. Vaithyanathan, and L. Chen, *Scripta Materialia*, **46**, 401–406 (2002).
- [160] Y. Wang, D. Banerjee, C. Su, and A. Khachaturyan, *Acta Materialia*, **46**, 2983 (1998).
- [161] A. Ardell, *Acta Metallurgica*, **16**, 511 (1968).
- [162] Y. Wang and A. Khachaturyan, *Philosophical Magazine A*, **72**, 1161 (1995).
- [163] A. Karma, *Physical Review Letters*, **87**(11), 1157011–1157014 (2001).